To the Graduate Council:

I am submitting herewith a dissertation written by Michael Patten Carpenter entitled "Alignment Processes and Shape Variations in ^{184}Pt and ^{183}Au." I have examined the final copy of this dissertation for form and content and recommend that it be accepted in partial fulfillment of the requirements for the degree of Doctor of Philosophy, with a major in Physics.

Leo L. Riedinger, Major Professor

We have read this dissertation
and recommend its acceptance:

Accepted for the Council:

Vice Provost
and Dean of the Graduate School

ALIGNMENT PROCESSES AND SHAPE VARIATIONS IN ^{184}Pt AND ^{183}Au

A Dissertation

Presented for the

Doctor of Philosophy

Degree

The University of Tennessee, Knoxville

Michael Patten Carpenter

March 1988

This dissertation
is
dedicated
to my wife
Jan

ACKNOWLEDGEMENTS

I would first like to acknowledge the Nuclear Physics group at the University of Tennessee of which I have been a member of for the past four and one-half years. I would like to thank this group for offering me the position of a research assistant and for steadily increasing my support over the years. It is my opinion that they have treated me fairly in all the aspects of my tenure with them. Thanks go to both Dr. C. R. Bingham and Dr. M. W. Guidry for their support and encouragement. Special thanks go to Dr. L. L. Riedinger, not only because he is my thesis advisor, but also for providing an atmosphere in which one is able grow professionally through the interaction with the many nuclear physicists who have visited the University through his direct involvement. My thanks for his friendship as well goes without saying.

I would also like to thank the two postdoctoral fellows, Dr. A. J. Larabee and Dr. V. P. Janzen, who I have had the pleasure to work directly with during my stay here. It has been my experience that the "postdocs" are at times saddled with the task of informing naive young minds about the pleasures of rapidly rotating nuclei. I have also been fortunate with my student associates. Lane Courtney has not only come to my rescue through our interactions at the University, but he has also been more than willing to offer me help when needed away from the office. I am also thankful to have been associated with my other fellow students, Wayne Kincaid and Xin-Tao Liu. While this list could continue to grow, I would like to cut it short here and give a thanks for the many friendships I have gained through my association with the Nuclear Physics group at the University of Tennessee. However, I would like to extend one more personal thanks to Dr. L. Zhou for her major contribution on the data analysis of ^{183}Au.

I would like to thank our experimental collaborators at Oak Ridge National Laboratories under the direction of Dr. N. R. Johnson, for having the time

and patience to deal with students from the University which come and use their facility. Certainly, great appreciation is extended to the staff at the McMaster University Tandem Accelerator for without them a large portion of the data for this thesis would not have been collected, nor good friendships made. A special thanks goes to Dr. J. C. Waddington for his help, advice and encouragement. I would also like to thank our experimental colleagues from the Research Institute for Phyiscs in Stockholm, the University de Montréal, and Chalk River Laboratories for their assistants and comments on the interpretation of the data presented here.

Finally, as an experimentalist, I greatly appreciate the opportunity I have had in discussing my research with the many theoreticians who I have had the pleasure to meet, both through Oak Ridge National Laboratory and the Joint Institute for Heavy-Ion Research. I would particularly like to thank Dr. G. Leander for his excellent course on nuclear theory, which provided me with a strong basis for tackling the theoretical aspects of this work, and Dr. J.-y. Zhang for his willingness to answer the many questions which arose during the writing of this work.

I would like to end this section with some personal acknowledgements. I would like to thank my family for the support and encouragement they have provided me over the years. A special acknowledgement goes to my sister, Kelly, because through her, I now understand about true strength and courage. And finally, I would like to thank my wife, Jan, not only for her continual support over the months it took to prepare this work, but also for her eternal pledge of love.

ABSTRACT

High-spin states in the transitional nuclei ^{184}Pt and ^{183}Au were measured via heavy-ion induced reactions. The three reactions used to study ^{184}Pt, ^{172}Yb(^{16}O,4n)^{184}Pt, ^{154}Sm(^{34}S,4n)^{184}Pt and ^{160}Yb(^{29}Si,4n)^{184}Pt, were run at beam energies ranging from 91 to 163 MeV. High-spin states in ^{183}Au were populated using the ^{152}Sm(^{35}Cl,4n)^{184}Pt reaction at 170 MeV. These measurements were performed at three separate facilities, the Holifield Institute for Heavy-Ion Research, McMaster University Tandem Laboratory, and Chalk River Laboratory, using multi-detector γ-ray spectrometers of varied sophistication.

Nuclear levels up to 37 $\hbar$ have been measured in ^{184}Pt. Six new side bands have been identified, and the spins and parities in five of these bands have been firmly established. Four of these side are associated with two-quasineutron configurations, while another side band has been assigned a two-quasiproton configuration.

Levels in ^{183}Au have been observed up to 61/2 $\hbar$. This work represents the first in-beam measurement performed on this nucleus. Four rotational bands have been identified. Two of these structures have been associated with the $\frac{1}{2}$[541] Nilsson configuration, and the other two bands have been assigned the $\frac{1}{2}$[530] and $\frac{1}{2}$[660] configurations. While heavier Au isotopes have identified rotational bands built on the $\frac{11}{2}$[505] Nilsson configuration, such a band has not bee observed in the present data on ^{183}Au.

From the present work, strong evidence has been found which indicates that both $\pi h_{9/2}$ ($\frac{1}{2}$[541]) and $\nu i_{13/2}$ ($\frac{9}{2}$[624]) quasiparticle alignments are occuring at low rotational frequencies in Pt and Au nuclei at $N = 104$ to 108. Since both pairs of quasiparticles occupy different states relative to the Fermi surface, they will polarize the nuclear core in opposite directions in the γ degree of freedom. Conclusions about the dependence of shape on these alignments comes from com-

parison of the spectroscopic data with a set of Cranked Hartree-Fock Bogolyubov calculations, which are performed using the shell correction method. Discrepancies between the present experimental evidence and theoretical predictions are also noted and suggestions for a possible resolution to these differences are also presented.

Contents

List of Figures

List of Tables

CHAPTER 1

INTRODUCTION

High-spin nuclear physics is the study of nuclei displaying collective rotation at high angular momentum. This work describes measurements of rotational bands in the deformed nuclei ^{184}Pt and ^{183}Au. High-spin states in these nuclei were populated via heavy-ion fusion reactions using S, Cl and O beams supplied by the Holifield Tandem Accelerator at Oak Ridge National Laboratory, the McMaster Tandem Accelerator at McMaster University, and the 12 MV tandem accelerator at Chalk River. The γ-ray data were collected using the multi-detector arrays available at these facilities. Extensive model calculations of the nuclear shape as a function of rotational frequency have been performed and compared with these measurements in order to make conclusions about the observed high-spin characteristics of the nuclei under consideration.

The idea that the nucleus might exhibit some type of collective rotation was first proposed by Bohr and Kalckar in 1937. However, it was not until the early fifties that nuclear rotational bands were first predicted and observed. Since then, nuclear rotation has been studied extensively by nuclear physicists, partly due to the fact that the collective nature enables a description of the observed nuclear spectra in terms of only a few degrees of freedom. Chapter 2 of this work will review the ideas of collective rotation in nuclei and will present some of the current theoretical models which are presently in use to describe nuclear structure in the regime of high-angular momentum.

Within the last decade a number of technical developments have given great impetus to the study of nuclei at high angular momentum. These developments have been in the areas of heavy-ion accelerators and multi-detector arrays. In the area of accelerators, a number of facilities now exist which can provide a va-

riety of beams with enough energy and beam intensity to transfer large amounts of angular momentum to the final system via a number of different nuclear reactions. The efficiency and sensitivity at which the emitted γ-rays are detected have also increased greatly with the design and building of multi-detector arrays. These arrays generally are composed of a large number of sodium iodide (NaI) or bismuth germanate (BGO) detectors (≈ 70) which measure the bulk properties of the nuclear event, such as the total γ-ray energy and multiplicity emitted during the nuclear reaction. These large groupings of detectors are coupled with a smaller number of Compton-suppressed Ge detectors (10-20) which measure with good resolution the energy of individual γ-rays. These technical developments have allowed for a large amount of experimental data to be taken on nuclei in the spin range of 20-40 $\hbar$. From this vast storehouse of data, much has been learned about the sharing of angular momentum between rotational and single particle modes in yrast and near-yrast excitations of the nucleus. Chapter 3 will review the mechanisms used for imparting large amounts of angular momentum to a nucleus and examine the experimental setups used in this study to make spectroscopic measurements on ^{184}Pt and ^{183}Au.

Quantum mechanically, a sphere cannot rotate. Therefore, to study collective nuclear rotation, one must choose nuclei whose static shapes are non-spherical. Nuclei which have nucleon numbers at or near closed shells prefer spherical shapes, but as more nucleons are added to the valence shell, the nucleus begins to take on a deformed structure. Fig. 1.1 shows regions in the $Z - N$ plane where one has found or expects to find deformed nuclei. In the past several years, the high-spin structure of nuclei on the neutron-deficient side of stability in region 2 has been studied extensively because of their high fission limit and large deformations. These nuclei are located in the rare-earth region of the periodic chart with nucleon number ranging from $150 \leq A \leq 190$. High-spin states have

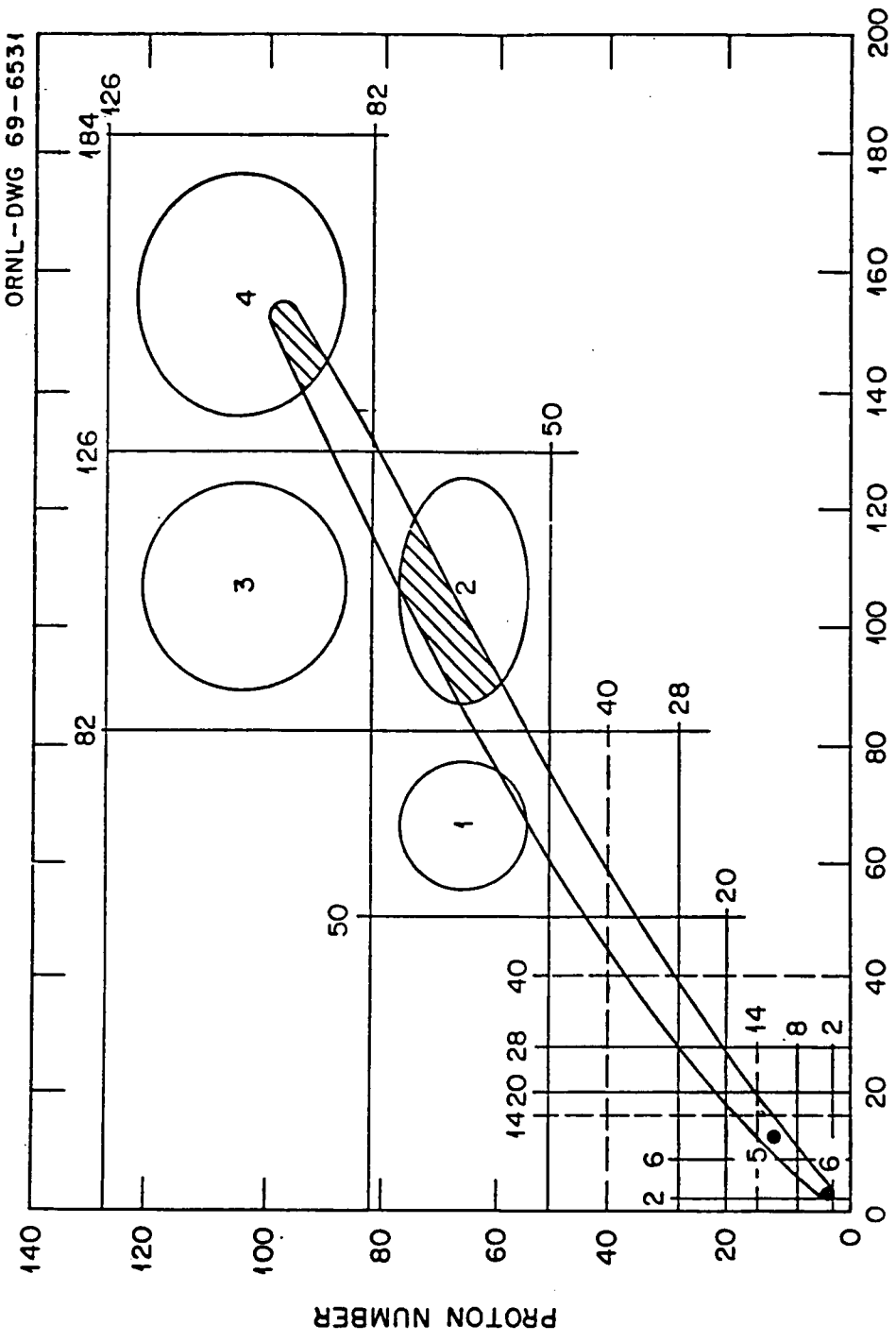

Figure 1.1: Regions of deformation as a function of neutron and proton number.

been observed to $I \geq 40\ \hbar$ in many of these nuclei. On the other hand, in the upper-part of this region, nuclei have not been examined as extensively via heavy-ion reactions, because it was thought that fission and charged particle emission would inhibit the population of high-spin states. In the last several years, a number of new measurements have shown that while fission does present a problem, observation of discrete states as high as 35 $\hbar$ along the yrast line (see this work) is possible with the right combination of beam and target.

The studies discussed in the following work are centered around two nuclei, ^{184}Pt ($N = 106$) and ^{183}Au ($N = 104$), which are situated in the upper part of region 2, right below the proton shell closure at lead. In this region, within the same nucleus, different structures have been observed which are associated with significantly varied shapes. These shapes are thought to fall within two categories; well-deformed prolate and slightly- to moderately-deformed oblate shapes. As a general rule, nuclei with their valence orbitals filled to mid-shell or lower favor prolate shapes, while nuclei with their upper shells filled favor less deformed oblate shapes. Thus, this shape "coexistence" found in these Pt-Au nuclei occurs due to the fact that a balance has been reached between the two competing structures. While the low-spin features associated with this shape coexistence has been well studied, the competition between these two shapes at higher spins is less known.

Because of the residual pairing force, pairs of nucleons in time reversed orbits couple together within the nuclear core. One effect rotation has on the nucleus is that the paired quasiparticles which have large individual components of angular momentum along the rotational axis feel the Coriolis force most strongly. The Coriolis force acts to decouple these high-j quasiparticles from the core and align them with the rotational axis. One consequence of the shape-coexistence phenomenon discussed above is that nuclei exhibiting it tend to have nuclear cores whose shapes are easily influenced by external forces. Since quasiparticles which

decouple from the nuclear core define their own equilibrium shapes, one might expect large fluctuations in the nuclear shape before and after these particles are aligned, if their preferred shape is much different from that of the core.

If one is to make predictions about the nuclear shape along the yrast line, it is important to determine the quasiparticle nature of the decoupling pairs. In some sense, the Pt-Hg transitional nuclei represent the last group of neutron deficient nuclei in region 2 of Fig. 1.1 where this quasiparticle nature has yet to be fully confirmed. The quasiparticles which are most likely to align first in this region are the $i_{13/2}$ quasineutrons and the $h_{9/2}$ quasiprotons. At $\hbar\omega \approx 0.0$ MeV for $N = 104$ and 106, these quasiparticles are associated with the $\frac{9}{2}[624]$ and $\frac{1}{2}[541]$ Nilsson configurations. Measurements by Beshai *et al.* (1986) on the higher spin levels in ^{184}Pt indicated that the $\nu i_{13/2}$ quasiparticles were most probably the only quasiparticles aligned below a rotational frequency of $\hbar\omega = 0.30$ MeV. However, Kahler *et al.* (1978) performed a similar measurement on ^{185}Au and concluded that the $h_{9/2}$ quasiproton pair, and not $i_{13/2}$ quasineutrons, were aligning at low rotational frequencies.

Since the polarizing effect aligning quasiparticles have on the nuclear core is dependent on where they lie with respect to the Fermi surface, the $\nu i_{13/2}$ (mid-shell) and $\pi h_{9/2}$ (low-shell) quasiparticles should polarize the nuclear core in different ways. Because the nuclear core should be sensitive to the aligning quasiparticles, the nuclei in the Pt-Au region allow one an opportunity to make conclusions about the shape effects by comparing the available spectroscopic data with the results from theoretical calculations, preferably calculations with some sense of self-consistency with respect to the varied parameters.

In order to establish which pairs of quasiparticles are aligned first and thus test the predictive powers of the theoretical models, recent studies have been undertaken on Ir, Pt and Au nuclei at $N = 106$ and $N = 104$. The nuclei reported

on in this work are a subset of this larger study. Chapter 4 of this work will discuss the establishment of the decay schemes for both ^{184}Pt and ^{183}Au. Chapter 5 will concentrate on the analysis of ^{184}Pt. Conclusions about the dependence of the nuclear shape on the quasiparticle configuration will be made from comparison of the spectroscopic data with the results from a set of total Routhian surface (TRS) calculations. These calculations permit a self-consistent determination of the shape parameters associated with the nucleus as a function of rotational frequency and quasiparticle configuration. Chapter 6 will examine the ^{183}Au data in detail, drawing on the implications of the ^{184}Pt data in an attempt to analyze the Ir-Au systematics at $N = 104$. Chapter 7 will summarize the conclusions reached from the analysis of these two nuclei and will suggest future experimental and theoretical work which should be done in order to help confirm these conclusions.

Recent results from this large study have been previously reported in Larabee *et al.* (1984 and 1986), M. P. Carpenter *et al.* (1985, 1986a, 1986b, 1987a and 1987b), L. L. Riedinger *et al.* (1986a, 1986b, 1987a, and 1987b) and V. P. Janzen *et al.* (1987).

CHAPTER 2

THEORY

2.1 Nuclear Angular Momentum

One encounters examples of rotating systems daily. For example, the path a baseball follows to home plate is dependent on the amount of angular momentum the pitcher imparts to the ball as he throws it. However, this path is not determined by the angular speed of the ball alone, rather the resulting motion is due to a complex coupling between rotation, air density, gravity, and the roughness of the ball. The earth is also a rotating system which possesses both spin and orbital angular momentum. These two modes are not as strongly coupled as they are in nuclear systems; however the spinning of the earth around an axis is worthy of review, because in some sense it can give insight into the properties of nuclear rotation.

The earth is not spherical, but rather slightly oblate. The flattening at the earth's poles is due to the centripetal acceleration produced by the rotating earth. If the earth were a liquid, rotation would deform it into the shape of an ellipsoid whose surface would be an equipotential surface of the combined fields produced by gravity and centripetal acceleration. In fact, the mean level of the earth's seas conforms rather closely to this equilibrium ellipsoid.

The atomic nucleus, unlike the rotating earth, is not a classical but rather a quantal system composed of a finite number of strongly-interacting fermions. Since fermions obey the Pauli principle, their very nature prevents them from getting very close to one another, even though the force binding them together is strongly attractive. This gives rise to a nuclear system which is not very dense, but unlike a gas, has a very well-defined surface.

When the nucleus is at or near the ground state, the nuclear level density is not very large; thus, the states available for individual nucleons to occupy are limited. Since nucleons are fermions, the Pauli principle prevents individual nucleons from strongly interacting with one another due to the lack of states for particles to scatter into. The resulting effect is that individual nucleons follow, to first order, unperturbed paths inside the nucleus similar to the orbiting of electrons in an atom. The single-particle motion of the nucleons can be described by a shell model which assumes that the individual nucleons are acted upon by an average field created by the contributions from all the nucleons. This model is known as the independent particle model (IPM).

Strong evidence for independent particle motion in nuclei comes from examining the energy required to separate the least bound neutron or proton from a nucleus as a function of either the neutron or proton number. For most nuclei, this separation energy is approximately 8 MeV; however, there are noticeable exceptions at "magic" neutron or proton numbers 2, 8, 20, 28, 50, 82 and 126,[1] where the separation energy becomes largest. This identical effect is observed for electrons as well and is a direct consequence of the shell structure of the electronic orbitals.

While the latter sections of this chapter describe in detail the relationship between the independent particle model and the collective rotation of nuclei, a short introduction to nuclear angular momentum is first in order. Because the nucleus is a quantal system, classical perceptions of rotation cannot always be applied to a rotating nucleus. For example, a rotating object presupposes a definite spatial orientation. A quantum sphere has no such orientation, and therefore, cannot rotate. However, if the sphere is deformed into a prolate ellipsoid, the symmetry axis can be used to specify the orientation of the system; thus, rotation

[1]Nucleon number 126 refers to neutrons only.

around an axis other than the symmetry axis is possible. In the case of axially symmetric deformations, the deformation only partially defines the orientation of the intrinsic coordinate system and rotations around the symmetry axis are still restricted (see Bohr and Mottelson, 1975).

This principle can be directly applied to nuclei. As is discussed in detail in the next section, at equilibrium, many nuclei are symmetrically deformed due to the nucleonic shell structure. Correspondingly, it is possible for these nuclei to rotate around an axis perpendicular to the symmetry axis. Microscopically, collective angular momentum is generated by the partial alignment of many of the nucleonic angular momenta. On the other hand, nuclei which are spherical are unable to rotate collectively. Angular momentum is generated in such systems by the excitation of individual nucleons to unoccupied nuclear states, which is similar to the excitation of electrons to excited atomic states.

Whether or not a nucleus generates angular momentum via collective rotation is reflected in the individual nuclear spectrum. The energy spectrum of a deformed nucleus generating collective angular momentum is regular and well correlated. In fact, the ground-state bands of many even-even deformed nuclei at spins below 12^+ follow quite nicely the $I(I+1)$ rule associated with a quantum mechanical rotor:

$$E = \frac{\hbar^2}{2\mathcal{J}} I(I+1), \tag{2.1}$$

where $\mathcal{J}$ is defined as the moment of inertia. In a spherical nucleus, the energy spectrum is irregular and dependent on the detailed spacings of the single-particle levels. Fig. 2.1 shows typical energy spectra associated with a well-deformed rotational nucleus and a near-spherical nucleus.

The generalized Hamiltonian used for the study of rotating nuclei utilizes

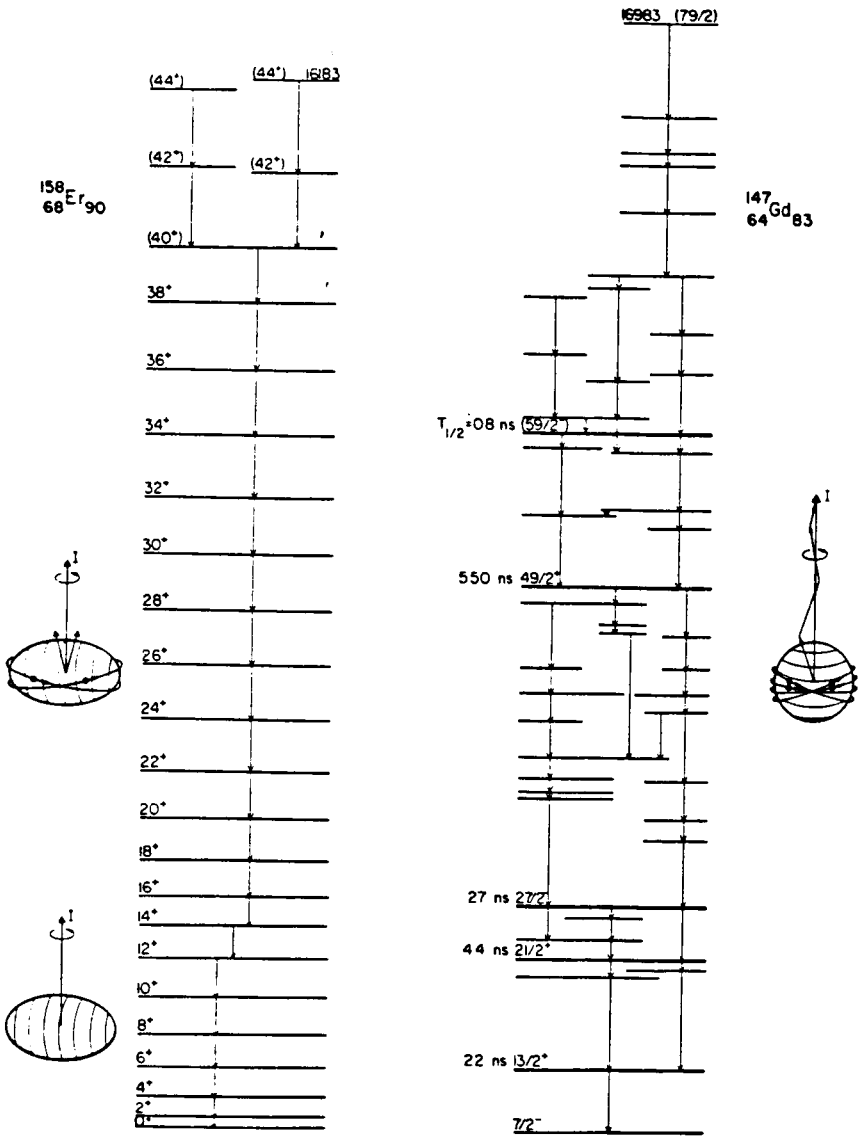

Figure 2.1: Typical level structures of a well-deformed and a near-spherical nucleus. Reproduced from Riezebos (1987).

the independent particle model in a rotating potential and can be written as

$$H^{\omega} = H - \omega J_x, \tag{2.2}$$

where H represents the average field and ωJ_x represents the Coriolis and centrifugal forces brought about by rotation. More explicitly, ω is the rotational frequency of the nucleus and J_x is the projection of the angular momentum vector onto the rotational axis. Fig. 2.2 shows a schematic diagram of a prolate nucleus rotating around an axis perpendicular to the symmetry axis.

The Hamiltonian, H^{ω}, is referred to as the cranking Hamiltonian and represents a transformation from the laboratory frame to the rotating body-fixed or intrinsic system.[1] The term cranking implies that calculations are done at a fixed ω. The use of the cranking Hamiltonian comes from a procedure suggested by Inglis (1954,1955) known as the cranking model. The transformation to the body fixed frame, which rotates with frequency, ω, with respect to the laboratory coordinate system, is preferable, because it reduces the time-dependent Shrödinger equation to a stationary equation. These two coordinate systems are related by the transformations

$$\begin{aligned} x' &= x \\ y' &= y\cos(\omega t) + z\sin(\omega t) \\ z' &= z\cos(\omega t) - y\sin(\omega t). \end{aligned} \tag{2.3}$$

While the quantum mechanical derivation of Eq. 2.2 is shown in section 2.7, it is instructive to see how this equation is derived classically. Following closely the derivation of Bengtsson and Garrett (1983), the kinetic energy, T, of an object in the body-fixed coordinate frame can be written, using the transformations

[1]This transformation is equivalent to Routh's procedure for such a change of variables in classical mechanics. Hence the eigenvalues calculated from Eq. 2.2 are often referred to as Routhians.

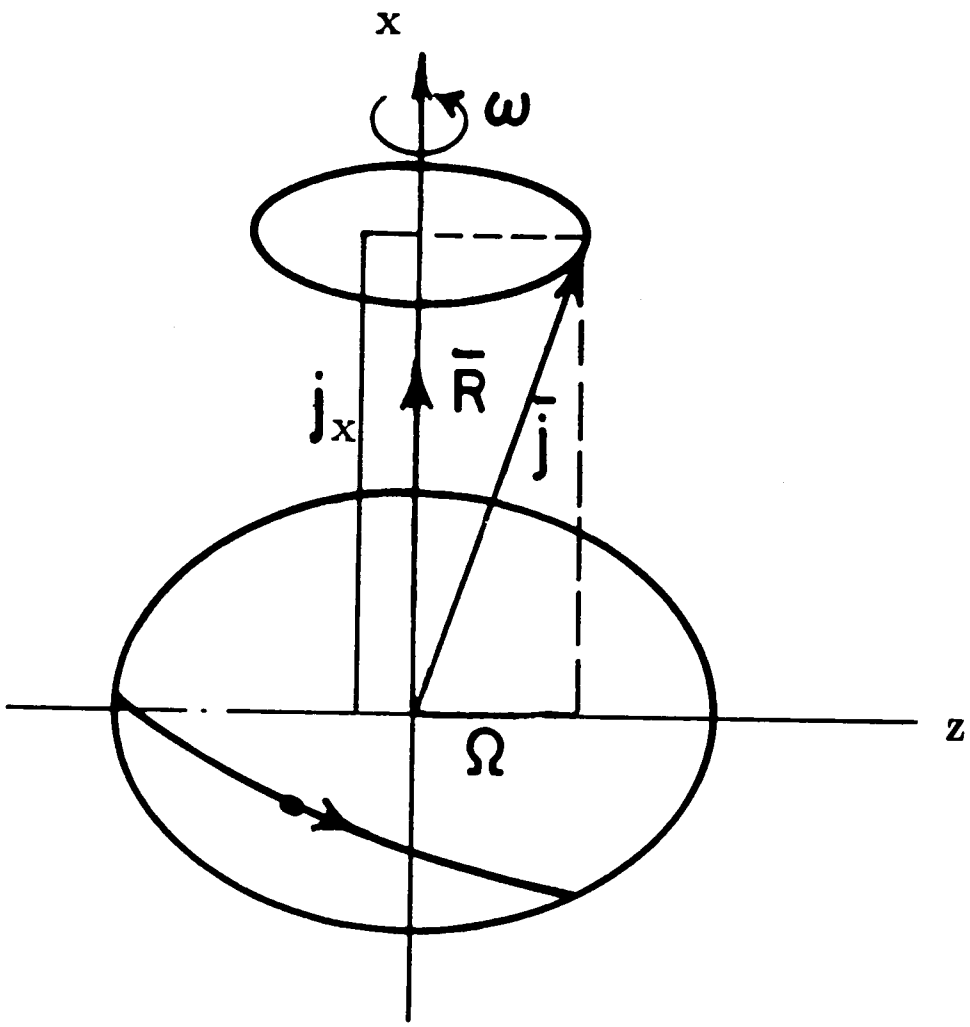

Figure 2.2: Schematic diagram of a nucleus rotating around an axis perpendicular to the symmetry axis.

above, as

$$T = \frac{1}{2}m\left\{\dot{x}'^2 + \dot{y}'^2 + \dot{z}'^2 - 2\omega(\dot{y}'z' - \dot{z}'y') + \omega^2(y'^2 + z'^2)\right\}. \tag{2.4}$$

If this object also moves in a potential, $V(x', y', z')$, the Lagrangian, L, is written as

$$L(x', y', z') = T(x', y', z') - V(x', y', z'). \tag{2.5}$$

It can be easily shown using the Lagrange equations that the total force acting on the object in the body-fixed frame is

$$m\ddot{\mathbf{r}}' = -\nabla V(x', y', z') + 2m\boldsymbol{\omega} \times \dot{\mathbf{r}}' - m\boldsymbol{\omega} \times (\boldsymbol{\omega} \times \mathbf{r}'). \tag{2.6}$$

The first term on the right hand side represents the "true force" acting on the object. The Coriolis and centrifugal forces are represented by the second and third terms, respectively. These terms in the equation of motion are often referred to as *inertial* or *fictitious forces*, because they are not due to interactions with other bodies, as are ordinary forces, but stem from the choice of the reference system. Whether or not one wishes to refer to them as "forces" is a matter of terminology; however, they do effect the motion of objects when viewed from the non-inertial coordinate system.

Before one constructs the Hamiltonian for the body-fixed system, the canonical momenta must be defined using $p_i' = \partial L/\partial \dot{x}_i'$. By utilizing the transformations of Eq. 2.4, one can express these momenta as

$$\begin{aligned} p_x'^2 &= (m\dot{x}')^2 \\ p_y'^2 &= m^2(\dot{y}'^2 - 2\omega\dot{y}'z' + \omega^2 z'^2) \\ p_z'^2 &= m^2(\dot{z}'^2 - 2\omega\dot{z}'y' + \omega^2 y'^2). \end{aligned} \tag{2.7}$$

The Hamiltonian, H^{ω}, expressed in the rotating coordinate system now becomes[1]

$$H^{\omega} = \frac{1}{2m}\mathbf{p}'^2 + V(x', y', z') - \omega(y'p'_z - z'p'_y). \tag{2.8}$$

The last term in Eq. 2.8 is immediately recognizable as the component of the angular momentum along the x-axis (from $\mathbf{L} = \mathbf{r} \times \mathbf{p}$). The first two terms in Eq. 2.8 are just what one would expect for the Hamiltonian in a non-rotating reference frame. Thus, H^{ω} may be rewritten as

$$H^{\omega} = H' - \omega L'_x. \tag{2.9}$$

If one is considering nuclear rotation, it must be realized that nucleons possess spin as well as orbital angular motion. Thus, L_x must be replaced by J_x in Eq. 2.9, where $J_x = L_x + S_x$. Once this replacement is made, Eq. 2.9 is identical to the nuclear cranking Hamiltonian in Eq. 2.2.

In concluding this section, the equivalency of equations 2.2 and 2.9 implies that Coriolis and centrifugal-like forces are present in both classical and quantal systems when viewed from the rotating coordinate frame. Referring back to the rotating earth, it has been shown that the classical perceptions of inertial forces also translate to the quantal system. However, the earth is a large body with a continuum of energy states, while the nucleus is a quantal system with a shell structure and a discrete set of energy states. Even though the rotating earth model helps one conceptualize the deforming effects rotation imposes on a nucleus, there are other degrees of freedom to be considered in a nucleus which are not applicable to a classical body. In short, one should be careful not to take the analogy between rotating classical and quantal objects too literally. Differences do exist, and one aspect of the study of rotating nuclei is ascertain what these differences are.

[1]The Hamiltonian is constructed by relating the Lagrangian to H^{ω} through the expression $H = \sum \dot{x}'_i \frac{\partial L}{\partial \dot{x}'_i} - L$.

2.2 Nuclear Ground States

Nuclei in their ground states can take on a number of different spheroidal shapes: spherical, oblate (two semi-major axes equal), prolate (two semi-minor axes equal), and triaxial (all three principal axes different). One possible parameterization of the nuclear surface is defined as

$$R(\theta,\phi) = R_0\left(1+\beta_{00}+\sum_{\lambda=1}^{\infty}\sum_{\mu=-\lambda}^{\lambda}\beta^*_{\lambda\mu}Y_{\lambda\mu}(\theta,\phi)\right), \tag{2.10}$$

where R_0 is the radius of a sphere with the same volume as the parameterized shape. For all but the highest excitation energies, the nuclear volume remains constant, independent of shape. The parameter β_{00} is determined by the requirement that the nuclear volume stay fixed for all deformations. Terms which include $\lambda = 1$ describe a shift of the whole system. The $\beta_{1\mu}$ constants are kept fixed by requiring that the origin coincides with the center of mass. This is fulfilled automatically, if only even values of λ are included in the sum of Eq. 2.10. Since the above requirements fix both β_{00} and $\beta_{1\mu}$, they are usually excluded in the parameterization of the nuclear shape. In the realm of high-spin nuclear structure, it is usually sufficient to include only the $\lambda = 2$ and $\lambda = 4$ degrees of freedom in the parameterization of Eq. 2.10 [1]

The equilibrium nuclear shape for the ground state is determined by the summed contributions from three effects: (1) that due to the microscopic single-particle characteristics of the nucleus, (2) contributions from the macroscopic binding energy and (3) the electrostatic repulsion resulting from the positively charged protons. The macroscopic binding energy, properties of which are similar to those of a liquid drop, is minimized for spherical shapes due to a minimum number of nucleons lying on the nuclear surface. On the other hand, the electrostatic repulsion

[1] It should be noted that some nuclei have octupole shapes, $\lambda = 3$, at non-zero excitation, although no cases have been found for nuclei in their ground state.

of the protons favors non-spherical shapes. This effect increases with increasing Z and leads to the fissioning of the heaviest nuclei.

The deforming effects induced by the single-particle structure of the nucleus are best illustrated by examining a plot of the single-particle energy levels as a function of the quadrupole deformation. Fig. 2.3 is an example of such a plot, where the single-neutron levels were calculated using an axially symmetric (Nilsson) potential with the quadrupole deformation parameterized by ϵ_2. Positive ϵ_2 values are associated with prolate shapes while negative ϵ_2 values correspond to oblate deformations. At $N = 82$ the single-neutron spectrum of states favors spherical shapes, because the single-particle orbitals around the Fermi surface[2] lie lowest in energy for non-deformed orbitals, *i.e.* $\epsilon_2 = 0$. As more nucleons are added to the system, they must occupy orbitals in the next shell, which are sloping steeply downward as $\mid \epsilon_2 \mid$ increases. The larger density of these downsloping orbitals for positive ϵ_2 values ensures that the single-particle states energetically favor prolate deformations in the lower portion of shell. The level densities in the middle of the shell also minimize for positive ϵ_2 values, while at the upper end of the shell, the single-particle densities energetically favor oblate deformations. Once again it should be mentioned that the overall equilibrium shape is dependent not only on the microscopic shell structure but also on macroscopic features as well. The coupling of these microscopic and macroscopic effects is the basis of the shell correction method, which will be discussed in section 2-8.

A good example of how the ground state shape of the nucleus changes as a function of nucleon number is seen by examining the nuclei on the neutron deficient side of the β-stability line in the rare-earth region (region 2 of Fig. 1-1). This region ranges from $Z = 62$ to 82 (Sm–Pb) and $N = 82$ to 120. Fig. 2.4

[2]Here the Fermi surface is the energy which separates the filled single-particle states below it with the empty single-particle states above it.

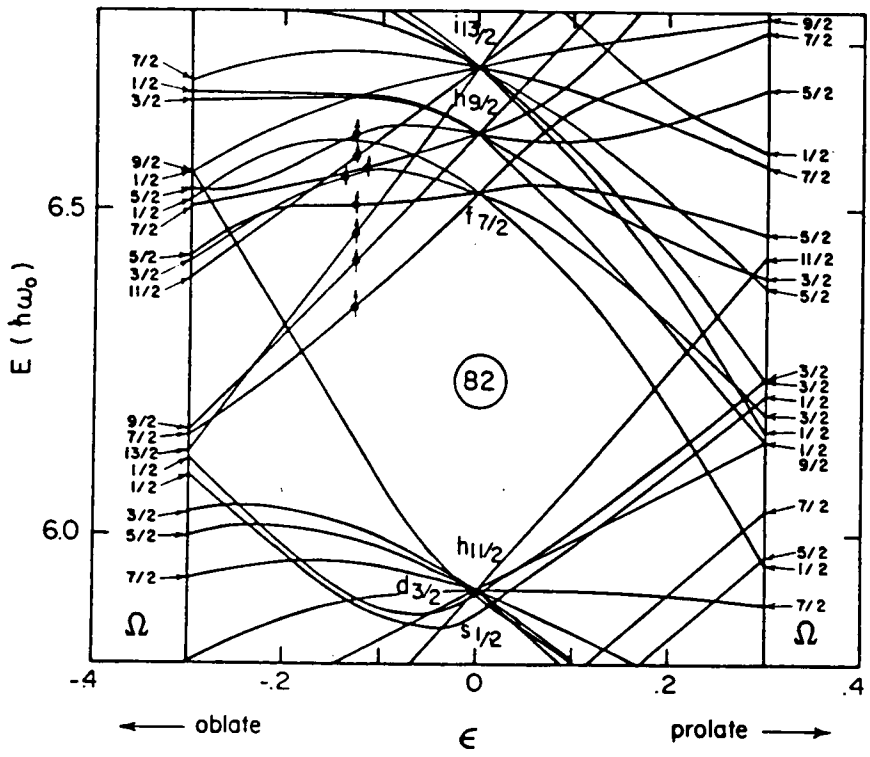

Figure 2.3: Calculated energy levels for independent neutron motion in a spheroidal potential (Nilsson) of quadrupole deformation ϵ_2. Reproduced from Garrett (1986).

shows the expected quadrupole and hexadecapole deformations for the ground state bands of the even-even nuclei in this region. These equilibrium values were calculated using the independent particle model with a Woods-Saxon potential coupled with the shell correction method (see section 2.8). The deformations were determined by minimizing the calculated energy with respect to β_2 and β_4.

One feature of Fig. 2.4 is the parabolic-like nature of the isotopic chains. This is partially explained by examining the single-particle levels as a function of shell filling. At the lower portion of this region, $N = 82$ to 86, nuclei take on near spherical shapes, because they are close to the $N = 82$ closed shell. As more neutrons are added to the valence shell, these nuclei begin to take on well-deformed prolate shapes. Fig. 2.4 shows that the transition from spherical to prolate shapes is not sharp but varies smoothly as a function of N. One can define the region from $N \approx 87$ to 91 as a transitional region, where the balance between spherical and deformed shapes is just beginning to favor prolate deformations. Such a region is interesting, because the shape competition between spherical and well-deformed shapes makes the nucleus "soft" with respect to deformation. Soft nuclei are greatly influenced by external forces, making them good candidates for studying the effects rotation and surface vibrations have on the nuclear structure. As one enters into the middle of the neutron shell, each isotopic chain reaches its maximum quadrupole deformation at $N \approx 102$. A decrease in the quadrupole deformation after this peak is partially due to the shell filling of the neutron orbitals into regions where less deformed oblate and near spherical shapes are energetically favored.

The hexadecapole degree of freedom (β_4) also shows a smoothly changing behavior with respect to N and Z. This is due to the fact that the nucleus favors positive β_4 values in the lower portion of the shell and negative values in the upper portion. The equilibrium hexadecapole value for a particular nucleus is determined by the influences due to both single-neutron and single-proton orbitals.

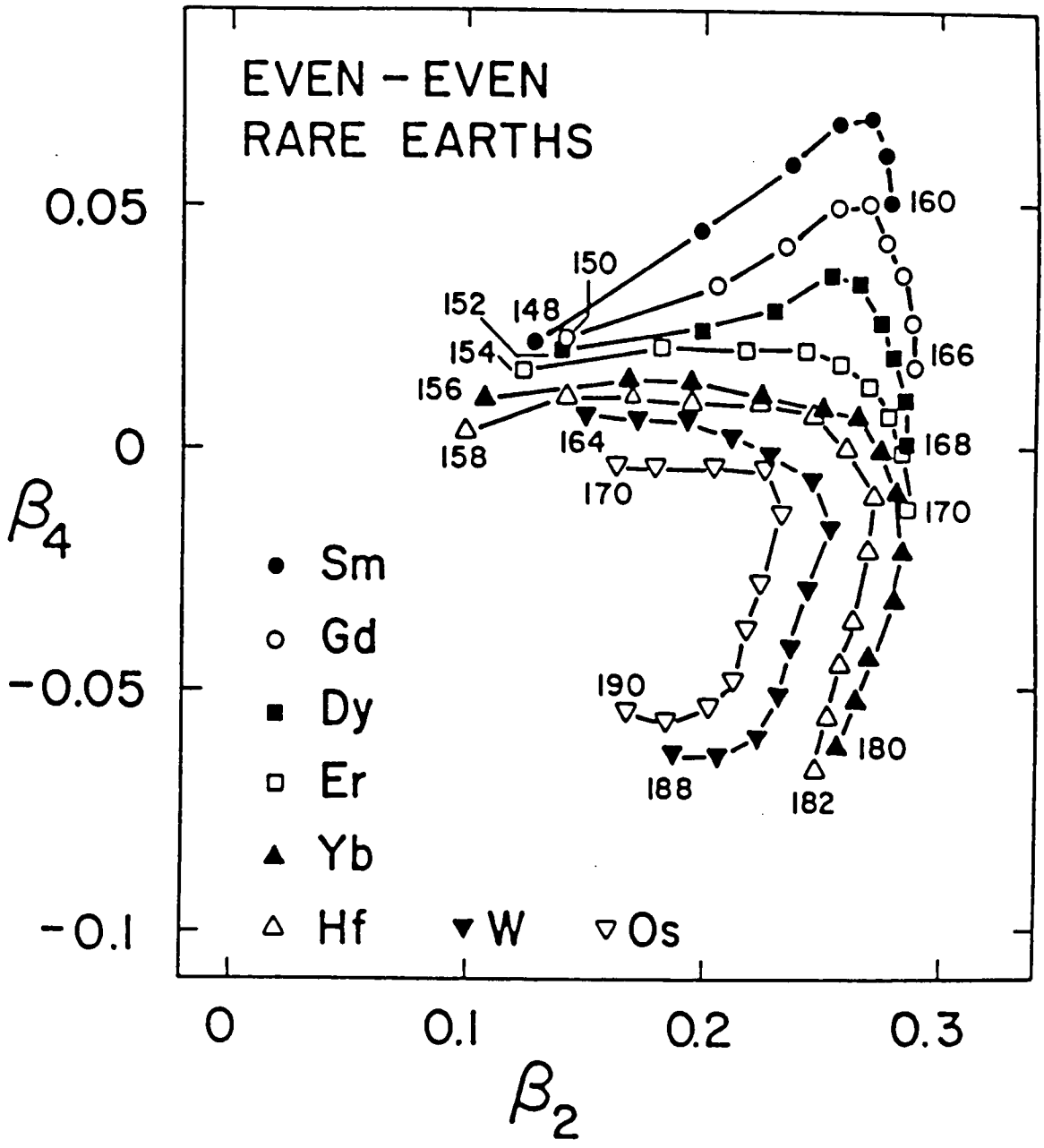

Figure 2.4: Predicted ground-state deformations for neutron deficient deformed nuclei in the rare-earth region, using a Woods-Saxon potential. The data represented were calculated using the shell correction method and minimizing the energy with respect to β_2 and β_4 (Riley and Nazarewicz, 1987).

Another feature of Fig. 2.4 is the continual decrease in the quadrupole deformation as a function of Z for constant N. This occurs because as more protons are added to the shell, they begin to approach the shell closure at $Z = 82$, where spherical shapes should dominate. This leads to the presence of another transitional region among the Pt-Hg nuclei at $N \approx 106$. This transitional region is markedly different from that at $N \approx 88$. Instead of having a gradual transition from well-deformed to near spherical shapes, both shapes are found to coexist in the same nucleus. The discovery of shape coexistence in the Hg isotopes at $Z = 80$ was especially surprising since they are so close to the $Z = 82$ closed proton shell. A microscopic understanding of the structure of these unexpected deformed bands has been proposed by Wood (1982) in terms of a proton-intruder model. In this picture, the $h_{9/2}$ orbitals, which lie above the $Z = 82$ shell gap at spherical shapes, are brought down in energy relative to the "normal" configuration by the attractive proton-neutron residual force. Since the "normal" configuration prefers the near-spherical oblate shape, it is the presence of the proton-intruder configuration which gives rise to the well-deformed prolate shape. The proton-neutron interaction is predicted to be strongest in this region when N lies in the middle of the shell, i.e. $N \approx 104$. Therefore, this shape-coexistence is not observed in the light Pt and Hg nuclei until $N < 110$. It should also be mentioned that calculations done by Bengtsson *et al.* (1987), utilizing the shell-correction method with both a Woods-Saxon and a Nilsson potential, have been able to qualitatively reproduce the relative energy differences between the coexisting shapes in the Pt and Hg isotopes. This is interesting, because the independent particle model assumes that there is no residual interaction between protons and neutrons. It has been proposed that this residual interaction comes into the model through the coupling of the microscopic single-particle orbitals to the collective deformation. It will be interesting to see if further investigations can uncover the relationship between the

independent particle model and the proton-neutron residual interaction.

2.3 Structure Along the Yrast Line

The previous section demonstrated how the nuclear shell structure determines the ground-state deformation of the nucleus. If excitation energy is added to the system, it can be used to excite either the nuclear single-particle or collective degrees of freedom. The distribution of this energy depends largely on the mechanism used to excite the nucleus. In a heavy-ion fusion reaction, a large amount of excitation energy and angular momentum is imparted to the compound system after fusion. Since the compound nucleus is highly excited, particle emission dominates over γ-radiation and several neutrons are evaporated. After particle emission is no longer probable, the highly excited final nucleus de-excites by a cascade of γ-rays. Fig. 2.5 is an illustration that summarizes the formation and subsequent decay of a compound nucleus. (Twin, 1987).

Statistical $E1$-transitions from the continuum are the first to be emitted by the nucleus (see section 3.2) after a heavy-ion fusion reaction, once γ-ray emission begins to compete with particle evaporation. After these γ rays have been emitted, the residual nucleus is in an excited state at or the near the "yrast" line. The yrast line is defined as the line connecting the "yrast" levels, and an yrast level is that nuclear energy state of a given angular momentum having the lowest excitation energy.[1] Since the excitation energy of a yrast level is used entirely to generate angular momentum, there is a minimum amount of intrinsic excitation of the nucleus in the region near the yrast line. This fact coupled with the low level densities associated with yrast states makes this region easier to study and understand than those at higher excitations. Near closed shells, the yrast line

[1] *Yrast* is a Swedish term meaning "dizziest". This term was applied to nuclear levels, because for a given energy the yrast level has the highest angular momentum, *i.e.* is the "dizziest" state at that energy (Grover, 1967).

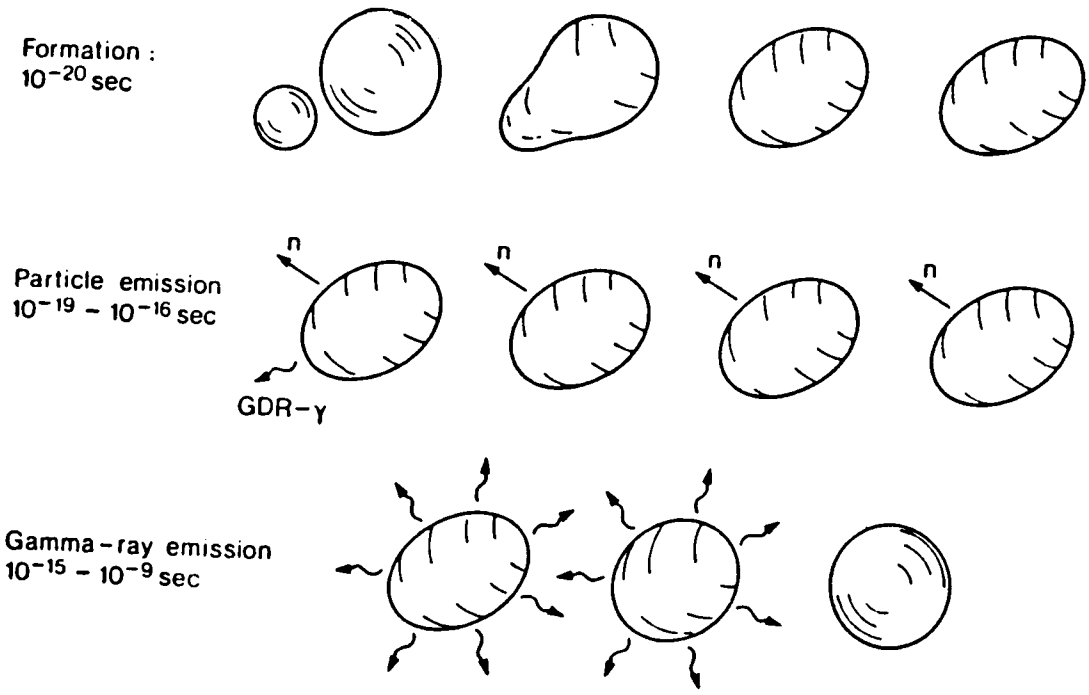

Figure 2.5: Schematic of the formation and decay of a compound nucleus. Reproduced from Twin (1987).

is composed of levels having different intrinsic structures with small transition matrix elements connecting them. For deformed nuclei, this line corresponds to a rotational band, and the de-excitation process takes place by "collective" $E2$ transitions.

In the ground state, all nucleons are paired up into time reversed orbits due to a residual pairing force (see section 2.6). If the average separation between nuclear energy levels near the Fermi surface is approximately 300 keV or less as is the case for deformed nuclei, the nucleus becomes superfluid, and nucleonic pairs may scatter to unoccupied orbitals near the Fermi surface without costing the system any loss in energy. One piece of experimental evidence supporting the existence of pair correlations is the reduction of the observed moments of inertia by two to three times the rigid-body value at low angular momentum. This is due to strong irrotational (superfluid) components introduced into the flow pattern of nuclei by the pairing correlations.

Once the nucleus begins to rotate, the Coriolis and centrifugal forces counteract the pairing correlations and try to align the individual nuclear angular momentum vectors along the rotational axis. This effect is illustrated in Fig. 2.6. It is the competition between the residual pairing force and the rotational forces which dictates any change in the nuclear structure at low and medium spins along the yrast line. For low angular momentum, the structure of the nucleus is very similar to that of the ground-state. However, as I increases, the Coriolis force becomes stronger and should eventually dominate over the pairing force. Mottelson and Valatin (1960) were the first to recognize this possibility. By following closely the formalism used to show the collapse of superconductivity in metals due to an increasing external magnetic field (Meissner effect), they predicted that at $I \approx 12\ \hbar$ for $A \approx 180$ a total collapse in the pair correlations should occur due to the strength of the Coriolis force [*Coriolis anti-pairing* (*CAP*)]. At the time of

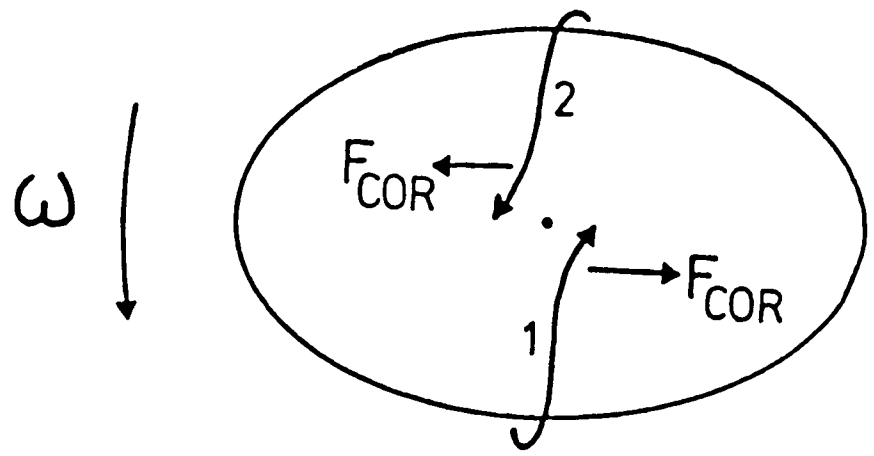

Figure 2.6: Diagram illustrating the Coriolis and centrifugal force vectors (large arrows) for nucleons moving in time reversed orbits in deformed nucleus rotating about an axis perpendicular to the symmetry axis.

their prediction, states had been observed only up to 8 $\hbar$ for $A = 180$. Thus, the first major prediction regarding the effects of rotation on nuclear structure challenged the experimental community to develop methods for populating and detecting nuclear states to higher angular momentum.

Mottelson and Valatin reasoned that a completely different intrinsic structure from that of the ground state should be present in nuclei at $I > I_c$. This structure would involve the complete disassociation of the paired particles from one another resulting in uncorrelated single-particle motion. They further hypothesized that this change would be marked by a rapid increase in the moment of inertia. Such a signature was first observed in the yrast band of ^{160}Dy (Johnson *et al.*, 1972), which was found to abruptly change at $I = 16^+$. This change was marked by a compression of energy levels in the nuclear spectrum and has come to be known as backbending. The backbending phenomenon results in a large increase in the moment of inertia, which had been predicted by Mottelson and Valatin as resulting from the quenching of pairing correlations by the CAP effect.

However, the moment of inertia in ^{160}Dy after the backbend was found to be less than the rigid-body value, indicating that the pairing correlations had not been completely eliminated. To address this, Stephens and Simon (1972) offered another explanation which attributed the backbending effect, not to the "breaking" of all nucleon pairs, but rather to the decoupling of only a single pair of high-j nucleons from their time reversed orbits and their immediate alignment with the rotational axis. This picture is now the accepted explanation for the backbending phenomena and is referred to as the rotational alignment scheme (RAL) (see Fig. 2.7).

The decoupling of only a single-pair of nucleons due to rotation is possible, because the Coriolis and centrifugal forces depend not only on the rotational frequency, but also on the amount of angular momentum projected on to the rotational axis, J_x (see Eq. 2.10). Since J_x is composed of a sum over all single particle contributions ($\sum j_x$), the Coriolis force acts most strongly on particles with the largest values of j_x.

Fig. 2.7 shows a schematic representation of rotational alignment involving two $i_{13/2}$ particles with projections $\pm\Omega$ along the the symmetry axis of a prolate nucleus. Fig. 2.7a shows the nucleus in its ground state, with the nucleonic pair orbiting the nucleus in time reversed orbits. When the Coriolis force on this pair of nucleons overcomes the pairing force, the two particles decouple from the core and align their angular momentum vectors as close to the rotational axis as possible (Fig. 2.7b). The extra angular momentum gained through the decoupling process is referred to as the single-particle alignment, i, and it is just the sum of the angular momenta of the two aligned particles along the rotational axis. For example, the alignment of two $i_{13/2}$ particles can add as much as 12 $\hbar$ units of angular momentum to the nuclear system.

Once a pair aligns, the yrast band is no longer identified with the ground

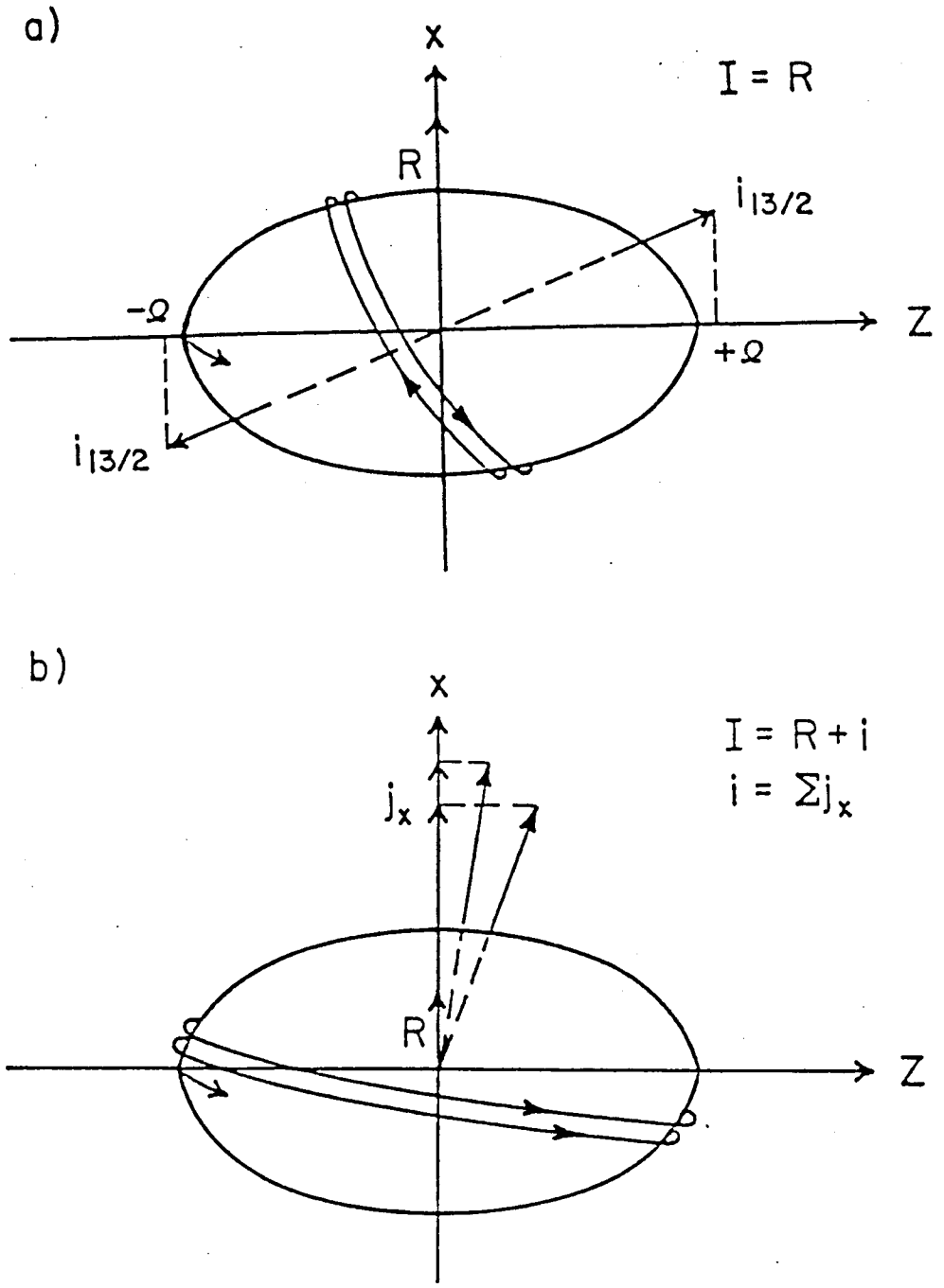

Figure 2.7: Schematic sketch showing a time-reversed pair of $i_{13/2}$ particles of a prolate nucleus in its ground state (a) and the alignment of same pair due to the Coriolis force (b). The quantum number Ω represents the projection of the particle angular momentum on the symmetry axis.

band but rather with a rotational band built upon the two aligned particles. This band is referred to as the Stockholm or "S" band. However, it is really a two-quasiparticle band, because the aligned configuration is made up of an admixture of particle and hole states due to the pairing force (see section 2.6). The alignment of quasiparticles certainly decreases the pairing correlations, because they block orbitals into which other pairs could scatter. However, it is clear that after the first backbend, pairing correlations, while reduced, still exist. One unanswered question concerning the nuclear structure is at what rotational frequency do the pairing correlations cease to exist. A good review of the current status of the investigations into this question is given by Garrett (1986).

Not only are pair correlations reduced as quasiparticles are aligned, but these quasiparticles can also effect the overall equilibrium shape of the nucleus. Since these quasiparticles are decoupled from the core, they define their own average field and shape. For example, decoupled quasiparticles which have their angular momentum vectors aligned with the rotational axis have a density distribution independent of the nuclear core. The final nuclear shape will depend on to what extent the aligned quasiparticles effect the equilibrium shape of the core. If the nuclear core is soft, triaxial shapes are expected with the alignment of only one or two pairs of high-j quasiparticles. Section 2.9 will examine more closely the deforming effects of aligned high-j quasiparticles.

Eventually, when enough particles are aligned, the pairing correlations cease to exist, and the yrast line finally enters the uncorrelated region first predicted by Mottelson and Valatin. Band crossings still occur in this region, but they are crossings involving single-particle states and not between paired quasiparticle configurations. These crossings come about because the Coriolis and centrifugal forces continually act to lower in energy single-particle states with a large component of angular momentum along the rotational axis. For a prolate nucleus,

the alignment of a sufficient number of nucleonic angular momenta parallel to the rotational axis results in the nucleus taking on an oblate shape with its angular momentum vector aligned along the symmetry axis. This occurs because of the clustering of the particles around the "waist" of the nucleus (see Fig. 2.8). When the rotational and symmetry axes are one and the same, angular momentum can only be generated by single-particle excitations. This is done by either exciting particles to higher lying orbitals or by the rearrangement of the yrast configurations due to unpaired band crossings. Such a transition from a collective prolate shape to a non-collective oblate shape results in a band termination, *i.e.* the point where the collective rotational band ends and single-particle excitations take over. It should be noted that rotational bands still exist at large angular momentum; however, they no longer lie lowest in energy. Within the last several years, examples of band termination have been observed in rare-earth nuclei (Baktash *et al.*, 1985), and much has been learned about the single-particle nature of these bands (Ragnarsson *et al.*, 1986).

At even higher rotational energies, other shape changes are predicted to occur, where the nucleus undergoes a transition from oblate to triaxial to prolate shapes before it fissions. One such transition may be to a superdeformed shape, where the ratio of the semi-major to minor axis is approximately 2:1. Such a transition has a classical analog: Jacobi (1834) predicted that for very rapid rotations, an axially symmetric oblate spheroid would become unstable resulting in a strongly elongated triaxial shape. This is referred to as the Jacobi instability, and there are a number of astronomical bodies whose shapes suggest that they were formed by a collision resulting in the rapid rotation of the system (see Garrett, 1986).

Cohen, Plasil, and Świątecki (1974) showed that, if only the macroscopic properties of the nucleus are considered, the interplay between the Coulomb, sur-

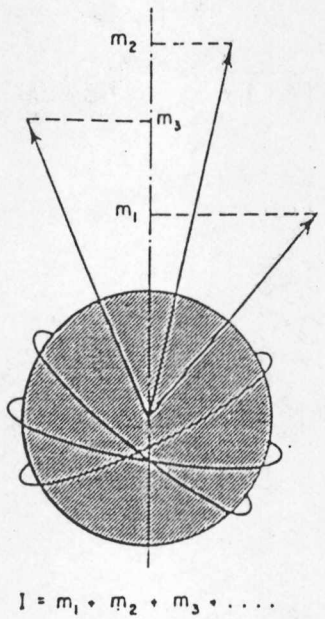

Figure 2.8: Pedalogical figure showing three unpaired valence particles orbiting a spherical nucleus. The intrinsic angular momentum vectors of each are also shown. The three particles cluster at the nuclear "waist" forming an oblate spheroid with the intrinsic angular momentum vector of the nucleus aligned parallel with the symmetry axis. Reproduced from Garrett (1986).

face, and rotational energies could also lead to the occurrence of strongly deformed nuclear equilibrium shapes ($\beta_2 \approx 0.6$) at high angular momentum. On the other hand, stable shell structures have been predicted for large deformations (Strutinsky, 1968), which also should help favor these superdeformed shapes. Since both macroscopic and microscopic properties seemed to favor superdeformed shapes in some nuclei at high angular momentum, physicists have wondered whether structures built on these shapes could be observed. The first conclusive evidence for the existence of superdeformed structures brought about by rotation was found in the continuum γ-ray spectra of ^{152}Dy (Nyako *et al.*, 1984). Recently, a rotational band has been identified with discrete levels observed up to $I = 60^+$ in ^{152}Dy (Twin *et al.*, 1986). Other examples of largely deformed bands have been found in the Ce, Nd and Gd isotopes. The identification of superdeformed bands in nuclei

has opened a new chapter in high-spin studies, and it will be interesting to see what new information is gained on nuclear structure at high angular momentum by studying these bands.

The above discussion is a generalized description about what type of nuclear structure one might find in different angular momentum regimes along the yrast line. Since the observed phenomena are very dependent on the shell structure, many nuclei will not exhibit all of the structures discussed above. For example, the Dy nuclei with $N = 82$ and 84 are predicted to be spherical up to $I \approx 55\ \hbar$ along the yrast line, where a structural change to a superdeformed shape is predicted. On the other hand, the well-deformed Dy nuclei are predicted to be good rotors for spins up to 70 $\hbar$. Clearly, one would like to observe discrete levels along the yrast line as high in angular momentum as possible in order to explore and study nuclear structure under the most extreme conditions of rapid rotation.

2.4 Phenomenological Description of Nuclear Spectra

The "roadmap" of a nucleus is its energy decay scheme. Whether a nucleus has single-particle or rotational characteristics is immediately evident from a diagram of the energy level scheme (Fig. 2.1). Since the level density near the yrast line is quite low, the nuclear energy levels can be mapped out fairly well at low and medium spins in this region. For deformed nuclei, rotational bands built on the lower lying one-(odd-A) and two-quasiparticle (even-A) excitations and vibrational states are also observed. In order to identify the nature of the quasiparticle alignment processes and to follow the gradual quenching of the pairing correlations, one must make comparisons between the yrast and multi-quasiparticle bands. Phenomenological models have been constructed that allow for the extraction of information about the collective and single-particle degrees of freedom from the nuclear level schemes. This information can then be used to

compare experimental findings with theoretical predictions.

2.4.1 Nuclear Moments of Inertia

Clearly, one collective parameter associated with a rotating body is its moment of inertia. Eq. 2.1 is an example of how the moment of inertia is used to parameterize the excitation energy of a nucleus as a function of angular momentum. Eq. 2.1 is valid providing the nuclear moment of inertia remains constant and the $I(I+1)$ rule is observed. Actually, nuclei are not perfect rotors, and while this parameterization gives a good fit for the first few energy levels along the yrast line, larger and larger deviations between calculated and actual nuclear energy levels occur as I increases. This fact led to an attempt to parameterize the energy of rotational bands by an expansion in powers of $I(I+1)$,

$$E\left(I(I+1)\right) = A \cdot I(I+1) + B \cdot \left(I(I+1)\right)^2 + C \cdot \left(I(I+1)\right)^3 + \cdots \quad . \tag{2.11}$$

While this allows for a better fit at slightly higher spins for some nuclei, there are many cases in which the convergence of the fit is very poor even at low spins. Harris (1965) derived an alternative expansion for E using powers of ω^2 (rotational frequency)

$$E = \alpha\omega^2 + \beta\omega^4 + \gamma\omega^6 + \cdots \quad . \tag{2.12}$$

This formalism is a generalization of the Inglis cranking model and gives very good agreement with the energies of the ground-state band in deformed nuclei before the first band crossing. Reducing the Harris model to two parameters yields the expression,

$$E = \frac{1}{2}\left(\mathcal{J}_0 + 3C\omega^2\right)\omega^2. \tag{2.13}$$

This two-parameter formula can be shown to be equivalent to the variable moment of inertia (VMI) model suggested and developed by Mariscotti, Scharff-Goldhaber,

and Buck (1969). The results from both of these models show that the moment of inertia is not constant but varies as a function of rotational frequency,

$$\mathcal{J} = \mathcal{J}_0 + \mathcal{J}_1\omega^2, \tag{2.14}$$

where $\mathcal{J}_1$ is proportional to C in Eq. 2.13.

Fig. 2.9 shows a moment of inertia plot for several even-even nuclei in the upper rare earth region as a function of $(\hbar\omega)^2$. In order to give the expected result in the pure-rotor limit, $\mathcal{J}$ is taken to be related to the energy spacings by (see Eq. 2.1)

$$2\mathcal{J}/\hbar^2 = (4I-2)/\Delta E_{I,(I-2)}. \tag{2.15}$$

Since the energy and the spin are the observable quantities, the next question to consider is how to express, in a phenomenological way, the rotational frequency. Classically, the rotational frequency is related to the angular momentum through Hamilton's equation,

$$\omega = \frac{dE}{dI}. \tag{2.16}$$

Since E and I are not continuous functions, ω can be expressed as a function of finite differences,

$$\hbar\omega = \frac{\Delta E_{I,(I-2)}}{[I(I+1)-(I-1)(I-2)]^{1/2}}. \tag{2.17}$$

When one uses the above prescriptions, the plots of $\mathcal{J}$ vs ω^2 show two striking features (see Fig. 2.9): (1) $\mathcal{J}$ does increase smoothly as a function of rotational frequency, and (2) at a critical frequency there is large rapid increase in the moment of inertia. The later feature is due to the rotational alignment of a pair of quasiparticles (backbending). As was discussed in the previous section, this is a single-particle effect and is not included in either the Harris or VMI models. On the other hand, the smooth increase in the moment of inertia is a collective effect, and it is important to examine the major causes of this increase.

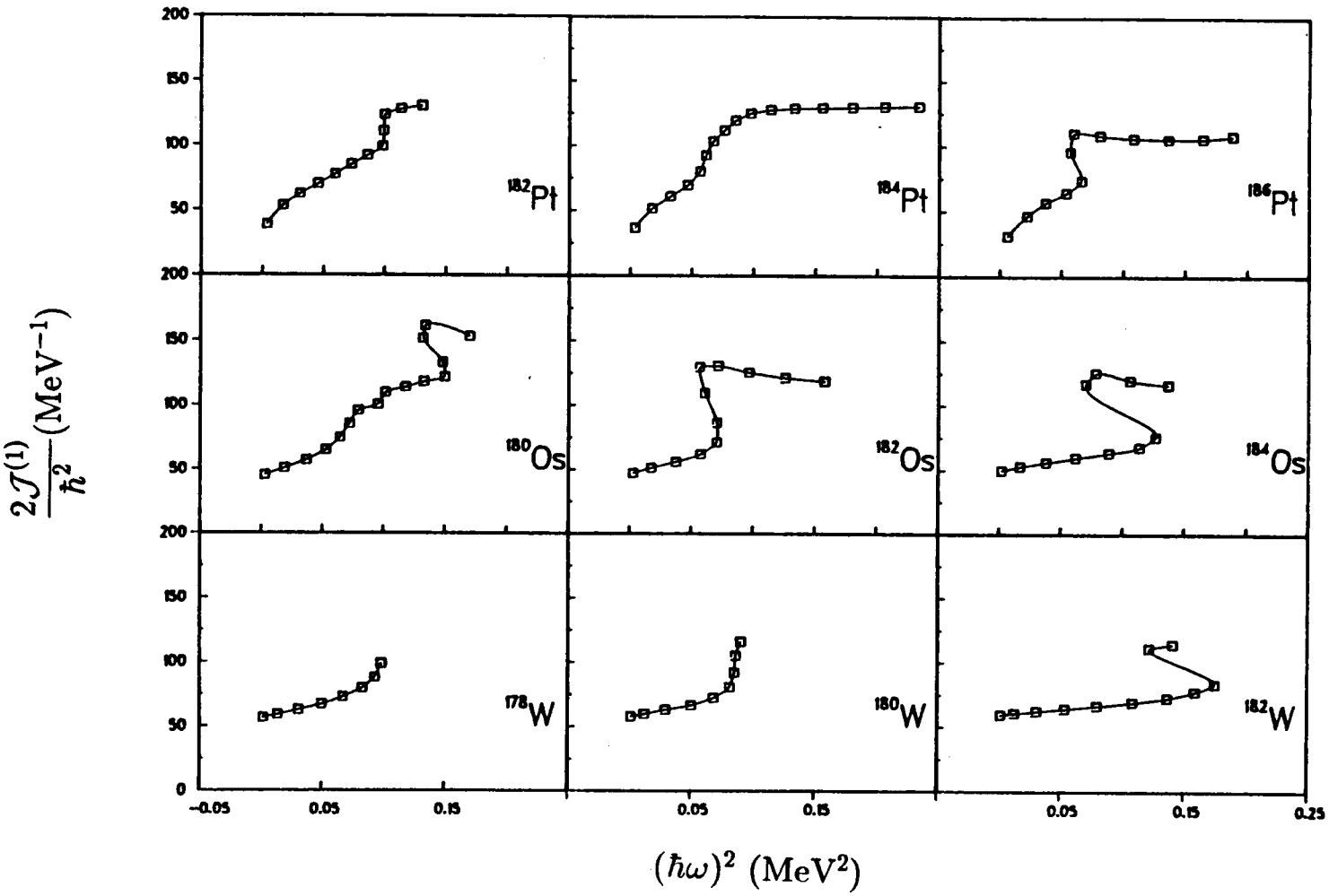

Figure 2.9: The moment of inertia as a function of $(\hbar\omega)^2$ for even-even nuclei ranging from W ($Z = 74$) to Pt ($Z = 78$).

If nuclei were perfect rotors, not only would Eq. 2.1 describe exactly the energy of the ground-state band, but the value of $\mathcal{J}$ should agree with the moment of inertia of a rigid body. The rigid-body moment of inertia can be expressed as a function of the nuclear deformation parameters β and γ by the expression,

$$\mathcal{J}_{rig} = \mathcal{J}_{sphere} \left\{ 1 - (\frac{5}{4\pi})^{1/2} \beta \cos(\gamma + 120^0) \right\}, \tag{2.18}$$

where

$$\mathcal{J}_{sphere} = \frac{0.0277}{2} A^{5/3} \frac{\hbar}{\mathrm{MeV}}. \tag{2.19}$$

The parameter β measures the deviation from spherical shapes and γ is a measure of the triaxiality. However, the actual value of the moment of inertia for a deformed nucleus in its ground state is about one-half to one-third of that given by the rigid-body value. As discussed above, this large discrepancy is due to the pairing correlations. Since the pairing correlations are gradually destroyed by the CAP effect, one would expect a gradual increase in the moment of inertia also. This is what is observed in Fig. 2.9 before the backbend, and once the pairing correlations completely disappear, the nuclear moment of inertia should equal the rigid-body value. Since the value of the moment of inertia is directly related to the strength of the pairing force, the quenching of pairing in principle could be monitored by observing the increase of $\mathcal{J}$ as a function of rotational frequency. This is difficult, since the moment of inertia is influenced by other dynamical changes such as deformation, shell effects and particle alignment, all of which may be prominent at high spins (Herskind, 1984).

One problem with the VMI and Harris models is that they only consider collective effects, and this is reflected in the smooth variation of the moment of inertia as a function of rotational frequency. Bohr and Mottelson (1981) have proposed two alternative definitions of the nuclear moment of inertia, which reflect the different aspects of nuclear dynamics. These two definitions are expressed in

terms of the first and second derivative of the total energy:

$$\mathcal{J}^{(1)} = \frac{\hbar^2}{2}\left(\frac{dE}{d(I^2)}\right)^{-1} = \hbar\frac{I}{\omega} \tag{2.20}$$

$$\mathcal{J}^{(2)} = \hbar^2\left(\frac{d^2E}{dI^2}\right)^{-1} = \hbar\frac{dI}{d\omega} \tag{2.21}$$

and follow directly from Eq. 2.16. Following Bohr and Mottelson, $\mathcal{J}^{(1)}$ and $\mathcal{J}^{(2)}$ are referred to as the kinematical and dynamical moments of inertia. Using these definitions, one is able to make predictions about the pairing strength (de Voigt *et al.*, 1983 and Herskind, 1984), and the contributions to the moment of inertia due to collective and single-particle effects (Bohr and Mottelson, 1981). Section 5-3 gives examples of how $\mathcal{J}^{(2)}$ is used to resolve close-lying band crossings, which occur in several nuclei in the Pt-Au region.

2.4.2 Nuclear Level Scheme Transformed to the Rotating Intrinsic System

To eliminate the time dependence of the Schrödinger equation, one solves nuclear Hamiltonian for a rotating nucleus in the body-fixed or intrinsic frame of reference (see section 2.1). In order for one to compare theoretical calculations directly with experimental data, it is convenient to transform the nuclear level scheme into the intrinsic frame. This transformation has the added advantage of allowing for the extraction of the single-particle properties from the nuclear level scheme.

For a nucleus rotating in an average field with its rotational axis perpendicular to the symmetry axis, the nuclear Hamiltonian in the lab frame is related to the Hamiltonian in the intrinsic frame by the term ωI_x, where ω is the rotational frequency and I_x is the projection of the total angular momentum onto the rotational axis (see Eq. 2.2). Classically, the energy in the rotating system, E', is

related to the excitation energy, E, in the lab system by the transformation

$$E' = E - \omega I_x, \tag{2.22}$$

where the term, ωI_x, is associated with both the Coriolis and centrifugal forces. This transformation may be directly applied to the nuclear level scheme if appropriate expressions for ω and I_x are constructed from the measured quantities E and I of the nuclear spectra.

I_x is related to the measured total angular momentum, I, and its projection onto the nuclear symmetry axis, K, through geometrical arguments such that

$$I_x = [I(I+1) - K^2]^{1/2} \approx [(I+\frac{1}{2})^2 - K^2]^{1/2}. \tag{2.23}$$

The rotational frequency is defined in a similar manner as in section 2.4.1 by the method of finite differences

$$\hbar\omega = \frac{E(I+1) - E(I-1)}{I_x(I+1) - I_x(I-1)}. \tag{2.24}$$

This expression follows directly from Hamilton's equation, which is expressed as $\omega = dE/dI_x$. Since Eq. 2.23 and Eq. 2.24 relate I_x and ω to the measured nuclear energy levels, the level scheme can be transformed into the intrinsic frame utilizing Eq. 2.22, where E is taken to be the average energy between two adjacent energy levels in a rotational band.

The Routhian, E', contains information about the collective and single particle properties of the nucleus. Since rotational bands are built on one and two-quasiparticle configurations, it is instructive to extract the single-particle behavior from E'. This is done by constructing a phenomenological expression which is related to the energy of the rotating core of nucleons. In section 2.4.1, it was shown that the excitation energy in the ground band of even-even nuclei is reproduced fairly well by expanding the rotational frequency in powers of ω^2 (Eq. 2.12). In

many cases, it is sufficient to include only the first two terms in this expansion (Harris, 1965). The result is an expression which reproduces the energy of the collective core. Classically, the total angular momentum is related to the moment of inertia by

$$I_x = \omega \mathcal{J}. \tag{2.25}$$

Combining this equation with the expression for the moment of inertia in the two parameter Harris formula (Eq. 2.13) yields

$$I_x^{(g)} = \omega \mathcal{J}_0 + \omega^3 \mathcal{J}_1, \tag{2.26}$$

where $I_x^{(g)}$ is the reference angular momentum of the rotating core. Integrating $I_x^{(g)}$ with respect to ω yields the energy of the core in the rotating frame (*i.e.* $I_x = -dE/d\omega$ from Hamilton's equations)

$$\begin{aligned} E_g^{'} &= -\int I_x^{(g)}(\omega) d\omega \\ &= -\frac{\omega^2}{2}\mathcal{J}_0 - \frac{\omega^4}{4}\mathcal{J}_1 + \frac{1}{8\mathcal{J}_0}, \end{aligned} \tag{2.27}$$

where the term $\frac{1}{8\mathcal{J}_0}$ is a constant of integration and has been added so that $E_g^{'} \approx 0$ at $I = 0$ (Bengtsson and Frauendorf, 1979a and 1979b). Equations 2.26 and 2.27 are the phenomenological representations for the quasiparticle vacuum, and this translates into the ground band for even-even nuclei. The parameters $\mathcal{J}_0$ and $\mathcal{J}_1$ are chosen so as to describe the ground band as well as possible.

For one to extract the single-particle properties from the nuclear level scheme, the single-particle Routhian and single-particle angular momentum are defined by subtracting the appropriate reference:

$$e'(\omega) = E'(\omega) - E_g^{'}(\omega) + \Delta_{o-e} \tag{2.28}$$

and

$$i(\omega) = I_x(\omega) - I_x^{(g)}(\omega). \tag{2.29}$$

The odd-even mass difference, Δ_{o-e}, is added only to odd-A nuclei. This is done because the excitation for even-even nuclei is measured with respect to the zero-quasiparticle ground state. In contrast, for odd-A systems the excitation energy is measured relative to the lowest single-quasiparticle state. Thus, it is necessary to include the quasiparticle energy of the odd-A ground state, which is approximately equal to the neutron (or proton) pairing gap. This allows a direct comparison between the excited quasiparticle energies of the odd and even systems.

2.5 The Independent Particle Model

In the previous section, phenomological models were discussed which allowed for the extraction of information concerning the collective and single-particle properties of the nucleus from the nuclear level scheme. This approach was a semi-classical treatment, applying classical expressions for the the rotational frequency and angular momentum to the discrete energy levels of the quantal nuclear system. This same information can be calculated in a purely theoretical approach, utilizing quantum mechanics. The next sections of this chapter will concentrate on the theoretical models which are presently in use to describe the properties of the nucleus at high angular momentum

As was reviewed in section 2.1, the nuclear force is mainly a short-range two-body force. However, when many nucleons are present in the nucleus, it becomes an enormously complicated problem to solve for the individual interactions of one nucleon with all the other nucleons. One approach to decrease the complexity of the problem is to assume that all the nucleons contribute to create an average force field which acts independently on the individual nucleons. This approximation is known as the independent particle model (IPM).

The choice of the one-body potential is limited by the known properties of the nucleonic potential. Damgaard *et al.* (1969) have reasoned that the satu-

rating properties of the nucleon-nucleon force leads to the existence of a nuclear surface. It then follows from the short-range character of the force that the average potential must be such that either (a) the equipotential surfaces are scalar transforms of the nuclear surface, or (b) the normal derivative of the potential has a constant magnitude along the nuclear surface. The two most utilized one-body potentials in nuclear structure calculations each satisfy one of the above conditions. They are the Nilsson or modified oscillator potential (Nilsson, 1955), which meets criterion (a), and the Woods-Saxon potential (Woods and Saxon, 1954), which is constructed to adhere to condition (b).

Fig. 2.10 shows an example of the Woods-Saxon and harmonic oscillator potentials in the spherical limit. The Woods-Saxon potential is the more realistic of the two, because it describes the nuclear density more accurately than the harmonic oscillator potential. For example, the Woods-Saxon potential is nearly constant inside the nucleus, which reflects the saturation of the nucleon-nucleon force, and it goes rapidly to zero near the nucleonic surface, where the concentration of nucleons is much less dense. On the other hand, the harmonic oscillator potential does not give a constant value in the interior of the nucleus, while at $r > R$, it diverges to positive infinity. However, Nilsson (1955) showed that for bound states many of the deficiencies of the harmonic oscillator potential could be overcome by making several modifications to the Hamiltonian. Since both the Woods-Saxon and modified oscillator potentials are in use today, a review of the two will be made in order to demonstrate their similarities and differences.

2.5.1 Nilsson or Modified Oscillator Potential

Historically, the first "realistic" deformed single-particle potential used for nuclear structure calculations was the modified oscillator potential introduced by Nilsson in 1955. In its general form, the modified oscillator potential of Nilsson

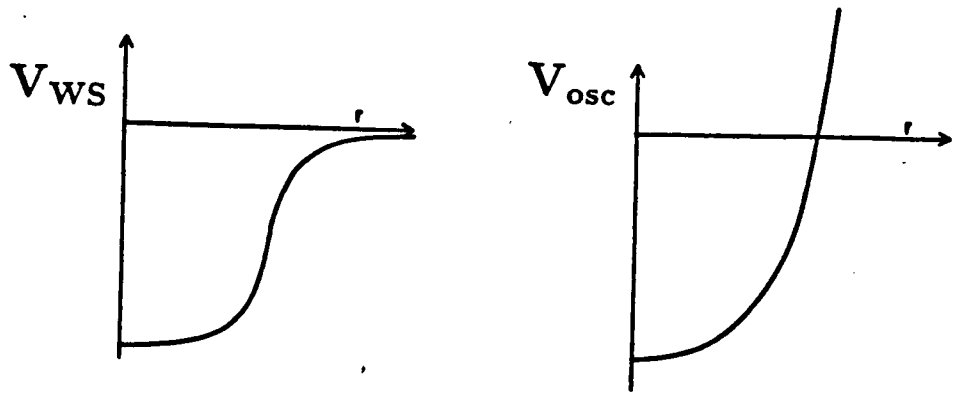

Figure 2.10: Examples of two one-body potentials used in nuclear structure calculations: (a) Woods-Saxon (b) harmonic oscillator.

is written as

$$V_{\rm mo} = V_{\rm osc} - 2\kappa\hbar\omega_0[\mathbf{l}_t \cdot \mathbf{s} - \mu(\mathbf{l}_t^2 - <\mathbf{l}_t^2>)], \tag{2.30}$$

where for axial symmetry

$$V_{\rm osc} = \frac{m\omega_0^2}{2}[(1+\frac{1}{3}\epsilon_2)^2(x^2+y^2) + (1-\frac{2}{3}\epsilon_2)^2 z^2]\ . \tag{2.31}$$

The quadrupole deformation is parameterized by ϵ_2, and it is expressed as a function of the components of the angular frequency $(\omega_x, \omega_y, \omega_z)$[1]. The final expression for $V_{\rm osc}$ is expressed in stretched coordinates, *e.g.* $x_t = x[(m\omega_x)/\hbar]^2$, which yields the expression

$$V_{\rm osc} = \frac{1}{2}\hbar\omega_0(\epsilon_2)\rho^2\left[1 - \frac{2}{3}\epsilon_2 P_2(\cos\theta_t)\right], \tag{2.32}$$

where $\rho = (x_t^2 + y_t^2 + z_t^2)$ and $\cos\theta_t = z_t/\rho$. The functional form of Eq. 2.32 is similar to the parameterization of the nuclear surface in Eq. 2.10. Thus, it can be concluded that the equipotential surfaces of $V_{\rm osc}$ are scalar transformations of the nuclear surface, showing that this potential meets criterion (a) described above. However, since $V_{\rm osc}$ is expressed in stretched coordinates, the deformation

[1]For axial symmetry $\omega_x = \omega_y = \omega_\perp$.

parameters of the deformed oscillator potential ($\epsilon_{\lambda\mu}$'s) do not equate directly with those of Eq. 2.10 ($\beta_{\lambda\mu}$'s). If only axial symmetric quadrupole deformations are considered for both cases, one gets the relationship

$$\epsilon_2 \approx 0.95\beta_2 \ . \tag{2.33}$$

The transformation to stretched coordinates is very critical, because the mixtures between different major shells N and N' are very small, such that they can be treated by perturbation theory or ignored entirely. This greatly reduces the single particle space over which calculations must be done. The term $\hbar\omega_0$, which appears in Eq. 2.32, is determined by the condition that the volume of the nucleus must be a constant independent of the deformation. Higher multipolarity terms corresponding to the deformation may also be added to the oscillator potential (Nilsson *et al.*, 1969) as well as terms which describe triaxial shapes (Andersson *et al.*, 1976).

While $V_{\rm osc}$ is expressed in a form which includes deformation, Eq. 2.32 cannot reproduce the experimentally observed shell structures, *e.g.* the magic numbers. To remedy this, Nilsson added the remaining terms of Eq. 2.30, which include a spin-orbit term, $\mathbf{l}_t \cdot \mathbf{s}$, and a term dependent on $\mathbf{l}_t^2$, where $\mathbf{l}_t$ is the orbital angular momentum defined in the stretched coordinate frame. The spin-orbit term is introduced in order to take into account the strong spin-orbit effects of the nucleon-nucleon force. The $\mathbf{l}_t^2$ term is completely phenomological and was included by Nilsson as to lower in energy the high-j single-particle levels.

The parameters κ and μ of Eq. 2.30 are fit so as to reproduce the observed single-particle levels. Since there is no explicit expression for the Coulomb potential included in $V_{\rm mo}$, any difference in the neutron and proton potentials is brought about by using different κ and μ values for each of them. It has also been found that κ and μ must change as a function of shell number, N, so as to best

describe the experimental single particle levels. Finally, $\dot{\omega}_0$ is defined[1] such that $\dot{\omega}_0 = \omega_0$ when $\epsilon = 0$, where

$$\hbar\dot{\omega}_0 \approx 41/A^{1/3} \text{ MeV}. \tag{2.34}$$

The main advantage of the modified oscillator potential is its simplicity. Since the major shell number, N, is treated approximately as a good quantum number even for deformed nuclei, nuclear structure calculations are greatly simplified. By smoothly varying the parameters $\hbar\dot{\omega}_0$, κ and μ as a function of N and Z, a very good description of the single-particle spectra is obtained for many nuclei. In fact, the modified oscillator potential is the most widely used potential for the calculation of the single-particle properties of nuclei as a function of angular momentum. Its major disadvantage is the inclusion of the completely phenomenological $(\mathbf{l}_t^2 - < \mathbf{l}_t^2 >)$ term in the Hamiltonian, because this has a tendency to artificially lower the single-particle states of the high-j orbitals. This effect is more prominent for heavier nuclei, which have a higher concentration of high-j orbitals near the Fermi surface. However, this effect can be compensated for by arbitrarily shifting the orbitals which are adversely affected. This may solve the problem for placement of single-particle energy levels, but may cause larger discrepancies in the calculated wave functions.

2.5.2 Wood-Saxon Potential

As was discussed above, the Woods-Saxon potential is more "realistic" than the harmonic oscillator potential. It includes in its functional form a shape which closely resembles that of the nuclear density; thus, phenomological terms similar to the $(\mathbf{l}_t^2 - < \mathbf{l}_t^2 >)$ term of the modified oscillator potential need not be

[1]Nilsson *et al.*, (1969) showed that $\hbar\dot{\omega}_0$ should be a function of N and Z for both protons and neutrons, but for the present description the above approximation is sufficient.

added. The Woods-Saxon potential, unlike $V_{\rm osc}$, includes the Coulomb interaction directly in the Hamiltonian.

The Woods-Saxon potential in its general form is expressed as

$$V_{\rm ws} = V_{\rm c}(\mathbf{r};\hat{\beta}) + V_{\rm so}(\mathbf{r};\hat{\beta}) + \frac{1}{2}(1+\tau_3)V_{\rm coul}(\mathbf{r};\hat{\beta}), \tag{2.35}$$

where

$$V_{\rm c}(\mathbf{r};\hat{\beta}) = \frac{V_0}{1+\exp[{\rm dist}(\mathbf{r};\hat{\beta};R_0)/a]}, \quad V_0 > 0 \tag{2.36}$$

and

$$V_{\rm so}(\mathbf{r};\hat{\beta}) = -\lambda_{\rm so}\left[\frac{\hbar}{2mc}\right]^2 {\rm grad}\left[\frac{V_0}{1+\exp[{\rm dist}(\mathbf{r};\hat{\beta};R_{\rm so})/a_{\rm so}]}\right] . \tag{2.37}$$

$V_{\rm c}$ is the central potential whose dependence on r in the spherical limit is plotted in Fig. 2.10. Its dependence on the spatial coordinates is contained in ${\rm dist}(\mathbf{r};\hat{\beta};R_0)$, which represents the distance from a point $\mathbf{r}$ to the nuclear surface. The shape of the nuclear surface is assumed to follow the parameterization expressed in Eq. 2.10. If only axially symmetric quadrupole (β_2) and hexadecapole (β_4) deformations are considered, Eq. 2.10 is expressed as

$$R(\theta) = C(\beta_2,\beta_4)R_0\left[1+\beta_2 Y_{20}(\cos\theta)+\beta_4 Y_{40}(\cos\theta)\right] . \tag{2.38}$$

The parameter a in Eq. 2.36 represents the nuclear skin distance. Because of the short-range characteristics of the nucleon-nucleon force, a is assumed to be constant, independent of the shape of the nuclear surface. This in turn places an added restriction on ${\rm dist}(\mathbf{r};\hat{\beta};R_0)$ such that the normal derivative of $V_{\rm c}$ must be a constant along the nuclear surface, and thus fulfilling criterion (b) for the one-body potential discussed above. The spin-orbit term of the potential does not seem to resemble the simple $\mathbf{l}\cdot\mathbf{s}$ term in the Nilsson model. However, Bohr and Mottelson (1969) have shown that $\mathbf{l}\cdot\mathbf{s}$ should be replaced with $\mathbf{s}\cdot\mathbf{p}\times\nabla\mathbf{V}$, and this leads to the above parameterization of $V_{\rm so}$. Finally, V_0 represents the depth of

the potential well at $r = 0$, and R_0 is assumed to follow the usual parameterization $R_0 = r_0 A^{1/3}$.

When one is performing numerical calculations, there are six parameters in Eq. 2.35 which must be defined: V_0, r_0, r_{so}, λ_{so}, a and a_{so}. Several systematic studies of deformed nuclei for $A > 40$ have been performed (Dudek and Werner, 1978; Dudek *et al.*, 1979) to fit the above parameters to reproduce known experimental data. It has been found that these parameters vary smoothly as a function of N and Z, similar to the varying of the κ and μ terms in the Nilsson model. It should also be noted that a single set of parameter values has also been developed for the Woods-Saxon potential (Dudek *et al.*, 1981), which can be applied to a wide range of deformed nuclei. These so called universal parameters are mainly used when one is interested in exploring systematic trends among nuclei in different regions of the periodic table.

The main advantage of the Woods-Saxon potential is that it realistically duplicates the major points of the two-body interaction without the introduction of any unphysical terms. Therefore, this potential not only will reproduce the experimentally observed single-particle levels, but the theoretical wave functions are also more realistic, allowing for the calculation of other nuclear properties such as transition probabilities and quadrupole moments. The major disadvantage of this potential is that it is a more difficult potential with which to make calculations. If the harmonic oscillator basis is used, large mixtures between different major shells are encountered, forcing the calculations to be done over a very large single-particle space (*e.g.* N=12 for rare-earth nuclei). However, as more powerful computers become easily accessible to physicists, this disadvantage is becoming less critical, making the Woods-Saxon potential a more excepted tool in nuclear-structure calculations.

2.5.3 Comparison Between the Nilsson and Woods-Saxon Potentials

In general, if one is interested in calculating single-particle levels, the Nilsson or Woods-Saxon potentials do equally well if a good job has been done in fitting the adjustable parameters to the experimentally known single-particle levels. For example, work on ^{185}Au has led to a new set of (κ, μ) parameters for the $N = 5$ and $N = 6$ proton shells in order to give better agreement between calculated and experimental results (Zhang *et al.*, 1987). When a minimization is done with respect to the quadrupole (ϵ_2) and hexadecapole (ϵ_4) deformation parameters utilizing the shell-correction method, all observed band heads in ^{185}Au are fairly well reproduced, including both oblate and prolate structures. This same calculation was also done using the Woods-Saxon potential utilizing the universal parameters of Dudek *et al.* (1981), giving similarly satisfying results (Larabee *et al.*, 1986). However, if one performs similar calculations on ^{184}Pt using the same parameter sets, one finds a large discrepancy between the two models when comparing the energy differences between the two 0^+ states, the lowest of which represents a prolate shape and the other an oblate shape. Fig. 2.11 shows that while the agreement between theoretical and experimental values is quite good for the prolate-oblate energy difference (V_{po}) in the Pt isotopes using a Woods-Saxon potential, this same agreement is not reached if a Nilsson potential is used. However, if one examines the same calculations for the Hg isotopes, the discrepancy between the two models is still a constant while the experimental data falls in between the predictions of the two models.

In conclusion, while similar results are obtained for the band head energies in ^{185}Au by using the adjusted Nilsson parameters of Zhang *et al.*, and the universal Woods-Saxon parameters of Dudek *et al.*, similar agreement is not obtained by examining the V_{po} of the even-even neighbor nuclei. In the case of the Nilsson calculations, the discrepancy in the calculated prolate-oblate energy

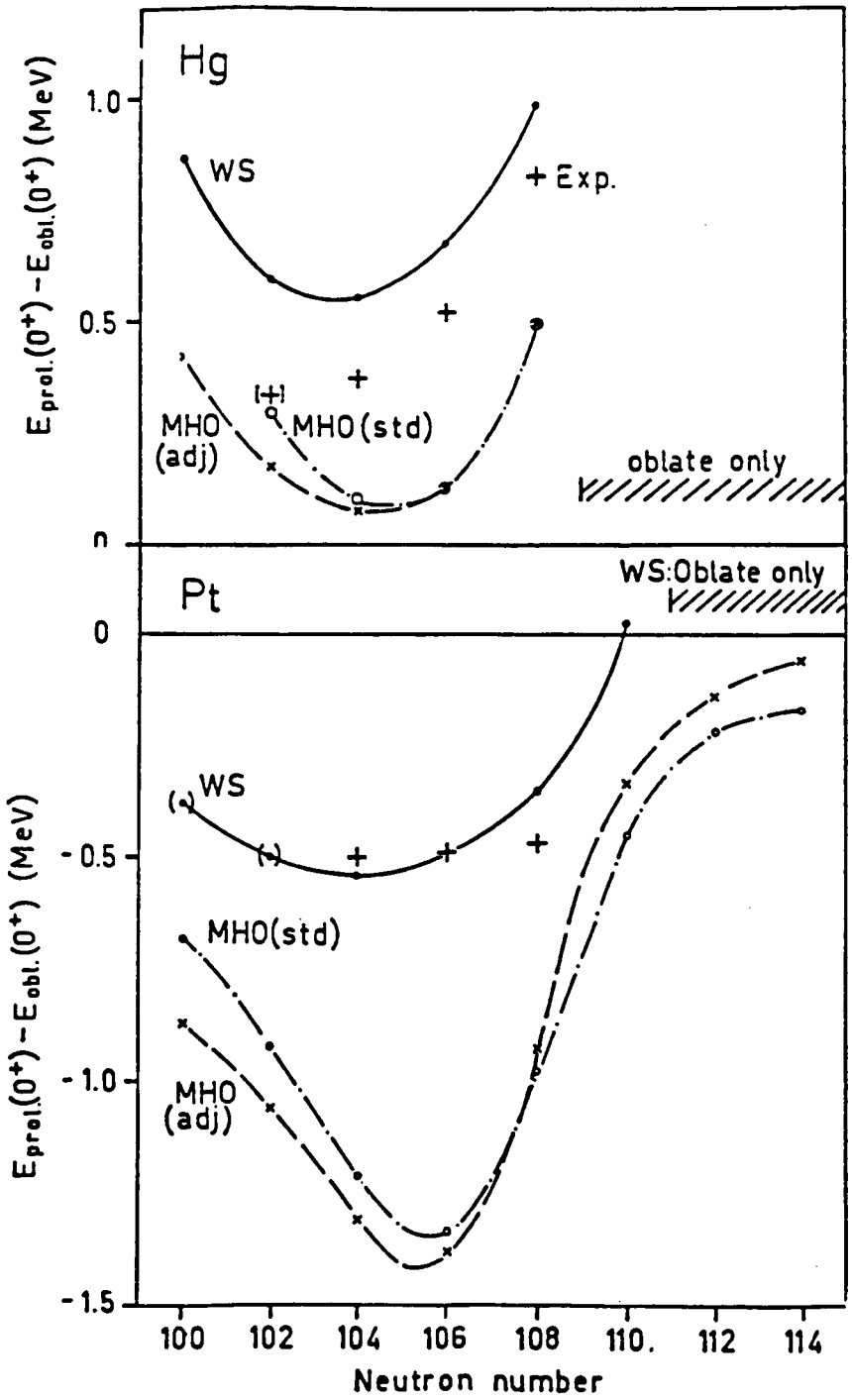

Figure 2.11: Calculated prolate-oblate energy differences obtained with the Woods-Saxon potential and the Nilsson potential. The crosses show the experimental energy difference between the two lowest 0^+ states. Reproduced from Bengtsson *et al.* (1987).

difference seems to be due to a preference of the model for prolate shapes in this region. By examining *both* the Pt and Hg results for the calculated V_{po}, one cannot say which potential is best in this region. The fact that they give such differing results suggests that some fundamental difference between the two models may exist when applied to nuclear structure calculations in this transitional region. A closer examination of the two potentials should be carried out, applying the results to higher spins in order to clear up these discrepancies. However, it is clear that if one wishes to go beyond the predictions of the single-particle energy levels and examine properties associated with the wave functions, one should favor using the Woods-Saxon potential over the Nilsson potential.

2.6 Pairing

The independent particle model assumes that the individual nucleons interact only with the average field. However, since the nucleon-nucleon force is such a strong force, one might expect residual two-body forces to play some type of role in the one-body potential approximation. One such residual force, which is directly related to the strong nuclear force and the Pauli principle, is the pairing force.

The most energetically efficient way for the nucleons to rearrange themselves is into time-reversed pairs. This guarantees the largest overlap between the nucleonic wave functions and the minimization of the ground state energy. The IPM as discussed in section 2.5 does not take into account these correlations; thus, some modification to the IPM is in order if one is to reproduce the experimentally observed energy spacings.

Experimentally, there are several signatures which confirm the existence of a residual pairing force in nuclei. One is that the ground state spins of all even-even nuclei are zero, indicating that all these nuclei regardless of their masses

must have their individual angular momenta coupled in such a way as to give a spin of zero. Another piece of evidence is found in spherical nuclei, where angular momentum is generated by single-particle excitations as opposed to collective rotations. In these nuclei a difference in energy of approximately 1 MeV is found between the ground 0^+ state and the next energy level associated with two unpaired nucleons. This lowering in energy of the nuclear ground state is indicative of a force which acts only between pairs of nucleons in time reversed orbits. The existence of pairing in nuclei is also supported by the systematically smaller binding energy of odd-mass nuclei compared to even-even nuclei. This difference is directly related to the lowering in energy of the 0^+ states in the even-even nuclei indicating that this state is much more tightly bound than the excited particle states. In the simple model, the addition of an unpaired particle to the even-even core would result in placing it into one of the particle states which lies 1 MeV above the ground state. This results in a lower binding energy for the odd-mass system and therefore accounts for the observed mass difference.

Another consequence of the pairing force is the existence of pair correlations in deformed nuclei which leads to nuclear superfluidity. From Fig. 2.3, it can be seen that the addition of deformation into the average field results in a decrease in the average energy spacing of the independent particle levels. If this spacing becomes sufficiently small and the degeneracy of the time-reversed orbits is maintained, there is a probability that a pair of particles may scatter from one set of time reversed orbitals to another set which has nearly the same energy. In this manner, superfluid correlations arise between sets of degenerate time-reversed orbitals.

In the language of second quantization a two-body force which can scatter time-reversed pairs of particles is included into the Hamiltonian of the IPM in the

form

$$H = \sum_{\nu} e_{\nu} a_{\nu}^{\dagger} a_{\nu} - G \sum_{\mu,\nu>0} a_{\mu}^{\dagger} a_{\overline{\mu}}^{\dagger} a_{\nu} a_{\overline{\nu}}, \tag{2.39}$$

where the e_ν's are the single-particle energies of the nucleons in the average field and G is the strength of the pairing force. When deriving the pairing force from realistic effective interactions, one expects G to be configuration dependent. However, calculations are simplified if a constant value of G is used which only acts on states lying near the Fermi surface.[1] This simplification is reasonable since the residual interaction of Eq. 2.39 is rather weak and scatters nucleon pairs in a narrow band around the Fermi surface.

Since pairs of particles near the Fermi surface are continually being scattered in and out of the available single-particle states, the wave functions used must also represent this idea. Bardeen, Cooper, and Schrieffer (1957) approximated the ground state wave function for such a physical case by

$$|BCS\rangle = \prod_{\mu>0} (u_\mu + v_\mu a_\mu^{\dagger} a_{\overline{\mu}}^{\dagger}) |0\rangle , \tag{2.40}$$

where $|0\rangle$ represents the wave function containing no nucleons. The amplitudes u_μ and v_μ are associated with the probability that the pair state $(\mu, \overline{\mu})$ is either empty or occupied such that $u_\mu^2 + v_\mu^2 = 1$. To determine the coefficients u_μ and v_μ, one minimizes $\langle BCS| H |BCS\rangle$. However, the BCS wave functions do not conserve particle number, and a further restriction must be applied to the Hamiltonian such that the average number of nucleons is a constant. This is accomplished by adding the Lagrange multiplier λ to the Hamiltonian such that

$$H = \sum_{\nu} (e_\nu - \lambda) a_\nu^{\dagger} a_\nu - G \sum_{\mu,\nu>0} a_\mu^{\dagger} a_{\overline{\mu}}^{\dagger} a_\nu a_{\overline{\nu}}, \tag{2.41}$$

where λ is the average Fermi surface associated with the average particle number.

[1]This parameterization of the pairing interaction is equivalent to a monopole pair interaction. In principle higher order terms can be added to the two-body pairing force which would include scattering of time-reversed pairs into states which are not time-reversed sets, resulting in a configuration dependent pairing interaction (see J-y. Zhang *et al.*, 1983).

In order for one to evaluate the matrix elements of Eq. 2.41, a transformation is made from the particle space to a gauge space known as the quasiparticle space. This is known as a Bogolyubov transformation, and it has the advantage of reducing the two-body operator associated with the pairing force to a one-body operator. The transformation is such that the new creation and destruction operators in the quasiparticle space are related to the operators in the particle space by

$$\alpha_\mu^\dagger = u_\mu a_\mu^\dagger - v_\mu a_{\bar{\mu}}, \quad \alpha_\mu = u_\mu a_\mu - v_\mu a_{\bar{\mu}}^\dagger. \tag{2.42}$$

The term quasiparticle is used to describe the new space, because the calculated energy levels are now states which are associated with the probability that a nucleon pair occupies the state, *i.e.* the state is part hole and part particle.

If one operates on the ground state wave function described in Eq. 2.39 with the quasiparticle destruction operator, one discovers that

$$\alpha_\mu \left| BCS \right\rangle = 0 \quad \text{for all } \mu. \tag{2.43}$$

Thus, the ground state in the quasiparticle space represents the quasiparticle vacuum. This is analogous to the independent-particle model where the sharp Fermi surface behaves like a vacuum to particle and hole operators. By diagonalizing Eq. 2.41, an expression for the energy of a single quasiparticle can be written as

$$E_\nu = \sqrt{(e'_\nu - \lambda)^2 + \Delta^2}, \tag{2.44}$$

where

$$e'_\nu = e_\nu - G v_\nu^2, \quad \Delta = G \sum_{\mu>0} u_\mu v_\mu. \tag{2.45}$$

The energy e'_ν is referred to as the renormalized single-particle energy in the orbital ν, and Δ, as can be inferred from Eq. 2.44, is associated with the energy difference between the ground-state and the first excited quasiparticle state. For an even-even nucleus this difference is at least 2Δ, since the first excited state must have at least two quasiparticles present.

2.7 Cranked Hartree-Fock-Bogolyubov

In the previous two sections, details have been discussed concerning the theoretical treatment of the independent particle model with and without the inclusion of a residual pairing force. It was also shown that if the two-body pairing force is included in the Hamiltonian, a transformation to a quasiparticle space allows the complete Hamiltonian to be expressed in terms of one-body operators. This procedure is often referred to as the Hartree-Fock-Bogolyubov (HFB) method; however, it should not be confused with the fuller self-consistent Hartree-Fock procedures, which utilize realistic nucleon-nucleon force expressions. The HFB procedure can also be applied to the cranking Hamiltonian (Eq. 2.2). This method, known as HFB cranking, allows for a description of the nucleus in terms of elementary quasiparticle excitations in the rotating frame. In this section, only an outline of the procedure will be discussed. For a much fuller description of the HFBC solutions, the reader is referred to Ring and Schuck (1980), Szymański (1983), Bengtsson and Garrett (1983), de Voigt, Dudek and Szymański (1983), or Dudek (1983).

In section 2.1, a classical derivation of the cranking Hamiltonian was given; however, this same Hamiltonian can be also be derived using non-classical methods. The motion of a nonrelativistic quantum object is described by the time-dependent Schödinger equation. For a nucleus in the laboratory system, this is simply

$$i\hbar\frac{\partial}{\partial t}\psi = H\psi. \tag{2.46}$$

One major assumption of the cranking model is that the form of the nuclear potential in the rotating frame is identical to the form in the non-rotating coordinate system, neither of which depend on time. Using this assumption, one is able to

transform both ψ and H into the rotating frame by means of the rotation operator,

$$\mathcal{R} = e^{-i\omega t J_x \hbar}, \tag{2.47}$$

as

$$\psi = \mathcal{R}\psi' \tag{2.48}$$

and

$$H' = \mathcal{R}H\mathcal{R}^{-1}. \tag{2.49}$$

By inserting Eq. 2.48 and 2.49 into the Schödinger equation, one obtains

$$i\hbar\frac{\partial}{\partial t}\psi' = (H' - \omega J_x)\psi' = H^\omega\psi'. \tag{2.50}$$

Since H and H' have the same form, this equation is identical to the cranking Hamiltonian given in in Eq. 2.2. Again, it should be noted that cranking implies that all calculations are done at constant ω.

Since H^ω does not depend on time, the solutions to Eq. 2.2 is reduced to the eigenvalue problem of H^ω, making calculations much simpler than those done in the laboratory frame. It should be noted that the eigenvalues of H^ω do not represent the total energies and that a transformation back to the lab frame must be made to get the real energies of the system.

In the language of second quantization, the body-fix Hamiltonian, H^ω, is expressed as

$$H^\omega = \sum_{\nu\nu'}(e_{\nu\nu'} - \hbar\omega(j_x)_{\nu\nu'} - \lambda\delta_{\nu\nu'})a^\dagger_\nu a_{\nu'} - \frac{1}{4}G\sum_{\mu\nu} a^\dagger_\mu a^\dagger_{\overline{\mu}} a_\nu a_{\overline{\nu}}, \tag{2.51}$$

where the summation is done over the basis states specified[1]. Again because of pairing, one must introduce the Lagrange multiplier λ, which is constrained by the condition that the average particle number equals the total number of nucleons for which the calculation is being performed.

[1]For both the modified oscillator and Woods-Saxon potentials the basis set used is that of the anisotropic harmonic oscillator.

After the construction of the Hamiltonian, a transformation into the quasiparticle space must be done. A more general Bogolyubov transformation must be performed than is done in Eq. 2.42, where the quasiparticle operators are constructed entirely from degenerate ($\pm K$) levels, because the cranking Hamiltonian breaks time-reversal symmetry. The more generalized HFB quasiparticle creation and destruction operators are in fact linear combinations of all particle operators involved in the basis set, *e.g.*

$$\alpha_i^\dagger = \sum_\nu (U_{\nu i} a_\nu^\dagger + V_{\nu i} a_\nu), \quad \alpha_j = \sum_\nu (V_{\nu j}^* a_\nu^\dagger + U_{\nu j}^* a_\nu). \tag{2.52}$$

By utilizing the inverse to the above transformation, the Hamiltonian of Eq. 2.51 is expressed in the quasiparticle representation in the general form

$$H^\omega = H_0 + H_{11} + H_{20} + H_4, \tag{2.53}$$

where H_0 contains terms with no α operators, H_{11} contains quasiparticle operators of the form $\alpha^\dagger\alpha$, H_{20} has operators with combinations $\alpha^\dagger\alpha^\dagger$ and $\alpha\alpha$, and H_4 contains all terms associated with two-body operators, *e.g.* $\alpha\alpha\alpha^\dagger\alpha^\dagger$. The inclusion of H_4 in the Hamiltonian is disappointing since one goal of the Bogolyubov transformation is to reduce H^ω to an expression with only one-body operators. However, if the contributions from H_4 are small, it can be ignored. If one makes this assumption, Eq. 2.53 reduces to an expression which contains only one-body operators. Since the U_{ij}'s and V_{ij}'s have yet to be defined, H_{20} is eliminated by requiring these coefficients to have values such that $H_{20} = 0$. H_{11} can now be written such that

$$H_{11} = \sum_{ij,\alpha\beta} \left[\nu_{\alpha\beta}(U_{\alpha i}^* U_{\beta j} - V_{\alpha j} V_{\beta i}^*) + \Delta_{\alpha\beta} U_{\alpha i}^* V_{\beta j}^* + \Delta_{\alpha\beta}^* V_{\alpha i}^* U_{\beta j} \right] \alpha_i^\dagger \alpha_j, \tag{2.54}$$

where

$$\nu_{\alpha\beta} = e_{\alpha\beta} - \lambda\delta_{\alpha\beta} - \hbar\omega(j_x)_{\alpha\beta} + 4G \sum_{\gamma\delta i} V_{\gamma i} V_{\delta i}^* \tag{2.55}$$

and

$$\Delta_{\alpha\beta} = 2G \sum_{\gamma\delta i} U_{\delta i} V^*_{\gamma i}. \tag{2.56}$$

If one compares the above expressions for $\nu_{\alpha\beta}$ and $\Delta_{\alpha\beta}$ to those for the renormalized single-particle energy and Δ in Eq. 2.45, it is evident that these expressions have the same physical basis. Thus, the terms $\nu_{\alpha\beta}$ and $\Delta_{\alpha\beta}$ are referred to as the self-consistent single-particle Routhian and the self-consistent pairing field, respectively. It follows from this same logic that the matrix elements of V and U are analogues to the v_ν and u_ν terms of section 2.6, which are associated with the probabilities that a quasiparticle state is occupied or empty. Part of the complexity of the above expressions is traced to the breaking of the time-reversal symmetry by rotation.

There is one other requirement which is placed on H_{11}:

$$\sum_{\alpha\beta} \left[\nu_{\alpha\beta}(U^*_{\alpha i} U_{betaj} - V_{\alpha j} V^*_{\beta i}) + \Delta_{\alpha\beta} U^*_{\alpha i} V^*_{\beta j} + \Delta^*_{\alpha\beta} V^*_{\alpha i} U_{\beta j} \right] = E^\omega_i \delta_{ij} \tag{2.57}$$

such that E^ω_i must be a real number. Finally, it can be shown that the above approximations and requirements leads to the following nonlinear equations for U and V:

$$\sum_\beta (\nu_{\alpha\beta} U_{\beta i} + \Delta_{\alpha\beta} V_{\beta i}) = +E^\omega_i U_{\alpha i}, \tag{2.58}$$

$$\sum_\beta (\nu^*_{\alpha\beta} U_{\beta i} + \Delta^*_{\alpha\beta} V_{\beta i}) = -E^\omega_i V_{\beta i}, \tag{2.59}$$

where E^ω_i is the quasiparticle energy for state i. These last two equations are known as the HFBC equations.

The HFBC equations are solved self-consistently by applying an iterative procedure to find the matrices U and V and simultaneously the quasiparticle Routhians, E^ω_i. The final Hamiltonian takes the form

$$H^\omega = H_0 + H_{11}, \tag{2.60}$$

where H_0 is interpreted as representing the quasiparticle vacuum and H_{11} describes the quasiparticle excitations.

The space over which the diagonalization of H^ω is done is greatly reduced if one takes into consideration the symmetries of the Hamiltonian. The cranking Hamiltonian is parity invariant if one considers only even multipolarity terms in the expansion of the nuclear potential. It follows that parity is a good quantum number and that the matrix representation of H^ω is split into two sub-matrices. The separate solutions are identified by the parity quantum number $\pi = +1$ or -1.

While the original Hamiltonian, H, preserves time reversal invariance, the $(-\omega J_x)$ term breaks this degeneracy. However, there is one symmetry which still remains, in addition to parity, and that is the invariance of H^ω with respect to the rotation around an axis perpendicular to the symmetry axis. This is defined by

$$\mathcal{R}_x \psi_\alpha = e^{-i\pi j_x} \psi_\alpha = e^{-i\pi\alpha} \psi_\alpha, \tag{2.61}$$

where ψ_α denotes a wave function with signature α. The signature for a single-particle state can have the values $\alpha = -1/2$ or $+1/2$. The signature of a state is sometimes designated by the quantum number r which is the eigenvalue of $\mathcal{R}_x$ and is related to α by

$$r = e^{-i\pi\alpha}, \tag{2.62}$$

where r may take on the two values i or $-i$.

It should be noted, that at $\omega = 0$, time-reversed states with spin projections $+\Omega$ and $-\Omega$ on the symmetry axis are energetically degenerate. However, they may not have good signature with respect to the rotation axis. Goodman (1974) has shown that one can make a transformation from a basis in which Ω is a good quantum number into one in which the signature is a good quantum number. The new basis states represented by this transformation place added restrictions on $\Delta_{\alpha,\beta}$, $\nu_{\alpha,\beta}$, $(j_x)_{\alpha,\beta}$, $U_{\alpha,\beta}$ and $V_{\alpha,\beta}$ (see de Voigt *et al.*, 1983). This splits the

HFBC equations into two separate systems of equations, where each system corresponds to one of the two possible values of the signature. For each quasiparticle Routhian, E_i^{ω}, that belongs to the solution of signature $r = -i$, there exists a solution for signature $r = +i$ such that $E_i^{\omega} = -E_i^{\omega}$. Because of this relationship, only one system of HFBC equations need be solved to get the complete solution for both signatures; thus, reducing considerably the calculation time.

2.8 Quasiparticle Excitations and Diagrams

Once the theoretical quasiparticle Routhians have been calculated, they should be compared to experimental data. In section 2.4, several phenomological expressions are presented which allow for the transformation of the nuclear level scheme into the rotating reference frame. From these transformed expressions, information concerning the single-particle Routhians and angular momenta were also extracted. The following section concentrates on the physical interpretation of the HFBC quasiparticle Routhians and their relationship with experimental data.

Before proceeding, it is good to review the different effects one observes on the calculated energy levels as additional terms are added to the nuclear Hamiltonian. The effect these terms have on the single-particle levels is illustrated in Fig. 2.12. The left-most spectrum shows the calculated single-particle Nilsson states, assuming a quadrupole deformation of $\epsilon_2 = 0.242$. The center spectrum shows the quasiparticle energies, E_ν, when pairing correlations are added to the Hamiltonian ($\Delta = 0.87$ MeV). The addition of pairing results in the lowering of the completely paired state by an energy, $E_\nu = \sqrt{(e_\nu - \lambda)^2 + \Delta^2}$, with respect to the quasiparticle states (see section 2.6). Finally, the right-most spectrum shows the effect rotation has on the quasiparticle energies as a function of rotational frequency. Notice how the breaking of time reversal symmetry destroys the degeneracy of the paired quasiparticles at non-zero rotational frequencies.

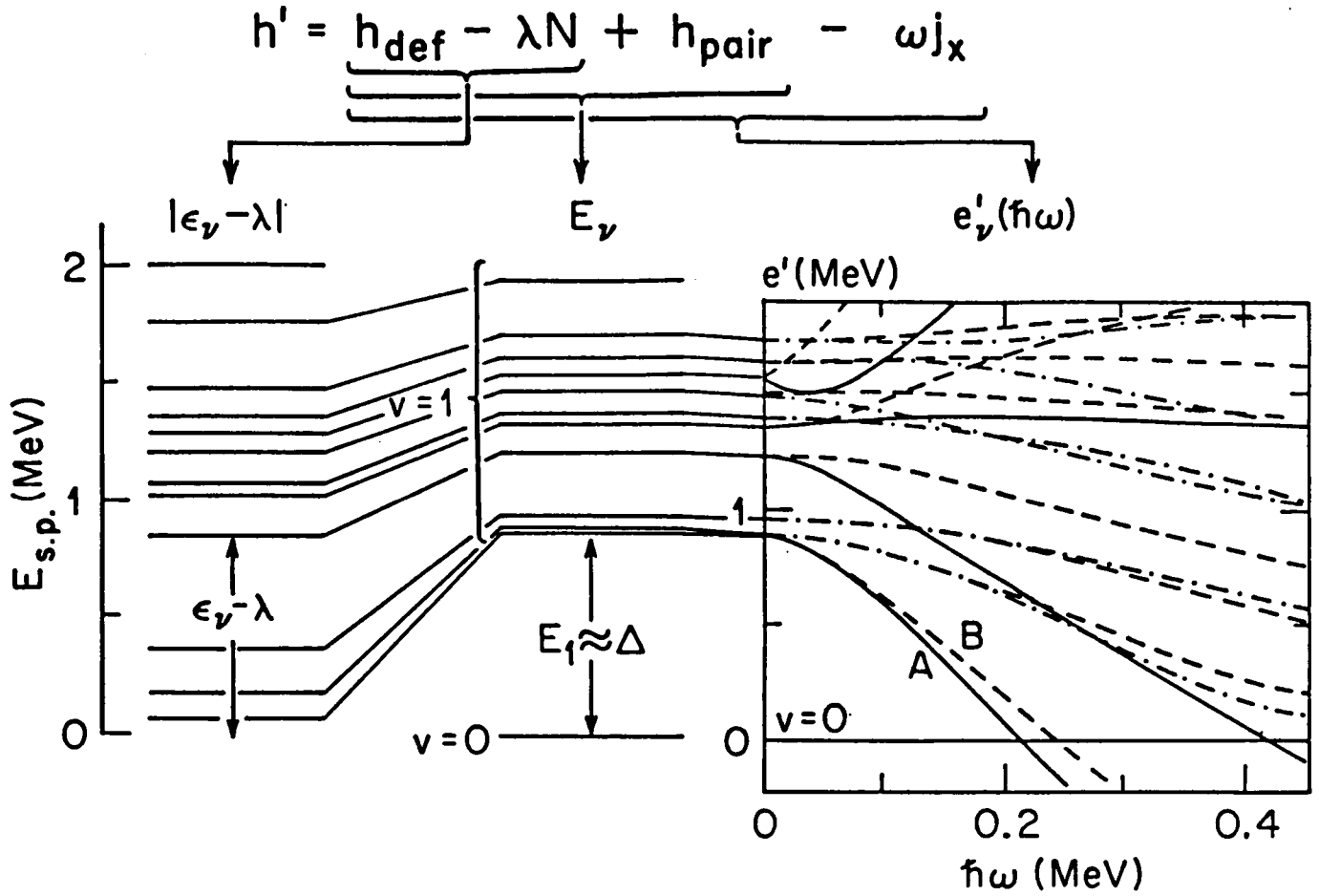

Figure 2.12: Spectra of Nilsson states (left), quasiparticle energies, E_ν, for the Nilsson model plus pair correlations (center), and Routhians, E^ω (right) depicting the effects of pair correlations and rotation on the quasiparticle orbitals.

The cranked shell model (CSM) of Bengtsson and Frauendorf (1979a,b) attempts to describe the observed nuclear spectrum in terms of quasiparticle excitations. The quasiparticle Routhians are calculated using the HFBC formalism; however, the self-consistency of the method is removed by fixing the deformation parameters, Δ and λ in the HFBC field equations to realistic values. In many cases, the calculated quasiparticle spectrum does not deviate significantly from the fully self-consistent calculations (see section 2.8), and the results agree very well with what is experimentally observed. However, in situations where the quasiparticle energies are particularly sensitive to the HFB parameters, self-consistent calculations may be necessary in order to make definite conclusions about the nuclear structure near the yrast line.

The main importance of the cranked shell model, as presented by Bengtsson and Frauendorf, is the presentation of the theoretical results in the form of quasiparticle diagrams, where the quasiparticle level energies are plotted as a function of the rotational frequencies. Fig. 2.13 shows such a diagram for the quasineutron levels in ^{184}Pt using a Woods-Saxon potential as the average field. Values for the HFBC parameters ($\beta_2 = 0.225$, $\beta_4 = -0.029$, $\gamma = 0°$, and $\Delta = 0.89$ MeV) were taken from a fully self-consistent calculation for the ground band at $\hbar\omega = 0.0$ MeV. Both positive and negative parity solutions are included in the diagram along with both possible values of the signature. The $(\pi, \alpha) = (+, 1/2)$, $(+, -1/2)$, $(-, 1/2)$ and $(-, -1/2)$ states are denoted by solid, short-dashed, dot-dashed, and long-dashed curves. Several of the states are labeled by the asymptotic quantum numbers at zero rotational frequency. While this designation is not necessarily correct for the Woods-Saxon potential which mixes states with different major-shell quantum number, N, it is used to bring about some consistency in the identification of the quasiparticle states independent of the potential used. The individual quasiparticle trajectories are labeled using a generic labeling scheme which can be

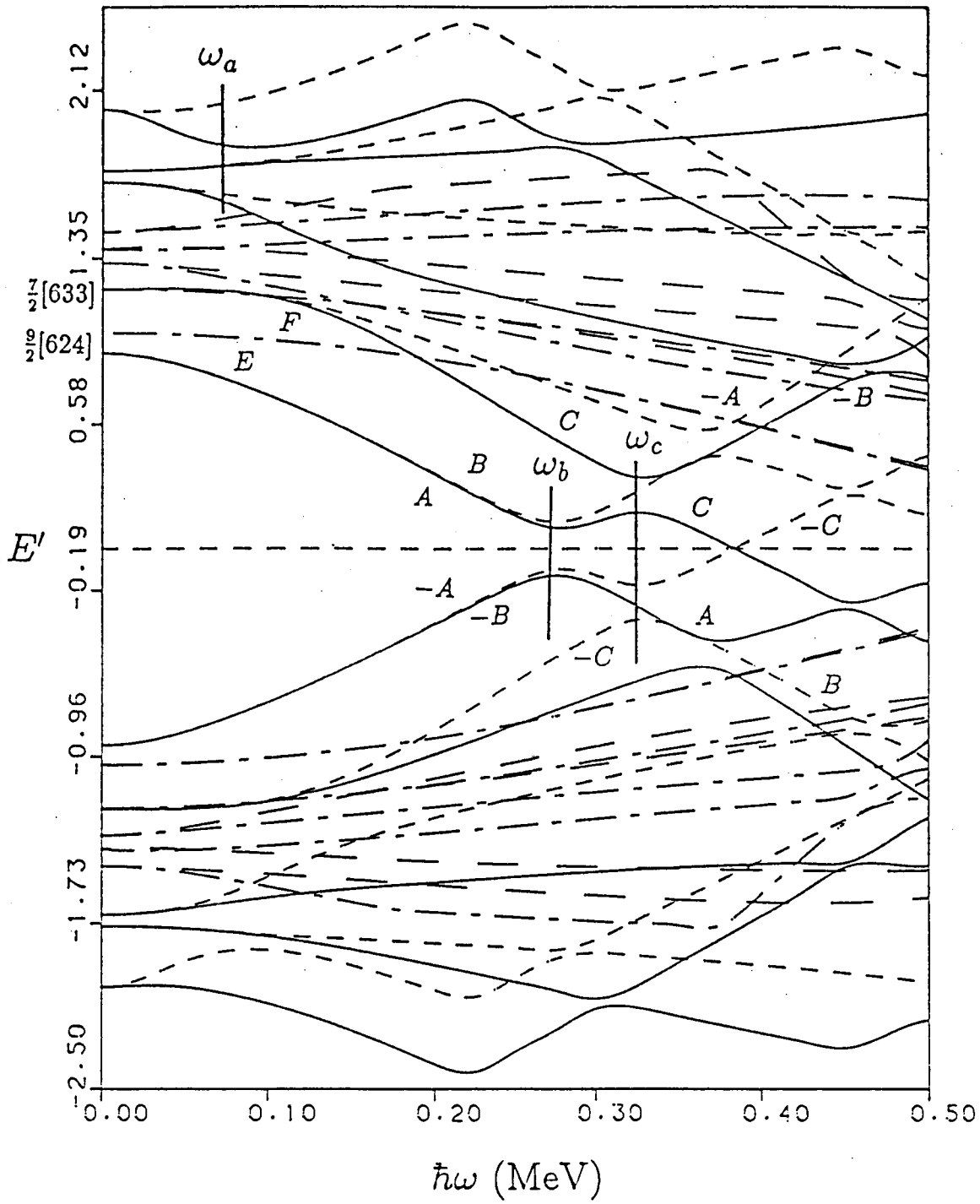

Figure 2.13: Quasineutron diagram for ^{184}Pt ($Z = 78$) using a Woods-Saxon potential. The values for β_2, β_4 and Δ were calculated self-consistently at $\hbar\omega = 0.0$ MeV.

applied to any quasiparticle diagram. This scheme is given in Table 2.1. Capital letters are used for quasineutrons while lower case letters are used to designate quasiprotons. The symmetry in the diagram around $E^{\omega} = 0$ results in the fact that for every quasiparticle state, E_i^{ω}, with signature $r = +i$, there is a corresponding state with $r = -i$ such that $E_i^{\omega} = -E_{\bar{i}}^{\omega}$.

Since the HFBC formalism does not consider interactions between the quasiparticles, a simple sum of all the occupied quasiparticle levels does not give the correct total energy in the rotating frame. Thus, it is only instructive to talk about quasiparticle excitations with respect to a reference. At low rotational frequencies, this reference is the quasiparticle vacuum, $|vac\rangle$. For even-even nuclei, $|vac\rangle$ is defined as the state in which all quasiparticle levels below the zero energy are filled, and those above are empty. The Fermi surface, λ, is calculated under the condition that $< N >$ equals the particle number.

Excitations of the system are obtained by operating on the vacuum with quasiparticle creation and annihilation operators, $\alpha_i^{\dagger}$ and $\alpha_{\bar{i}}$. Because there are twice as many quasiparticle states as single-particle states, it then follows that if E_i^{ω} is occupied, its conjugate state, $-E_i^{\omega}$, is unoccupied. For odd-nuclei the vacuum is defined as the $(n-1)$ even system, where n is the total number of particles. The Fermi surface is still calculated so that $< N >$ equals the particle number; however the odd-particle is treated in terms of one-quasiparticle excitations with respect to the vacuum, *i.e.* one-quasiparticle is promoted above the Fermi surface leaving an unoccupied level below the Fermi surface. Since $|vac\rangle$ is used as a reference to describe the quasiparticle excitations, its energy may be set to zero. For this reason, quasiparticle states with $E_i^{\omega} < 0$ are considered non-physical solutions. The excitation energy of a particular multi-quasiparticle state is simply the sum of the occupied quasiparticle levels. Differentiation of the cranking Hamiltonian with respect to the rotational frequency leads to the canonical relationship

Table 2.1: Convention used for the labeling of the quasiparticle trajectories. The subscript n indicates that the trajectory is the nth trajectory for a particular set of quantum numbers (π, α).

	Label	
$(\pi,\alpha)_n$	Quasineutron	Quasiproton
$(+,+\frac{1}{2})_1$	A	a
$(+,-\frac{1}{2})_1$	B	b
$(+,+\frac{1}{2})_2$	C	c
$(+,-\frac{1}{2})_2$	D	d
$(-,+\frac{1}{2})_1$	E	e
$(-,-\frac{1}{2})_1$	F	f
$(-,+\frac{1}{2})_2$	G	g
$(-,-\frac{1}{2})_2$	H	h

$$\langle i | j_x | i \rangle = -\frac{1}{\hbar}\frac{dE_i^\omega}{d\omega}, \tag{2.63}$$

where j_x is the angular momentum of the quasiparticle level projected onto the rotational axis. If a quasiparticle occupies the state E_i^ω, the the negative slope of its curve in a quasiparticle diagram represents its contribution to the total angular momentum and is referred to as the quasiparticle alignment. Since both E_i^ω and $< j_x >_i$ are additive quantities, the total quasiparticle energy and alignment of a multi-quasiparticle configurations are

$$e' = \sum_i E_i^\omega \tag{2.64}$$

and

$$i = \sum_k < j_x >_k . \tag{2.65}$$

These expressions are the theoretical analogues to the phenomenological single-particle Routhian and alignment expressions constructed in section 2.4 for the experimental data (see Eq. 2.28 and 2.29). The total signature of a multi-quasiparticle configuration is determined by

$$\alpha_{tot} = \sum_i \alpha_i. \tag{2.66}$$

The total signature also places a restriction on spins of the rotational band built upon this configuration, where

$$I = \alpha_{tot} + 2n \quad \text{where } n = 0, 1, 2, \cdots. \tag{2.67}$$

Finally, the parity of the multi-quasiparticle configuration is given by the relationship

$$\pi_{tot} = \prod_i \pi_i. \tag{2.68}$$

As a rule, multi-quasiparticle excitations of an even-particle system can only consist of an even number of quasiparticles and those of an odd-system only an odd number of quasiparticles.

One noticable feature of Fig. 2.13 is that orbitals having the same quantum numbers (π, α) do not crisscross but instead interact and are repulsed by one another. These interaction areas are interpreted as crossing regions between quasiparticle configurations, where the quasiparticle trajectories actually "swap" their quasiparticle configurations. Fig. 2.13 labels three such interaction points at critical frequencies ω_a, ω_b, and ω_c. The first crossing at ω_a occurs between quasiparticle orbitals which are unoccupied at non-zero rotational frequencies and have no immediate physical impact on the nuclear configuration. However, the second crossing at ω_b occurs between two occupied orbitals ($-A$ and $-B$) and two unoccupied orbitals (A and B). After the crossing, the interacting trajectories change configuration, and the orbitals A and B now lie lowest in energy relative to $-A$ and $-B$. The vacuum is still defined as the state for which the lowest N quasiparticle levels are occupied; thus, one can explain the band crossing at ω_b has a change in the vacuum configuration. Physically, band crossings between occupied and unoccupied quasiparticle orbitals are used to explain the backbending phenomenon described in section 2.3; thus, the rearrangement of the vacuum configuration represents the rotational alignment of a set of paired quasiparticles.

One of the experimental signatures of a backbend is a sudden gain in aligned angular momentum, i. In a quasiparticle diagram, the slope of a trajectory represents the component of the quasiparticle angular momentum along the rotational axis. Thus, the re-configuration of the quasiparticle orbitals at ω_b translates into a swapping of two upsloping trajectories with two downsloping trajectories. This results in a rapid change in the total angular momentum as is observed experimentally, where

$$i = -\frac{1}{\hbar}\frac{d}{d\omega}(E^{\omega}_{A} + E^{\omega}_{B}) \tag{2.69}$$

Crossing regions are designated by the labels of the initially unoccupied quasiparticle trajectories; thus, the crossing at ω_b is usually referred to as the (AB) crossing. The theoretical crossing frequency, ω_b, can be directly compared to the experimentally observed crossing frequency, which is obtained by plotting the experimental alignment, i, as a function of ω (see chapters 5 and 6). The initial vacuum configuration before the crossing corresponds to a two quasiparticle configuration after the crossing and is referred to as the ground configuration. Its phenomenological analogue is the parameterized ground band defined in section 2.4 whose energy is described by Eq. 2.27.

Another quantity which can be extracted from the quasiparticle diagrams is the interaction strength $|V|$. This quantity is read directly from the quasiparticle diagram by taking one-half the distance of closest approach between two interacting bands. Thus, for the (AB) crossing described above, this translates into

$$|V| = \frac{1}{2}(|E^{\omega}_{A}| - |E^{\omega}_{-B}|) \tag{2.70}$$

at ω_b. The strength of this interaction appears to be related to the sharpness of the experimental backbend. A weak interaction (small $|V|$) results in the classic backbending phenomenon observed in an I_x vs. ω plot while a strong interaction (large $|V|$) should correspond to a smooth upbend in the same experimental plot.

The third crossing marked in Fig. 2.13 (ω_c) occurs between trajectories which are not degenerate at $\omega = 0$ (BC). The BC crossing can only occur under special circumstances, *i.e.* when the trajectory A is occupied and the trajectory B is not. For example, if one is considering a rotational band built on the AE two-quasineutron configuration, the quasiparticle trajectories labeled A and E are occupied while those label $-A$ and $-E$ are unoccupied in Fig. 2.13 for $\omega < \omega_b$. At $\omega = \omega_b$, trajectory A interacts with trajectory $-B$. Since both orbitals are occupied, the exchange of quasiparticles between them is prohibited. On the other hand, interacting trajectories B and $-A$ are both unoccupied and do not contribute to the occupation structure of the nucleus. The orbitals occupied immediately after the AB crossing are the same as those before the crossing; thus, the nucleus has not changed its configuration. In this example, the AB crossing does not occur and is said to be "blocked". However, at the higher rotational frequency, ω_c, crossings between the B and $-C$ and between C and $-B$ do occur. Physically, this translates into the rotational alignment of a second pair of quasiparticles, and it is labeled as the BC crossing.

Because excited quasiparticle orbitals block specific band crossings, the absence of a band crossing in a multi-quasiparticle rotational band at a frequency in which one is expected immediately helps confirm the quasiparticle configuration of the crossing. Odd-even nuclei are ideal for this type of investigation, since the one-quasiparticle bands only block crossings involving the excited quasiparticle. These types of blocking arguments will be discussed in greater detail in chapters 5 and 6.

2.9 Nuclear Shapes at High Angular Momentum

2.9.1 Influence of Aligned Quasiparticles on the Nuclear Shape

As discussed in section 2.3, the Coriolis force generated by a rotating nucleus causes individual pairs of high-j quasiparticles to align their spins with the rotational axis. These aligned quasiparticles define their own potential field; thus, due to the short range nature of the nuclear force, their own shape. The final nuclear shape depends on how well these quasiparticles are able to "imprint" their shape onto the rotating nuclear core. The cores of well-deformed nuclei are quite "stiff", and their shapes are not greatly influenced by aligning quasiparticles. However, nuclei in transitional regions have relatively "soft" cores; thus, aligning quasiparticles may significantly modify the overall equilibrium shapes of these nuclei. It should also be noted that the shape of the core itself is influenced by rotation but to a lessor degree than the deforming effects imposed by the aligned quasiparticles. For example, centrifugal forces cause an elongation or "stretching" of the core.

Most deformed nuclei are either oblate or prolate in their ground state; however, at higher rotational frequencies, triaxial shapes in many nuclei are expected. Fig. 2.14 shows a polar coordinate system where the radius, β_2, measures the deviation from spherical shapes, and the angle γ measures the triaxiality of the nuclear shape. For $\gamma = 0°$, prolate shapes with the rotational axis perpendicular to the symmetry axis are defined. The same relationship between the rotational and symmetry axes exist for oblate shapes at $\gamma = -60°$. Therefore, nuclei whose shapes range from $-60°$ to $0°$ usually exhibit some type of collective motion. The $\gamma = 60°$ and $\gamma = 120°$ axes define oblate and prolate nuclear shapes, respectively, for the condition when the rotational axis is parallel to the symmetry axis. Collective rotation is not permitted for these orientations (see section 2.2); thus these

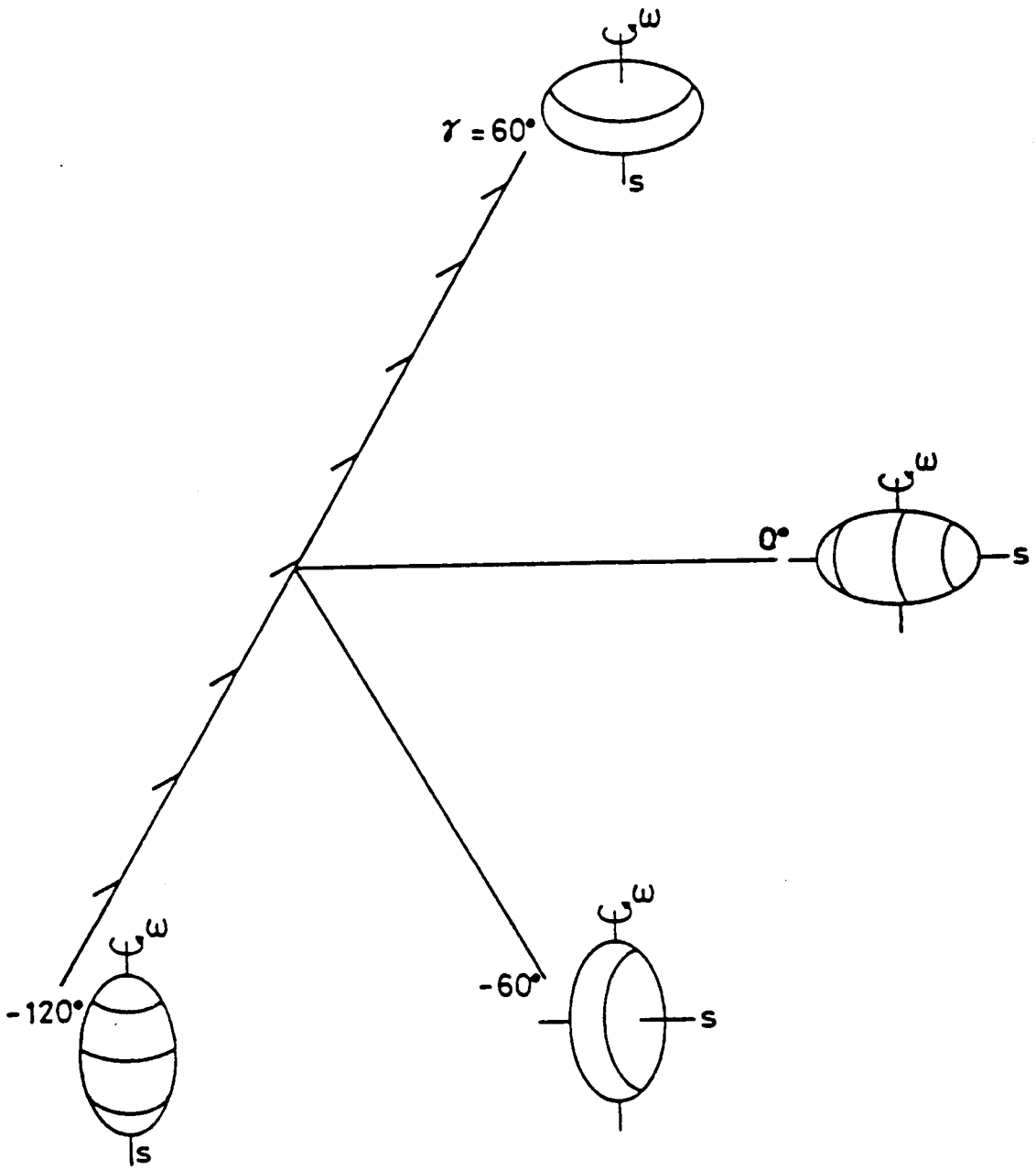

Figure 2.14: Quadrupole shapes in a polar coordinate system. The radius, β_2, measures the deviation from spherical shape. The angle, γ, gives the triaxiality and the orientation with respect to the axis of rotation.

radial lines of constant γ are referred to as the non-collective oblate and prolate axes. This prescription pictured in Fig. 2.14 is referred to as the Lund convention.

To determine the effects of aligning quasiparticles on the nuclear shape, Leander and Frauendorf (1982) have calculated the quasiparticle energies for a single $h_{11/2}$ proton shell as a function of the γ deformation. Cranked shell model calculations were done for different values of the Fermi energy (λ) using a modified oscillator potential and fixing the remaining parameters (ϵ_2=0.2, $\Delta = 0.1\hbar\omega_0$ and $\omega = 0.03\hbar\omega_0$). Fig. 2.15a summarizes the results for these calculations by showing the Routhians for the lowest lying quasiparticle trajectories of opposite signature as a function of γ for nine different values of the Fermi energy. Fig. 2.15b shows the energies in oscillator units of each Fermi level used in the calculation along with the non-rotating $h_{11/2}$ single-particle levels at two γ-values, 0° and 60°. Two features are clearly evident in Fig. 2.15a:

1. The minimum of the quasiparticle trajectories for the favored signature[1] has a relatively smooth γ dependence as the Fermi level moves through the shell.

2. In general the unfavored signature has a weaker dependence on γ and λ than the favored signature.

The γ dependence of the favored signature allows one to make definite predictions about the nuclear shape as a result of the alignment of a pair of quasiparticles. For example, in γ-soft nuclei where the potential energy surface is fairly flat over the γ plane, the sharp minimum of the favored signature should stabilize the nuclear shape. On the other hand, if the core has a well defined potential-energy minimum at some other value of γ than that for the quasiparticle Routhian, the quasiparticle exerts a "driving force" in γ proportional to the gradient of the quasiparticle trajectory. The final shape of the nucleus is a result of the balance

[1]The favored signature is the signature which lies lowest in energy. Or in more physical terms, it is the signature for quasiparticle configuration is most aligned.

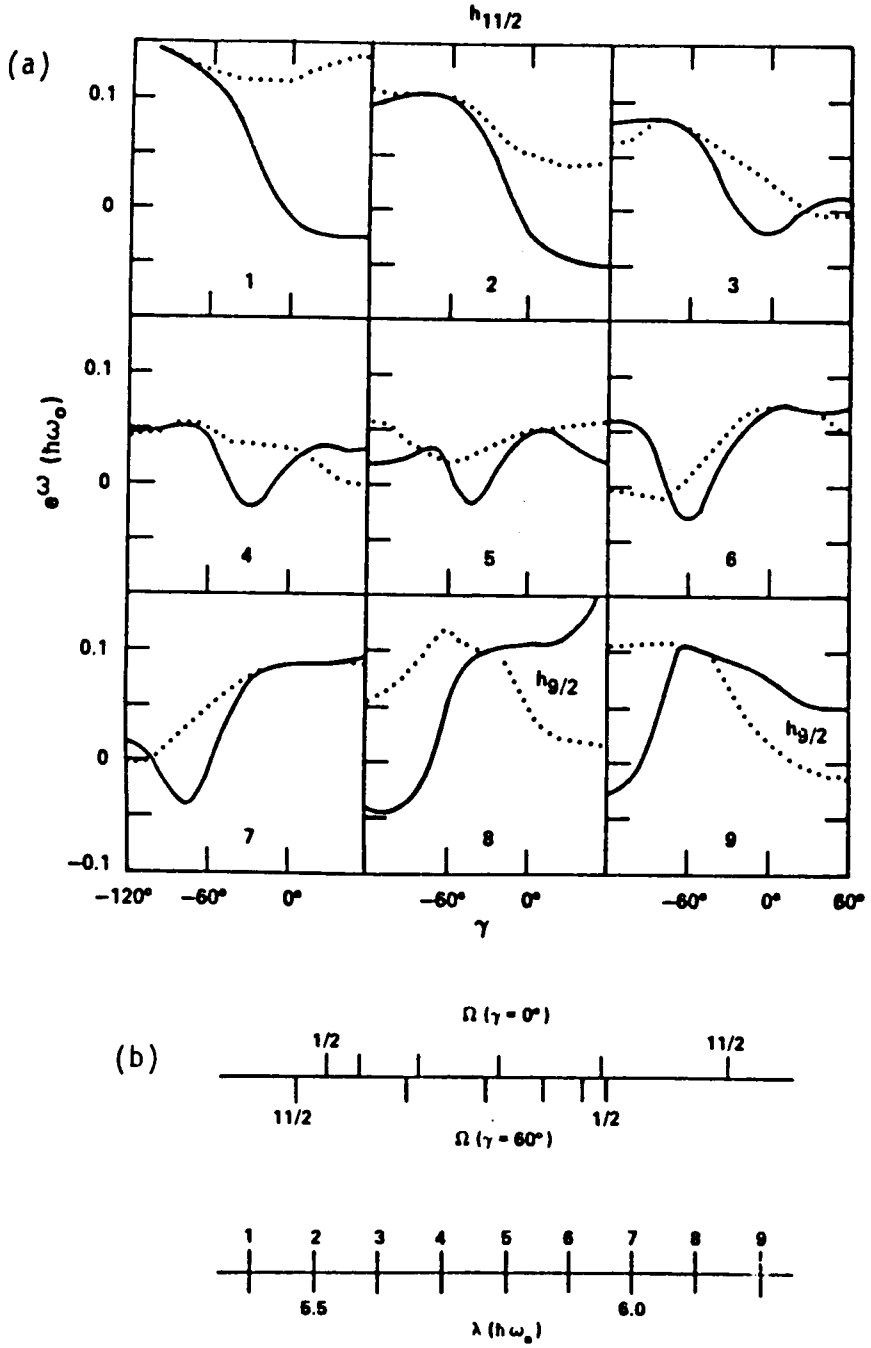

Figure 2.15: The quasiparticle energies as a function of the γ deformation of the lowest favored (solid lines) and unfavored (dashed lines) signatures in the $h_{11/2}$ subshell for nine different values of the Fermi level. Part b of the figure shows the value of the Fermi energy used for each diagram in oscillator units. Also pictured are the non-rotating $h_{11/2}$ single-particle levels at two γ-values, 0° and 60°. Reproduced from Leander *et al.* (1982).

reached between the driving forces of the quasiparticles and the restoring force of the core.

The weaker dependence of the unfavored signature on the γ deformation results in a significant energy difference between the two signatures in the region where the favored signature minimizes in γ. Since this "signature splitting" varies as a function of γ, one is able to use this as a gauge to indicate the onset of deformation effects in odd-A nuclei, where rotational bands of opposite signatures are built on the same one-quasiparticle configuration. For example in diagram 6 of Fig. 2.15, the signature splitting varies smoothly as a function of γ between $0°$ and $-60°$. By comparing and matching the experimentally observed signature splitting with that in the diagram, one is able to get an indication of the deformation driving effects of the excited quasiparticle. However, when this is done, the energy of the core should be added to both signatures and the energy difference between them as a function of deformation should then be extracted.

If the nuclei under consideration have cores which are "soft" with respect to deformation, one should also consider the effect aligning quasiparticles have on the axial deformation. Chen and Leander (1987) have made a similar investigation, as was done for the γ degree of freedom discussed above, by varying the quasiparticle Routhians as a function of ϵ_2. Fig. 2.16 shows the axial-driving force, $-de'/d\epsilon_2$, generated by rotating $h_{11/2}$ quasiparticle orbits for several values of the Fermi level. When the Fermi level lies low in the shell (solid curves), strong driving forces are generated by the quasiparticles as they are displaced from their equilibrium positions ($-de'/d\epsilon_2 = 0$) similarly to the strong restoring force generated by a spring as it is displaced further from its equilibrium position. The Routhians for these quasiparticle trajectories minimize between $0.23 \leq \epsilon_2 \leq 0.33$. This same effect is present when the Fermi level lies high in the shell (long-dashed curves); however, the Routhians minimize in a slightly lower ϵ_2 range ($0.18 \leq \epsilon_2 \leq 0.30$) than for the

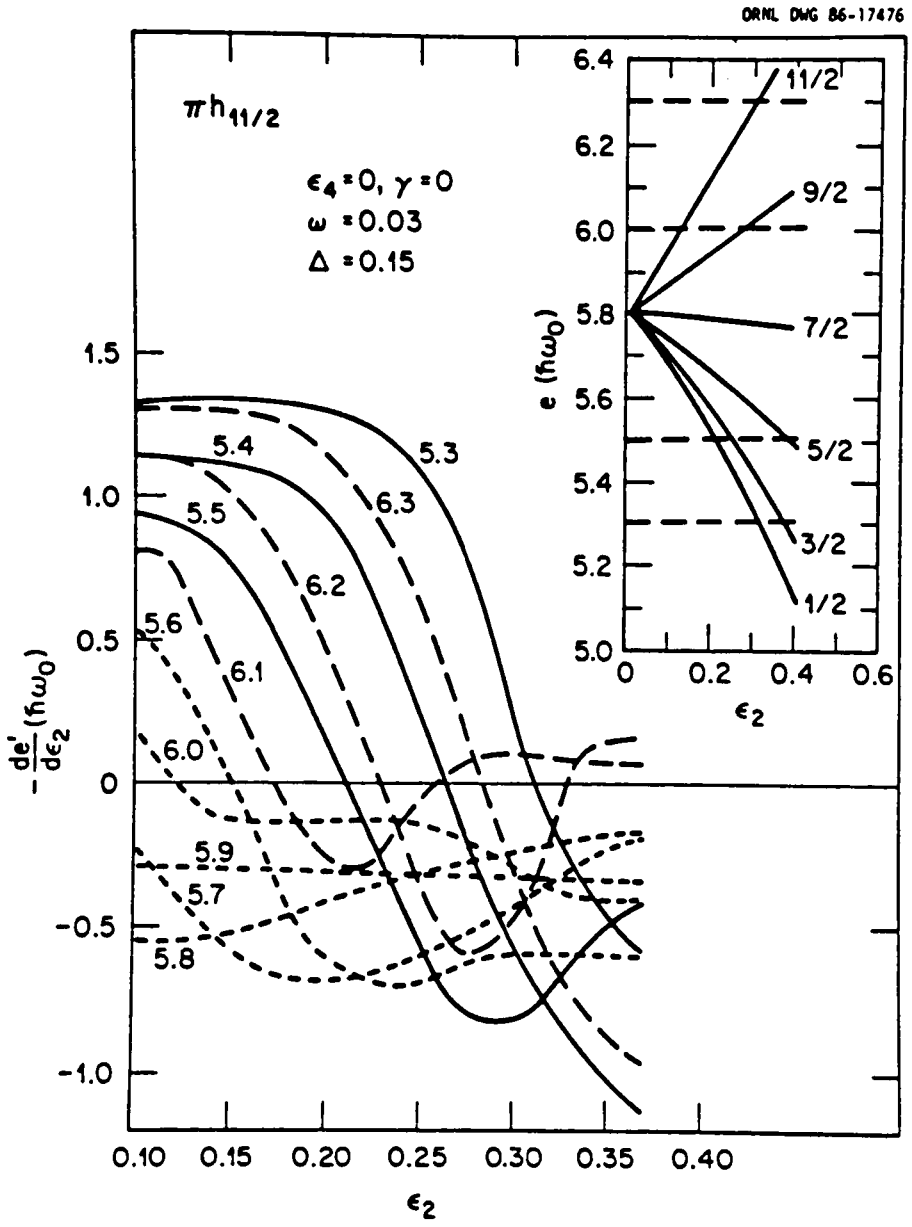

Figure 2.16: The quadrupole-driving force versus ϵ_2 for rotating $h_{11/2}$ quasiparticles for various placements of the Fermi level.

former case. On the other hand, when the Fermi level is placed in the middle of the shell (short dashed curves), the driving force is towards spherical shapes and remains relatively constant as a function of the quadrupole deformation.

While both of the discussions above involving deformation-driving forces generated by quasiparticles focused on the $h_{11/2}$ subshell, similar effects should be observed in other high-j subshells as well, *i.e.* $h_{9/2}$ and $i_{13/2}$. Thus, figures 2.15 and 2.16 can also be used as a qualitative guide for determining the γ and quadrupole driving forces generated by aligning high-j quasiparticles.

2.9.2 Shell Correction Method

The calculation of the quasiparticle energies using the HFBC formalism allows for the description of the nucleus in the rotating frame in terms of elementary quasiparticle excitations. It was shown in section 2.8 that the results of these calculations are best represented in the form of quasiparticle diagrams. From these diagrams, one can immediately extract band crossing frequencies, single-particle alignments and interaction potentials. However, one is unable to directly conclude anything about the nuclear shape, since the deformation parameters are fixed for the calculation. One solution to this problem might be to minimize the total energy of each quasiparticle Routhian with respect to the deformation parameters. Unfortunately, the energy of the vacuum, which the quasiparticle excitations are measured with respect to, does not represent the energy of the nucleus, because interactions between quasiparticles are not included in the HFBC formalism. Therefore, if one is to determine the shape of the nucleus in the rotating frame, self-consistently with respect to the deformation parameters of the average field, one must use a procedure which calculates the total energy in the rotating frame correctly.

The shell correction method allows for the calculation of the total energy

of the nucleus using a phenomenological one-body expression for the potential. It also links together two well established models of the atomic nucleus: the liquid drop model, which describes well the bulk properties of the nucleus, and the shell model, which describes features of the nucleus that depend on the level structure of the single-particle states. A good example illustrating the need for this type of procedure is found in a plot of the binding energy per nucleon (B/A) versus the nucleon number. Fig. 2.17 shows both the experimental values of B/A for β-stable odd-A nuclei and a calculated curve of B/A based on the liquid drop model. The calculated curve reproduces the overall features of the experimental data but not the oscillating fine structure. The deviation between experimental and calculated values is due to the fact that the nucleus has single-particle levels which are discrete with large energy gaps between major shells, while the liquid drop model assumes that the nucleus has a smooth continuous distribution of levels.

The total energy of the nucleus can be calculated using Hartree-Fock theory due to the fact that this method includes in a realistic manner the effective two-body interaction:

$$E_0 = \sum_m e_m^{(HF)} - \frac{1}{2}\int \rho(\mathbf{r})\rho(\mathbf{r}')V(\mathbf{r},\mathbf{r}')d^3r d^3r', \tag{2.71}$$

where $V(\mathbf{r},\mathbf{r}')$ is the effective two-body interaction and the sum runs over the occupied HF orbitals with self-consistent energies $e_m^{(HF)}$. Strutinsky (1968) showed that the Hartree-Fock energies could be replaced by single-particle energies calculated using a phenomenological one-body potential if the total energy was expressed as

$$E_0 \approx E_{sc} = E^{LD} + \delta E_{sh}, \tag{2.72}$$

where E^{LD} is the liquid drop energy, E_{sc} is the shell corrected energy, and δE_{sh} is the shell correction term which contains all fluctuations caused by the non-uniform distribution of the single-particle levels near the Fermi surface. Eq. 2.72 seems to

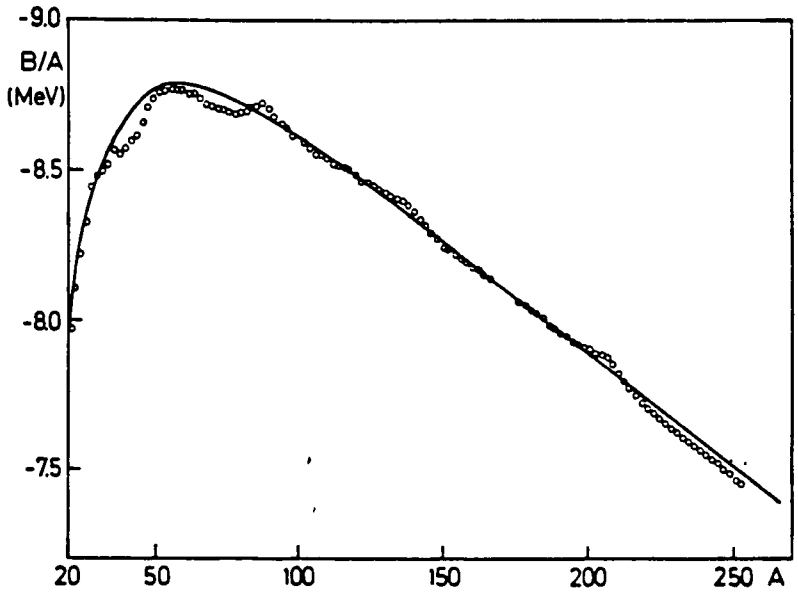

Figure 2.17: Both experimental and calculated values of the binding energy per nucleon for β-stable odd-A nuclei. The theoretical curve was calculated using an expression based on the Weizsäcker semi-empirical mass formula (Ring and Shuck, 1980).

agree well with what is observed in Fig. 2.17, *i.e.* that the shell effects are only a minor modification to the total energy.

In order to determine the shell correction term, one begins by calculating the single-particle energies in the independent particle model using either a Nilsson or Woods-Saxon potential. The total shell model energy is then defined as the sum of the occupied single-particle orbitals,

$$E_{sh} = \sum_{i=1}^{n} e_i. \tag{2.73}$$

This energy is split into a sum of two terms: the shell correction energy, δE_{sh}, and a "smooth" energy, $< \tilde{E}_{sh} >$, associated with the liquid drop term. Thus, δE_{sh} can be expressed as

$$\delta E_{sh} = E_{sh} - < \tilde{E} > . \tag{2.74}$$

One method for extracting $< \tilde{E} >$ from the total shell energy involves the replace-

ment of the single particle density of states

$$g(e) = \sum_i \delta(e - e_i) \tag{2.75}$$

with an expression which varies smoothly as a function of the energy. In this procedure, the expression for the "smooth" density of states is given by

$$\tilde{g}(e) = \frac{1}{\gamma} \int_{-\infty}^{+\infty} \xi \frac{(e' - e)}{\gamma} g(e') de', \tag{2.76}$$

where γ is the energy width around the Fermi surface for which the smoothing is done, and ξ is the smoothing function. There is no functional limitation on ξ,; however, it must fulfil the condition

$$\tilde{g}(e) = \frac{1}{\gamma} \int_{-\infty}^{+\infty} \xi \frac{(e' - e)}{\gamma} \tilde{g}(e') de', \tag{2.77}$$

which guaranties that ξ is in fact a smoothing function. Once $\tilde{g}(e)$ is determined, the smoothed part of the shell energy can be calculated:

$$< \tilde{E} >= \int_{-\infty}^{\tilde{\lambda}} e\tilde{g}(e) de, \tag{2.78}$$

where $\tilde{\lambda}$ is the Fermi energy for $< \tilde{E} >$ and is determined by the condition of particle conservation:

$$N = \int_{-\infty}^{\tilde{\lambda}} \tilde{g}(e) de. \tag{2.79}$$

Results of the averaging procedure should not depend on the averaging parameter, γ, and this condition is fulfilled if $\partial(\delta E_{sh})/\partial\gamma = 0$. This condition should be checked when using potentials like the Woods-Saxon, which have unbound states, because these states can play an important role in the smoothing procedure.

The shell correction method can also be extended to the region of high angular momentum. Some of the initial work done is this area is found in Bengtsson *et al.* (1975) or Andersson *et al.* (1976). Currently, this method, known as the Strutinsky cranking procedure, is one of the most useful microscopic tools

for describing nuclear shapes under the condition of rapid rotation. Only a short summary of the method is presented in this work, and it follows closely the more detailed derivation presented by Dudek (1987).

The first step in generalizing the shell correction method for the case of rotation is to replace the calculated single-particle energies, e_i, with the single-particle Routhians, e_i^ω, where e_i^ω is calculated from the Hamiltonian $(H_{ws} - \omega J_x)$. The liquid drop energy is also modified by adding the rotational energy of the liquid drop

$$E_{rot} = \frac{1}{2}\mathcal{J}\omega^2, \tag{2.80}$$

where $\mathcal{J}$ is the classical moment of inertia. Following the definition of the shell correction energy in Eq. 2.72, the total Routhian energy can be expressed as

$$R^\omega = E^{LD} - \frac{1}{2}\mathcal{J}\omega^2 + \delta E_{sh}^\omega, \tag{2.81}$$

where

$$\delta E_{sc}^\omega = \sum_{i=1}^{n} e_i^\omega - < \sum_{i=1}^{n} \tilde{e}_i^\omega >, \tag{2.82}$$

and it is understood that each term in the equation is dependent on the nuclear deformation parameters $(\beta_2, \beta_4, \gamma)$. After performing some algebraic manipulations, the total Routhian can be rewritten as

$$R^\omega = E^{LD} + \delta \tilde{E}_{sc}^{\omega=0} + \sum_i (e_i^\omega - e_i^{\omega=0}), \tag{2.83}$$

where the approximation of the classical rotational energy as a function of the shell correction energy has been made (Dudek, 1987):

$$< \sum_{i=1}^{n} \tilde{e}_i^{\omega=0} > - < \sum_{i=1}^{n} \tilde{e}_i^\omega > = \frac{1}{2}\mathcal{J}\omega^2. \tag{2.84}$$

Eq. 2.83 is very useful, because it eliminates the angular momentum dependence of the liquid drop and the shell correction energies. Pair properties are taken into

account by simply adding the pairing energy to R^ω, where

$$E^\omega_{pair} = < H^\omega >_{HFBC} - \sum_i e^\omega_i. \tag{2.85}$$

The energy represented by $< H^\omega >_{HFBC}$ is the sum of the individual quasiparticle energies which make up the vacuum configuration calculated self-consistently using the HFB equations. By performing several mathematical transformations, the total Routhian with pairing can be expressed as

$$R^\omega = E^{LD} + \delta\tilde{E}^{\omega=0}_{sh} + E^{\omega=0}_{pair} + \{< H^\omega > - < H^{\omega=0} >\}_{HFBC}. \tag{2.86}$$

Eq. 2.86 preserves the ω independence of the smoothed portion of the energy. R^ω is interpreted as the true absolute energy of the quasiparticle vacuum. Since the relative quasiparticle excitation energies, E^ω_i, are correct in the HFBC formalism, the total energy of excited configurations can also be calculated by adding the corresponding n-quasiparticle term:

$$R^\omega_{n-qp} = R^\omega + \sum_i E^\omega_i, \tag{2.87}$$

where E^ω_i is the quasiparticle energy.

2.9.3 Total Routhian Surface Calculations

In the previous subsection, a method for calculating the total Routhian energy without explicitly treating the interactions between quasiparticles was presented. This energy is dependent not only on the rotational frequency, but also on the deformation parameters as well. For the remainder of this chapter, a slightly reformulated expression for the total Routhian will be referred to than is expressed in Eq. 2.87. This expression is written as

$$E^\omega_{n-qp}(\hat{\beta}) = E^{\omega=0}_{Str}(\hat{\beta}) + E^\omega_{vac}(\hat{\beta}) + \sum_i E^\omega_i(\hat{\beta}), \tag{2.88}$$

where $E^{\omega=0}_{Str}(\hat{\beta})$ is the Strutinsky energy at $\omega = 0$ (see Eq. 2.86), $E^{\omega}_{vac}(\hat{\beta})$ is the total Routhian energy of the quasiparticle vacuum at ω, $E^{\omega}_{i}(\hat{\beta})$ is the excitation energy of quasiparticle i, and $\hat{\beta}$ represents the deformation parameters β_2, γ and β_4. In order to construct total Routhian surfaces, (TRS), this energy is calculated at discrete deformation points, $\hat{\beta}$, both for fixed ω and fixed quasiparticle configuration, in order to map out the Routhian energy as a function of deformation.

The theoretical equilibrium shape of the nucleus for a particular quasiparticle configuration is determined by finding at what deformation the TRS surface has a minimum. In many respects the form of Eq. 2.88 is very nice, because the Strutinsky energy need be calculated only once at $\omega = 0$. The remaining calculations at non-zero rotational frequencies involve only the calculation of the quasiparticle energies, using the HFBC-method discussed in section 2.7. Examples of TRS maps as a function of rotational frequency are shown in Fig. 2.18. It should also be noted that the total Routhian surface includes both the neutron and proton contributions to this energy.

To investigate the effect aligning quasiparticles have on the shape of the nucleus, Fig. 2.18 shows two TRS maps for the ground band of ^{184}Pt at frequencies $\hbar\omega = 0.15$ MeV and $\hbar\omega = 0.25$ MeV. Also pictured are γ-projections of the Routhian surface both for the total energy and the individual contributions from the quasiprotons and quasineutrons. These projections are constructed through the path of least resistance in the deformation plane (thick solid line of map). At $\hbar\omega = 0.15$, the equilibrium shape minimizes at $\beta_2 = 0.231$, $\beta_4 = -0.028$, and $\gamma = -3°$. The γ projections of the energy surface are very shallow in the vicinity of the energy minimum, indicating that the core represented by the ground configuration is soft with respect to deformation. At $\hbar\omega = 0.25$, a dramatic shift in the equilibrium shape is observed for all deformation values ($\beta_2 = 0.218$, $\beta_4 = -0.038$, and $\gamma = -15°$). The γ-projection remains virtually unchanged for the

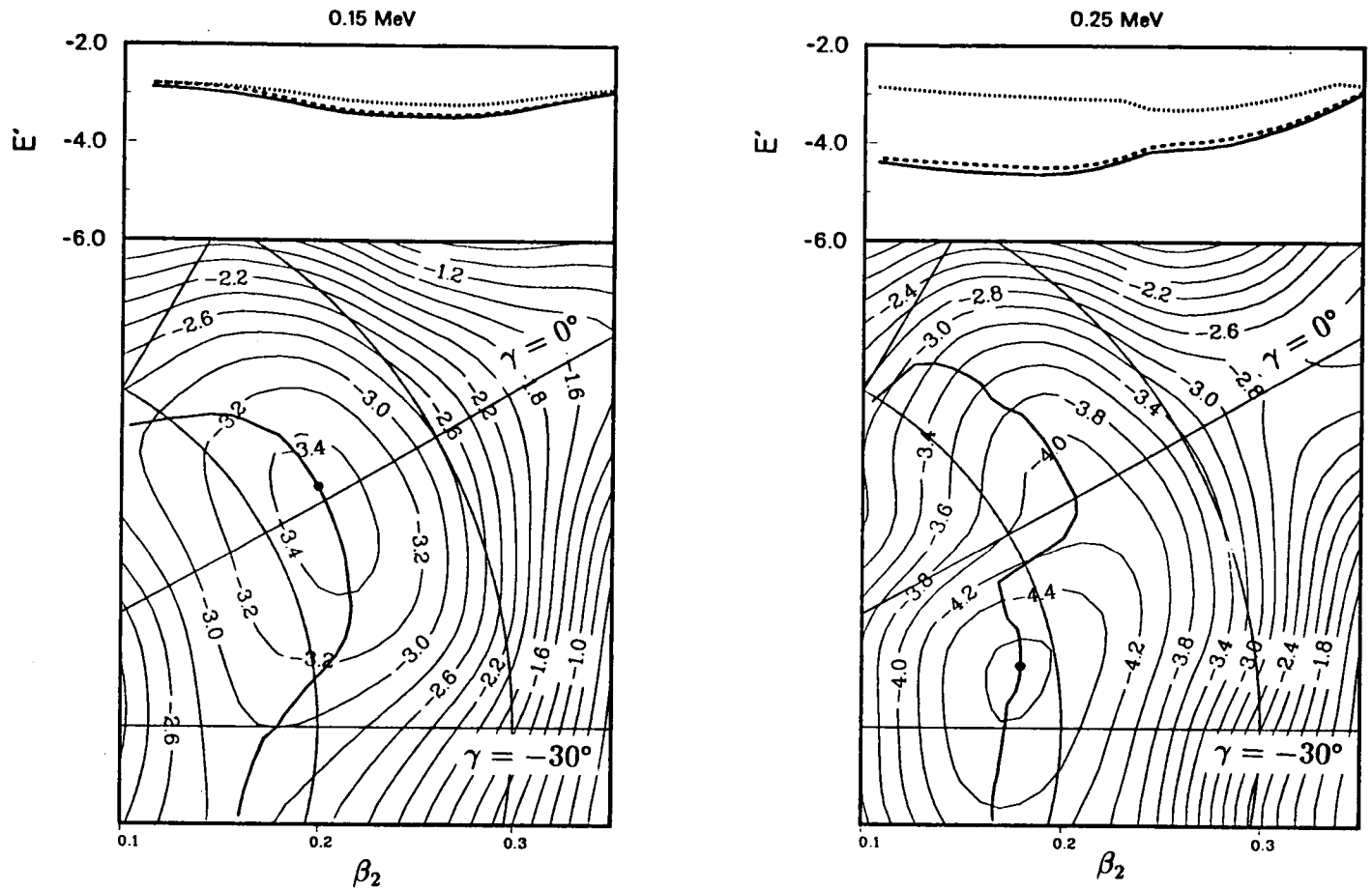

Figure 2.18: Total Routhian Surfaces for the yrast band in ^{184}Pt at rotational frequencies before and after the first band crossing. Also included in this figure are the γ-projections for the Total routhian energy and individual contributions from the quasiprotons and quasineutrons. The thick solid line on both maps indicate the path of this projection.

quasiproton contribution to the energy; however, the quasineutron projection has developed a minimum at $\gamma = -15°$. A CSM calculation using the deformation and pairing parameters indicated for the ground configuration at $\hbar\omega = 0.15$ shows that the $\nu i_{13/2}$ AB crossing should occur at $\hbar\omega_c \approx 0.23$ MeV. Thus, the nuclear shape change observed at $\hbar\omega = 0.25$ MeV is associated with this band crossing. Since the neutron Fermi level lies in the middle of the $\nu i_{13/2}$ shell, the deformation driving forces of the quasineutrons "push" the equilibrium shape towards negative γ-values and smaller quadrupole deformation as discussed in section 2.9.1. The shallowness in the Routhian surface for the ground configuration enables the aligning $\nu i_{13/2}$ quasiparticles to greatly influence the equilibrium shape of the nucleus.

In this example, information was obtained about the nuclear shape of the yrast band in ^{184}Pt as a function of rotational frequency. One was able to observe the softness with respect to deformation of the nuclear core and the strong driving forces generated by the aligning quasineutrons. Also, information about the crossing frequency was obtained, and it is also possible using this model to extract values for the single-particle alignment, i. In conclusion, these HFBC-calculations done self-consistently with respect to the deformation contain the same information available from CSM quasiparticle diagrams such as band crossing frequencies. One drawback to the model is that the HFBC-calculations must be done at many deformation points making the calculation a very laborious one. However, when large fluctuations in the nuclear shape occur due to quasiparticle alignment as is the case in transitional regions, the CSM model may be dangerous to use if the correct deformation parameters are not selected (see chapter 5). For these cases, it is very instructive to perform the fully self-consistent calculation and extract reasonable deformation values.

CHAPTER 3

EXPERIMENTAL TECHNIQUES

3.1 Introduction

The collective motion of nuclei has been studied extensively by both experimental and theoretical nuclear physicists for over thirty years, beginning with the pioneering work of Bohr and Mottelson in the early 1950's. The past decade has yielded a vast amount of new information on the interplay between collective and single-particle degrees of freedom in nuclei, leading to a fuller understanding of the nuclear structure near the yrast line. The accumulation of this new knowledge can be related to the implementation of two major developments: the use of heavy-ion accelerators for the formation of both stable and exotic nuclei in highly excited states, and the construction of multi-detector spectrometers for measuring with good efficiency and energy resolution the majority of the γ rays and particles emitted by the de-exciting nucleus.

The most efficient way to impart large amounts of angular momentum to a nucleus is through a heavy-ion fusion reaction. In such a reaction, heavy ions are accelerated onto an isotopically enriched target at energies slightly above the Coulomb barrier to form a highly excited compound nucleus by fusing the projectile and target nucleus together. The amount of angular momentum the nucleus can accommodate is finite, and if the bombarding energies are too high, the compound system will break apart or not form at all. Fig. 3.1 shows a plot of the maximum angular momentum that can be accommodated in β-stable nuclei as a function of A, assuming that the nucleus is an electrically charged rotating liquid drop with no intrinsic excitation energy (Cohen *et al.*, 1974). The decrease in ℓ_{max} for $A > 130$ is due to the increasing influence of the Coulomb force in lowering the

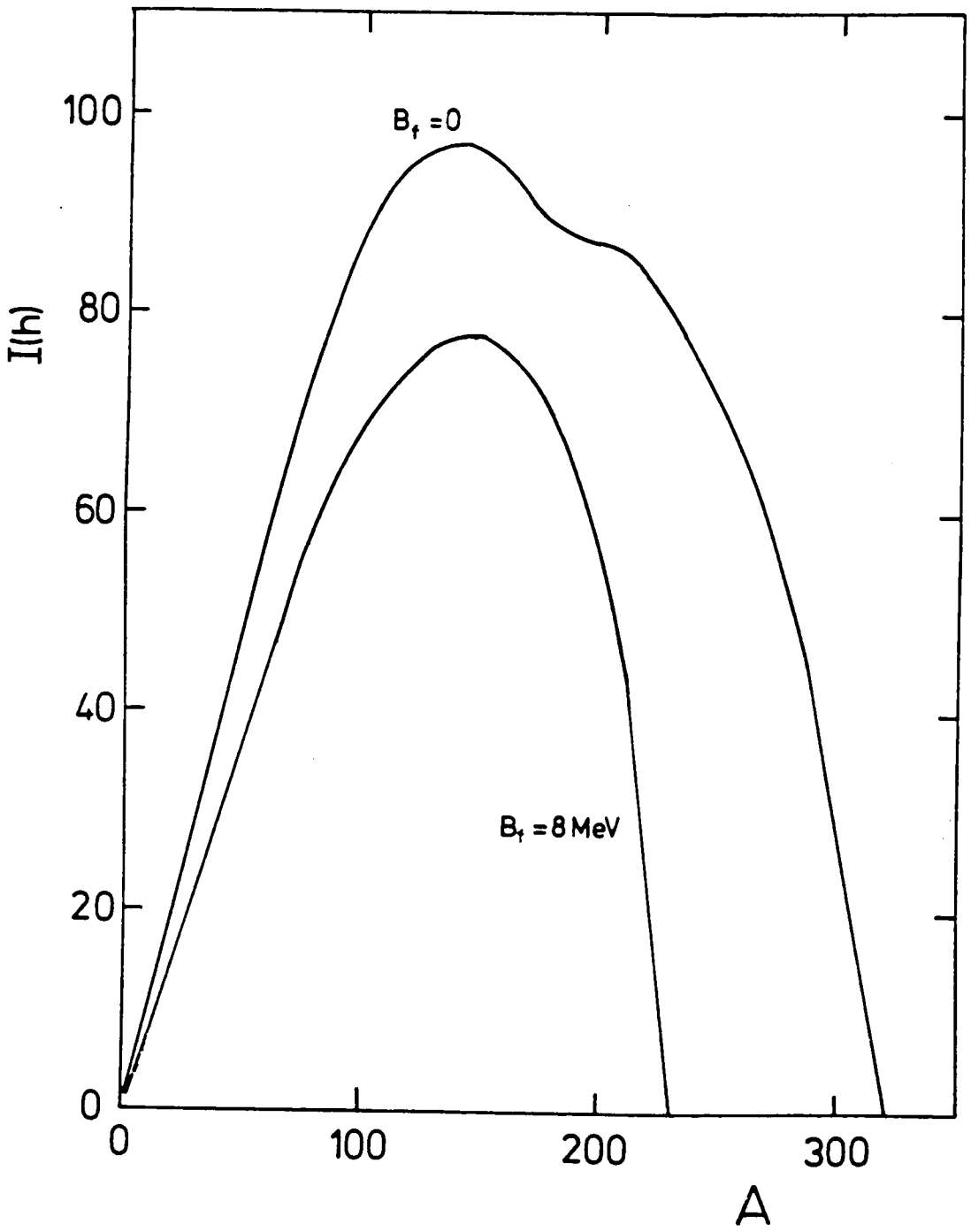

Figure 3.1: The curve lying highest in angular momentum represents the point at which the fission of a β-stable rotating nucleus with mass A is predicted to vanish (classical estimates). Below the lower lying curve, the fission barriers for the rotating β-stable nuclei are higher than 8 MeV. Reproduced from Riley (1984).

fission barrier. The lowering of the maximum angular momentum at the lighter masses is due to the lower surface energy and the higher rotational frequencies required by the smaller moments of inertia. The dashed curve in Fig. 3.1 shows the angular momentum required to lower the fission barrier of a nucleus to 8 MeV. This curve gives an indication of the maximum amount of angular momentum that a compound nucleus can accommodate to survive the risk of fission in the de-excitation process.

In the study of both nuclear structure at high angular momentum and nuclear reaction mechanisms, much information is gained by measuring the γ rays emitted in heavy-ion induced reactions. For a typical heavy-ion reaction, the average multiplicity of emitted γ rays can be as high as 30 per nucleus. The electromagnetic multipole moments of most of these γ rays have large admixtures of either dipole or quadrupole components. Since the spin direction of the compound nucleus after a heavy-ion collision is in the plane perpendicular to the beam axis, the radiation pattern of the γ rays covers the entire solid angle around the target. This is in contrast to the situation where the spin orientation of the nucleus is in a fixed direction and definite predictions about the plane in which the γ rays of different multipolarities are emitted can be made. Clearly if one is to measure all the γ rays emitted after a heavy-ion collision, the detectors used must surround the entire reaction chamber.

In many types of reaction studies, one is interested in measuring the total energy and angular momentum imparted to the nuclear system by the heavy-ion collision. Since the γ-ray multiplicity is related to the initial angular momentum of the compound nucleus[1], reaction studies require detectors which are able to efficiently measure the entire energy of each γ ray emitted in the heavy-ion reaction.

[1]For example, the first moment of the multiplicity distribution is given by $< M_\gamma >= \frac{1}{2} < I - I_0 > + k$, where M_γ is the γ-ray multiplicity; I, the angular momentum of the entry state; I_0, the angular momentum where the observed cascade terminates; and k, an empirical constant.

If one is to measure both the energy and multiplicity of an event, accurately, not only must the detectors used subtend a solid angle of nearly 4π, but the number of detectors in the spectrometer should be twice the maximum multiplicity to be measured (Jääskeläinen *et al.*, 1983). There are currently in use or under construction in both North America and Europe γ-ray spectrometers which meet the above criteria. Scintillation detectors made of sodium-iodide (NaI) or bismuth-germanate (BGO) material are used in these spectrometers because of their high efficiency in detecting γ rays. The total detected energy, H, for a heavy-ion reaction is measured by these spectrometers by summing the energies of the individual detected γ rays, and the detected multiplicity, K, is determined by the number of detectors firing for each event. Since these spectrometers are not 100% efficient in detecting γ rays, the total energy, E, and the total multiplicity, M, are calculated from H and K. Clearly, the closer H and K are to the actual values of E and M, the more accurately E and M are determined. Thus, the use of scintillation detectors in 4π spectrometers is useful when studying reaction mechanisms; however, their poor energy resolution makes it impossible to resolve individual γ rays in complicated energy spectra.

When one is probing the nuclear structure of discrete high-spin states at excitation energies near the yrast line, detectors are needed which measure with good precision the energy of the individual γ rays. Thus another type of detector other than one made of scintillation material must be used to resolve individual γ rays in the energy spectrum. Semiconductor detectors made of germanium (Ge) or silicon (Si) material have very good resolution in recording the energy response function of monoenergetic γ rays. Unfortunately, these detectors have a relatively low efficiency for detecting γ rays due to the low density of the semiconductor material and the deficiency in technology for building large volume semiconductor detectors. Because of their low efficiency, the γ-ray spectra of semiconductor

detectors have a large background associated with them due to the incomplete absorption of the γ ray in the crystal. In order to decrease the recording of this background radiation during an experiment, the semiconductor detector is surrounded by a detector made of scintillation material. The purpose of these scintillation detectors is to measure the γ rays which Compton scatter out of the semiconductor crystal. By rejecting the events associated with the simultaneous detection of a γ ray in the semiconductor and scintillation detector, one is able to suppress the background associated with the energy spectrum of the semiconductor detector. These scintillation detectors are known as Compton-suppression shields.

The design of 4π spectrometers must be flexible, because the study of different nuclear processes through the detection and identification of γ rays requires different types of detectors. For example, some reaction studies require that the reaction chamber be surrounded entirely by scintillation detectors so that the total energy and multiplicity of an event can be accurately recorded. On the other hand, experiments which measure the level structure of high angular momentum states are set up to record coincidences between γ rays. This is done because γ rays which are detected at the same time in different detectors are assumed to have been emitted by the same nucleus and belong to the same decay pathway. Ge detectors are used to determine the energy of the γ rays in coincidence with one another. Because of their low detection efficiency and large distance from the target (up to 25 cm in some 4π spectrometers), a large number of Ge detectors surrounded by Compton-suppression shields must be used to increase the rate at which coincidences are detected. However, by replacing part of the solid angle taken up by scintillation detectors with semiconductor detectors, one loses resolution in determining the total energy and multiplicity of the reaction on an event by event basis.

The experiments reported in this work were designed to measure γ rays in

coincidence with one other. The measurements were done at several institutions, utilizing a number of different heavy-ion reactions. To measure high-spin states in ^{184}Pt and ^{183}Au, a total of five experiments were performed, four on ^{184}Pt and one on ^{183}Au. These experiments were done at three separate facilities: (1) the Holifield Heavy Ion Research Facility at Oak Ridge National Laboratory, utilizing a 25 MV tandem accelerator, (2) the McMaster Tandem Accelerator Laboratory, using a 10 MV FN tandem accelerator, and (3) Chalk River National Laboratory (Canada), utilizing a 12 MV tandem accelerator. Each experiment utilized a γ-ray spectrometer equipped with intrinsic Ge detectors to measure discrete γ-ray transitions, and a set of auxiliary detectors (NaI or BGO) to isolate individual reaction channels. The spectrometers used ranged from the relatively simple Lotus spectrometer, set up with eight unsuppressed Ge detectors coupled with six NaI detectors, to the "state of the art" 8π Spectrometer, incorporating twenty Compton suppressed Ge and seventy-one BGO detectors. All the measurements were arranged to record γ-ray coincidences, except the McMaster experiment in June of 1986, which was designed to measure γ-ray angular distributions. A summary of each experiment can be found in Table 3.1.

3.2 Formation and De-excitation of the Compound Nuclear System

Many recent studies have been performed using heavy-ion reactions to study high-spin states of nuclei in the rare-earth region, where discrete energy levels have been observed with $I > 40\ \hbar$ in normally-deformed rotational bands and as high as 60 $\hbar$ (Twin *et al.*, 1986) in superdeformed bands. After a heavy-ion fusion reaction, the compound nucleus formed is usually left in a state of high excitation energy and angular momentum. While this is advantageous for studying the highest spins accessible to nuclei in the rare-earth region, it is a detriment for compound systems with low fission barriers. For nuclei with a large number of

Table 3.1: Summary of the reactions, spectrometers and facilities utilized for the work under discussion.

Reaction		Spectrometer	Facility	Date
^{154}Sm(^{34}S,4n)^{184}Pt	163 MeV	Spin Spectrometer	HHIRF	Aug. '84
^{172}Yb(^{16}O,4n)^{184}Pt	91 MeV	Lotus	McMaster	Feb. '86
^{172}Yb(^{16}O,4n)^{184}Pt	93 MeV	Lotus	McMaster	Jun. '86
^{160}Gd(^{29}Si,5n)^{184}Pt	150 MeV	8π Spectrometer	Chalk River	Jul. '87
^{152}Sm(^{35}Cl,4n)^{183}Au	170 MeV	Spin Spectrometer	HHIRF	Aug. '85

protons ($Z > 82$), the competition between the surface and Coulomb energies lowers the fission barrier with respect to angular momentum (see Fig. 3.1), and a cooler mechanism, other than a fusion reaction, must be used to populate high-spin states near the yrast line, *e.g.* multi-particle transfer reactions and Coulomb excitation. The Pt-Au nuclei examined in this study have a lower fission barrier than lighter rare-earth nuclei; however, with the right combination of beam energy, projectile and target, nuclear levels upto $I = 35\ \hbar$ have been observed in this research (see section 4.2). Since the choice of the reaction is critical to minimize fission and maximize angular momentum of the compound system in this region, a more detailed examination of heavy-ion reactions follows.

In the formation of a compound nucleus by the fusion of two smaller nuclei, the energy of the collision must be larger than the Coulomb barrier. This critical energy is given by

$$E_{CB} = 1.44\frac{Z_1 Z_2}{R_{CB}}, \tag{3.1}$$

where Z_1 and Z_2 refer to the proton number of the projectile and target respectively; R_{CB} is the Coulomb radius in fermis; and E_{CB} is given in MeV. This simple definition of the Coulomb barrier is based on the cutoff model where R_{CB} is defined such that for distances larger than R_{CB} the interactions are purely Coulombic, whereas for smaller distances, the nuclear interaction dominates and

fusion can take place. From this definition, R_{CB} cannot be equal to the simple sum of the effective matter radii of the target and projectile, but must be taken to include some effective range of the nuclear force. Experimental values deduced from phase-shift analysis of elastic scattering data show that over a wide range of masses and energies (see Bass, 1980)

$$R_{CB} = R_1 + R_2 + 3.0(\pm 0.5)\text{fm}, \tag{3.2}$$

where R_i is defined as the point where the nuclear charge density has dropped to one half its central value. For Eq. 3.2, the value of R_i has been deduced from electron scattering:

$$R_i = 1.12A_i^{1/3} - 0.94A_i^{-1/3}\ [\text{fm}], \tag{3.3}$$

where A_i is the atomic mass of the nucleus. A simpler parameterization of R_{CB} is also employed which has been deduced from scattering measurements for ^{3}He, ^{4}He and heavier ions using a smooth cut-off model (Fran and Venter, 1963):

$$R_{CB} \approx (1.4\text{-}1.5) \times (A_1^{1/3} + A_2^{1/3})\text{fm}, \tag{3.4}$$

where R_{CB} is defined now as the distance of approach at which there is a 50% probability of a non-elastic event occurring.

Because heavy-ion collisions involve the interactions between relatively large pieces of nuclear matter in which case the kinetic energy is shared among all the nucleons, classical treatments are used to calculate the total energy and angular momentum brought into the system by the collision. By using the sharp cut-off model which assumes there is a sharp boundary separating the elastic from the inelastic channels (see description of R_{CB} above), one is able to show that the maximum angular momentum leading to a reaction is,

$$\ell_{max} = 0.219R_{CB}\left[\mu(E_{CM} - E_{CB})\right]^{1/2}, \tag{3.5}$$

where $E_{CM} = \frac{A_2}{A_1 + A_2} E_{LAB}$ is the energy in the center of mass system in MeV; and $\mu = \frac{A_1 A_2}{A_1 + A_2}$ is the reduced mass of the system in mass units. It should be noted that the more distant collisions, which involve the highest ℓ waves, lead to transfer and deep inelastic collisions, so that the ℓ_{max} for the compound nucleus is lower than that given in Eq. 3.5. The maximum energy transferred in the reaction is given by the simple relationship

$$E_{ex}^{max} = E_{CM} + Q, \tag{3.6}$$

where the Q-value is the difference in rest mass energy of the reactants and the products in MeV.

Once the compound nucleus is created, it retains no knowledge of how it was formed. Thus statistical models can be used to describe the decay of the compound system (see Blatt and Weisskopf, 1952). If one is to study high angular momentum states, the final reaction products of interest should retain a large portion of the initial angular momentum. Clearly, fission of the compound system is undesirable, since most of the angular momentum goes into the relative motion of the fragments. In order to prevent fission, the highly excited system must lose energy by another decay process, and at such excitation energies, this is only possible through particle evaporation. For particle evaporation to compete with fission, the compound system must exist for 10^{-18} to 10^{-17} seconds before it begins to decay. For this to be possible, a fission barrier on the order of the neutron binding energy is needed (see Fig. 3.1).

For particles to be evaporated, they must overcome a centrifugal barrier given by,

$$E_\ell = \frac{\hbar^2}{2\mu R_{int}^2} \ell(\ell + 1), \tag{3.7}$$

where R_{int} is the interaction radius and is approximately equal to R_{CB}; μ is the reduced mass of the particle and compound system; ℓ is the angular momentum

of the particle to be evaporated; and E_ℓ is in MeV. Charged particles must also overcome the Coulomb barrier. These two potential barriers limit the possibilities for particle evaporation to the lightest systems, *i.e.* neutrons, protons and α-particles[1]. For compound systems with $A < 100$, the Coulomb barrier is low enough that all three types or particle emission compete. Thus, a large number of different reaction channels are available for the final product. This makes spectroscopy difficult in this region, because it is difficult to sort out the γ rays associated with each residual nucleus. For nuclei in the rare-earth region, the Coulomb barrier is high enough to suppress the emission of charged particles at intermediate bombarding energies and neutron evaporation dominates. However, for very neutron-deficient nuclei in this region, charge particle evaporation is once again competitive with neutron emission.

The binding energy for a single neutron is approximately 8 MeV, and statistical model calculations show (Hillis *et al.*, 1979) that on the average neutrons emitted by the nucleus after a heavy-ion reaction have 2 MeV of kinetic energy. While these energies are significant, the amount of angular momentum the emitted neutron possesses is only one or two units. Therefore, the residual nuclei vary significantly in excitation energy but little in angular momentum from the compound system. Fig. 3.2 shows the population in excitation energy and angular momentum of the different neutron-evaporation channels resulting from the ^{124}Sn(^{40}Ar,xn)$^{164-x}$Er reaction at a beam energy of 147 MeV. Notice how the regions associated with the fewest number of evaporated neutrons lie noticeably higher in excitation energy than those with the greatest number of evaporated neutrons.

[1]There is a small probability (2000:1) that a very high energy γ ray will compete with particle emission. These transitions are thought to be the de-excitation of the giant resonances of the compound system and may offer a chance to probe the nuclear structure at even higher angular momentum and energy (Newton *et al.*, 1981).

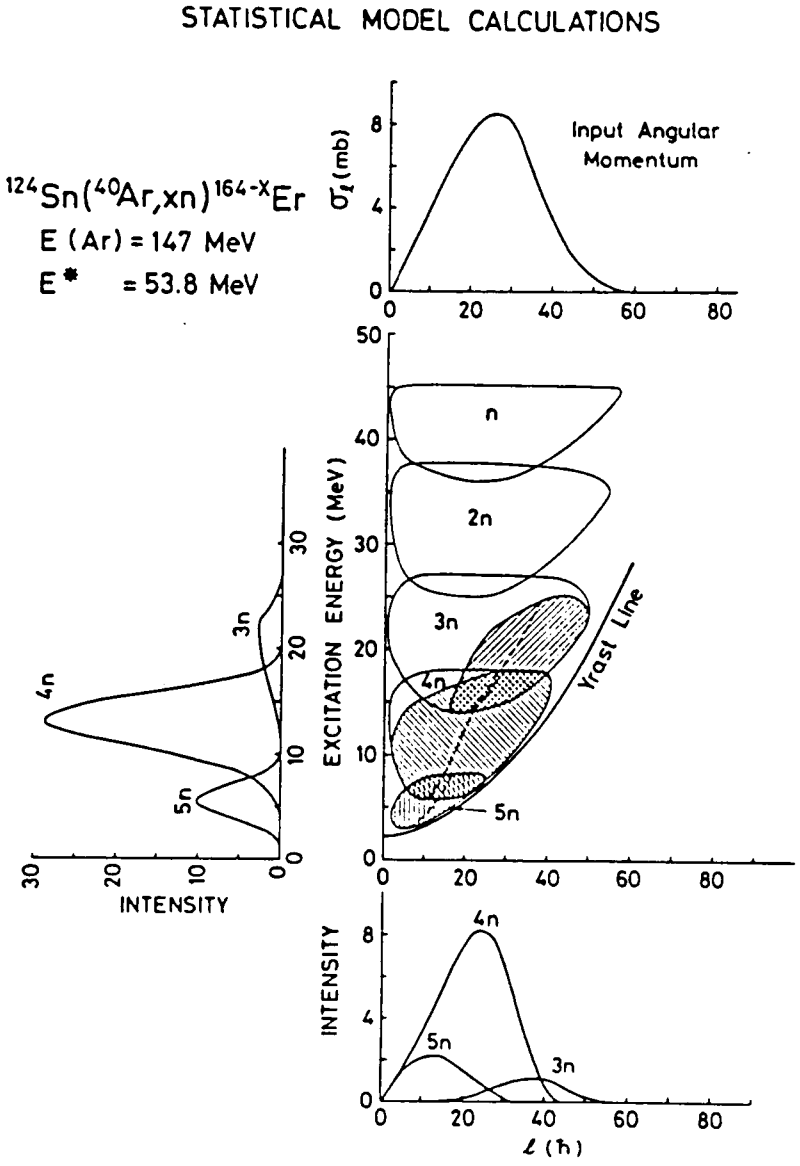

Figure 3.2: Statistical model calculations by Hillis *et al.* (1979) showing the population as a function of excitation energy and angular momentum of the system after the emission of 1–5 neutrons resulting from the $^{124}Sn(^{40}Ar,xn)^{164-x}Er$ reaction at 147 MeV. Reproduced from Bengtsson and Garrett (1983).

The shaded regions of Fig. 3.2 for the 3n–5n populations indicate where γ-ray emission begins. Even though the excitation of the initial compound nucleus is kept constant for the calculation, there is a large spread in the the excitation energy and angular momentum of the residual products in the γ-ray region. For example, the 3n population cloud covers a large region of angular momentum space. On the other hand, the region associated with γ-ray de-excitation for the same channel covers only the higher angular momentum portion of the cloud. This is due to the fact that at lower angular momentum, the 3n channel still has enough intrinsic energy to emit particles. This intrinsic energy is sometimes referred to as the temperature, and it is defined as the difference between the excitation energy and the energy of the yrast line corresponding to the same angular momentum. Thus, a property of heavy-ion reactions is that the residual nuclei having the fewest evaporated neutrons lie highest in excitation energy and angular momentum. Therefore, by making the appropriate choice of target, projectile, and beam energy, one is able to excite the nucleus of interest to the highest angular momentum accessible.

Once the decaying nucleus has a temperature near the binding energy of a single neutron, γ-ray emission begins to compete with particle evaporation. This region of competition is known as an entry state, since it defines the origin of the γ-cascade. The γ rays emitted by the nucleus are classified in two categories: those which cool the residual nuclei by taking away large amounts of energy but little angular momentum, called "statistical", and those which dissipate the angular momentum but not the temperature, called "yrast-like". The two types of transitions compete with each other in all regions of angular momentum and excitation energy.

Statistical transitions are defined as, such because their transition probabilities depend largely on the initial and final density of states as opposed to

the transition matrix elements between individual states. Thus, these transitions dominate over yrast-like decays at energies significantly above the yrast line, where the level densities are very large. Calculations have also shown that the statistical $E1$ transitions dominate over the $M1$ and $E2$ statistical transitions. In deformed nuclei, the statistical transitions bring the nucleus into a region where there are large quadrupole matrix elements between individual states and lower level densities. This causes an increase in the transition probabilities of the yrast-like electric quadrupole ($\Delta I = 2$) transitions over the statistical $E1$ decays. Thus, yrast-like transitions dominate in this region. However, individual γ rays emitted in this region cannot be resolved in the γ-ray spectrum, because the level densities are still too high to allow for any single rotational pathway to dominate. This region is usually referred to as the "collective" continuum. In the vicinity of the yrast line, the level densities are low enough that discrete γ-ray transitions are observed in the γ-ray spectrum. From these transitions, energy level diagrams are constructed of the yrast and near-yrast rotational bands. Information about the nuclear structure in the different realms of spin and temperature can be extracted by studying the different types of γ-ray cascades discussed above. Fig. 3.3 is a subset of Fig. 3.2, showing only the portion of the statistical model calculation dealing with γ-ray emission. It also indicates the regions of excitation energy and spin where the three types of γ-ray transitions dominate. The work herein is concerned wholly with the examination of the discrete transitions, and the physics which can be deduced from studying them.

Table 3.2 lists the γ-ray intensities for the yrast band in ^{184}Pt for the three reactions used in this research. The intensity for the transitions in the ^{16}O induced-reaction fall off more quickly at higher spin than that for the ^{34}S and ^{29}Si reactions. This is easily explained by calculating the maximum angular momentum and excitation energy brought into the reaction for the three cases

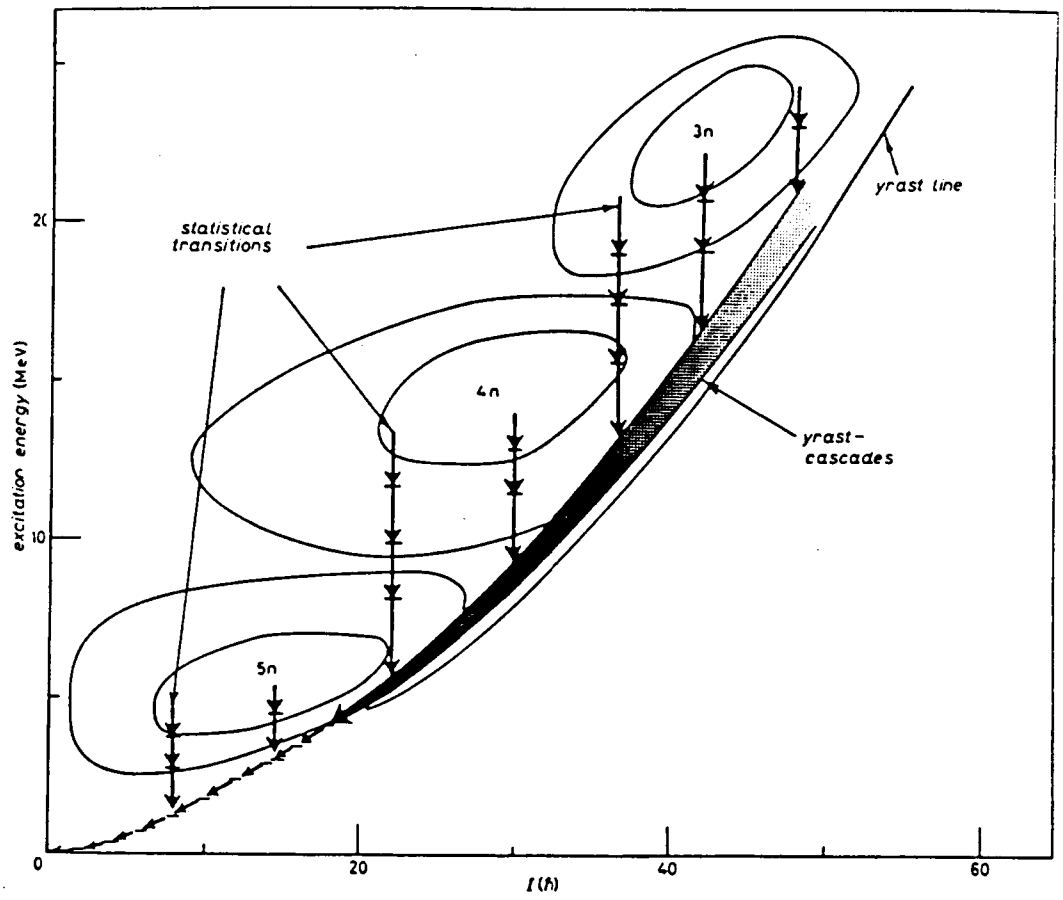

Figure 3.3: Schematic diagram of the γ-ray de-excitation scheme for the ^{124}Sn(^{40}Ar,xn)$^{164-x}$Er reaction. The contours indicate the γ-ray emitting regions for the 3n-5n evaporation residues predicted by the statistical model calculations of Hillis *et al.* (1979). Reproduced from Bengtsson and Garrett (1983).

Table 3.2: Gamma-ray intensities for the higher spin states in the yrast band of ^{184}Pt for three different heavy-ion reactions in this work. The intensities have been normalized with respect to the 4^+ to 2^+ transition which was assumed to have an intensity of 100 units.

Energy(keV)	Transition	^{16}O + ^{172}Yb	^{34}S + ^{154}Sm	^{29}Si + ^{160}Gd
556	$16^+ \rightarrow 14^+$	50.4	51.6	54.1
586	$18^+ \rightarrow 16^+$	34.7	33.8	38.4
624	$20^+ \rightarrow 18^+$	22.2	26.7	27.1
674	$22^+ \rightarrow 20^+$	11.2	20.9	17.5
730	$24^+ \rightarrow 22^+$	3.1	7.3	7.6
789	$26^+ \rightarrow 24^+$		4.9	6.5
850	$28^+ \rightarrow 26^+$			—
908	$30^+ \rightarrow 28^+$			3.7

using equations 3.5 and 3.6. At 91 MeV, the oxygen reaction brings in a maximum of 36 $\hbar$ of angular momentum and 56 MeV of excitation energy into the system. On the other hand, for the ^{34}S and ^{29}Si reactions, ℓ_{max} is 59 and 62 $\hbar$ and E^{ex}_{max} is 68 and 73 MeV for their respective compound systems. The large increase in ℓ_{max} going from the lighter to heavier projectiles is the major reason for the favoring of high spin states by the heavier projectiles. However, the increase in population intensity is only a few units, where one might reasonably expect a more substantial increase in the observed high-spin states. While an increase in ℓ_{max} does not necessarily result in an increase in I_γ along the yrast line, a closer investigation of this suppression of high-spin states along the yrast line in ^{184}Pt for the heavier projectiles is warranted to determine if fission or some other process can explain this phenomenon.

Glagola *et al.* (1984) have measured the effects of large angular momenta on the fission properties of Pt compound systems. Fig. 3.4 shows the measured fusion-fission and calculated total cross sections for the ^{186}Pt compound system using the ^{16}O+^{170}Yb and ^{32}S+^{154}Sm reactions. While these reactions differ slightly

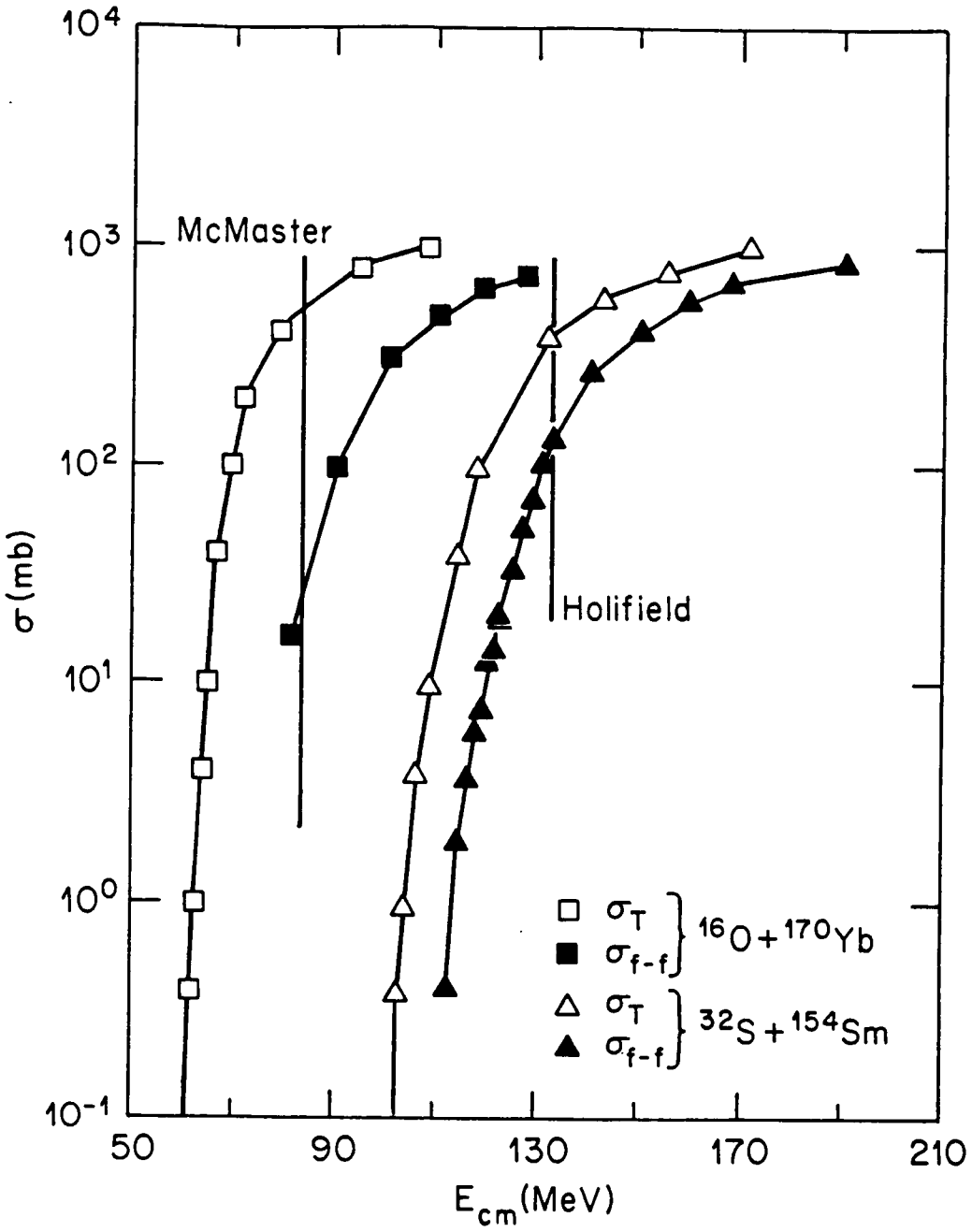

Figure 3.4: Measured fusion-fission cross section for the $^{16}O+^{170}Yb$ and $^{32}S+^{154}Sm$ reactions. The open symbols are the calculated total fusion cross sections (Glagola *et al.*, 1984).

from the reactions used in this study ($^{16}O+^{172}Yb$ and $^{34}S+^{154}Sm$), qualitative arguments should apply from one reaction to the other. The fusion-fission cross section is associated with the situation where the projectile and target fuse together, forming the compound system which subsequently decays via fission. The fusion-fission cross section is expressed as

$$\sigma_{f\text{-}f} = \pi\lambda \sum_{\ell=o}^{\infty} (2\ell+1) T_\ell P_\ell^f, \tag{3.8}$$

where T_ℓ is the angular-momentum-dependent barrier transmission coefficient and P_ℓ^f is the angular-momentum-dependent fission probability. From the figure, it is clear that the percentage of the cross section associated with fission is much higher for the sulfur than the oxygen reaction, at the beam energies used for this work. One does not gain higher angular momenta in the Pt system without a price: the loss of a substantial amount of the compound system to fission.

In order for one to estimate the cross sections for fission and other reaction channels before performing the experiment, statistical model calculations, similar to those referred to above, should be performed. One such computer program, PACE, is available at the Holifield facility. Fig. 3.5 shows a plot of the cross sections predicted by PACE for the $^{160}Gd+^{29}S$ reaction as a function of the beam energy. These calculations show that the 151 MeV beam energy used in the Chalk River experiment was a good choice. At lower bombarding energies, one would maximize the cross section for ^{184}Pt, however, a smaller amount of angular momentum is brought into the system. On the other hand, higher bombarding energies result in a decrease in the ^{184}Pt (5n) cross section and an increase in the fission, and 6n and 7n cross sections.

In conclusion, it should be mentioned that it was once generally believed that very high-spin states in the Pt and Au nuclei could not be populated through heavy-ion fusion reactions because of the low fission barriers. The present work

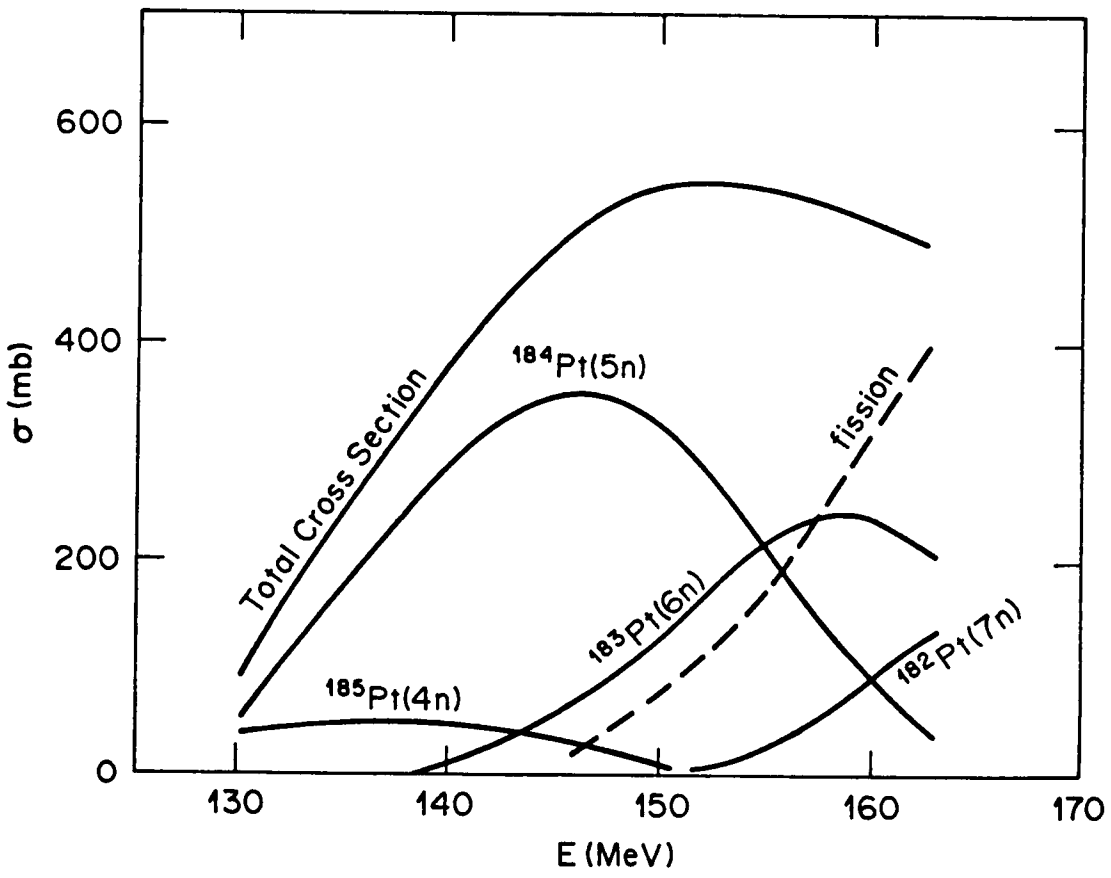

Figure 3.5: PACE calculations for the cross sections of the final reaction channels for the ^{160}Gd+^{29}S reaction as a function of bombarding energy.

has shown that the angular momentum dependence of fission does limit one in the maximum angular momentum obtainable in this region; however, it should be noted that by using a large number of Compton-suppressed Ge detectors in a 4π spectrometer, discrete states as high as of 35 $\hbar$ have been observed in ^{184}Pt in this work. While this I_{max} is smaller than that obtained in lighter rare-earth nuclei, it is much higher than what was thought possible.

3.3 Gamma-ray Spectrometers

As discussed in section 3.1, the large amount of experimental knowledge which has been gained in the past decade on nuclei under the condition of rapid rotation is a direct consequence of the building of large γ-ray spectrometers. Several different spectrometers were used to collect the experimental data reported in this work, ranging significantly in their degree of complexity. This offers a chance to explore the advantages of using one detection system over another. However, a review of detection systems in general, and a description of the spectrometers used are first in order.

3.3.1 Description of Detectors

The detectors currently used in γ-ray spectrometers fall into two categories: semiconductor detectors, which have good energy resolution but low γ-ray detection efficiency, and scintillation detectors, which offer good efficiency but low energy resolution for detecting γ rays. The semiconductor detector consists of a single crystal of germanium or silicon placed under high voltage at liquid nitrogen temperature. Electron-hole pairs are produced when electrons absorb the energy of an incoming γ ray or x ray. These pairs, under bias, produce a current whose strength is detected and amplified with a pulse height proportional to the energy of the incident photon. The energy resolution of semiconductor detectors is deter-

mined by system noise in the electronics and the randomness of the electron-hole pair production in the detector crystal. Both these effects produce a fluctuation in the pulse height for photons of the same energy.

Most present day spectrometers are equipped with high purity n-type coaxial Ge detectors. They have several advantages over their predecessors, Ge(Li) detectors, which are doped with lithium to compensate for impurities in the germanium. Ge(Li) detectors must continually be stored at liquid nitrogen temperatures to reduce the mobility of the Li atoms. On the other hand, high-purity Ge detectors need only be placed under low temperatures when biased with voltage to prevent thermal excitation of electron-hole pairs. The overall performance of Ge detectors is also better than that of Ge(Li) detectors, allowing for a greater energy range at which photons are detected efficiently (3 keV to 10 MeV). The energy resolution of Ge detectors (measured as the width of the energy response function of monoenergetic γ rays at half of its maximum height, FWHM) is approximately 2 keV for the 1.33 MeV γ ray emitted by ^{60}Co. While the energy resolution for detecting γ rays is quite good for high-purity Ge detectors, the relative detection efficiency is only on the order of 20 to 30 percent, where the relative efficiency is defined as the ratio of the absolute germanium detector efficiency to the efficiency of a 3-in. by 3-in. NaI(Tl) detector at 25.0 cm., using the 1.33 MeV peak in ^{60}Co. Two factors contribute to the Ge detectors lower efficiency compared to NaI: (1) the density of the NaI material is larger than Ge, and (2) the volume of a Ge crystal is limited by current technology.

If one is interested in measuring the bulk properties of a heavy-ion reaction such as the total energy and multiplicity of the event, a large number of scintillation detectors are placed in the spectrometer in order to measure a large fraction of the γ rays emitted during the reaction. Briefly, a scintillation detector works under the following principle. First, an electron associated with the main

crystal material absorbs the energy of an incoming photon and is ionized into the conduction band. The orbital vacancy resulting from the photon absorption is filled and characteristic x rays are emitted. The ionized electron moves, under bias, through the crystal and is trapped by an impurity which has been carefully added to the crystal material. The kinetic energy of the electron is converted into excitation energy of the atomic impurity. The trapping atom is in a highly excited state and de-excites by emitting electromagnetic radiation. The total radiation emitted by all processes is collected by a photomultiplier, which in turn generates an output signal whose pulse height is proportional to the energy of the initial photon. The degradation of the energy resolution of monoenergetic photons is due mainly to the different secondary processes associated with the ionized electron and the efficiency at which the light is collected by the photomultiplier tube.

Historically, sodium-iodide crystals activated with thallium, Na(Tl), have been the scintillation material used to detect x rays and γ rays. Thus, the first large gamma-ray spectrometers at Oak Ridge National Laboratory (Sarantites *et al.*, 1980) and Darmstadt-Heidelberg (Simon 1980) were built using 72 NaI(Tl) and 162 NaI(Tl) detectors respectively. It has recently become economically feasible to make scintillation detectors using bismuth-germanate crystals ($Bi_4(GeO_4)_3$). The higher density of the BGO material (7.13 g/cm^3) compared to NaI (3.67 g/cm^3) makes the total absorption of the γ ray a much more probable event. Thus BGO detectors can be built smaller but offer the same detection efficiency as NaI detectors, leading to the construction of more compact spectrometers. In fact, the most recently built γ-ray spectrometers at Chalk River and Argonne National Laboratory utilize BGO rather than NaI detectors. It should be noted that the energy resolution for NaI is better than that for BGO because of the superior light emittance of the NaI material.

Another type of scintillation detector used in large γ-ray arrays is a

Compton-suppression shield which surrounds the Ge detector and whose purpose is to measure γ rays scattering out of the Ge crystal. Because of the low detection efficiency of the Ge crystal, a Ge γ-ray spectrum has a large background component associated with the Compton-scattered photons. Since the main purpose of the Compton shield is to veto unwanted events, good efficiency for detecting Compton events is the main requirement for these counters. Fig. 3.6 shows a schematic diagram of a full BGO Compton-suppressed Ge detector unit used in the Spin Spectrometer at Oak Ridge National Laboratory. Since the Compton shield entirely surrounds the Ge detector, its size is greatly limited if placed in a spectrometer which holds many detectors. A shield made of BGO material offers a significant advantage in efficiency over NaI material. Johnson *et al.* (1985) have measured the effectiveness of this suppression device, and Fig. 3.7 shows ^{60}Co spectra taken with the unit. The top spectrum contains the unsuppressed spectrum as seen by the Ge detector. The middle spectrum shows the portion of events which is rejected by the suppression shield. The bottom spectrum shows the results when the Ge and shield are used to record data. The test data reveal that the suppression below the full energy Co peaks is almost a factor of five. The rejection of Compton events and enhancement of photo-peak events enables one to resolve very weak γ-ray peaks which are buried in the background of unsuppressed Ge spectra (see section 3.3.4).

3.3.2 The McMaster Lotus

The McMaster Lotus was built in the 1960's to study γ-ray angular correlations using NaI detectors. The device consists of four to five mobile "arms" mounted on a circular platform. These arms can be rotated horizontally to the desired angular position with an accuracy of one degree. Mounted on the arms are cylindrical canisters which originally were used to hold NaI detectors. The canis-

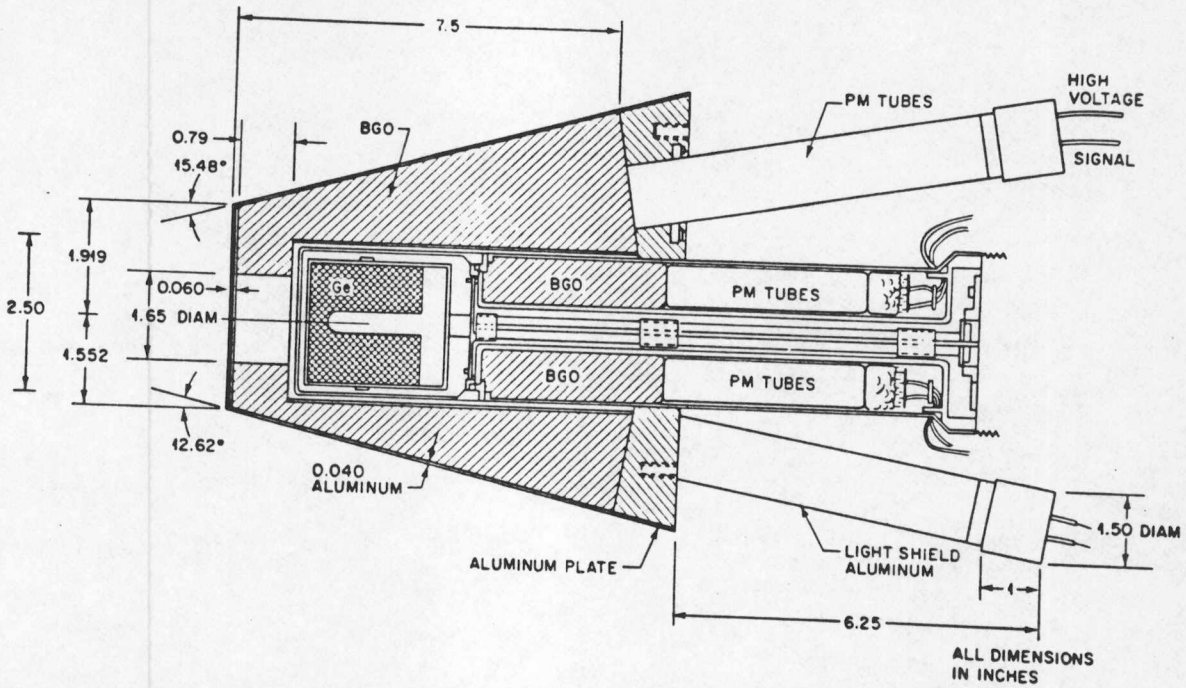

Figure 3.6: Schematic of a BGO Compton-suppression shield used in the Spin Spectrometer. Reproduced from Johnson *et al.* (1985).

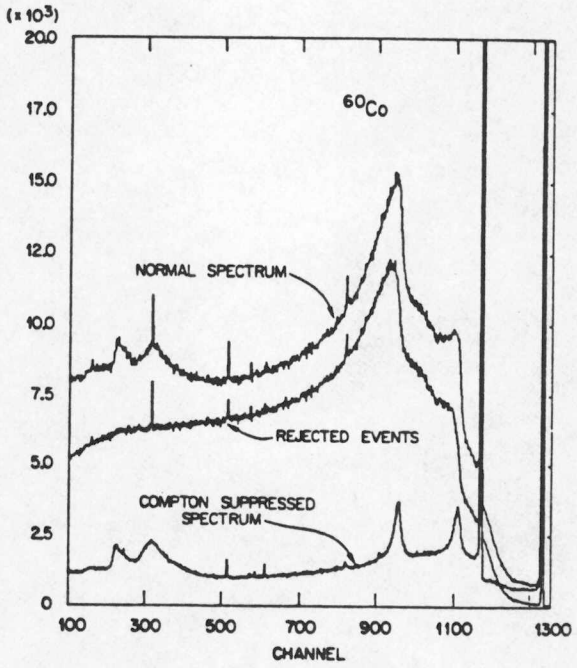

Figure 3.7: ^{60}Co spectra taken with the Compton-suppression unit shown in Fig. 3-6. Note that the heights of the full-energy peaks at 1173 and 1333 keV are off scale, but have been normalized in these data. Reproduced from Johnson *et al.* (1985).

Table 3.3: Angular positions and distance from the target of the Ge detectors in the McMaster Lotus for the ^{184}Pt coincidence experiment. The angle θ is measured with respect to the beam axis, and ϕ is from the vertical axis perpendicular to the beam line.

Ge id	$\theta°$	$\phi°$	d(cm)	Ge id	$\theta°$	$\phi°$	d(cm)
1	89.8	90.0	12.0	5	58.9	−92.3	11.2
2	116.5	102.0	12.0	6	95.0	−90.2	11.0
3	6.1	94.6	12.5	7	45.2	90.1	11.0
4	29.8	−94.6	10.8	8	95.0	−57.5	11.3

ters can be rotated vertically along the arms and may also be positioned with a high degree of angular accuracy.

For the two experiments on ^{184}Pt using the Lotus, the spectrometer was modified to hold both NaI and Ge detectors. Six NaI detectors were used solely as a multiplicity filter to prevent the recording of data associated with low multiplicity events, such as Coulomb excitation of the beam or target or γ rays associated with the beta decay of the residual nuclei. The signals from the photomultiplier tubes of the NaI detectors are fed directly into a fast coincidence unit. An output pulse is generated if at least one NaI counter fires. A second output pulse is produced if at least two detectors fire within 100 ns of each other.

Eight Ge detectors were used for the γ-coincidence experiment. Table 3.3 lists the angular positions of the detectors with respect to the beam line and their distance from the target. All eight were n-type coaxial intrinsic Ge detectors manufactured by ORTEC. Each detector had 0.9 mm of Cd and 0.35 mm of Cu placed on its front face to absorb x rays. A 1.0 mm cylindrical piece of Pb was placed around the barrel of each detector to prevent γ rays from scattering between detectors. Five Ge detectors were used for the angular distribution experiment, and they were placed at 0°, 30°, 45°, 60° and 90° with respect to the beam line. None of the Ge detectors in either experiment were surrounded by Compton-

suppression devices.

3.3.3 The Spin Spectrometer

The Spin Spectrometer in the Holifield facility at Oak Ridge National Laboratory is one of the first γ-ray spectrometers constructed whose detectors cover almost the entire solid angle of the reaction chamber, in order to measure the total γ-ray energy and multiplicity resulting from a heavy-ion reaction. The building of the spectrometer was done by the research group headed by D. G. Sarantites at Washington University in St. Louis, Missouri. For a detailed description of the device see Jääskeläinen *et al.* (1983).

Without any external detectors, the Spin Spectrometer holds seventy-two NaI(Tl) detectors. They are clustered closely together, approximating a hollow sphere with a radius of 17.8 cm. Twelve of the NaI detectors are regularly shaped pentagons. The remaining 60 detectors are identical irregularly shaped hexagons. Each pentagon is surrounded by five hexagonal detectors. The solid angle of each of the detectors is 1.34% of 4π for a total solid angle of 96.8%. The 3.2% loss is due to the wall thickness of the aluminum cans housing the NaI crystals and the internal light-reflecting material inside the cans. The NaI detectors are bolted together by clamps which are connected by radial rods to the vertices of the supporting frame. The frame is split into two halves that stand on two independently movable platforms. This allows for the two halves to be separated for access into the inner portion of the ball. Jääskeläinen *et al.* (1983) have measured the performance of each NaI detector. The average energy resolution of the detectors for the 1.3 MeV γ ray in ^{60}Co is 82.5 keV FWHM with a count rate of 50,000 c/s. The average time resolution is 2.1 ns FHWM with a threshold set at 80 keV.

If experiments are performed using Compton-suppressed Ge detectors, one NaI detector must be removed for each shielded or bare Ge detector placed

in the spectrometer. A photograph of the Spin Spectrometer with Ge counters can be found in Fig. 3.8. For the ^{184}Pt experiment in August of 1984, five Ge and two Ge(Li) detectors were used, six of which were surrounded by NaI Compton-suppression shields. No absorbers were placed on the fronts of any detectors. The ^{183}Au experiment performed a year later utilized eleven Ge detectors and nine Compton-suppression shields. Ta, Cd, and Cu absorbers of 0.1 in., 0.04 in., and 0.005 in., respectively, were used. For forward Ge detectors, all three absorbers were placed on the front faces, but only Cd and Cu were used on the backward detectors. The distance from the front center of the Ge crystal to the target was between 21 and 23 cm for these detectors in both experiments. A summary of the angular positions of the Ge detectors for each experiment can be found in Table 3.4.

When using the Spin Spectrometer, the γ-ray energies and time signals for each individual detector, the total γ-ray fold and energy of the event, and any other information associated with other types of particle detectors which might be placed inside the ball can be recorded on an event by event basis. For discrete γ-ray studies, it is usually sufficient to record information associated with the individual Ge detectors and parameters associated with the total detected energy and fold of each individual event, because the NaI detectors in such an experiment are used as a filter to separate reaction channels.

3.3.4 The 8π Spectrometer

The 8π Spectrometer, located at Chalk River National Laboratory in Ontario, Canada, in many ways represents a "state of the art" γ-ray spectrometer. Its geometry is identical to the Spin Spectrometer; however, the internal ball is composed of BGO instead of NaI detectors. Coupled with the BGO detectors are twenty BGO Compton suppressed Ge detectors which are placed into

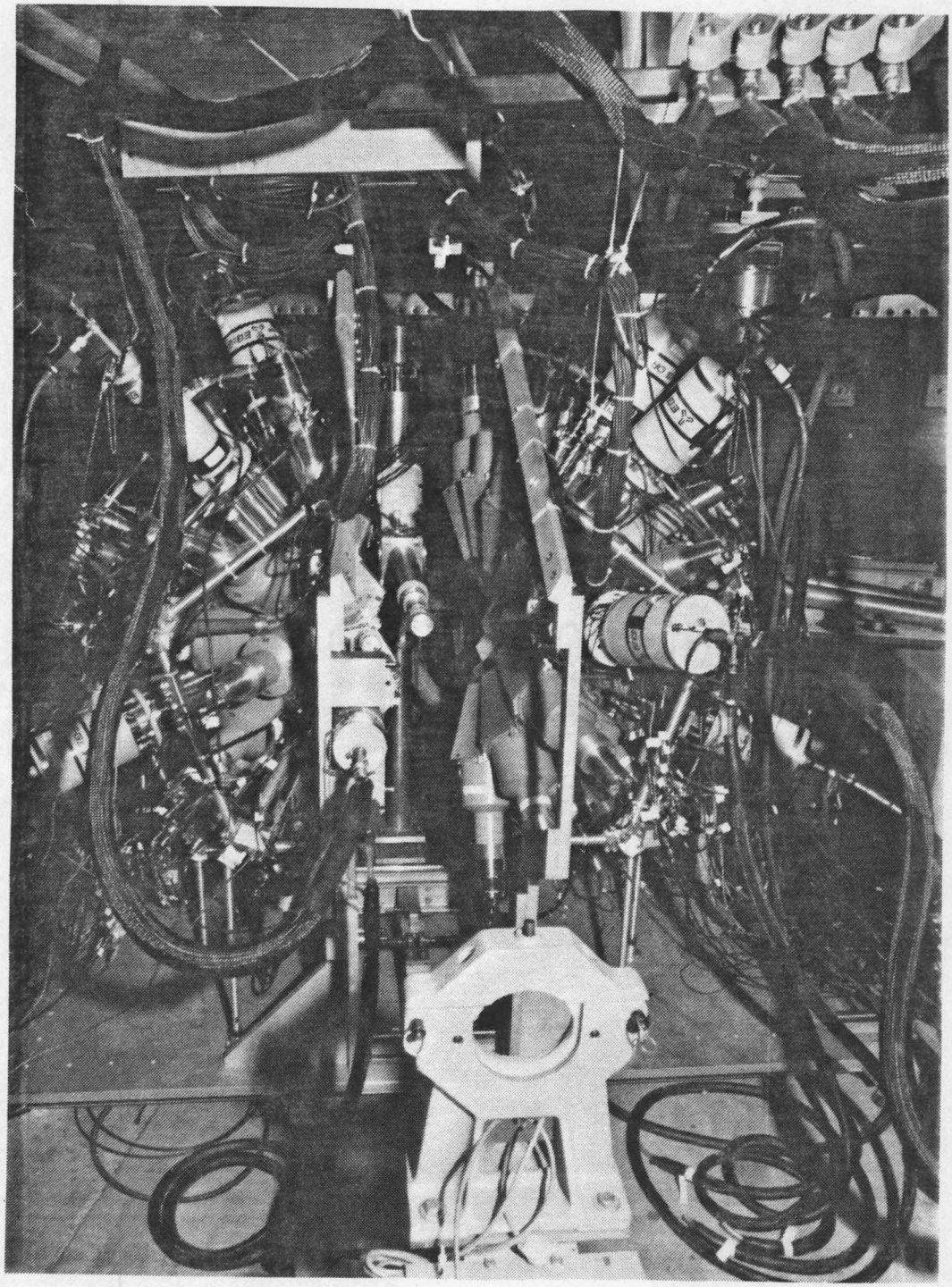

Figure 3.8: Photograph of the Spin Spectrometer fully setup for a γ-γ coincidence experiment.

Table 3.4: Angular positions of Ge detectors in the two Spin Spectrometer experiments.

Ge	^{184}Pt		^{183}Au		Ge	^{184}Pt		^{183}Au	
id	$\theta°$	$\phi°$	$\theta°$	$\phi°$	id	$\theta°$	$\phi°$	$\theta°$	$\phi°$
$1^{1,2}$	63.4	36.0	63.4	−36.0	7^{2}	155.6	166.9	155.6	−49.1
$2^{1,2}$	116.6	−72.0	63.4	108.0	8			92.7	−5.4
$3^{1,2}$	116.6	72.0	116.6	−72.0	9^{2}			155.6	94.9
$4^{1,2}$	63.4	−108.0	116.6	72.0	10^{2}			0.0	0.0
$5^{1,2}$	63.4	−36.0	24.4	85.1	11			63.4	36.0
$6^{1,2}$	0.0	0.0	24.4	−58.9					

[1]NaI Compton suppressed for ^{184}Pt experiment.
[2]NaI Compton suppressed for ^{183}Au experiment.

the spectrometer through openings in the internal ball. Thus, unlike the Spin Spectrometer, the full complement of BGO and Ge detectors can be used in tandem with each other. The Ge detectors are placed around the spectrometer in four separate rings of five detectors each. These rings are located at 37°, 79°, 101° and 143° with respect to the beam direction. The distance from the target to the center front face of each Ge crystal is 22.8 cm. The ^{184}Pt experiment performed at Chalk River used the full complement of BGO and Compton-suppressed Ge detectors.

3.3.5 Effects of Suppression

As reported above, the three experiments on ^{184}Pt were done with no suppression (McMaster), partial NaI suppression (Holifield), and complete BGO suppression (Chalk River). Fig. 3.9a shows the spectra from a suppressed Ge detector and unsuppressed Ge(Li) detector taken during the Holifield experiment on ^{184}Pt. The y-scale has been chosen so as to accent the background component of the each spectrum. From this figure, it is obvious that the background associated with the suppressed detector is noticeably lower than that of the unsuppressed

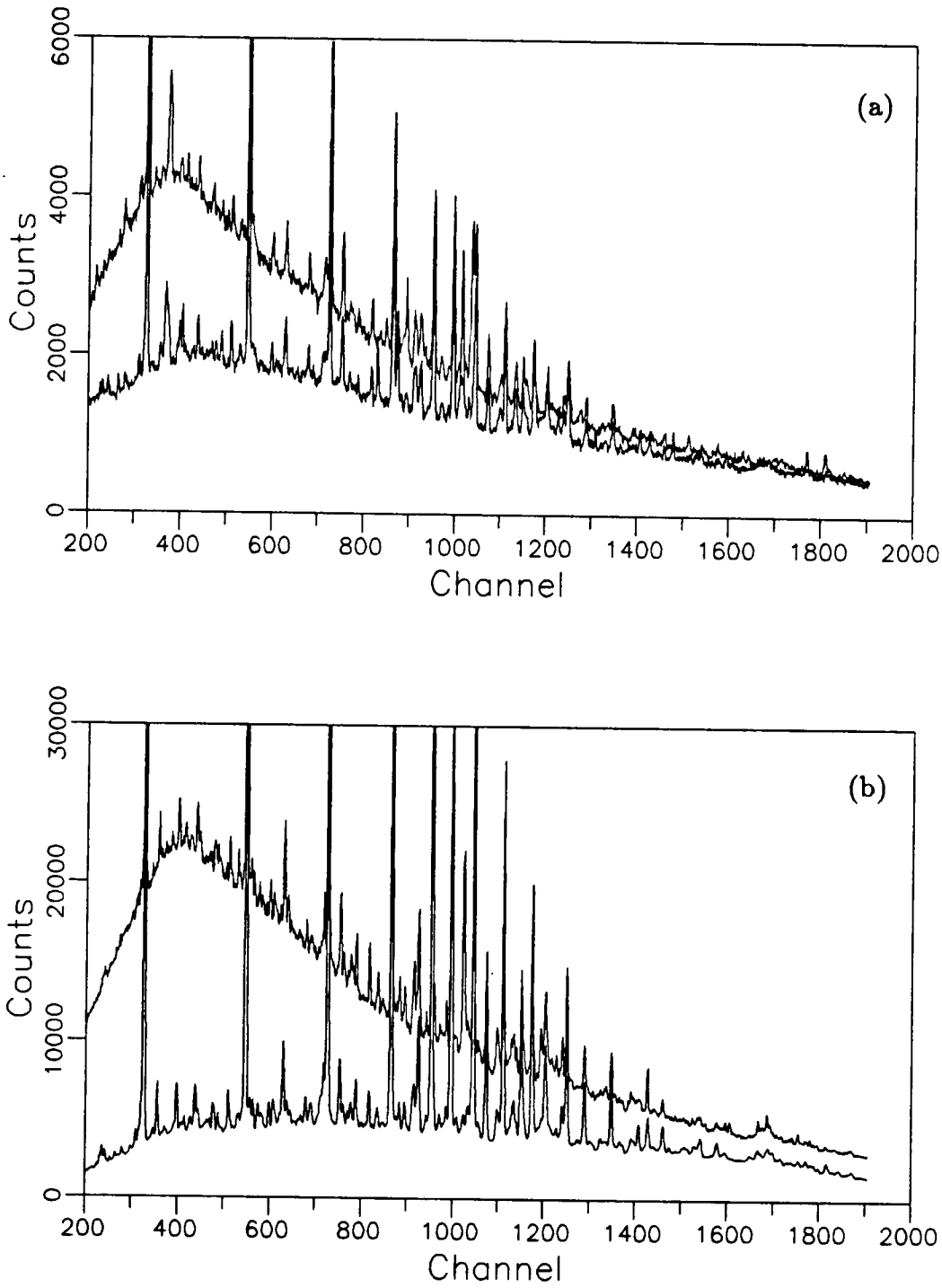

Figure 3.9: (a) Spectra of a suppressed and unsuppressed Ge detector taken during the ^{184}Pt experiment in the Spin Spectrometer; (b) total Ge projections from the McMaster and Chalk River experiments on Pt.

detector at the lower energies, and at the highest energies, the two spectra converge. Fig. 3.9b shows the total Ge projections from the McMaster and Chalk River experiments on ^{184}Pt. The spectra have been normalized to the areas of the 273 keV ($4^+ \rightarrow 2^+$) transition. While the overall shape of the background in the McMaster spectrum is similar to that of the unsuppressed Ge(Li) detector in (a), the background associated with the Chalk River projection is lower and more flat than the suppressed Ge detector in (a). This is a direct consequence of better detection efficiency of the BGO suppressor over a NaI suppressor. In conclusion, Fig. 3.9 represents a recent historical summary of the quality of data taken with Ge detectors, ranging from the high background associated with a "bare" Ge, to the improved spectrum taken with the addition of NaI suppression, and finally to the superior quality of data taken when using BGO material in the suppression devices.

3.4 Electronic Setup

The philosophy behind a γ-γ coincidence experiment is that if two detectors measure γ rays at almost identical times, these γ rays are then assumed to belong to a particular decay pathway in a given nucleus, ignoring random coincidences. When this occurs, the γ rays are said to be in coincidence with each other. A larger number of coincidence γ rays will more clearly define this energy pathway. The electronic setup determines what time scale constitutes a coincidence event, and whether or not, the time and energy information associated with the γ rays of the event should be recorded for later analysis. Even though the data described in this work were taken during five separate experiments, only the setups for two experiments are examined in detail: the ^{184}Pt coincidence experiment in the Lotus, and the ^{183}Au experiment in the Spin Spectrometer. These two experiments were chosen, because the ^{184}Pt measurement represents a relatively simple electronic

setup, and the ^{183}Au experiment a more complicated electronic setup of a γ-ray spectrometer.

3.4.1 ^{184}Pt Coincidence Experiment in the McMaster Lotus

Fig. 3.10 shows a block diagram of the electronics setup used for the ^{184}Pt coincidence experiment in the McMaster Lotus. Two identical output signals were taken from the preamplifier of each Ge detector. One output was used as an energy signal, and the other was used for the timing of the event. The analog energy signals were shaped and amplified by a linear amplifier. This signal was then passed through a "linear-gate and stretcher" device to produce a more suitable pulse shape for the analog-to-digital converter (ADC). The timing signal was first shaped by a timing filter amplifier (TFA), and the sharp timing pulse was generated by passing the output from the TFA into a constant fraction discriminator (CFD). The threshold of all CFDs were set to approximately 50 keV using an ^{241}Am radioactive source.

Since the NaI detectors were used only as a multiplicity filter, the individual outputs were not connected to ADCs. Instead, the signals from the photomultiplier tubes of all six NaI detectors were fed directly into the NaI coincidence unit located next to the Lotus. This unit generated an output signal whenever a single NaI counter fired, and a second output logic pulse was generated when two NaI detectors measured events within 100 ns of each other.

The remainder of the electronics was dedicated to defining the requirements for coincidence events which would be recorded to tape. As the schematic diagram shows in Fig. 3.10, the logic pulse of each Ge time signal was simultaneously connected to the input of a strobe device and a multi-logic unit. The purpose of the multi-logic unit was to determine the number of Ge detectors in a time coincidence. Two of the output signals from this unit were used to gate

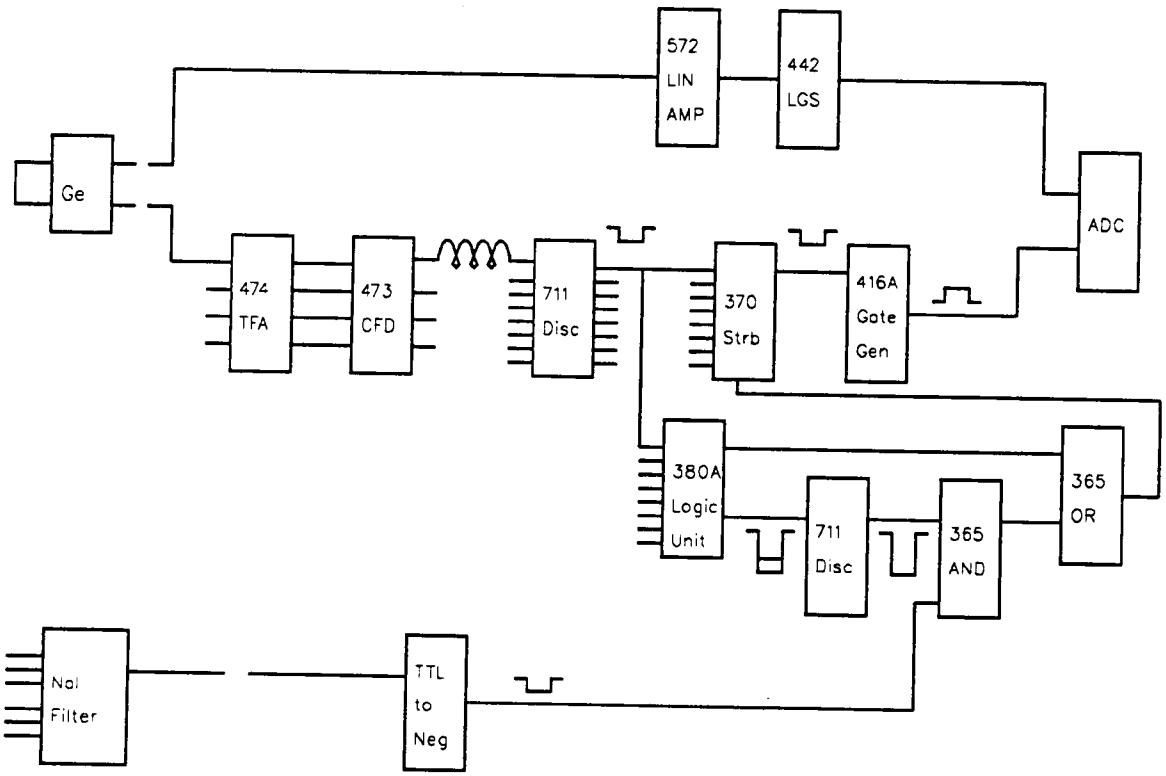

Figure 3.10: Block diagram of the electronic setup used in the γ-coincidence experiment on ^{184}Pt at the McMaster Tandem Accelerator Laboratory.

coincidence events. One signal indicated when three or more of the 70 nano-sec wide time pulses from the Ge detectors overlapped each other. The other signal specified when two or more Ge time pulses overlapped one another. The output of this last signal was connected to the input of a logical-AND device along with the "any 1" NaI output. Thus, there were two requirements which defined an accepted coincidence event: three or more Ge detectors in coincidence, or two or more Ge detectors in coincidence with a single NaI detector. Both these signals were sent to a logic-OR device whose output was used to gate the strobe. The strobe produced an output for each Ge firing during the event, and these outputs were used to gate the individual Ge ADCs. Once gated the ADC sent its energy signal to a VAX 780 computer where the digital output signals associated with the γ-ray energies were written to tape.

3.4.2 ^{183}Au Coincidence Experiment in the Spin Spectrometer

Fig. 3.11 is a schematic diagram of the electronics setup for the ^{183}Au experiment in the Spin Spectrometer. This setup is divided into two parts: the electronics associated with the NaI detectors, and the electronics connected with the Ge detectors. The cabling of the NaI detectors has been permanently set up for the Spin Spectrometer and provides output signals for the energy, time, and time difference[1] of each individual NaI detector. The basic timing for each pulse is established by a front-edge CFD. The output from this CFD stops a time-to-digital converter (TDC), sets a detector identification bit in a gated latch, and serves as an input to the time difference unit. Connected to this gated latch is a 72-channel digital multiplicity summer (fast fold select in Fig. 3.11). This summer provides a fast method of vetoing events of low multiplicity. The ADCs and individual latches are gated by an external strobe signal. This signal also acts as a

[1]This is a time difference between the front-edge and rear-edge CFDs.

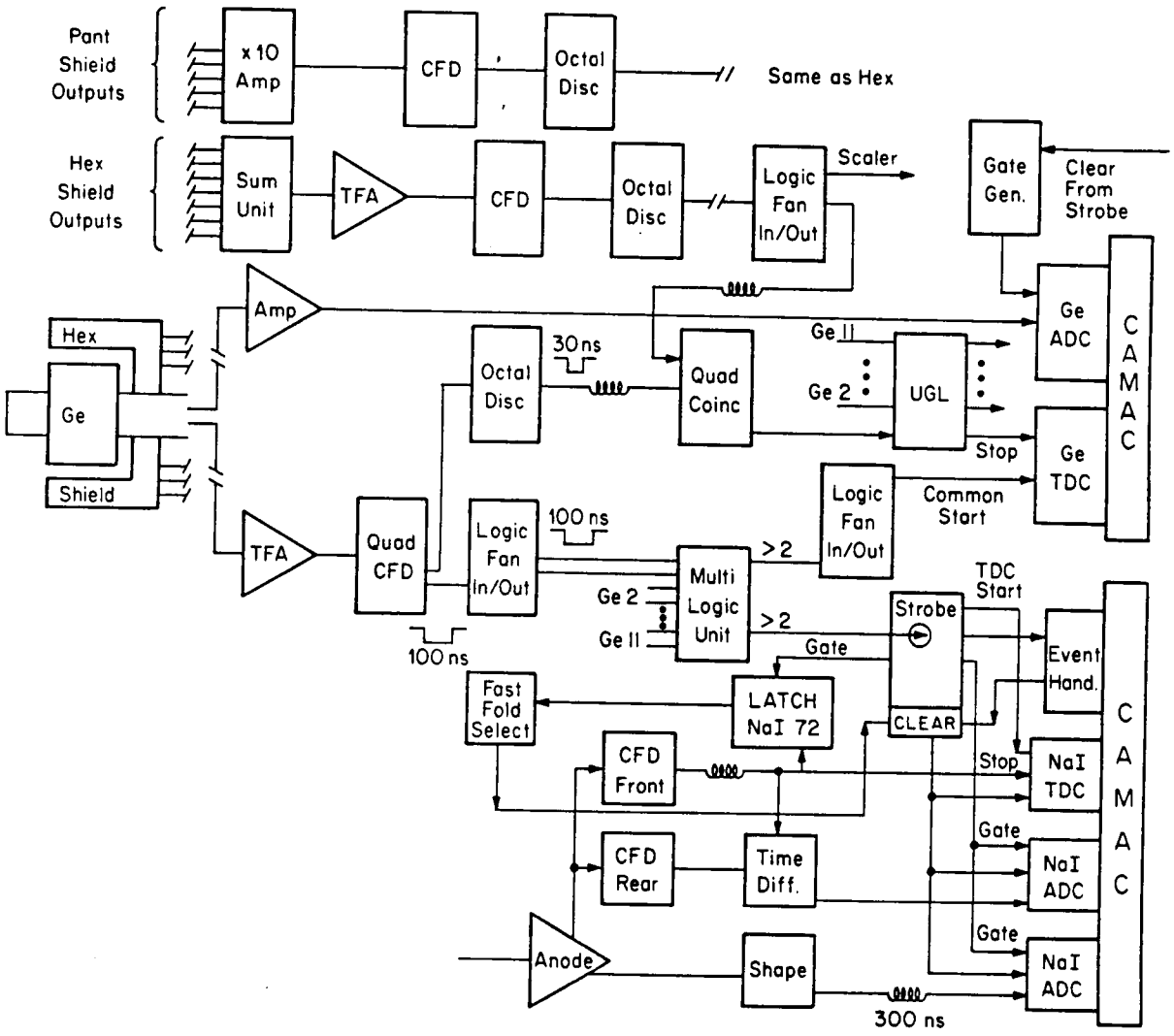

Figure 3.11: Schematic diagram of the ^{183}Au experiment in the Spin Spectrometer.

common start for all the TDCs. The operating characteristics of all NaI counters are stored in a computer disk file. The setup and data-acquisition programs use this file to obtain the needed information on each detector.

All the detector ADCs, detector TDCs and miscellaneous registers must be CAMAC compatible.[1] The entire data-acquisition system is monitored by the Event Handler, a CAMAC-based controller which makes the final decision on which events are written to tape. The Event Handler is controlled by computer software, giving one the ability to calculate other parameters connected with the event before sending the data to the computer.

For the ^{183}Au experiment, eleven Ge detectors and nine NaI Compton-suppression shields were used. The same setup employed in the McMaster experiment was used here to generate the initial time logic pulse and shape the energy signal, except for the absence of a linear-gate stretcher. The Compton-suppression shields were set up in two basic configurations depending on whether they replaced a hexagonal or pentagonal NaI. Each hexagonal shield had six photomultipliers connected to it. After these tubes were properly gain matched, the six outputs were connected to a summing unit. This unit takes all six inputs, sums them together, and produces a single output. This output signal was then shaped by a TFA, and the sharp time pulse was produced by a CFD. Each pentagonal suppressor had only five photomultiplier tubes connected to the NaI crystal. The five outputs from the shield were connected to a sixteen channel "$\times$10"-amplifier, which summed all the signals and amplified it ten times. The output from this device was sent directly to a CFD to produce a logic time pulse.

The coincidence logic for the experiment was done in the following way. Each Ge detector had two identical 100 nano-second wide time signals which were connected to a multi-logic unit. Thus, for two Ge detectors whose time pulses

[1]CAMAC is an acronym for computer automated measurement and control.

overlapped, the unit would detect a multiplicity of four. If the unit measured more than two overlapping time signals, an output signal was sent to the strobe which gated the ADCs and TDCs of all the detectors in the Spin Spectrometer. At the same time, the the timing signal of each Compton-suppressed Ge detector and its corresponding shield were connected to the input of the same logic unit. If the Ge detector was not in coincidence with the shield, its signal was allowed to pass on to the users gated latch to set a bit for that detector. The final decision on whether to write the event to tape was made by the Event Handler which checked the user-gated latch to determine whether or not at least two Ge detectors had their latch bit set. Once an event was accepted, the Event Handler read the ADCs and TDCs of all the detectors whose gated latch bits had been set. Both the energy and time signal were then sent to the Concurrent computer (formally a Perkin-Elmer 32/20) and written to magnetic tape for permanent storage.

The electronics for the ^{184}Pt experiment in the Spin Spectrometer was very similar to the ^{183}Au setup. The electronics for the 8π Spectrometer, using ECL cabling and individually programmable CAMAC units, is slightly more complicated than the setup described above. The largest difference between the Spin Spectrometer and 8π Spectrometer electronics setup is the presence of the CAMAC booster (CAB) for the latter. This device is a small micro-computer with a sufficient amount of memory to manipulate the incoming data before it is written to tape. For example, all of the Ge detectors are gain matched by the CAB. Thus, scanning of the data can be done immediately without performing a lengthy prescan (see section 3.5).

3.5 Experimental Data

Once the data have been stored on tape, it must be rewritten and stored in the computer in a format which enables one to have easy access to the data.

One common approach for analyzing γ-ray coincidence data is to construct two-dimensional histograms of the recorded Ge energies. Each element of this two-dimensional matrix corresponds to the number of times coincidences of specified energies were recorded on tape. Coincidence matrices are usually referred to as being symmetric or unsymmetric. A symmetric matrix has a single coincidence written into the matrix twice. For example, a coincidence between γ_1 and γ_2 would be written in the array element corresponding to the channels (γ_1, γ_2) and at the same time written to the element corresponding to (γ_2, γ_1). An unsymmetrized matrix records only one of these combinations which is determined during the play back. By collecting a large amount of data, one is able to construct a level scheme of a nucleus by projecting out γ ray peaks and observing what other γ rays are in coincidence with them. This procedure is known as gating and will be discussed in greater detail in Chapter 4.

Because Ge detectors have a low efficiency for measuring the full energy of a γ ray, many of the coincidences consist of Compton scattered events. Compton-suppression shields are used to decrease the amount of these events recorded onto tape. However, the shields are not one-hundred percent efficient; thus, some of the events recorded onto tape will be associated with Compton events. Compton-Compton events refer to the situation where two Compton scattered events are detected in coincidence, and Compton-photopeak events occur when one Compton and one fully detected γ ray are in coincidence. When analyzing coincidence data, it is important to remove the portion of the data associated with the Compton events. This is called the background, and there are several methods which are employed to remove these unwanted events from the meaningful data. These methods will be discussed in more detail in Chapter 4.

3.5.1 ^{184}Pt McMaster Coincidence Data

For the ^{184}Pt coincidence experiment, a ^{16}O beam at 91 MeV was incident on a ^{172}Yb target. The target consisted of a single 2 mg/cm^2 thick foil of ^{172}Yb. Evaporated onto the foil was a 6.4 mg/cm^2 thick ^{208}Pb backing. The data rate during the experiment averaged 3500 events/second. One-third of the data taken were Ge triple events. Triple coincidences greatly enhance the data, because for every three Ge detectors firing in coincidence, there are six detector combinations which can be used in a symmetrized coincidence matrix. For a two-fold coincidence, there are only two such combinations. A total of forty-one data tapes were taken during the experiment.

A 4096 by 4096 γ-ray coincidence matrix was constructed by playing back all the data tapes, shifting the gains of each Ge detector to 0.37 keV/channel, and histogramming the gained shifted energies into the matrix on disk. All possible coincidences for each event within the energy range of 1.5 MeV were included in the matrix. The symmetrized matrix contained a total of 367 million coincidences. The total projection of the matrix is shown in Fig. 3.12a. As can be seen, ^{184}Pt is clearly the most dominant residual nucleus in the spectrum.

For data analysis, a background subtraction of the entire coincidence matrix was performed using the method of Palameta and Waddington (1985). This method is designed to subtract from the matrix all events not related to discrete γ-ray coincidences such as Compton-Compton, Compton-photopeak and continuum-photopeak events. Fig. 3.12b shows the total projection of the subtracted matrix. This matrix contains only 7.8 million events or approximately 2% of the original data.

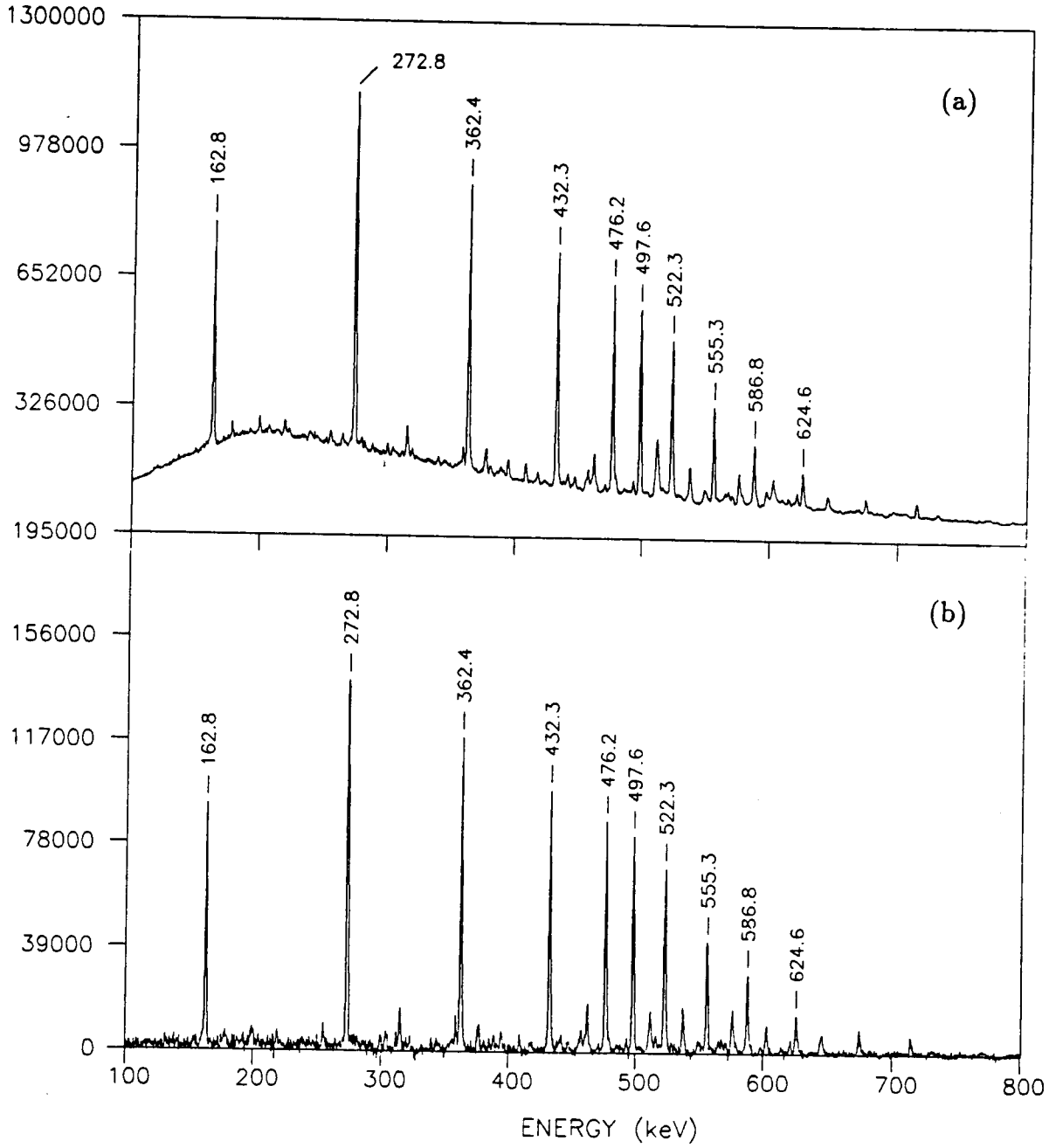

Figure 3.12: Total projections of coincidence matrices for (a) the raw data from the ^{184}Pt McMaster experiment, and (b) the same data after background subtraction of the entire two-dimensional matrix. The labeled peaks correspond to the observed transitions in the yrast band of ^{184}Pt.

3.5.2 ^{184}Pt Oak Ridge Coincidence Data

High-spin states were populated in ^{184}Pt via the ^{154}Sm(^{34}S,4n) reaction at a beam energy of 163 MeV. The beam was supplied by the Holifield Tandem Accelerator. The ^{154}Sm target was enriched to ninety-eight percent and consisted of a single unbacked 1 mg/cm^2 thick foil. The accepted triggers for the experiment averaged between 300 to 500 events/sec with a beam current on target of 35 to 40 nano-amps. The beam energy was chosen so that the 4n channel would be the most dominant by-product. However, there was a significant portion of ^{183}Pt (5n) produced, allowing for data analysis to be done on this nucleus as well (see Nyberg *et al.*, 1987).

For each accepted event, the energy and time information of all detectors measuring a γ ray were recorded onto tape. The gain of each NaI detector was initially set to 5 keV/channel, providing a 10 MeV range with the 2048-channel ADCs. This gain matching was done automatically by the computer through an iterative procedure, using the two well separated γ-ray energies in ^{88}Y. The Ge detectors gains were manually set to 0.25 keV/channel during the setup of the experiment. This allowed for a 2 MeV range in the 8192-channel ADCs used for the Ge energy signals. A total of 129 data tapes were written during the experiment.

Before a coincidence matrix was constructed, the data were rewritten to tape in a format more conducive for data analysis. During this "prescan", the gains of all detectors were recalculated on an event by event basis. This was most critical for the Ge detectors so that good energy resolution would be preserved when adding the detectors together in a coincidence matrix. The Ge detectors were calibrated using previously known γ-ray energies in ^{184}Pt. Gain matching of the NaI detectors is less critical than for discrete line spectroscopy; however, it was done to refine the pre-set gains and to take into account the non-linearity of

the photomultiplier tubes at higher energies. Different sources were used covering an energy region ranging from 120 keV (^{75}Se) to 4440 keV (Pu-Be source). Each detector was also corrected for Doppler shifting using a calculated correction factor.

Since NaI detectors are sensitive to the detection of neutrons, some of the NaI energies recorded on tape correspond to neutrons instead of γ rays. To define the γ-ray multiplicity and total energy for each event as well as possible, the neutrons must be separated from the γ-ray data. The time it takes for neutrons to travel from the recoiling nucleus to a NaI detector is measurably longer ($\approx$ 10 nsec) than the time of flight for γ rays. The time resolution of a NaI detector is sufficient to distinguish this difference. Neutrons were separated from the γ-ray data during the prescan by setting narrow time windows on each NaI time spectrum. These time windows varied as a function of energy for two reasons: the timing of the NaI detector is better at higher γ-ray energies, and the timing pulses from the constant fractions in use for the NaI detectors vary smoothly in time as a function of the energy pulse height. In order to define the zero time, t_0, of each nuclear event, a three step iterative process was used to calculate t_0 on an event by event basis (see Jääskeläinen *et al.*, 1983). The first process in this iterative procedure is to align the time centroids for each NaI detector. Thus the NaI time spectra were shifted on an event by event basis by an appropriate amount during the prescan. The firing time of each NaI for an event was judged against the calculated t_0. The time windows were checked for each detector, and if a particular NaI time signal did not fall within the gate, it was rejected and not written to the prescan tape.

Before the gain shifted energies were written to the prescan tape, the total detected energy (H) and multiplicity (K) were calculated. Detectors associated with neutrons were not included in these calculations. Both the NaI and Ge energies were used to determine H, while only the NaI detectors were used to

calculate K. Fig. 3.13 shows an H-K map for the ^{184}Pt (4n) and ^{183}Pt (5n) residual nuclei produced in this experiment. The evaporation of the extra neutron to produce ^{183}Pt leads to entry states of lower energy and multiplicity, which gives rise to the different H-K spectrum for the two reaction products. These maps were generated by first gating on strong discrete lines in each nucleus. A corresponding background map was also produced by gating on energies attributed to Compton events, and this was subtracted from the discrete maps to generate the two-dimensional histogram in Fig. 3.13. For every event, H and K were written to the prescan tape.

After the prescan was completed, three coincidence matrices were created by playing back the prescan tapes and gating on different H-K regions of Fig. 3.13. One matrix was generated to maximize ^{183}Pt by gating on low H and K, while another matrix was produced to favor the population of states in ^{184}Pt by gating on high H and K. The third matrix was generated by gating on the region not included in either of the other two matrices, yielding approximately the same population of ^{184}Pt and ^{183}Pt. Fig. 3.14 shows the total projection from each of the three matrices. Each matrix had an array dimension of 2048 by 2048 channels with a resolution of 0.5 keV/channel. The ^{184}Pt matrix contained 33 million counts in it. A background subtraction of the whole matrix was performed using the method of Palameta and Waddington (1985). The subtracted matrix contained 1.2 million events or 3.6% of the original data.

3.5.3 ^{183}Au Oak Ridge Coincidence Data

For the ^{183}Au coincidence experiment in the Spin Spectrometer, an excitation function was first performed using a ^{35}Cl beam at energies of 163 MeV, 170 MeV and 187 MeV incident on a 1 mg/cm^2 target of ^{152}Sm. After finishing the excitation function, it was decided that a beam energy of 170 MeV should be used

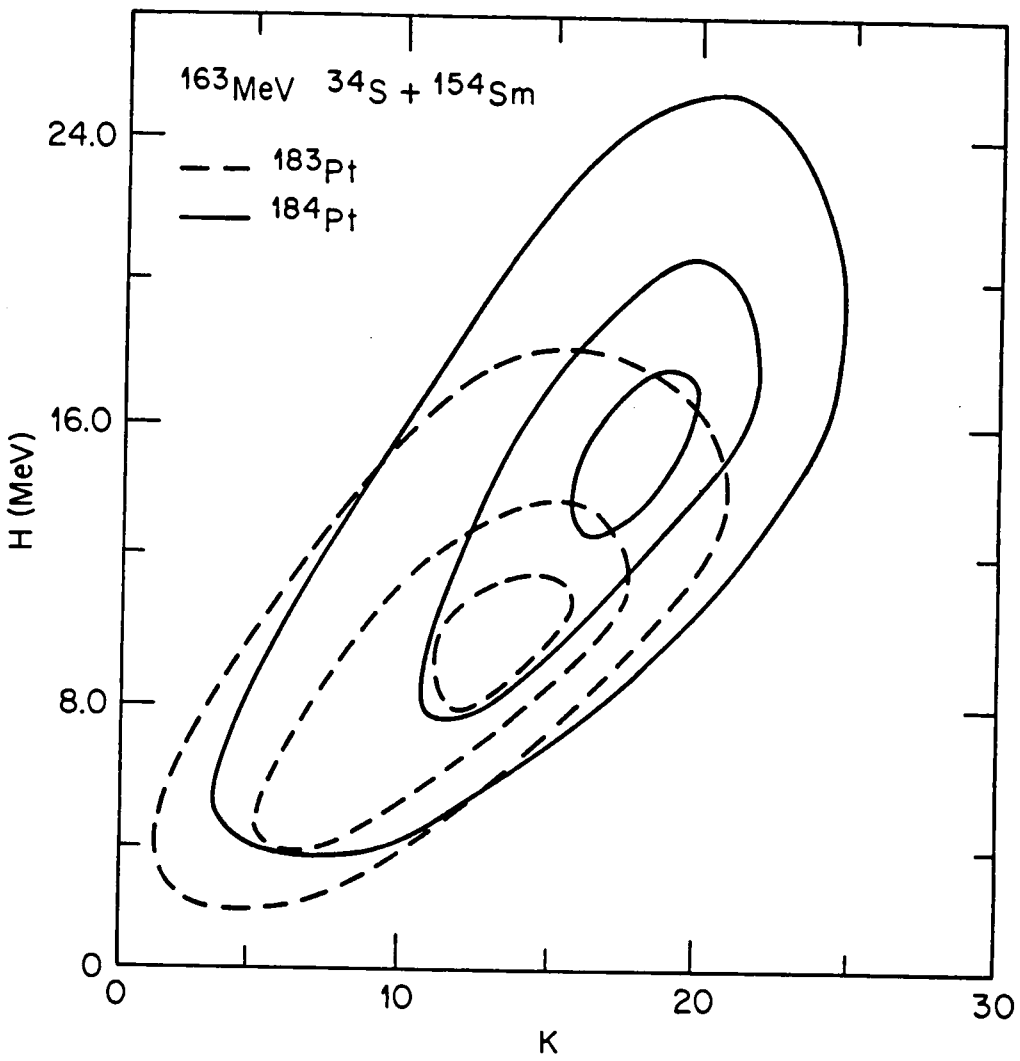

Figure 3.13: Two-dimensional total energy-fold (H-K) spectrum from the HHIRF ^{154}Sm(^{34}S,xn) reaction. Two different H-K distributions are clearly evident, corresponding to the two main Pt reaction products.

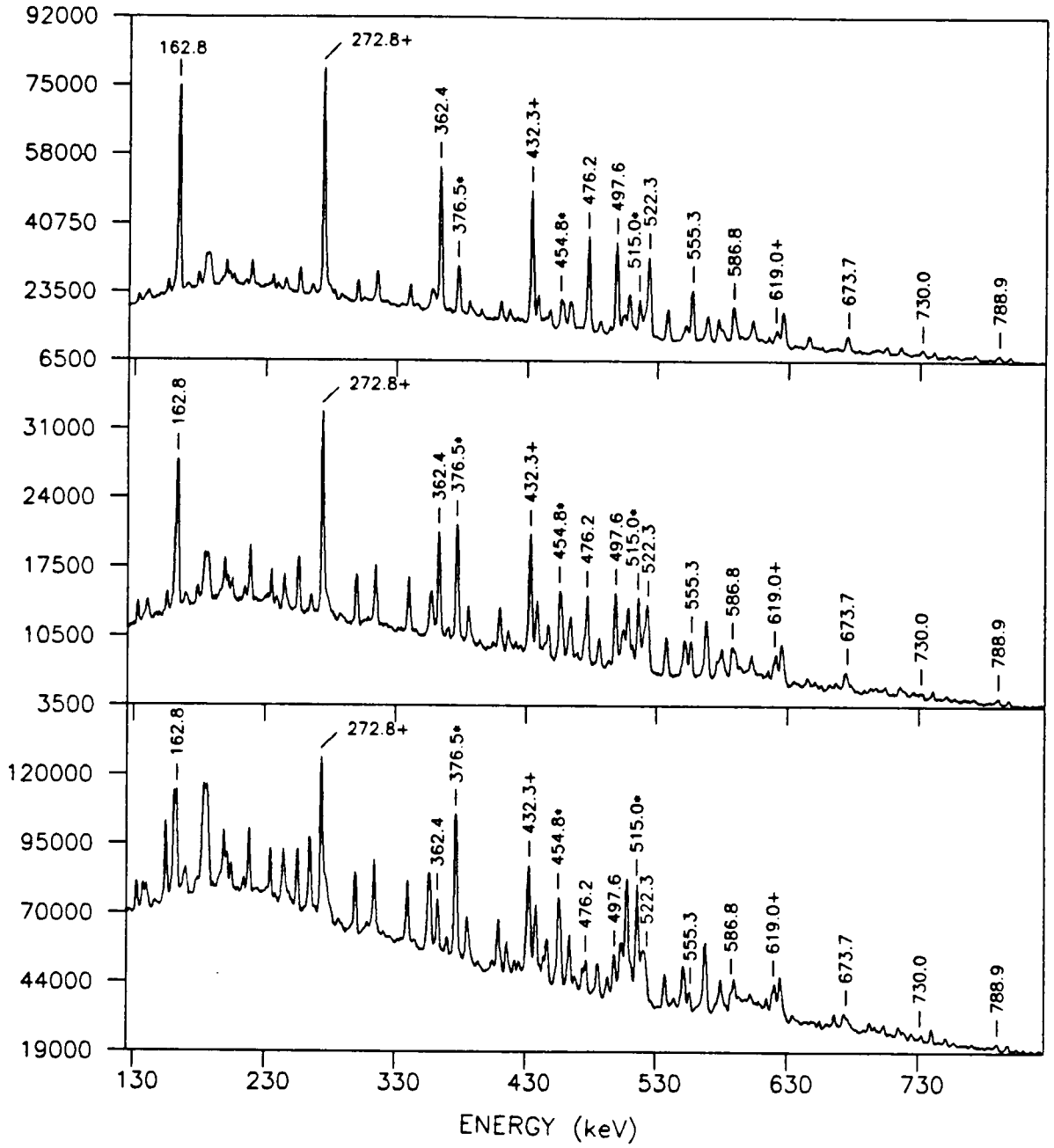

Figure 3.14: The total projections of the three coincidence matrices generated from the HHIRF ^{154}Sm(^{34}S,xn) reaction. The top spectrum was generated using high H-K selection. The middle spectrum was created by gating on the H-K region of highest overlap between the two reaction channels. The bottom spectrum corresponds to low H-K selectivity. Labeled energies marked with a (*) indicate ^{183}Pt transitions; those marked with a (+) are degenerate transistions found in both ^{184}Pt and ^{183}Pt and unmarked labeled energies indicate ^{184}Pt transitions.

to populate high-spin states in ^{183}Au, and the 1mg/cm^2 target was replaced with two 0.5 mg/cm^2 foils for the taking of coincidence data. The reason for using two thin foils over a single thick target lies in the fact that the residual nuclei, formed in the reaction, decay in flight. This makes it necessary for these nuclei to share a single recoil velocity or the γ-ray spectrum will show Doppler broadened peaks for higher energy γ rays ($E_\gamma \geq 700$ keV). With thin targets, the nuclear recoils are able to escape the foil without making many collisions with other target nuclei, allowing the recoiling nuclei to retain most of the velocity imparted to them in the heavy-ion collision. Since fewer projectile-target collisions are possible when using a thin foil, multi-foil targets are used to increase the production rate of compound nuclei. All foils of ^{152}Sm had a purity of 98%.

The energy and time signals of all detectors firing during an event were written to tape. The total number of Ge coincidence triggers ranged between 4000 and 5000 events/sec. However, the accepted triggers averaged between 800 and 1100 events/sec. The difference between the total and accepted triggers was due to the requirement that at least two clean Ge detectors must fire if the event was to be accepted by the Event Handler. The NaI gains were set to the standard 5.0 keV/channel by computer software, and the Ge gains were manually set to 0.2 keV/channel, yielding a 3.2 MeV range in the 16384-channel ADCs. A total of 154 data tapes were taken during the experiment.

A prescan was performed on these data, but it did not involve as much preparation as did the prescan for the ^{184}Pt Holifield data. The NaI detectors were calibrated assuming a linear relationship between energy and pulse height. The gain shifted Ge and NaI energies were used to calculate H, but only the detected NaI multiplicity was used to determine the fold. Neutrons were not separated from the γ-ray data, and no information concerning the individual NaI detectors were written to the prescan tapes. The gains of the individual Ge detectors were

matched using known γ-ray energies in ^{182}Pt and set to 0.2 keV/channel. Since the prescanned event lengths on tape were greatly truncated by the elimination of the individual NaI information, on the average, one prescan tape was written for every three data tapes. Each data tape took approximately one hour to prescan compared to the three hour per data tape it took for the ^{184}Pt prescan.

The linear calibration of the NaI detectors and the inclusion of neutrons in the calculation of H and K should result in less resolution among entry channels in the H-K plane. Fig. 3.15 shows the H-K maps for ^{182}Pt and ^{183}Au generated from the prescan tapes. While the separation between reaction channels is more diffuse than that obtained in the ^{184}Pt data at HHIRF, where neutrons have been removed from the coincidence data, this entry channel separation is sufficient to allow for the creation of relatively clean γ-γ matrices for each nucleus by gating on the appropriate region in the H-K plane. This fact is significant, because it shows that it is not necessary to separate neutrons from γ rays or to calibrate the individual NaI counters with great accuracy when using H and K information only to isolate different reaction channels.

A symmetrized coincidence matrix for ^{183}Au and one for ^{182}Pt were generated by gating on the applicable H-K regions in Fig. 3.15. Each matrix had 2048 by 2048 channels with the gain set at 0.8 keV/channel. The total number of coincidence events recorded in these matrices were 127 million and 88 million for ^{182}Pt and ^{183}Au , respectively. Fig. 3.16 shows the total projection from the ^{183}Au matrix. Since there are few common γ rays between ^{182}Pt and ^{183}Au, a second γ-ray coincidence matrix for ^{183}Au was generated using a wider H-K selection to increase statistics and improve the energy gain. This matrix was scanned as a 4096 by 4096 histogram with a gain of 0.2 keV/channel. One other scan was performed to generate several matrices to examine angular correlations among γ rays. The analysis of these matrices will be discussed fully in Chapter 4.

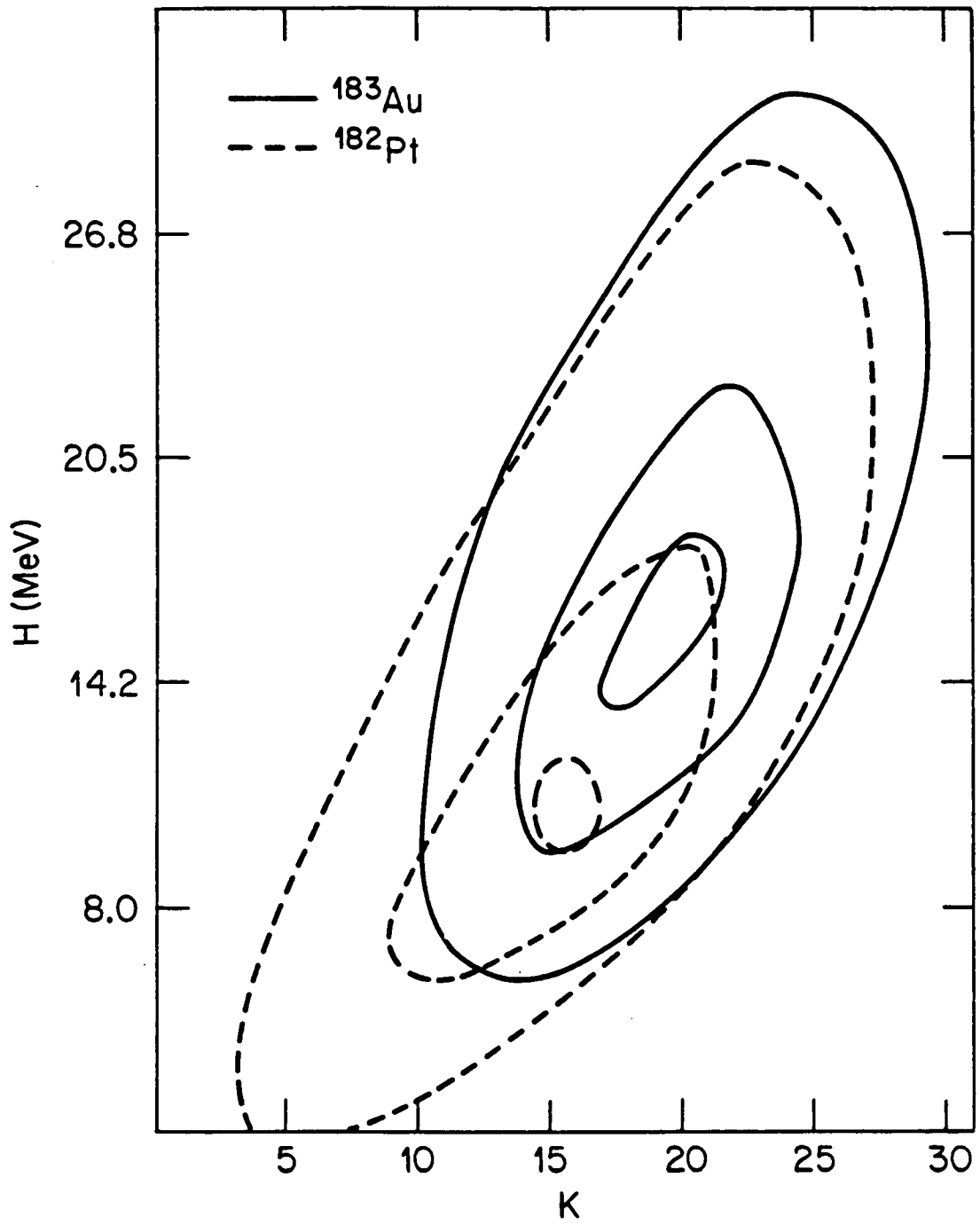

Figure 3.15: Two-dimensional total energy-fold (H-K) spectrum from the HHIRF ^{152}Sm(^{35}Cl,xn-xp) reaction.

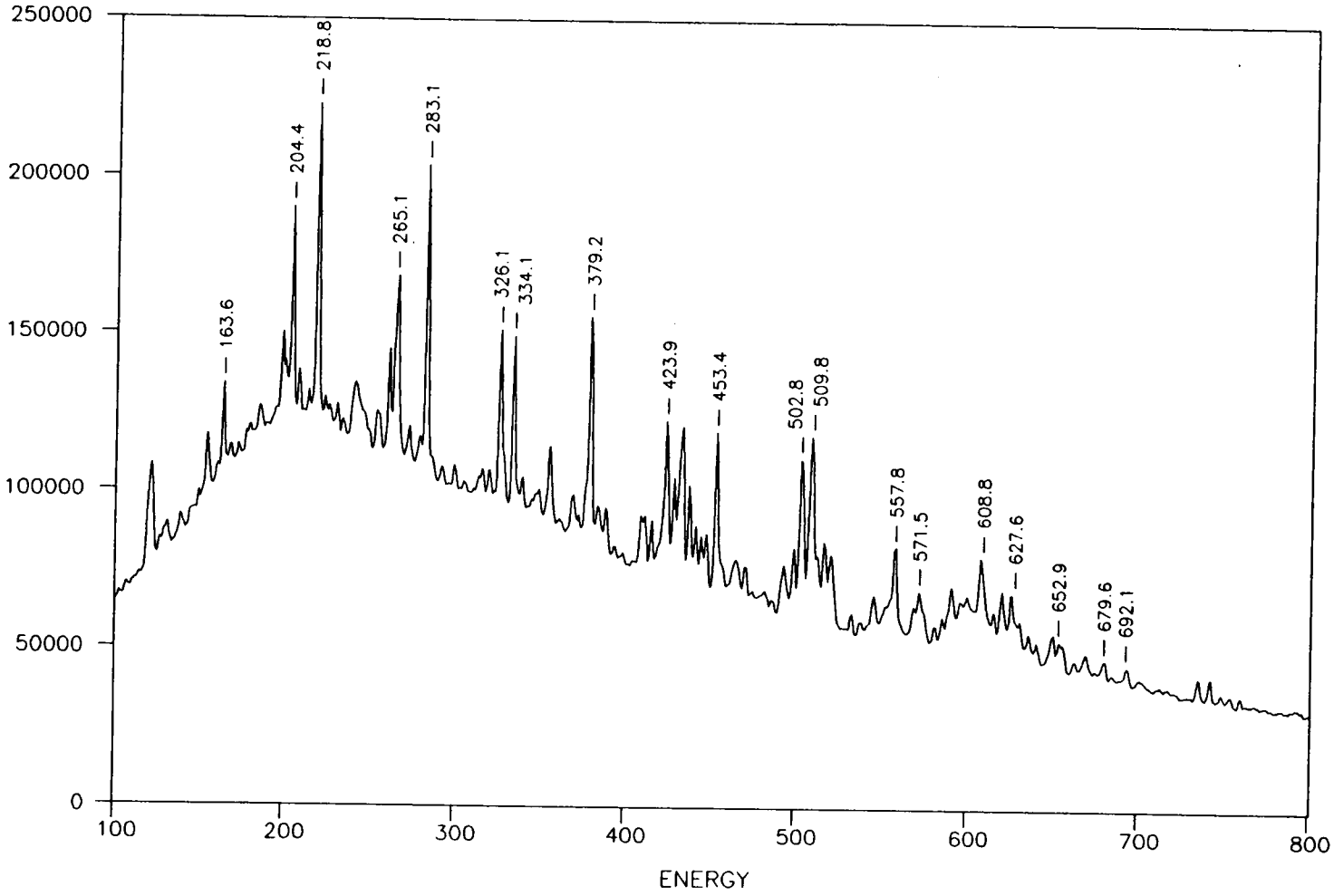

Figure 3.16: The total projection of the ^{183}Au coincidence matrix from data taken in the Spin Spectrometer. Selected transitions in ^{183}Au are labeled in the figure.

3.5.4 ^{184}Pt Chalk River Coincidence Data

For the ^{184}Pt coincidence experiment in the 8π Spectrometer, a ^{29}Si beam at 151 MeV was accelerated onto a ^{160}Gd target, using the Chalk River Tandem Accelerator. The target consisted of two self-supporting foils. One foil had a thickness of 750 μg/cm^2 while the other had a thickness of 600 μg/cm^2. Since the targets were unbacked, the beam was stopped in a lead foil at the rear end of the reaction chamber. The positioning of the lead foil was such that the γ rays produced by the interaction of the beam with the foil were shielded from the Ge detectors. Initially, 80 nano-amps of beam current was incident on the target, however problems with the ion-source caused the current to fluctuate considerably during the experiment. The threshold on the hardware summing device was set to eight; thus, all events with a hardware K of eight or less were rejected and not recorded to tape. Unlike the Spin Spectrometer, the 8π Spectrometer also had electronics to determine through hardware the total BGO energy of the reaction (H). A threshold was also placed on H, and its value was determined by the BGO multiplicity threshold. With a beam current of 80 nano-amps, the accepted Ge triggers averaged between 1400 and 1500 events/sec.

The information written to tape differed from the two Spin Spectrometer experiments. Only the Ge energy and time signals firing during an event were written to tape, while the information concerning the individual BGO detectors was discarded. The total BGO energy and multiplicity were calculated by the CAB (Camac Booster) and written to tape. Since BGO counters are not very sensitive in detecting neutrons, one does not lose resolution in H and K by not attempting to separate the neutrons from the γ-ray data. The BGO gains were initially set to 5.0 keV/channel by computer software using a ^{88}Y radioactive source. The gains of the Ge counters were also set in this manner to 0.25 keV/channel giving a range of 2.1 MeV in the 8192-channel ADCs. Since the foils used in the experiment were

unbacked, the recoils decayed in flight. Thus, the pre-set gains on the Ge counters changed for the four rings due to Doppler shifting. However, after data taking began, the average velocity of the recoiling nuclei was calculated to be 1.4% of the speed of light. This information was programmed into the CAB which in turn shifted the Ge energies to their original pre-set gains before writing the data to tape. Other information written to tape were: the BGO-$E2$ multiplicity, BGO-$E2$ hit pattern, and the Ge multiplicity. The BGO-$E2$ multiplicity is determined by gating the BGO energies by an energy window. The γ rays is this gate are all assumed to be pure electric quadrupole transitions. The BGO-$E2$ hit pattern corresponds to four different gated latches. Each bit in the latches corresponds to a specific BGO detector. A detectors bit is set if the γ-ray energy of the BGO counter falls within the $E2$ energy window. The BGO hit pattern can be used later to calculate the spin orientation of the nucleus (see Chapter 4). A total of 23 data tapes written at 6250 bpi. were taken during the experiment.

Since the gains of all twenty Ge detectors were matched on an event by event basis before before they were written to tape, a prescan of the tapes is not necessary. Two unsymmetrized γ-ray coincidence matrices were generated during the experiment: one was gated on low H and K to maximize the ^{183}Pt (6n) data, while the other was gated on higher H and K to maximize the ^{184}Pt (5n) data. Each matrix was 4096 by 4096 channels in length with the gain of each set to 0.5 keV/channel. Before data analysis began, each matrix was symmetrized. The total number of coincidence events recorded in the symmetrized matrices was 76.5 million and 130 million for ^{183}Pt and ^{184}Pt, respectively. Fig. 3.17 shows the total projections from each matrix to give an indication how good the H-K selectivity is. One other scan was done to generate the spin-orientation projections for the angular distribution analysis. How these projections were generated will be discussed in more detail in Chapter 4.

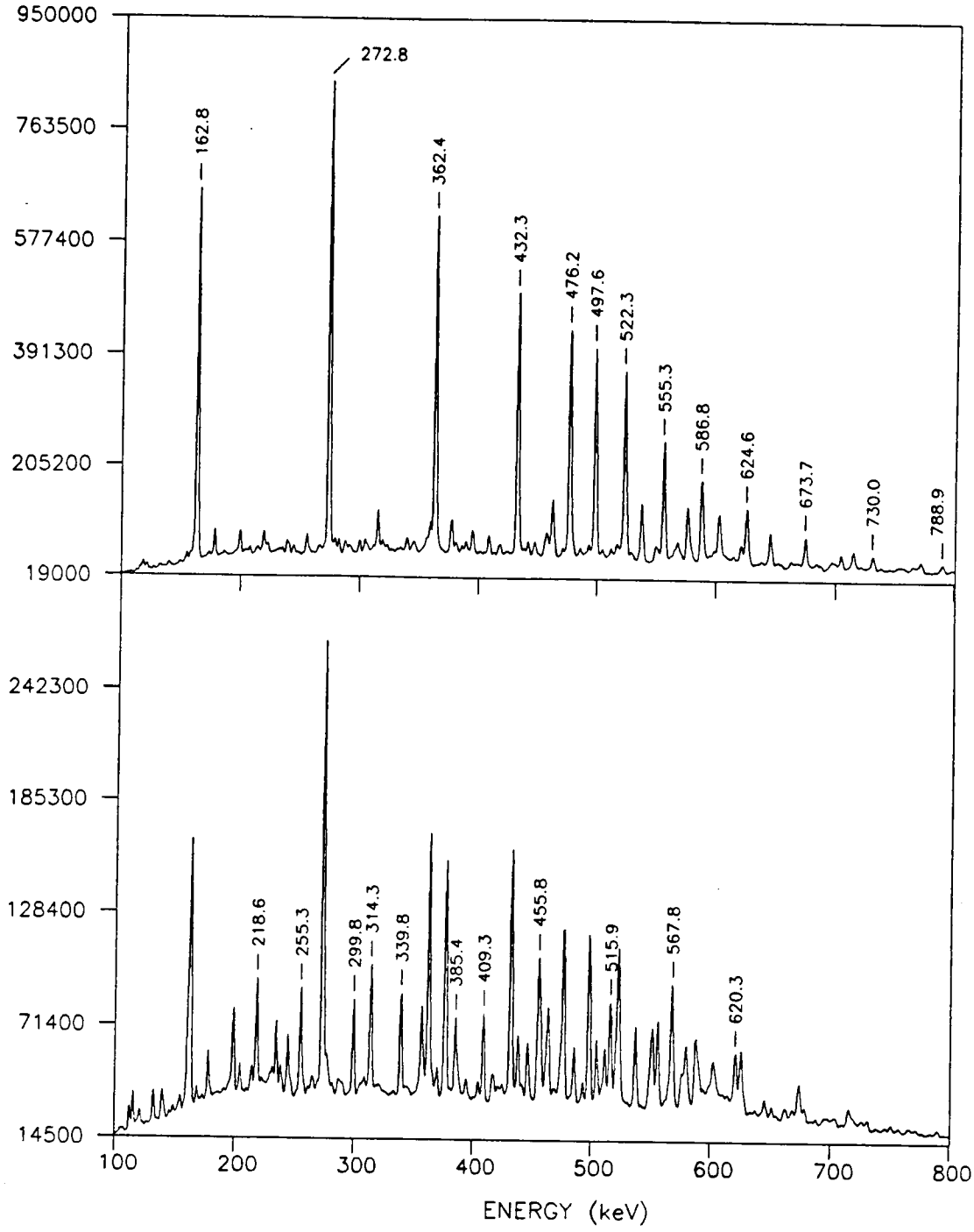

Figure 3.17: The total projections from the ^{184}Pt (top) and ^{183}Pt (bottom) coincidence matrices from data taken in the 8π Spectrometer. The labeled peaks in the top spectrum correspond to transitions in the yrast band of ^{184}Pt. Selected transitions in ^{183}Pt are labeled in the bottom spectrum.

CHAPTER 4

DATA ANALYSIS

4.1 Introduction

In the study of experimental high-spin nuclear physics, there are a number of different types of measurements which can be made to extract information concerning the nuclear structure. Many of these use γ-ray data to directly measure or infer conclusions about the structure of the nucleus at high angular momenta. For example, by measuring the lifetime of a nuclear state, the transition matrix element between the initial and final state is directly determined. However, before more specific measurements such as lifetime experiments are possible, the levels for which the nuclear properties are to be measured must already be known. Thus, the first step in acquiring high-spin knowledge on a specific nucleus is the establishment of its energy decay structure. As was discussed in the previous chapter, this is done by measuring γ-ray coincidences. The spin and parity of each level should also be established during this first step. To accomplish this, one must also measure the multipolarity of the γ rays de-exciting to or from each observed state.

4.1.1 Constructing Nuclear Level Schemes

By collecting a large amount of coincidence data, one is able to construct an energy decay scheme of a nucleus using a procedure known as "gating". This is a two step process, where (1) slices of the two-dimensional coincidence matrix are taken by projecting out γ-ray peaks observed in the total projection of the matrix, and (2) "background" spectra associated with each slice (or gate) are subtracted from these individual projections. The resulting spectra indicate which γ rays are in coincidence with the projected γ rays. From the examination of many gates, a

nuclear level scheme is constructed. The correct placement of each γ ray in the decay scheme is determined by intensity relationships. For example, by gating on a γ ray in a cascade which decays directly to the ground state, all γ rays which decay after the gated peak have equal intensity, since their pathway is singularly defined by the gate. On the other hand, those γ rays decaying before the gated peak have continually decreasing intensities due to the fact that at each level above the gate, many γ rays originating from higher lying states may decay into the level.

The large background associated with a Ge spectrum arises from Compton scattered and unresolved continuum γ rays. The use of Compton-suppression devices reduces considerably the background in a Ge spectrum (see Fig. 3.9), however the remaining background must also be subtracted from gates taken on these coincidence matrices as well. Fig. 4.1 shows an unsubtracted projection gated on the 4^+ to 2^+ transition in the yrast band of ^{184}Pt for the McMaster (unsuppressed) data and Chalk River (suppressed) data. The gated transition is present in both these spectra, because it is in coincidence with the γ rays associated with the background. If the background were eliminated from these gates, this γ ray would vanish from the projections, since a coincidence between the photopeak and itself is impossible.[1] The intensity of the gated transition is much larger in the unsuppressed data due the larger background coincidences.

To subtract the background from a gate, one must generate a spectrum representing the background in coincidence with the gated γ ray. One method for creating this background spectrum is to project out channels near the gated peak which are assumed to be background channels.[2] The resulting spectrum represents the energy response function of the background in the region near the peak. By making the channel width of the background gate as wide as the gate on

[1] This assumes that two γ rays of the same energy are not in coincidence with each other.

[2] A background channel is defined as a channel associated only with the Compton and continuum events.

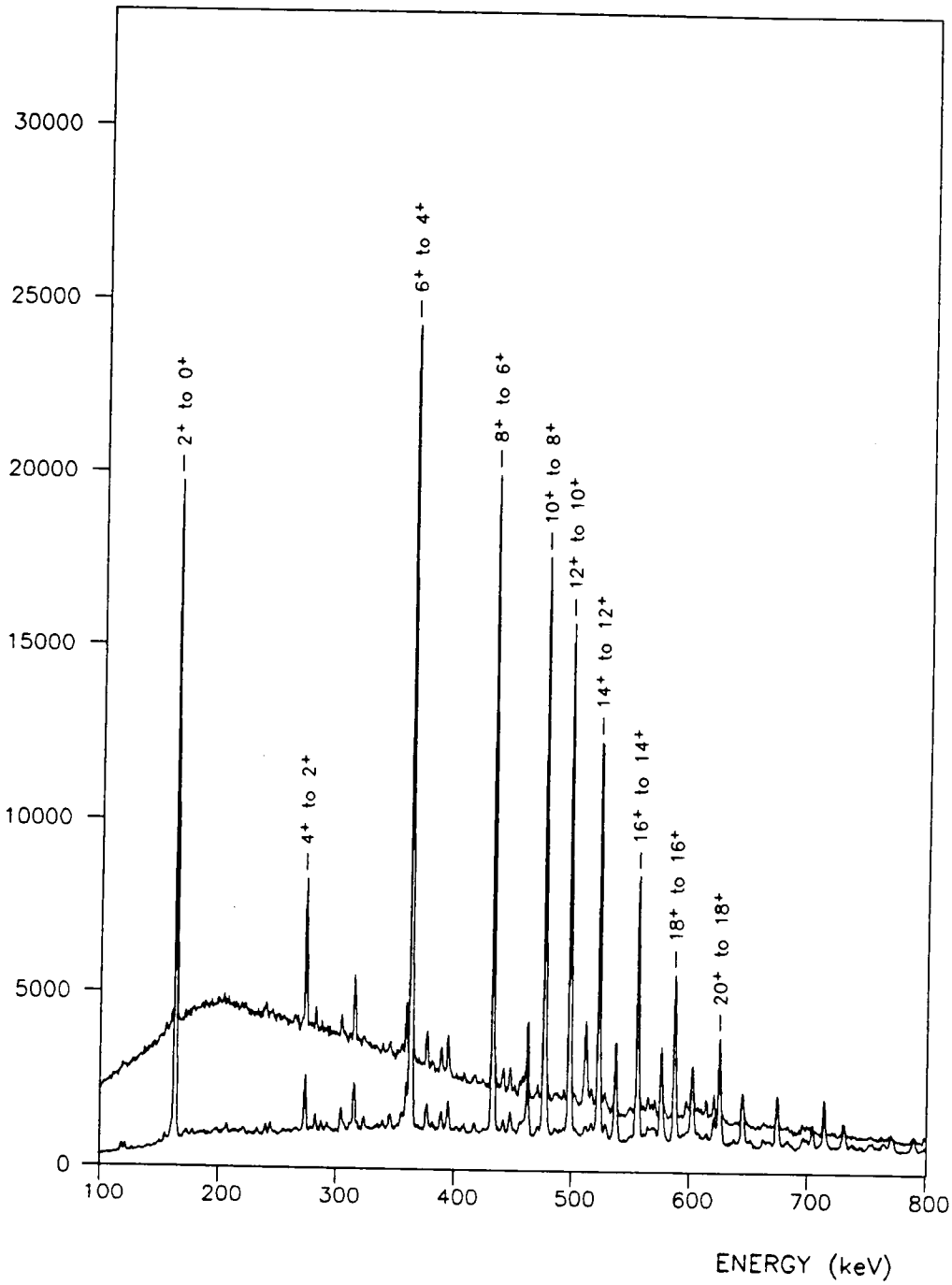

Figure 4.1: Unsubtracted projections gated on the 4^+ to 2^+ transition in ^{184}Pt from data taken in the McMaster Lotus using unsuppressed Ge counters and from data taken in the 8π Spectrometer using suppressed Ge detectors.

the discrete peak, one is able to subtract the background spectrum directly from the γ-ray gated projection (method 1).

In complicated Ge spectra, where there are many discrete peaks very close to each other, it is not always possible to find suitable background channels near the peaks of interest. To overcome this problem, one generates an average background projection by gating on a large number of background channels through out the entire energy range of the coincidence matrix and summing these gates together. Before subtracting this "universal background" from a gated spectrum, one must normalize the background projection to the portion of the gate associated with the background. This normalization factor is calculated by dividing the background area under the gate in the total projection by the total number of counts in the background spectrum. This procedure is based on the assumption that the individual gated spectra, which are summed together to form the "universal" background, are on the average equivalent, except for a constant factor. This implies that there is no energy dependence on the response of the background spectra. Palameta and Waddington (1985) have found this to be true in unsuppressed data, where the number of discrete lines in coincidence with the background is very large and come from the same reaction channel (method 2).

While both of these methods remove the background associated with the Compton and continuum events of the gate in coincidence with other γ rays, they do not remove background events where the gated discrete line is in coincidence with Compton events. Fig. 4.2a shows the same gate as in Fig. 4.1 with the background subtracted using the average background method described above. Note that the gated photopeak has vanished; however, a smooth Compton background exists underneath the discrete peaks. Palameta and Waddington have designed a method to subtract all background coincidences from a two-dimensional symmetrized matrix before gating on the discrete peaks is performed (method 3). This

method offers two advantages: (1) only photopeak-photopeak coincidences remain in the matrix, and (2) gates taken on this matrix can be immediately examined since the background has already been eliminated from the projections.

Briefly, the method works in the following way. The total projection of the symmetric coincidence matrix, $C(i,j)$, taken on one axis is defined as

$$P(i) = \sum_{j=1}^{N} C(i,j), \tag{4.1}$$

where N is the dimension of the matrix. A smooth fit, $f(i)$, is made to the continuous background under the discrete peaks in $P(i)$. A background channel in $P(i)$ is determined by the condition that $P(i) - f(i)$ is zero within statistical error. The average background spectrum is generated by gating on the entire set of background channels, K:

$$b(i) = \sum_{j \epsilon K} C(i,j). \tag{4.2}$$

The above procedure is equivalent to the average background method described above and a subtraction of $C(i,j)$ can be done to remove the Compton coincidences associated with each channel in the matrix by forming

$$C'(i,j) = C(i,j) - \frac{f(i)b(j)}{\sum_j b(j)}. \tag{4.3}$$

Photopeak-Compton coincidences still exist in the matrix after this subtraction. However, Palameta and Waddington have found that this remaining background is proportional to $f(j)$, and a more complete subtraction can be made by forming

$$C''(i,j) = C'(i,j) - \frac{f(j)d(i)}{\sum_{j \epsilon K} f(j)}, \tag{4.4}$$

where $d(i) = \sum_{j \epsilon K} C'(i,j)$. Fig. 4.2b shows a projection of the 4^+ to 2^+ transition gated on a fully subtracted matrix. The smooth Compton background still present in Fig. 4.2a has vanished. In conclusion, the most convenient method for subtracting background is to generate a subtracted coincidence matrix using the

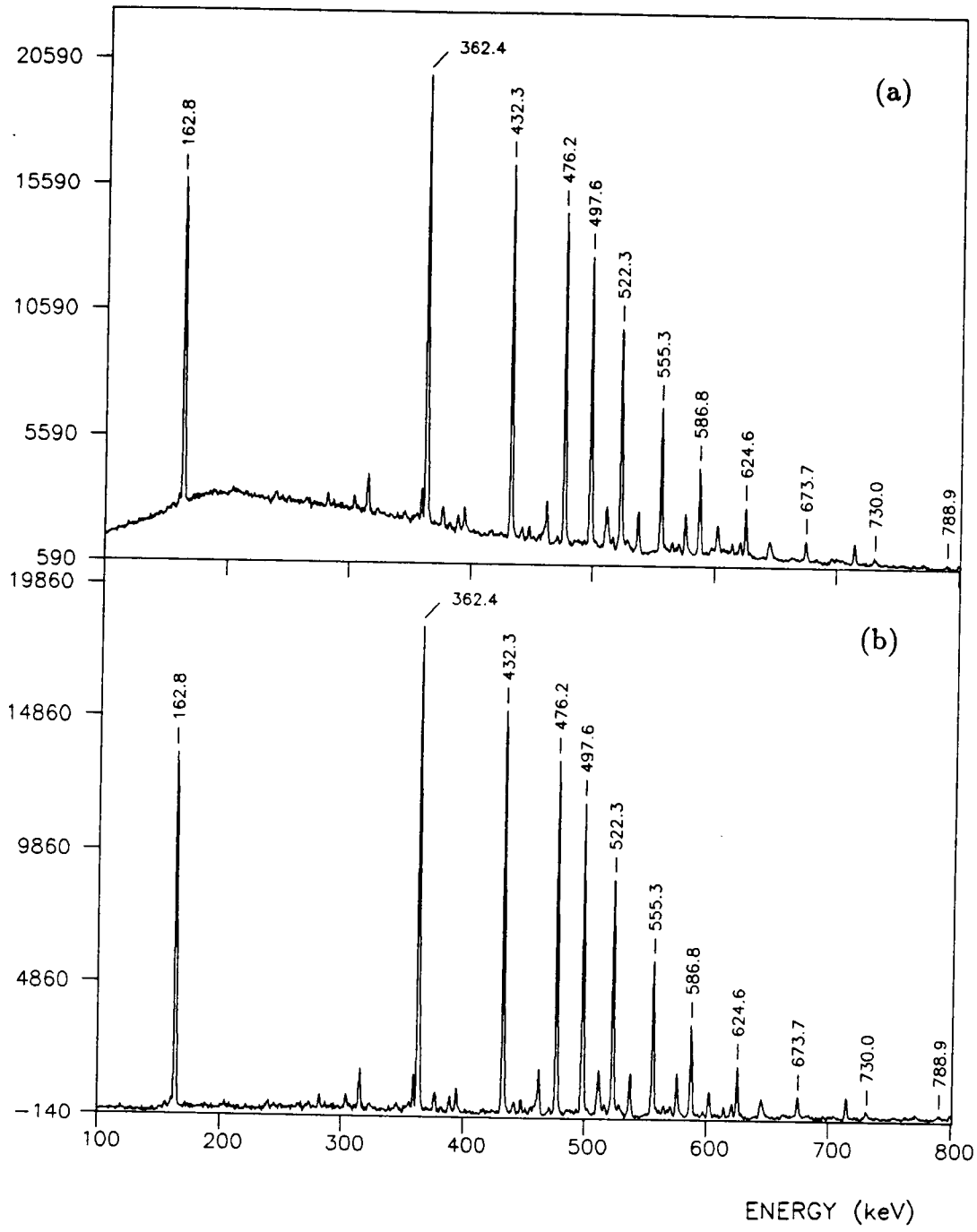

Figure 4.2: Gates on the 4^+ to 2^+ transition in the yrast band of ^{184}Pt using the data obtained in the McMaster coincidence experiment. Spectrum (a) was generated using subtraction method 2, and spectrum (b) was created using subtraction method 3. The labeled peaks correspond to yrast transitions.

Table 4.1: Description of subtraction methods used on each coincidence experiment reported on in this work.

Nucleus	Facility	Subtraction Methods Used
^{184}Pt	McMaster	1 and 3
^{184}Pt	Holifield	3
^{184}Pt	Chalk River	2
^{183}Au	Holifield	1 and 3

method of Palameta and Waddington. However, no allowances for correlations in the background is made by this method. One should be cautioned in using it on well suppressed data where structure in the background may exist and on data which have significant contributions from different residual nuclei, where the average background component from each residual nucleus may differ significantly. Further study of this method must be done to determine on what types of data it should be applied to. Table 4.1 lists the subtraction methods used on the data from each coincidence experiment.

4.1.2 Angular Distributions

In order to measure the spin and parity of each observed level in the nuclear decay scheme, one performs measurements to determine the electromagnetic multipolarity of the observed γ rays. The spatial distribution in which the γ rays of a given multipolarity are emitted is dependent on the spin direction of the nucleus and exhibits axial symmetry with respect to the spin direction (see Rose and Brink, 1967). Because of this axial symmetry, only the plane containing the spin direction need be defined to measure the multipole components of a γ ray. In heavy-ion fusion reactions, the final spin direction of the residual nucleus is in the plane perpendicular to the beam axis, *i.e.* $\mathbf{L} = \mathbf{r} \times \mathbf{p}$. Since the majority of the γ rays in a nuclear cascade are $\Delta I = 2$ electric quadrupole transitions, the

initial alignment of the angular momentum vector remains largely in this plane throughout the cascade. Thus, the final γ rays emitted between discrete states of the residual nuclei show angular distributions with respect to the beam axis. Experimentally, the angular distribution of each γ ray is determined by taking measurements at different θ angles, with respect to either the beam axis or the spin direction, and fitting these peak intensities to a function of the form :

$$W_{exp}(\theta) = \sum_k a_k P_k(\cos\theta), \tag{4.5}$$

where the a_k are coefficients which include both theoretical and experimental terms, and P_k represents Legendre polynomials. Only a summary and not a complete theoretical derivation of the angular distribution formula from first principles is presented in this work. For a complete description, one is referred to the review article by Rose and Brink (1967).

From a purely theoretical derivation, the parameter a_k may be replaced by A_k. The parameter A_k for a transition from an initial state J_1 to a final state J_2 is expressed as a function of two terms:

$$A_k(J_1 \rightarrow J_2) = B_k(J_1)\mathcal{F}_k(\delta LL'J_1J_2), \tag{4.6}$$

where L and L' refer to the 2^L and $2^{L'}$ components of the radiation and δ is the "mixing ratio" of these two. The $\mathcal{F}_k$ factors depend only on quantities which characterize the nuclear transition and are expressed in terms of the F-coefficients[1] of Ferentz and Rosenzweig (1955) and the mixing ratio:

$$\mathcal{F}_k(\delta LL'J_1J_2) = \frac{1}{1+\delta^2}\left\{F_k(LLJ_1J_2) + 2\delta F_k(LL'J_1J_2) + \delta^2 F_k(L'L'J_1J_2)\right\}. \tag{4.7}$$

The mixing ratio is expressed as a ratio of the reduced matrix elements,

$$\delta = \frac{< J_2 \parallel L' \parallel J_1 >}{< J_2 \parallel L \parallel J_1 >}, \tag{4.8}$$

[1]Explicit expressions for the F-coefficients can also be found in Yamazaki (1967) and Krane (1973).

where L stands for the lowest-order multipolarity occurring in the transition $J_1 \rightarrow J_2$. It should be stressed that, quantum mechanically, the measurement of angular distributions is a measurement of the ratio of reduced matrix elements, and not the matrix elements themselves.

While $\mathcal{F}_k$ in Eq. 4.6 contains the "nuclear information", $B_k(J_1)$ depends only on the nuclear alignment, and it is defined as

$$B_k(J_1) = \sum_{M_1}(-1)^{J_1-M_1}(2J_1+1)^{1/2}(J_1M_1J_1 - M_1 \mid k0)P_{J_1}(M_1), \tag{4.9}$$

where $P_{J_1}(M_1)$ is the population parameter which describes the relative population of the different magnetic substates, $(J_1M_1J_1 - M_1 \mid k0)$ is a Clebsch-Gordan coefficient, $B_k(J_1)$ is a statistical tensor and $B_0(J_1) = 0$. The explicit expression for the population parameter depends on which axis is chosen as the quantization axis. For example, if the angular momentum vector is defined as the quantization axis and is fully aligned in the plane perpendicular to the beam axis,

$$P_{J_1}(M_1) = \begin{cases} 1 & \text{if } M_1 = 0 \\ 0 & \text{if } M_1 \neq 0, \end{cases}$$

when measuring the angular distribution with respect to the beam axis. On the other hand, if one is measuring the angular distribution in the above example with respect to the spin direction, it becomes the quantization axis and

$$P_{J_1}(M_1) = \begin{cases} 0.5 & \text{if } M_1 = \pm J_1 \\ 0 & \text{if } M_1 \neq \pm J_1, \end{cases}$$

assuming the spin direction is known exactly. Fig. 4.3 shows the calculated angular distributions for the two cases described above using the function

$$W(\theta) = 1 + A_2P_2(\cos\theta) + A_4P_4(\cos\theta). \tag{4.10}$$

A comparison of the calculated A_2 and A_4 coefficients is listed in Table 4.2 for both cases, and several differences are immediately apparent:

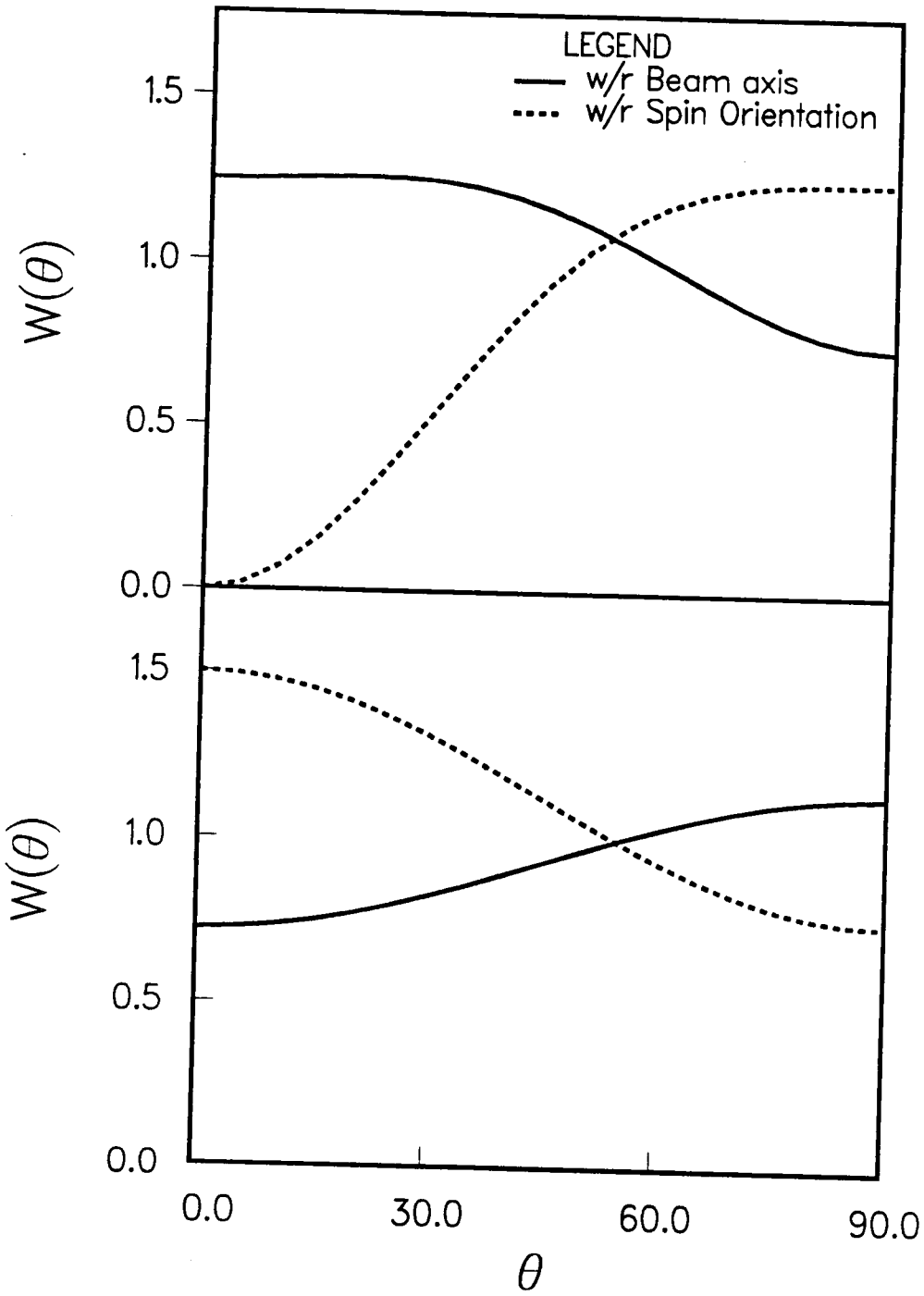

Figure 4.3: Comparison of the angular distributions about the nuclear spin axis and about the beam axis for (a) a $14 \rightarrow 12$ $E2$ transition and (b) a $14 \rightarrow 13$ pure $E1$ transition, assuming full alignment.

Table 4.2: Comparison of angular distribution coefficients measured with respect to the spin axis and the beam axis, assuming full alignment in both cases.

Orientation	Stretched Quadrupole $14 \rightarrow 12$		Stretched Dipole $14 \rightarrow 13$
	A_2	A_4	A_2
spin axis	-0.714	-0.286	$+0.500$
beam axis	$+0.397$	-0.152	-0.278

1. The A_2 coefficients have opposite signs for the two different types of angular distribution measurements. This is expected, since the axes which define $\theta = 0°$ for the two cases are perpendicular to each other. Thus, the difference in the signs of A_2 is directly related to the definition of the quantization axis.

2. The coefficients measured with respect to the spin orientation are larger. Therefore, they have better sensitivity in the fully aligned case than those measured with respect to the beam axis. This can be very advantageous when trying to determine the angular distributions of very weak peaks whose measured intensities have large errors associated with them.

One other difference between the two methods which is not apparent from table 4.2 is that the A-coefficients for the spin axis are independent of spin, whereas for the beam axis, the coefficients decrease with increasing spin.

4.2 Level Scheme for ^{184}Pt

Several previous studies had established the low-energy level structure of ^{184}Pt utilizing both radioactive decay and heavy-ion reactions. Burde *et al.* (1966) were the first to establish the existence of a 1.1 msec isomer at 1843.8 keV. The radioactive decay studies of Finger *et al.* (1972) and Calliau *et al.* (1974) established both the second 0^+ state at 492 keV associated with the coexisting oblate

structure and the quasi-vibrational γ-band. In beam studies by Burde *et al.* (1967) identified the yrast band up to the 16^+ level, while Beshai *et al.* (1976) extended the known levels of this band up to 20^+. The current level structure of ^{184}Pt established by the three measurements reported on in this work is shown in Fig. 4.4. Six new transitions are added to the yrast band, and seven new side bands built on two and four-quasiparticle excitations have been identified. Since the Chalk River measurement establishes each band to the highest observed spins, all gates shown in the following subsections are from the data taken in the 8π Spectrometer.

4.2.1 ^{184}Pt Angular Distributions With Respect to the Beam Axis

A separate experiment was performed to measure the angular distributions with respect to the beam axis for ^{184}Pt, using five Ge detectors placed at θ angles 0°, 30°, 45°, 60° and 90°. An accepted event consisted of a single Ge detector in coincidence with the six-element NaI multiplicity filter located in the McMaster Lotus. Ge-Ge coincidences were not required, because this would measure angular correlations with respect to the beam axis and not angular distributions (see Krane, 1973). Angular correlations between the Ge detectors and NaI filter are small since the detectors which make up the filter are positioned symmetrically around the beam axis.

As discussed above, a heavy-ion fusion reaction leaves the initial spin of the compound nucleus in a plane perpendicular to the beam axis. However, before the first discrete transition is observed, both particle and γ rays have been emitted from the aligned nucleus and some statistical distribution of the magnetic substates is expected in the alignment of angular momentum vectors of the residual nuclei. Several studies have shown (*e.g.* Nolan and Butler, 1981) that this statistical distribution can be approximated by assuming a Gaussian distribution for the

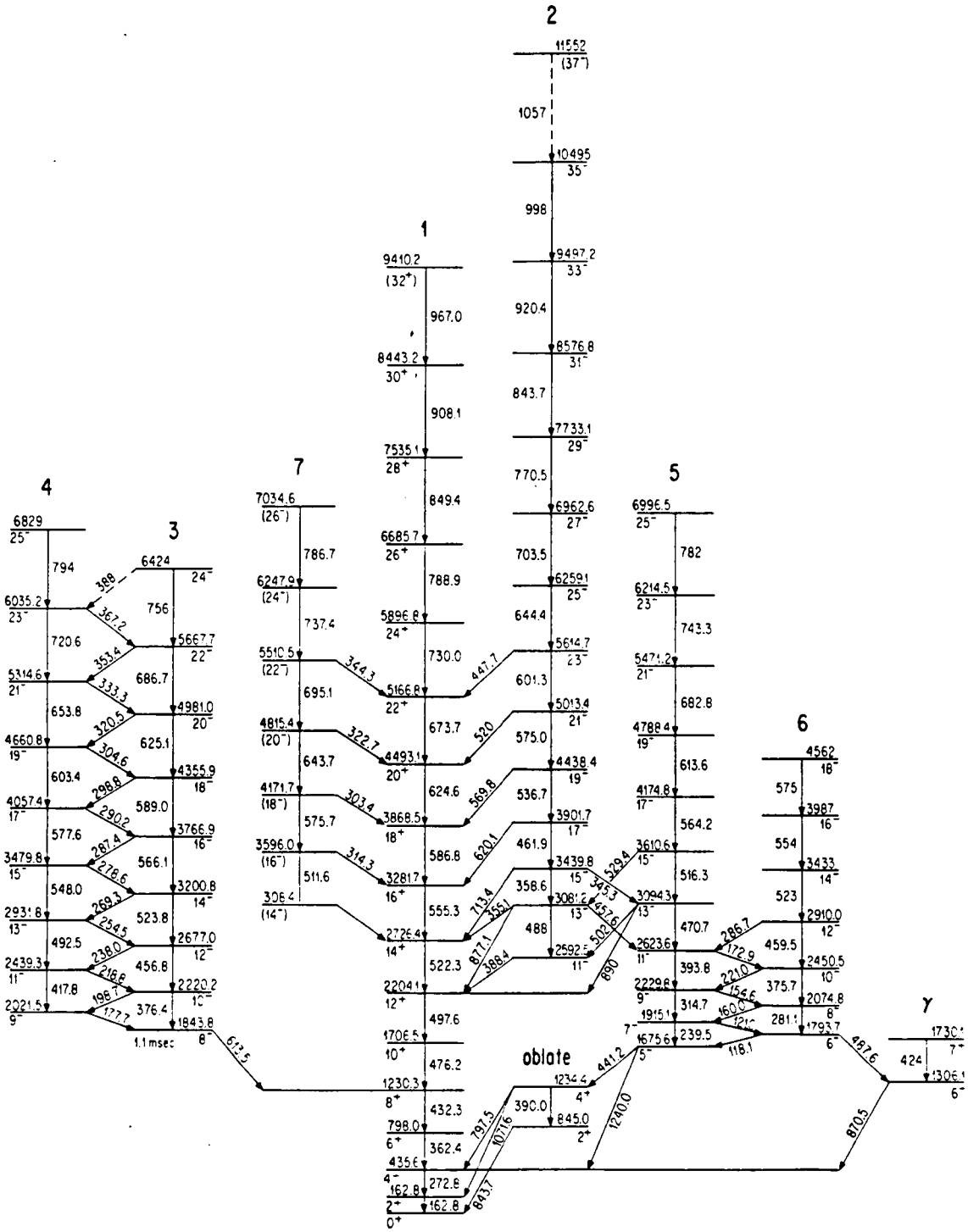

Figure 4.4: Level structure of ^{184}Pt.

population parameter,

$$P_J(m) = \frac{\exp\left(-\frac{m^2}{2\sigma^2}\right)}{\sum_{m'=-J}^{J} \exp\left(-\frac{m'^2}{2\sigma^2}\right)}, \tag{4.11}$$

where σ represents the width of the statistical distribution.

To correctly measure angular distributions, one should use a single detector, placing it at different θ angles with respect to the beam axis, to record Ge data. Each Ge spectrum is normalized for constant count rates with respect to a monitor detector, which is kept fixed throughout the experiment. The use of five different Ge detectors in the angular distribution measurement created two major difficulties in calculating A_2 and A_4 coefficients, which are not encountered in single detector experiments. Both these difficulties are connected with the determination of the detector efficiency as a function of γ-ray transition energy. Detector efficiencies are usually calculated by taking radioactive-source data, correcting the area of each γ-ray peak in the spectrum by its relative intensity, and fitting the intensities to a functional form which is thought to best represent the efficiency of the detector.

The first difficulty involved the actual determination of the efficiency for each detector. For the angular distribution experiment on ^{184}Pt, data were taken using ^{152}Eu and ^{133}Ba radioactive sources. The efficiency of each Ge detector was calculated by first normalizing the relative intensities of the ^{133}Ba data to that of ^{152}Eu and then fitting the intensities from both sources to the function

$$\begin{aligned}
\log_{10}(Eff) = &\quad A_1 + B_1 \log(E_\gamma) && \text{for } E_\gamma < E_1 \\
= &\quad A_0 + C_1(\log(E_\gamma) - E_0)^4 && \text{for } E_1 < E_\gamma < E_0 \\
= &\quad A_0 + C_2(E_\gamma - E_0)^2 && \text{for } E_0 < E_\gamma < E_2 \\
= &\quad A_2 + B_2 \log(E_\gamma) && \text{for } E_\gamma > E_2.
\end{aligned} \tag{4.12}$$

While the fit reproduced the data well for $E_\gamma > 250$, the function used for the lower transition energies noticeably deviated from the data for all detectors. Thus, angular distributions calculated at the lowest energies should only be viewed as good approximations to the actual values, since the renormalization for the efficiency has some error associated with it.

The other difficulty stems from the angular correlations which arise by requiring coincidences between a Ge detector and the NaI multiplicity filter. Since the efficiency curve of each detector is determined from source data without any coincidence requirements, this efficiency may not represent the efficiency of the detector when data are taken in coincidence mode. If the angular correlations are not very large, the relationship between the singles and coincidence efficiency for all energies is approximated by a numerical constant. Since the coincidence efficiency was not measured in this experiment, this constant cannot be determined from our source data. However, it is crucial that the singles efficiencies be corrected, if the angular distributions are to be calculated correctly.

The coincidence efficiencies were properly renormalized by calculating the expected angular intensities for five strong $E2$ transitions in ^{184}Pt (272.8, 362.4, 432.3, 476.2 and 497.6 keV) using the expression,

$$W(\theta) = a_0 \left(1 + Q_2 A_2 P_2(\cos\theta) + Q_4 A_4 P_4(\cos\theta)\right), \qquad (4.13)$$

where Q_k is a coefficient which corrects for the solid angle subtended by the detector (see Krane, 1972). These transitions were chosen since they lie in an energy region where the efficiency is well determined. The theoretical values for A_2 and A_4 were calculated by assuming a value for $\sigma/J = 0.25$ for all five transitions. Pilotte (1987) has measured the σ/J in an angular distribution measurement on ^{185}Pt and has found that it remains constant at 0.25 over the decay of the the yrast band. Since the reaction used in this measurement was almost identical to the re-

action utilized for the ^{184}Pt angular distribution experiment (^{174}Yb(^{16}O,5n)^{185}Pt at 90 MeV), this same value has been assumed for the above data. The solid angle corrections (Q_2 and Q_4) were also determined and included in the calculations of $W(\theta)$. Once the theoretical values for $W(\theta)$ were found, a correction factor for each angle was determined for the five transitions by renormalizing the experimental angular distributions so that they agree with the theoretical values. A single correction factor was then determined for each angle by averaging over the separate $E2$ normalization constants.

Once each efficiency curve was renormalized, all fitted peak areas were corrected for the detector efficiencies. The 30° peak intensities were not used in the determination of the angular distribution coefficients, because the assumption that the singles efficiency deviated from the coincidence efficiency by an energy-independent constant was not correct for this angle. The cause of this anomaly may be due to an enhancement of the angular correlations between the 30° detector and the multiplicity filter. Table 4.3 lists the experimental A_2 and A_4 coefficients calculated using a least squares fit to the experimental intensities. The peak intensities are also indicated and were measured relative to the $4^+ \rightarrow 2^+$ transition in the yrast band of ^{184}Pt ,using the calculated a_o coefficients from the fitted angular distribution data. However, when multiplets prevented the determination of the intensity of certain transitions, gated spectra from the coincidence experiment were used, comparing the intensities of the peaks of interest with one whose intensity relative to the $4^+ \rightarrow 2^+$ transition was already known. It should be noted that intensities determined in this way are only approximations to the actual values; however, they do give a good indication of how strongly levels were populated during the experiment. The actual assignment of spins and parities to energy levels is discussed in the following subsections.

Table 4.3: Angular distribution data for ^{184}Pt.

Energy (keV)	Relative Gamma-ray Intensity	A_2	A_4	$I_i \rightarrow I_f$	Assigned Multi-polarity
118.3	2.0(2)	−0.903(279)	0.238(211)	$6^- \rightarrow 5^-$	$M1(E2)$
121.0	1.5(2)	−0.606(439)	−0.045(335)	$7^- \rightarrow 6^-$	$M1(E2)$
154.6[2]	1.4(3)			$8^- \rightarrow 7^-$	$M1(E2)$
160.0[2]	1.6(4)			$9^- \rightarrow 8^-$	$M1(E2)$
162.8	64.0(4)			$2^+ \rightarrow 0^+$	$E2$
172.9[3]				$11^- \rightarrow 10^-$	$M1(E2)$
177.7	5.8(1)	−0.858(35)	0.046(30)	$9^- \rightarrow 8^-$	$M1(E2)$
198.7	6.6(1)	−0.605(31)	0.053(27)	$10^- \rightarrow 9^-$	$M1(E2)$
218.8[2]	3.3(4)			$11^- \rightarrow 10^-$	$M1(E2)$
221.0[1]	0.7(2)			$10^- \rightarrow 9^-$	$M1(E2)$
238.0	2.4(1)	−0.841(51)	0.090(53)	$12^- \rightarrow 11^-$	$M1(E2)$
239.5	2.3(1)	0.153(44)	0.048(50)	$7^- \rightarrow 5^-$	$E2$
254.5	1.7(3)	−0.557(116)	0.073(97)	$13^- \rightarrow 12^-$	$M1(E2)$
269.3	3.4(2)	−0.531(137)	0.082(114)	$14^- \rightarrow 13^-$	$M1(E2)$
272.8	100.0(3)	0.342(8)	−0.120(7)	$4^+ \rightarrow 2^+$	$E2$
278.6	2.2(2)	−0.512(199)	0.341(168)	$15^- \rightarrow 14^-$	$M1(E2)$
281.1	2.7(2)	0.124(155)	0.110(134)	$8^- \rightarrow 6^-$	$E2$
286.7	1.0(1)	−0.259(135)	−0.042(145)	$12^- \rightarrow 11^-$	$M1(E2)$
287.4	1.6(1)	−0.961(70)	0.248(68)	$16^- \rightarrow 15^-$	$M1(E2)$
290.2	1.4(1)	−0.795(79)	−0.023(77)	$17^- \rightarrow 16^-$	$M1(E2)$
298.6[3]				$18^- \rightarrow 17^-$	$M1(E2)$
303.4	2.7(1)	0.357(54)	0.004(57)	$18^{(-)} \rightarrow 18^+$	$\Delta I = 0$
304.6	1.3(1)	−0.293(108)	−0.069(115)	$19^- \rightarrow 18^-$	$M1(E2)$
314.5[2]	3.4(3)			$(16^-) \rightarrow 16^+$	$\Delta I = 0$
314.7[2]	7.4(3)			$9^- \rightarrow 7^-$	$E2$
320.5	0.5(1)			$20^- \rightarrow 19^-$	$M1(E2)$
322.7	1.1(1)	0.668(155)	−0.083(156)	$(20^-) \rightarrow 20^-$	$\Delta I = 0$
344.3	1.1(1)			$(22^-) \rightarrow 22^-$	$\Delta I = 0$
345.3	1.7(1)	0.430(80)	0.118(87)	$15^- \rightarrow 13^-$	$E2$
355.1[2]	1.5(5)			$13^- \rightarrow 14^+$	$E1$
358.6	7.3(2)	0.332(79)	0.032(73)	$15^- \rightarrow 13^-$	$E2$
362.4	90.0(4)	0.335(10)	−0.086(10)	$6^+ \rightarrow 4^+$	$E2$
375.7[2]	3.3(9)			$10^- \rightarrow 8^-$	$E2$
376.4[2]	4.4(3)			$10^- \rightarrow 8^-$	$E2$
388.4[2]	4.2(4)			$11^- \rightarrow 12^+$	$E1$

Table 4.3: Continued.

Energy (keV)	Relative Gamma-ray Intensity	A_2	A_4	$I_i \rightarrow I_f$	Assigned Multi-polarity
390.0[1]	1.5(5)			$4^+ \rightarrow 2^+$	$E2$
393.8	7.0(1)	0.232(27)	−0.086(31)	$11^- \rightarrow 9^-$	$E2$
417.8	4.6(1)	0.254(31)	0.156(30)	$11^- \rightarrow 9^-$	$E2$
424.[1]	1.5(2)			$7^+ \rightarrow 6^+$	$\Delta I = 1$
432.3	91.7(4)	0.325(8)	−0.079(8)	$8^+ \rightarrow 6^+$	$E2$
441.2	5.4(2)	−0.369(74)	−0.147(79)	$5^- \rightarrow 4^+$	$E1$
456.8[1]	4.8(3)			$12^- \rightarrow 10^-$	$E2$
457.6[1]	5.3(1)			$13^- \rightarrow 11^-$	$E2$
469.5	4.3(1)	0.381(59)	−0.11(63)	$12^- \rightarrow 10^-$	$E2$
461.9	16.3(2)	0.387(17)	−0.081(19)	$17^- \rightarrow 15^-$	$E2$
470.7	3.1(2)	0.395(92)	−0.250(122)	$13^- \rightarrow 11^-$	$E2$
476.2	82.1(3)	0.335(6)	−0.092(7)	$10^+ \rightarrow 8^+$	$E2$
487.6	1.2(1)			$6^- \rightarrow 6^+$	$E1$
488.	1.0(1)			$13^- \rightarrow 11^-$	$E2$
492.5	5.6(1)	0.349(34)	−0.070(34)	$13^- \rightarrow 11^-$	$E2$
497.6	79.0(4)	0.310(9)	−0.064(10)	$12^+ \rightarrow 10^+$	$E2$
502.[1]	1.0(5)			$13^- \rightarrow 11^-$	$E2$
516.3[2]	3.0(3)			$15^- \rightarrow 13^-$	$E2$
522.3	69.3(3)	0.331(6)	−0.087(7)	$14^+ \rightarrow 12^+$	$E2$
523.[3]				$14^- \rightarrow 12^-$	$E2$
523.8[3]				$14^- \rightarrow 12^-$	$E2$
529.4	1.6(2)			$15^- \rightarrow 13^-$	$E2$
536.7	21.0(1)	0.265(10)	−0.075(12)	$19^- \rightarrow 17^-$	$E2$
548.0[1]	5.7(4)			$15^- \rightarrow 13^-$	$E2$
554.[3]				$16^- \rightarrow 14^-$	$E2$
555.3	50.4(3)	0.342(10)	−0.077(10)	$16^+ \rightarrow 14^+$	$E2$
564.2	5.0(2)	0.369(72)	−0.102(72)	$17^- \rightarrow 15^-$	$E2$
566.1[1]	3.1(3)			$16^- \rightarrow 14^-$	$E2$
569.8[1]	4.7(2)			$19^- \rightarrow 18^+$	$E1$
575.[4]				$18^- \rightarrow 16^-$	$E2$
575.0[4]	18.8(2)	0.298(18)	−0.089(19)	$21^- \rightarrow 19^-$	$E2$
575.7[4]				$(18^-) \rightarrow (16^-)$	$E2$
577.6[1]	4.1(3)			$17^- \rightarrow 15^-$	$E2$
586.8	34.4(2)	0.308(11)	−0.073(11)	$18^+ \rightarrow 16^+$	$E2$
589.0[3]				$18^- \rightarrow 16^-$	$E2$

Table 4.3: Continued.

Energy (keV)	Relative Gamma-ray Intensity	A_2	A_4	$I_i \rightarrow I_f$	Assigned Multi-polarity
601.3	14.3(2)	0.285(25)	−0.073(25)	$23^- \rightarrow 21^-$	$E2$
603.4[1]	1.7(4)			$19^- \rightarrow 17^-$	$E2$
613.5				$8^- \rightarrow 8^+$	$E1$
613.6[1]	3.6(3)			$19^- \rightarrow 17^-$	$E2$
620.1[1]	7.2(3)			$17^- \rightarrow 16^+$	$E2$
624.6	22.2(1)	0.313(13)	−0.074(12)	$20^+ \rightarrow 18^+$	$E2$
625.1[1]	1.6(3)			$20^- \rightarrow 18^-$	$E2$
643.7[3]				$(20^-) \rightarrow (18^-)$	$E2$
644.4	9.9(1)	0.168(25)	0.108(188)	$25^- \rightarrow 23^-$	$E2$
653.8[1]	1.2(2)			$21^- \rightarrow 19^-$	$E2$
673.7	11.2(1)	0.233(19)	−0.083(19)	$22^+ \rightarrow 20^+$	$E2$
682.8	1.2(1)	0.371(211)	−0.188(198)	$21^- \rightarrow 19^-$	$E2$
686.7[1]	1.2(2)			$22^- \rightarrow 20^-$	$E2$
695.1[3]				$(22^-) \rightarrow (20^-)$	$E2$
703.5	2.1(1)	0.217(113)	−0.145(108)	$27^- \rightarrow 25^-$	$E2$
713.4	8.5(1)	−0.253(27)	0.024(27)	$15^- \rightarrow 14^+$	$E1$
720.6	0.8(1)			$23^- \rightarrow 21^-$	$E2$
730.0	3.1(1)	0.164(60)	−0.039(62)	$24^+ \rightarrow 22^+$	$E2$
770.5[3]				$29^- \rightarrow 27^-$	$E2$
788.9[2]	1.1(2)			$26^+ \rightarrow 24^+$	$E2$
798.9	1.4(1)	0.396(175)	−0.055(156)	$4^+ \rightarrow 4^+$	$M1(E2)$
843.7[3]				$2^+ \rightarrow 0^+$	$E2$
849.4[3]				$28^+ \rightarrow 26^+$	$E2$
870.5	1.4(1)	0.246(148)	0.320(139)	$6^+ \rightarrow 4^+$	$E2$
877.1	2.3(1)	−0.077(101)	0.126(99)	$13^- \rightarrow 12^+$	$E1$
890.[3]				$13^- \rightarrow 12^+$	$E1$
1071.6	2.0(1)	0.265(101)	−0.079(95)	$4^+ \rightarrow 2^+$	$E2$
1240.0[2]	5.5(7)			$5^- \rightarrow 4^+$	$E1$

[1]Intensity is extracted from the total projection.
[2]Intensity is extracted from the gated spectra.
[3] Unable to extract information on transition.
[4]The angular distribution and intensity of the 575.0 keV transition is really the summed contribution of the 575., 575.0 and 575.8 keV transition.

4.2.2 Spin Orientation on ^{184}Pt

For the ^{184}Pt experiment in the 8π Spectrometer, angular distributions were measured with respect to the direction of the nuclear-spin axis. The nuclear-spin axis is determined for each nuclear event from the analysis of the BGO hit pattern[1] of an $E2$ cascade. Because of the cylindrical symmetry of the γ radiation with respect to the beam axis, the angular distributions are dependent on only the angle θ between the detected γ ray and the nuclear spin axis. Since each stretched $E2$ is spatially distributed according to the probability,

$$w(\theta) = 1 - \cos^4\theta, \tag{4.14}$$

the hit-pattern should lie predominantly in a plane perpendicular to the spin direction.

If one assumes that the angular momentum vector of the nucleus lies in the plane perpendicular to the beam axis, the problem for determining the spin direction is reduced to one of two-dimensions. A tensor is defined whose eigenvectors represent directions of γ-ray flux (see Ward *et al.*, 1984):

$$\begin{vmatrix} \sum y^2 & \sum yz \\ \sum zy & \sum z^2 \end{vmatrix}, \tag{4.15}$$

where z_i and y_i are the coordinates of each hit detector projected on the plane perpendicular to the beam axis. The shortest eigenvector of the tensor defines the direction of the nuclear spin. This last fact follows directly from Eq. 4.14, since the spin direction ideally should have no γ-ray flux for a stretched $E2$ cascade.

To measure angular distributions with respect to the nuclear spin direction in the 8π Spectrometer, this work took the following strategy. A scan was performed in which the spin direction, using the above prescriptions, was calculated on an event-by-event basis if the BGO $E2$ multiplicity, L, was greater than

[1]The BGO hit pattern is defined for each event by the BGO detectors which measure γ rays that have energies most associated with stretched $E2$ transitions.

Table 4.4: The relationship between ϕ and θ for the $\pm 79°$ rings and $\pm 37°$ rings. The value of ϕ represents the angular centroid in $\Delta\phi$ for each histogrammed spectrum.

ϕ	4.5	13.5	22.5	31.5	40.5	49.5	58.5	67.5	76.5	85.5
θ ($\pm 79°$ rings)	11.7	17.2	24.8	33.1	41.7	50.4	59.1	67.9	76.7	85.6
θ ($\pm 37°$ rings)	53.1	54.2	56.2	59.1	62.8	67.0	71.8	76.7	81.9	87.3

three. An angle ϕ measured in the yz-plane was then determined for each Ge detector on either the 79° or 101° ring which fired during the event, where ϕ is defined as the angle between the calculated spin direction and the projection of the detector of interest onto the yz-plane. The measured γ-ray energy is then histogrammed into one of ten spectra depending on its value of ϕ. Since the $\Delta\phi$ intervals for each spectrum are equivalent, this insures an equal statistical distribution of all ten detectors into each spectrum. Thus, any efficiency correction of these spectra is not necessary for calculating angular distributions. This is very advantageous in light of the problems described in subsection 4.2.1 when measuring angular distributions with multi-detector arrays.

Since the angular distributions are calculated with respect to the angle, θ, between the spin axis and the detector, θ must be determined. A simple geometric relationship exists between θ and ϕ,

$$\theta = \arctan\left[\frac{(\cos^2\alpha\sin^2\phi + \sin^2\alpha)^{1/2}}{\cos\alpha\cos\phi}\right], \tag{4.16}$$

where α is the angle between the yz-plane and the ring of Ge detectors. Table 4.4 lists the relationship between the ϕ and θ for both the $\pm 79°$ and $\pm 37°$ Ge rings. This table illustrates the reason for using the 79° rings over the 37° rings; the angular range in θ is much larger.

The angular distribution coefficients for a γ-ray transition were calculated by fitting the peak intensities from each of the ten binned spectra to the standard

angular distribution function. Since it is not necessary to renormalize the peak areas, this calculation is straight forward. Table 4.5 shows the calculated A_2 and A_4 coefficients for the γ-ray transitions in ^{184}Pt. The intensities of the peaks were determined from the a_0 coefficients normalized by the efficiency. All intensities are expressed relative to the $4^+ \rightarrow 2^+$ yrast transition. When multiplets prevented the determination of the intensity of certain transitions, gated spectra were used, comparing the intensities of the peaks of interest with one whose intensity relative to the $4^+ \rightarrow 2^+$ transition has already been determined.

Since the use of spin orientation data to determine the angular distributions of individual γ-ray transitions using Ge spectra is a recent experimental innovation, it is not clear how one should handle the effects of the uncertainty in the spin direction on the measured angular distribution coefficients. The accuracy in the determination of the nuclear spin direction must be dependent on how many stretched $E2$ transitions are used to define this axis. This uncertainty should behave similarly to the statistical de-alignment, which is represented by the population parameter, $P(m)$. For this work, a form of $P(m)$ is proposed which represents the population parameter for the case when the spin and quantization axes are parallel:

$$P_J(m) = \frac{\exp\left(-\frac{(j-|m|)^2}{2\sigma^2}\right)}{\sum_{m'=-J}^{J} \exp\left(-\frac{(J-|m'|)^2}{2\sigma^2}\right)}. \tag{4.17}$$

Fig. 4.5a shows a plot of the A_2 and A_4 coefficients for stretched dipole and quadrupole transitions as a function of the parameter σ/J. Fig. 4.5b shows a plot of the experimental A_2 and A_4 parameters for the yrast transitions as a function of spin. The A_2 coefficients clearly become more negative as a function of spin while the A_4 parameters cluster around 0. From part (a) of this figure, the measured $A_2 = -0.236$ for $I = 24$ corresponds to a $\sigma/J \approx 0.39$. Fig. 4.5a shows that the A_4 loses sensitivity quickly, reaching a roughly constant value of $+0.10$

Table 4.5: Summary of spin orientation analyisis for ^{184}Pt.

Energy (keV)	Relative Gamma-ray Intensity	A_2	A_4	$I_i \rightarrow I_f$	Assigned Multi-polarity
118.1	1.6(0)	0.113(44)	−0.068(53)	$6^- \rightarrow 5^-$	$M1(E2)$
121.0	1.3(0)	0.174(47)	−0.074(56)	$7^- \rightarrow 6^-$	$M1(E2)$
154.6	1.5(1)	0.244(93)	−0.084(126)	$9^- \rightarrow 8^-$	$M1(E2)$
160.0[2]	1.8(2)			$8^- \rightarrow 7^-$	$M1(E2)$
162.8	58.7(2)	−0.006(6)	0.015(8)	$2^+ \rightarrow 0^+$	$E2$
172.9	0.9(0)	0.231(64)	−0.178(87)	$11^- \rightarrow 10^-$	$M1(E2)$
177.7	5.4(0)	0.194(13)	0.034(18)	$9^- \rightarrow 8^-$	$M1(E2)$
198.7	5.3(0)	0.197(14)	0.026(18)	$10^- \rightarrow 9^-$	$M1(E2)$
218.8[2]	2.6(2)			$11^- \rightarrow 10^-$	$M1(E2)$
221.0				$10^- \rightarrow 9^-$	$M1(E2)$
238.0	3.6(1)	0.229(29)	−0.014(37)	$12^- \rightarrow 13^-$	$M1(E2)$
239.5	1.3(1)	−0.138(77)	−0.005(99)	$7^- \rightarrow 5^-$	$E2$
254.5[2]	2.4(2)			$13^- \rightarrow 12^-$	$M1(E2)$
269.3	2.8(1)	0.197(58)	0.019(71)	$14^- \rightarrow 13^-$	$M1(E2)$
272.8	100.0(2)	−0.044(4)	0.000(5)	$4^+ \rightarrow 2^+$	$E2$
278.6	1.3(3)			$15^- \rightarrow 14^-$	$M1(E2)$
281.1	3.1(1)	−0.040(63)	0.011(77)	$8^- \rightarrow 6^-$	$E2$
286.7				$12^- \rightarrow 11^-$	$M1(E2)$
287.4				$16^- \rightarrow 15^-$	$M1(E2)$
290.2	2.4(1)	0.311(44)	−0.032(59)	$17^- \rightarrow 16^-$	$M1(E2)$
298.8				$18^- \rightarrow 17^-$	$M1(E2)$
303.4	3.2(1)	−0.223(40)	−0.029(49)	$(18^-) \rightarrow 18^+$	(E1)
304.6	2.2(1)	0.257(57)	0.030(70)	$19^- \rightarrow 18^-$	$M1(E2)$
314.5				$(16^-) \rightarrow 16^+$	(E1)
314.7				$9^- \rightarrow 7^-$	$E2$
320.5	1.2(1)	0.278(110)	0.099(137)	$20^- \rightarrow 19^-$	$M1(E2)$
322.7	1.7(1)	−0.352(86)	0.024(106)	$(20^-) \rightarrow 20^-$	(E1)
333.3	1.8(1)	0.239(78)	−0.121(104)	$21^- \rightarrow 20^-$	$M1(E2)$
344.3				$(22^-) \rightarrow 22^-$	(E1)
345.3				$15^- \rightarrow 13^-$	$E2$
353.4	1.2(1)	0.251(139)	−0.154(183)	$22^- \rightarrow 21^-$	$M1(E2)$
355.1				$13^- \rightarrow 14^+$	$E1$
358.6	7.6(1)	−0.141(24)	−0.019(31)	$15^- \rightarrow 13^-$	$E2$
362.4	93.4(2)	−0.086(4)	−0.005(5)	$6^+ \rightarrow 4^+$	$E2$
367.2	1.0(1)	0.189(153)	−0.290(203)	$23^- \rightarrow 22^-$	$M1(E2)$
375.7				$10^- \rightarrow 8^-$	$E2$
376.4				$10^- \rightarrow 8^-$	$E2$
388.4				$11^- \rightarrow 12^+$	$E1$

Table 4.5: Continued.

Energy (keV)	Relative Gamma-ray Intensity	A_2	A_4	$I_i \rightarrow I_f$	Assigned Multi-polarity
390.0				$4^+ \rightarrow 2^+$	$E2$
393.8	7.7(1)	−0.062(19)	0.010(25)	$11^- \rightarrow 9^-$	$E2$
417.8	2.8(1)	−0.173(55)	0.132(82)	$11^- \rightarrow 9^-$	$E2$
424.				$7^+ \rightarrow 6^+$	$\Delta I = 1$
432.3	91.0(2)	−0.109(3)	−0.010(5)	$8^+ \rightarrow 6^+$	$E2$
441.2	5.8(1)	0.146(37)	−0.086(52)	$5^- \rightarrow 4^+$	$E1$
447.1				$23^- \rightarrow 22^+$	$E1$
456.8				$12^- \rightarrow 10^-$	$E2$
457.6				$13^- \rightarrow 11^-$	$E2$
459.5[1]	3.5(1)			$12^- \rightarrow 10^-$	$E2$
461.9	18.8(1)	−0.137(10)	−0.009(13)	$17^- \rightarrow 15^-$	$E2$
470.7	2.5(1)	−0.169(114)	0.134(145)	$13^- \rightarrow 11^-$	$E2$
476.2	83.2(2)	−0.131(6)	−0.016(7)	$10^+ \rightarrow 8^+$	$E2$
487.6				$6^- \rightarrow 6^+$	$E1$
488.				$13^- \rightarrow 11^-$	$E2$
492.5	4.4(1)	−0.155(50)	−0.031(66)	$13^- \rightarrow 11^-$	$E2$
497.6	80.5(2)	−0.143(5)	−0.007(6)	$12^+ \rightarrow 10^+$	$E2$
502.				$13^- \rightarrow 11^-$	$E2$
511.6				$(16^-) \rightarrow (14^-)$	$E2$
516.3	3.1(1)	−0.253(60)	0.053(77)	$15^- \rightarrow 13^-$	$E2$
522.3	77.6(2)	−0.146(4)	−0.017(5)	$14^+ \rightarrow 12^+$	$E2$
523.				$14^- \rightarrow 12^-$	$E2$
523.8				$14^- \rightarrow 12^-$	$E2$
529.4	1.1(1)	−0.260(175)	−0.132(227)	$15^- \rightarrow 13^-$	$E2$
536.7	21.6(2)	−0.135(12)	−0.002(16)	$19^- \rightarrow 17^-$	$E2$
548.0	6.0(1)	−0.209(39)	−0.001(49)	$15^- \rightarrow 13^-$	$E2$
554.				$16^- \rightarrow 14^-$	$E2$
555.3	54.1(1)	−0.164(5)	−0.005(7)	$16^+ \rightarrow 14^+$	$E2$
564.2	5.8(1)	−0.163(31)	−0.096(43)	$17^- \rightarrow 15^-$	$E2$
566.1				$16^- \rightarrow 14^-$	$E2$
569.8	4.0(1)	0.208(53)	−0.052(68)	$19^- \rightarrow 18^+$	$E1$
575.7				$18^- \rightarrow 16^-$	$E2$
575.0				$21^- \rightarrow 19^-$	$E2$
576.				$(18^-) \rightarrow (16^-)$	$E2$
577.6	5.4(1)	−0.148(41)	0.024(53)	$17^- \rightarrow 15^-$	$E2$
586.8	38.3(1)	−0.166(86)	−0.021(9)	$18^+ \rightarrow 16^+$	$E2$
589.0				$18^- \rightarrow 16^-$	$E2$
601.3	16.6(1)	−0.165(30)	−0.026(37)	$23^- \rightarrow 21^-$	$E2$

Table 4.5: Continued.

Energy (keV)	Relative Gamma-ray Intensity	A_2	A_4	$I_i \rightarrow I_f$	Assigned Multi-polarity
603.4				$19^- \rightarrow 17^-$	$E2$
613.5[3]				$8^- \rightarrow 8^+$	$E1$
613.6	2.0(1)	−0.309(119)	−0.022(153)	$19^- \rightarrow 17^-$	$E2$
620.1				$17^- \rightarrow 16^+$	$E1$
624.6	27.1(1)	−0.196(10)	−0.027(13)	$20^- \rightarrow 18^-$	$E2$
625.1				$20^- \rightarrow 18^-$	$E2$
643.7				$(20^-) \rightarrow (20^-)$	$E2$
644.4				$25^- \rightarrow 23^-$	$E2$
653.8	0.9(1)			$21^- \rightarrow 19^-$	$E2$
673.7	17.5(1)	−0.211(14)	−0.011(12)	$22^+ \rightarrow 20^+$	$E2$
682.8				$21^- \rightarrow 19^-$	$E2$
686.7	2.3(1)			$22^- \rightarrow 20^-$	$E2$
695.1				$(22^-) \rightarrow (20^-)$	$E2$
703.5				$27^- \rightarrow 25^-$	$E2$
713.4	13.3(1)	0.117(18)	−0.009(22)	$15^- \rightarrow 14^+$	$E1$
720.6	0.9(1)	0.257(225)	−0.152(276)	$23^- \rightarrow 21^-$	$E2$
730.0	7.6(1)	−0.236(26)	0.011(32)	$24^+ \rightarrow 22^+$	$E2$
737.4[1]	1.3(1)			$(24^-) \rightarrow (22^-)$	$E2$
743.3[1]	0.6(1)			$23^- \rightarrow 21^-$	$E2$
756.				$24^- \rightarrow 22^-$	$E2$
770.5	6.7(1)	−0.126(34)	−0.048(42)	$29^- \rightarrow 27^-$	$E2$
782.[1]	0.5(2)			$25^- \rightarrow 23^-$	$E2$
786.7	1.0(1)			$(26^-) \rightarrow (24^-)$	$E2$
788.9	6.3(1)	−0.242(42)	0.087(53)	$26^+ \rightarrow 24^+$	$E2$
794.	1.0(1)	−0.206(231)	0.219(298)	$25^- \rightarrow 23^-$	$E2$
797.5	2.8(1)	−0.165(77)	−0.011(99)	$4^+ \rightarrow 4^+$	$M1(E2)$
843.7				$2^+ \rightarrow 0^+$	$E2$
849.4				$28^+ \rightarrow 26^+$	$E2$
870.5				$6^+ \rightarrow 4^+$	$E2$
877.1				$13^- \rightarrow 12^+$	$E1$
890.				$13^- \rightarrow 12^+$	$E1$
908.1	3.7(1)	0.014(60)	−0.071(075)	$30^+ \rightarrow 28^+$	$E2$
920.4	1.7(1)	−0.257(129)	−0.134(160)	$33^- \rightarrow 31^-$	$E2$
967.0				$32^+ \rightarrow 30^+$	$E2$
998.0				$35^+ \rightarrow 33^+$	$E2$
1056.0				$33^+ \rightarrow 31^+$	$E2$
1071.6	1.4(1)	0.004(173)	0.204(211)	$4^+ \rightarrow 2^+$	$E2$
1240.0	3.4(1)	−0.054(58)	0.046(75)	$5^- \rightarrow 4^+$	$E2$

at $\sigma/J \approx 0.35$. Since, the measured A_2 coefficients correspond to σ/J values of 0.39 or greater, the small values obtained for the A_4 coefficients for all transitions are quite reasonable and expected.

It is disappointing to find that the measured A_2 values obtained from our data are only 35%, at best, of the fully aligned value. The extracted σ/J parameters vary significantly with spin, and below $I = 16$, are twice as large as the nearly constant value of 0.25 extracted from angular distribution data measured with respect to the beam axis. If the population parameter, $P(m)$, were only dependent on the de-alignment, then both methods should give similar results for σ/J. Obviously, statistical deviations in the accuracy at which the spin axis is determined influences the value of σ/J. These deviations should be a function of the number of stretched transitions, L, used to determine the spin orientation. A threshold of $L = 4$ was used for these data, and it would be interesting to see the effect on the sensitivity of the angular distribution coefficients as the threshold is increased. Other mechanism may effect the sensitivity as well, and hopefully, future investigations will uncover what these mechanism are and how they influence the expression for $P(m)$ given in Eq. 4.17.

Even though values for A_2 and A_4 are much smaller than the fully aligned value, the data show that one should have no problem in distinguishing stretched dipole transitions from stretched quadrupole transitions. Another quantity which one wishes to extract from the angular distribution data is the mixing ratio, δ, which is defined in Eq. 4.8. In angular distribution measurements with respect to the beam axis, δ is usually determined from both the A_2 and A_4 coefficients for a $\Delta I = 1$ mixed ($M1$-$E2$) transition, due to the fact that the A_2 coefficient is multi-valued as a function of δ. Fig. 4.6 shows a plot of both the A_2 and A_4 parameters of the $14 \rightarrow 13$ transition as a function of the $\arctan(\delta)$ for different values of σ/J. An $\arctan(\delta) = 0°$ corresponds to a stretched dipole transition

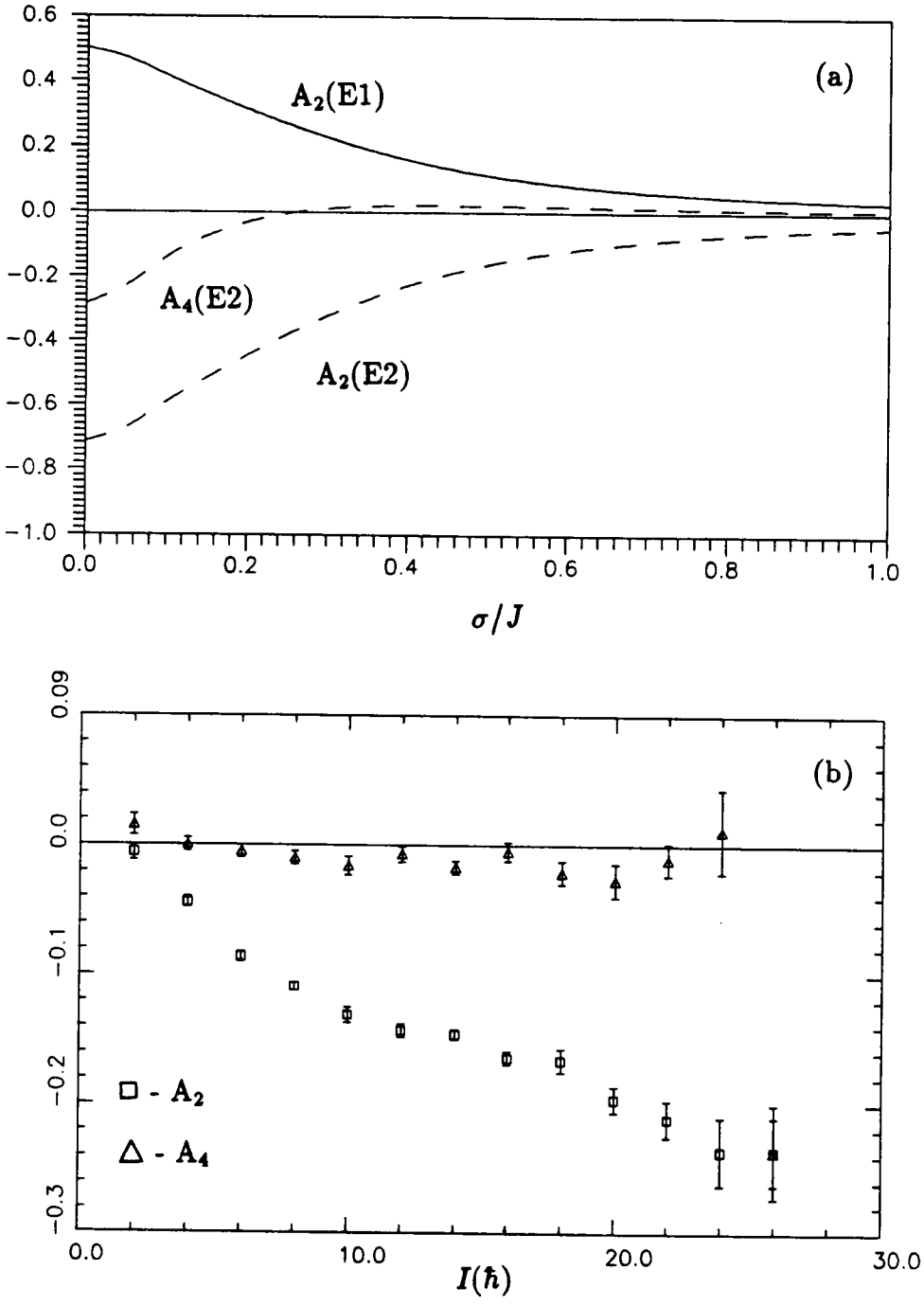

Figure 4.5: (a) Calculated A_2 and A_4 coefficients for stretched dipole and quadrupole transitions as a function of σ/J. (b) Experimental values of A_2 and A_4 coefficients for selected stretched transitions plotted as a function of I in the yrast band of ^{184}Pt.

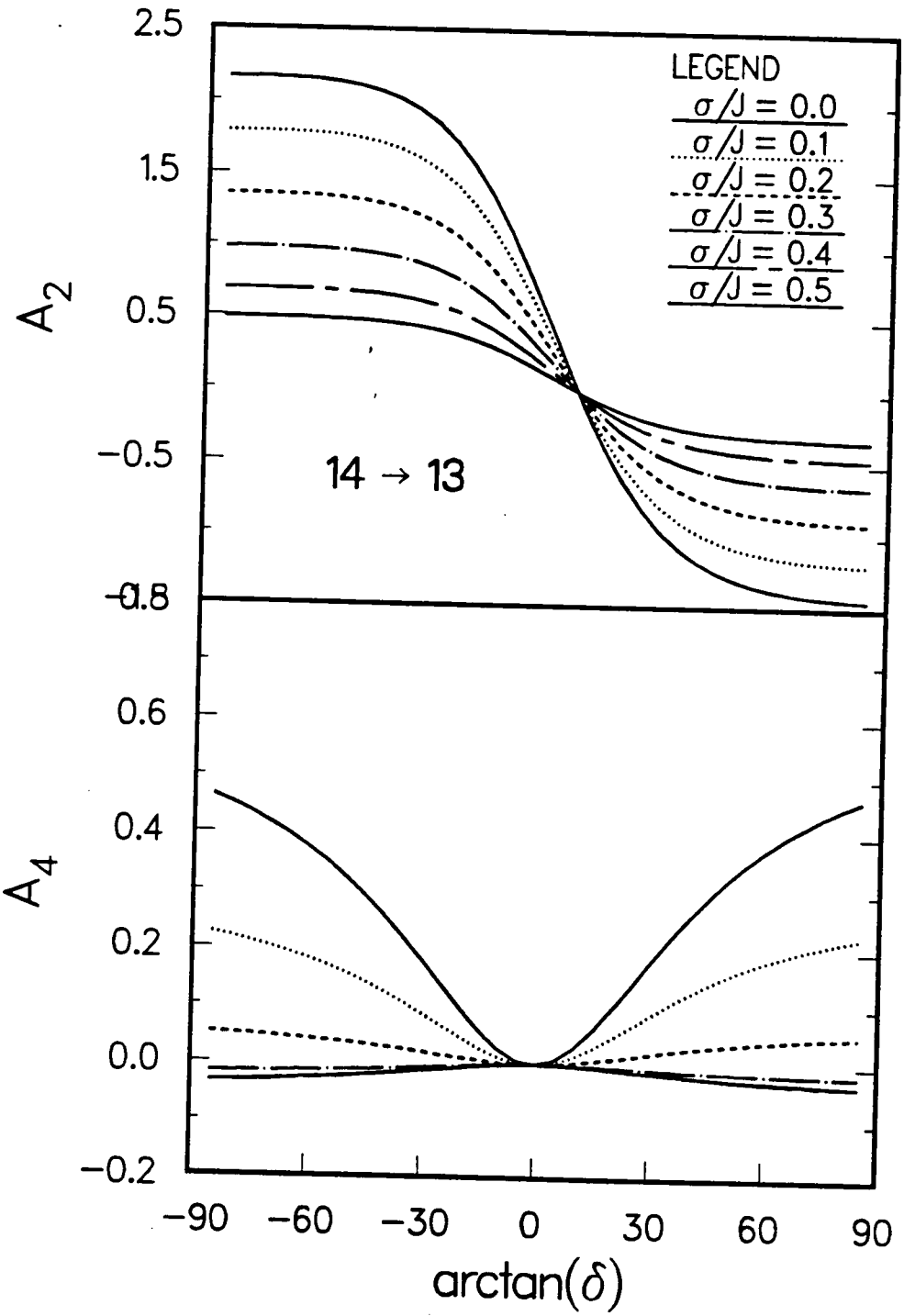

Figure 4.6: The angular distribution coefficients, A_2 and A_4, for the $14 \rightarrow 13$ transition plotted as a function of arctan(δ) for different values of σ/J.

while an $\arctan(\delta) = \pm 90°$ describes pure quadrupole radiation. It is clear from this figure that there is virtually no sensitivity in the A_4 coefficient as a function of the mixing ratio for the values of σ/J associated with our data, *i.e.* $\sigma/J \geq 0.38$. On the other hand, the A_2 coefficient does retain a detectable amount of sensitivity when comparing large mixing to small mixing; however, these values saturate at $\arctan(\delta) \approx \pm 35°$ ($\delta = 0.7$). Therefore, one should be able to extract a δ from the A_2 coefficient of spin orientation data if the amount of $E2$ component is not very large. To determine the mixing ratio in the presence of a large quadrupole contribution, one must use the A_4 component, but for the data under discussion, the effective de-alignment is too large to allow any sensitivity in the A_4 coefficient.

4.2.3 Yrast Band

As reported above, the yrast band in ^{184}Pt has been identified up to $I = 32^+$. The Oak Ridge measurement had established the level scheme up to 26^+, but poor statistics prevented any further additions to this band. The McMaster data confirmed the previous assignments; however, the superior statistics over the Oak Ridge data allowed for the tentative assignment of the 849.4 keV ($28^+ \rightarrow 26^+$) transition to the level scheme. The Chalk River measurement confirmed this assignment and in addition yielded two more transitions to the top of the band. Fig. 4.7 shows a sum of five gates lying high in the band (673.7 through 908.1) taken from the Chalk River data. These gates were chosen, because they allow for a clean spectrum showing only the yrast transitions. The γ rays up to the 908.1 keV ($30^+ \rightarrow 28^+$) transition are clearly seen in this figure. The identification of the 32^+ level in this decay scheme is confirmed by gating on the 967 keV transition and weakly observing the other γ ray transitions associated with the yrast band. From Fig. 4.7, it appears that the 908.1 keV transition has a wider peak width than the other transitions. One explanation for this width could be the presence of

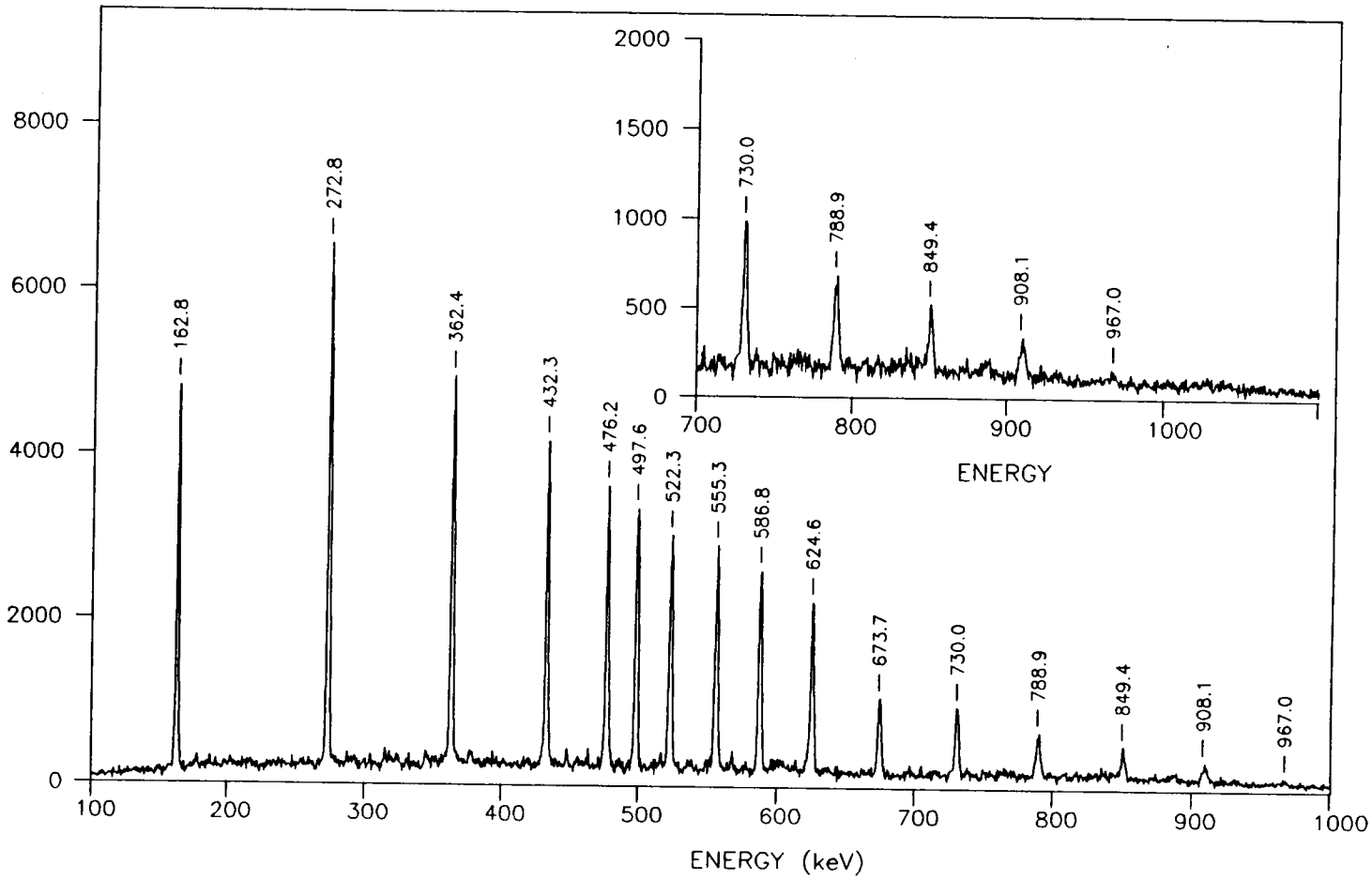

Figure 4.7: Sum of gates on the 673.7, 730.0, 788.9, 849.4 and 908.1 transitions in the yrast band of ^{184}Pt.

another γ ray in this band with almost the same energy as the 908.1 keV transition. However, a gate on this transition does not confirm this. The likely explanation is that this level decays very quickly while the recoils are still in the target. This leads to a slight Doppler broadening of the peak. This would also explain why the 967.0 keV transition is not seen more clearly in the figure, because the intensity of the peak is spread out over a wider energy. range than the 908.1 keV transition.

4.2.4 Band 2

The lowest level identified in band 2 is the 11^- state at 2592.5 keV, and this band is established tentatively up to $I = 37^-$ at 11551 keV. Both the Oak Ridge and McMaster data were able to identify this band up to the 770.5 keV transition. The final four transitions were placed by the Chalk River data. Fig. 4.8 shows a sum of four gates on transitions 770.5 keV through 998 keV, all of which lie near the top of this band. From the figure, the yrast band is clearly seen up to $I = 24^+$, indicating that there is continual side feeding from band 2 to the yrast line. However, discrete peaks can only be identified up to the 447.7 keV ($23^- \rightarrow 22^+$) crossing transition. While the presence of crossing transitions between the two bands at higher spins is suggested by the summed gates, the intensities of these inter-band transitions are too low to identify them in the gated spectra and are not included in the level scheme. Both angular distribution and spin orientation data strongly suggest that the multipolarity of these inter-band transitions is purely dipole, leading to the assignment of odd spins to this band (see Tables 4.3 and 4.5). The parity of the band is established by the electric quadrupole transitions between bands 2 and 5, due to the fact that parity in band 5 had been previously established by Burde *et al.* (1966) based on a conversion electron measurement. Most of the decay out of band 2 occurs at the 3439.8 keV (15^-) level via the 713.4 keV transition to the 2726.4 keV (14^+) level in the yrast

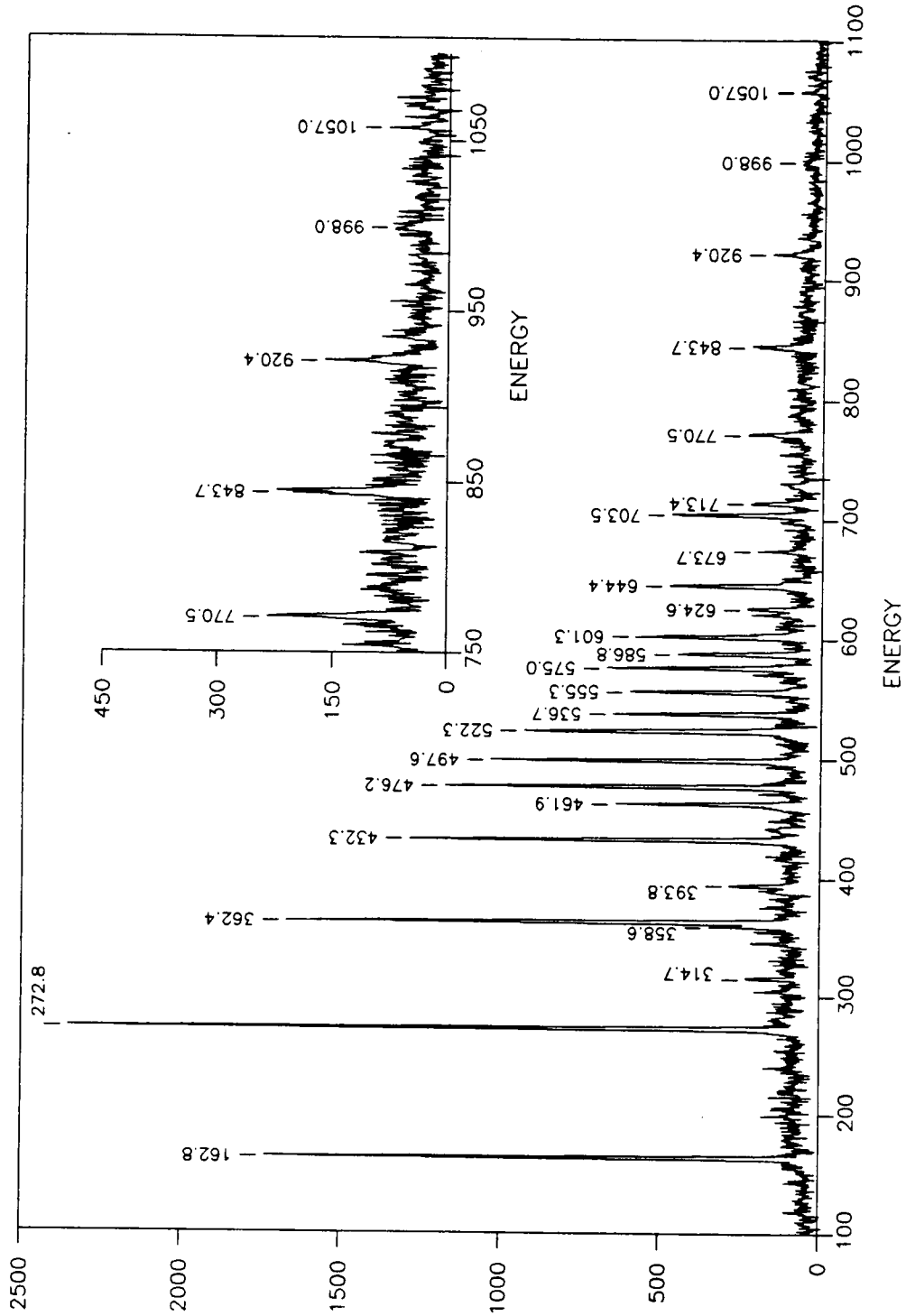

Figure 4.8: Sum of gates on the 770.5, 843.7, 920.4 and 998 keV transitions in Band 2 of ^{184}Pt.

band or to a lesser degree by the 345.3 transition to the 3094.3 keV (13^-) level in band 5. The decay of the 3081.2 keV (13^-) level proceeds through four branches: the 355.1 keV and the 877.1 keV transitions to the 2726.4 keV (14^+) and 2204.1 keV (12^+) levels in the yrast band, the 457.6 transition to the 2623.6 keV (11^-) level in band 5, and the 488 transition to the last known level in band 2, which is the least preferred of the four decays.

4.2.5 Bands 3 and 4

Two strongly coupled rotational bands labeled 3 and 4 in Fig. 4.4 are thought to be built upon the 1843.8 keV (8^-) level. The spin, parity and lifetime of this state was first established by Burde *et al.* (1966). The 1.1 msec lifetime is much longer than the time window for defining coincidence events ($\approx$ 100 nano-sec) between the rotational sequence and the yrast band; thus, there are no coincidence data which link these two bands with any other band in ^{184}Pt. However, from the known systematics of the region and indirect experimental evidence, we strongly believe that our placement of these two bands in ^{184}Pt is correct.

Fig. 4.9 shows a sum of gates taken on the two lowest $\Delta I = 1$ crossing transitions (177.7 and 198.7 keV) which connect these two bands. The smooth regularity of both the $M1$-$E2$ sequence and the stretched $E2$ cascades shows that these two bands are "strongly" coupled together, indicating little or no $K = 1/2$ admixtures in the wave functions of these two bands. Such strongly coupled bands with high K components built on an 8^- isomeric state have been observed in the lower Z isotones of ^{184}Pt, *e.g.* ^{182}Os (Fahlander and Dracoulis, 1982). Thus, the placement of these two bands on top of the 1843.8 keV level agrees well with the systematics of the even-even $N = 106$ nuclei. It should also be noted that bands 3 and 4 have been observed in the McMaster and Chalk River data with intensities on the order of 5% relative to the yrast band. By observing the relative intensities

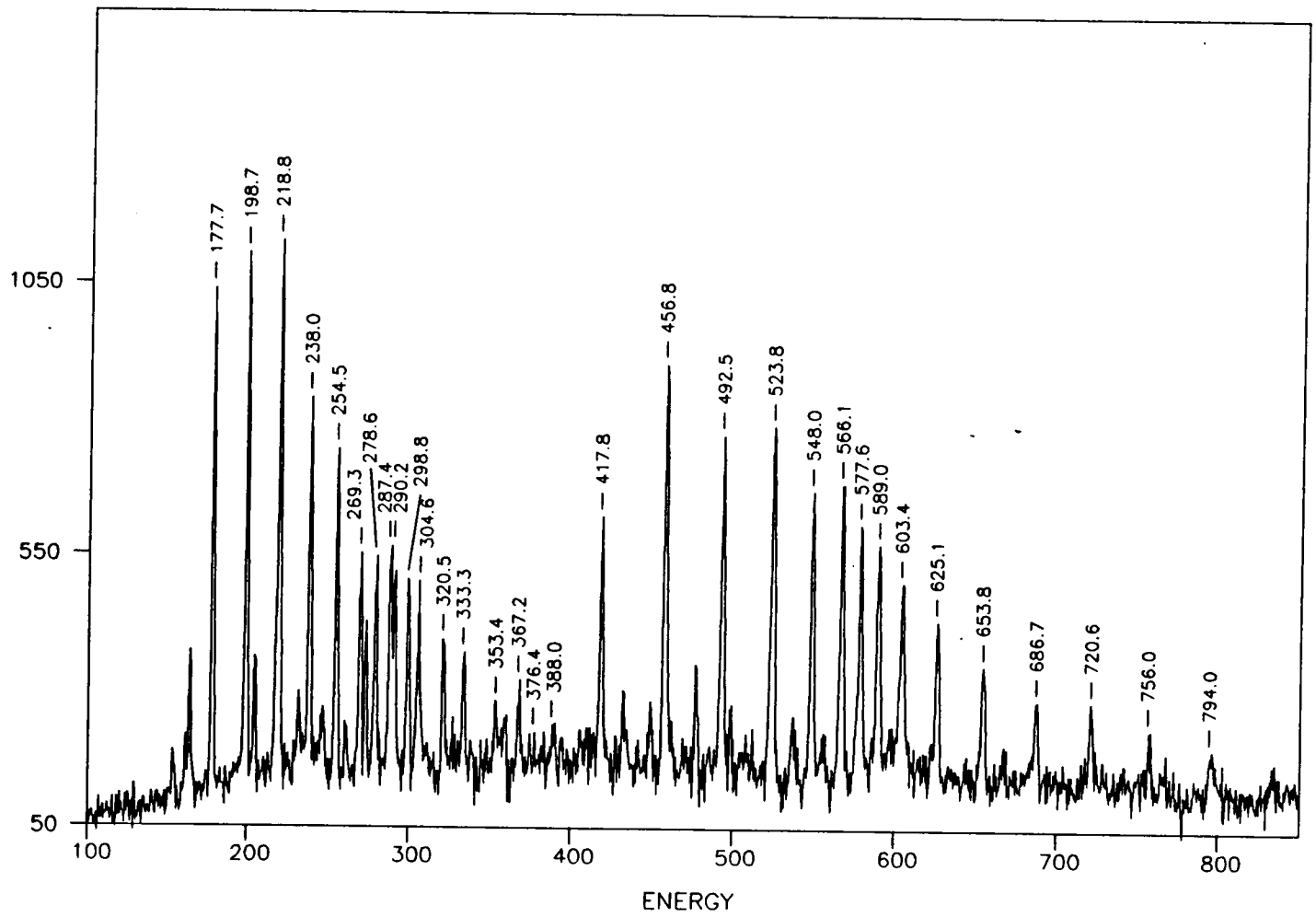

Figure 4.9: Sum of the two lowest $\Delta I = 1$ crossing transitions connecting bands 3 and 4 in ^{184}Pt (177.7 keV and 198.7 keV).

of the two major residual nuclei, ^{183}Pt and ^{184}Pt, as a function of H and K, one observes that bands 3 and 4 are most enhanced at higher total energy and fold regions. This indicates that these bands are in ^{184}Pt as opposed to ^{183}Pt. ^{185}Pt is ruled out since its decay scheme is well known from previous in-beam studies (Pilotte *et al.*, 1987), and its population in this experiment was very weak.

From the McMaster data, band 3 and 4 have been identified up to the 5667.7 keV (22^-) and 6035.2 keV (23^-) level, respectively. The whole sequence of crossing transitions up to the 320.4 keV γ ray have also been seen in this experiment. The Chalk River data has yielded one new transition to the decay scheme of each band and four other crossing transitions. The last inter-band transition observed (388 keV) is dashed, because its existence is suggested by the sum of gates and not from the gate on this transition.

4.2.6 Bands 5 and 6

As mentioned above, the spin and parity of the 1675.6 keV level in band 5 had previously been established by Burde *et al.* (1966). In this same work, the 1793.7 keV level was also observed in band 6; however, it was given the assignment 6^+ base on the conversion electron coefficient of the 118.1 keV transition. The recent measurements on ^{184}Pt have identified rotational structures built on both of these levels with $\Delta = I$ transitions connecting the lower members of the bands. Both the angular distribution and spin orientation data suggest that these transitions have little or no quadrupole admixture; thus, it is unclear from our data whether or not these crossing transitions are $E1$ or $M1$. However, even though the electron work should establish the parity of the band, there are compelling reasons to question the assignment of positive parity to the 1793.7 keV level. The presence of the $\Delta I = 1$ transitions indicate that these bands have large matrix elements between them, suggesting that they are signature partners. It should

be noted that mixing between positive and negative parity bands is observed in octupole type structures. However, the lack of observing any such structure in this region makes the identification of band 6 as an octupole band less likely. Also, structures similar to bands 5 and 6 with negative parity have been observed in ^{182}Os. These observations suggest that the parity of band 6 should be negative, and this assignment has been given to band 6 in this work.

Band 5 decays to both the oblate and prolate ground bands via the 441.2 keV and 1240.0 keV transitions, respectively. Fig. 4.10a shows a sum of spectra whose gated energies are on transitions which appear in this band. As is shown in the figure, band 2 is seen quite clearly, confirming that it does decay to band 5 as indicated in the level scheme of Fig. 4.4. The McMaster data were able to establish band 5 up to the 5471.2 keV level (21^-). Two higher transitions have been identified in the Chalk River data establishing the band up to $I = 25^-$.

At the lowest observed level (1793.7 keV), band 6 decays to band 5 and the γ band via the 118.1 keV and 487.6 keV transitions, respectively. The first three members of the band are well established by the gates and the additivity of the crossing transitions. However, the placement of the last three transitions (523, 554 and 575 keV) in band 6 is tentative, due to the apparent weak population of the corresponding levels and the presence of more intense γ rays, with the similar energies appearing elsewhere in the decay scheme. For example, a 523.8 keV transition in coincidence with a 577.6 keV transition is observed between bands 3 and 4, while both a 575.0 and 575.7 keV transition in bands 2 and 7, respectively, is in coincidence with the 555.3 and 522.3 transitions of the yrast band. Complicating the matter even further is the fact that the 575.0 keV transition in band 2 is in coincidence with a large number of observed γ rays in bands 5 and 6. Also, there are other γ rays with similar energies as those of the bottom three transitions in band 6 (281.1, 375.7 and 459.5) which appear in ^{184}Pt, ^{183}Pt and ^{185}Pt. Since

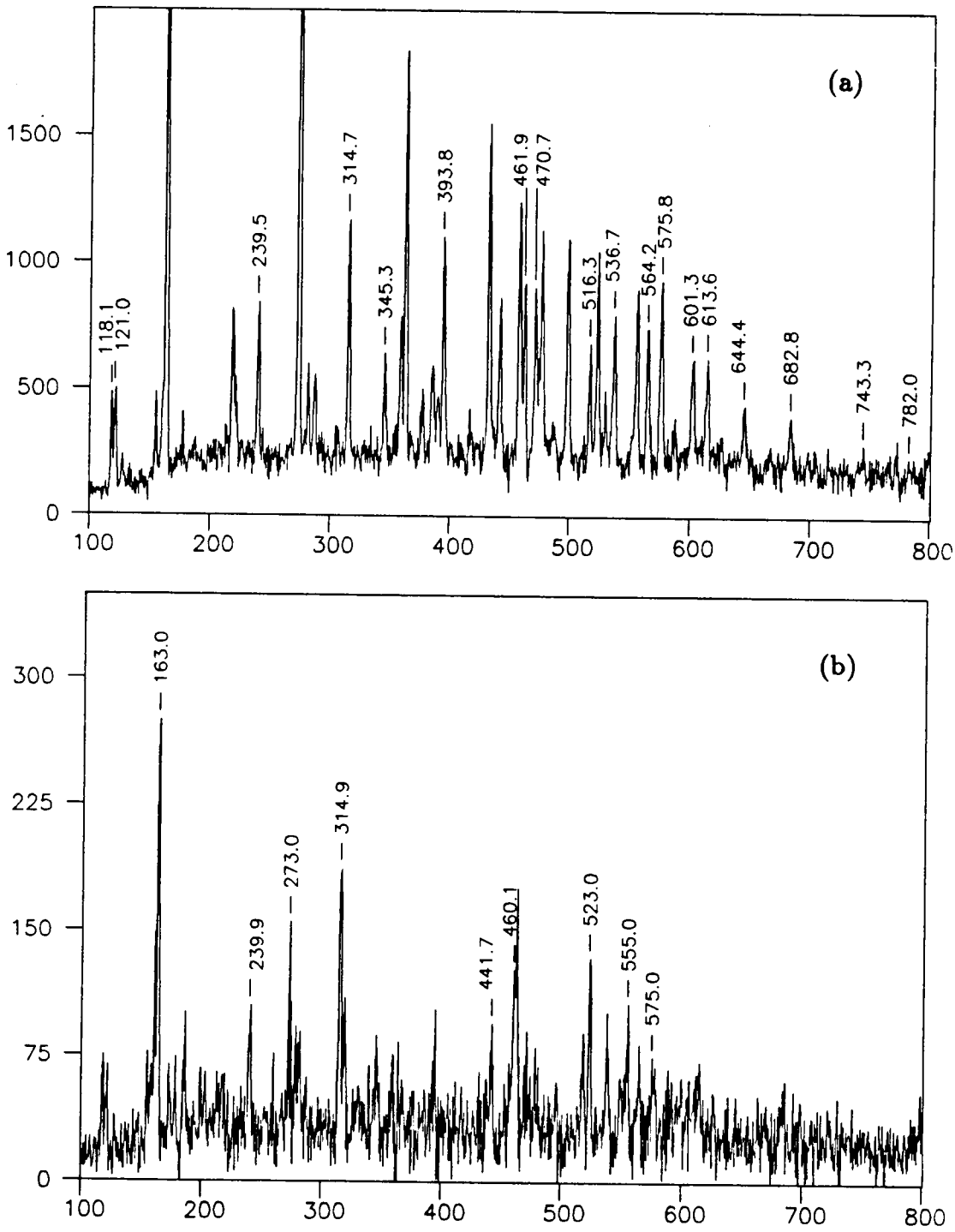

Figure 4.10: (a) Sum of gates in band 5. (b) Gate on 221.0 keV transition.

these transitions are also in coincidence with γ rays whose energies are degenerate with those at the top of the band, gates on these transitions are only suggestive and do not establish with upmost certainty the indicated level structure of band 6 to the highest spins. One piece of evidence which lends strong support to the current assignments in band 6 is the gate on the 221.0 keV transition (10^- to 9^-) shown in Fig. 4.10b. This gate clearly shows the three transitions in question. The fact that the gate does not show other members of the yrast band, which are not in coincidence with band 6, indicates that the background subtraction is reasonable. This is important, since the 554 and 523 keV transitions are also found in the yrast band, and one must be certain that their presence in a gate with poor statistics is not due to improper background subtraction. In summary, while the placement of the last three transitions in band 6 are not disputed by the gates, these coincidences appear strongly in two other places in this level scheme. Thus, while it is believed that these assignments are correct, it should be noted that the evidence supporting their placement is not irrefutable.

4.2.7 Band 7

Band 7 is observed to decay to the yrast band via the 358, 314.3, 303.4, 322.7, and 344.3 keV transitions. These transitions have been identified as $\Delta I = 0$ transitions based on the measured A_2 coefficients from both the angular distribution and spin orientation analysis. The A_2 coefficient for a $\Delta I = 0$ transition, which has a large dipole component, should be marginally larger than that for a stretched quadrupole transition of the same spin. The spin orientation data give an $A_2 = -0.233$ and -0.352 for the 303.7 and 322.6 keV interband transitions. The stretched $E2$ transitions in the yrast band which immediately follow these γ rays, 586.8 and 624.6 keV, have A_2 coefficients equal to -0.166 and -0.196. A similar relationship between these transitions is also found in the angular distribu-

tion data. This observation favors $\Delta I = 0$ assignment over stretched quadrupole. This conclusion is supported by the fact that if the spins in band 7 were to increase by 2 units over their current assignments, this band would become yrast which seems unlikely due to the fact that the present yrast band is populated much more strongly than band 7 at all observed spins. It should be noted that a $\Delta I = 1$ assignment for these transitions, with a large quadrupole admixture is also suggested by the value of the A_2 coefficients. However, in this case, the A_4 coefficients would be large. The angular distribution data show that the A_4 coefficients for these crossing transitions are small, indicating that $\Delta I = 0$ assignments are the most probable for these crossing transitions.

Fig. 4.11 shows a sum of several clean gates in this band. With the McMaster data, the 575.7, 643.7 and 695.1 keV transitions in this band were placed, while the Chalk River data added two more transitions on top of the 5510.5 keV level. These data were used also able to identify the lowest level of this band at 3084.4 keV. This level was identified due to the fact that the H-K gating of the 8π Spectrometer was able to eliminate nearly all events associated with electron-positron annihilations. This was not possible in the McMaster data, because a gate taken on the 511.6 keV transition, yielded random coincidences between the annihilation peak and yrast transitions; thus overshadowing the 511.6 transition in band 7.

4.2.8 Band 8

One other rotational band has been identified in ^{184}Pt, however its connection to the yrast band has not been established. Fig. 4.12 shows a gate on the 528 keV transition, and the the level structure of this band, and the inset to the figure indicated the proposed decay sequence of the band. It is clear that band 8 must feed into the yrast band around $I = 12\ \hbar$ due to the absence of any yrast

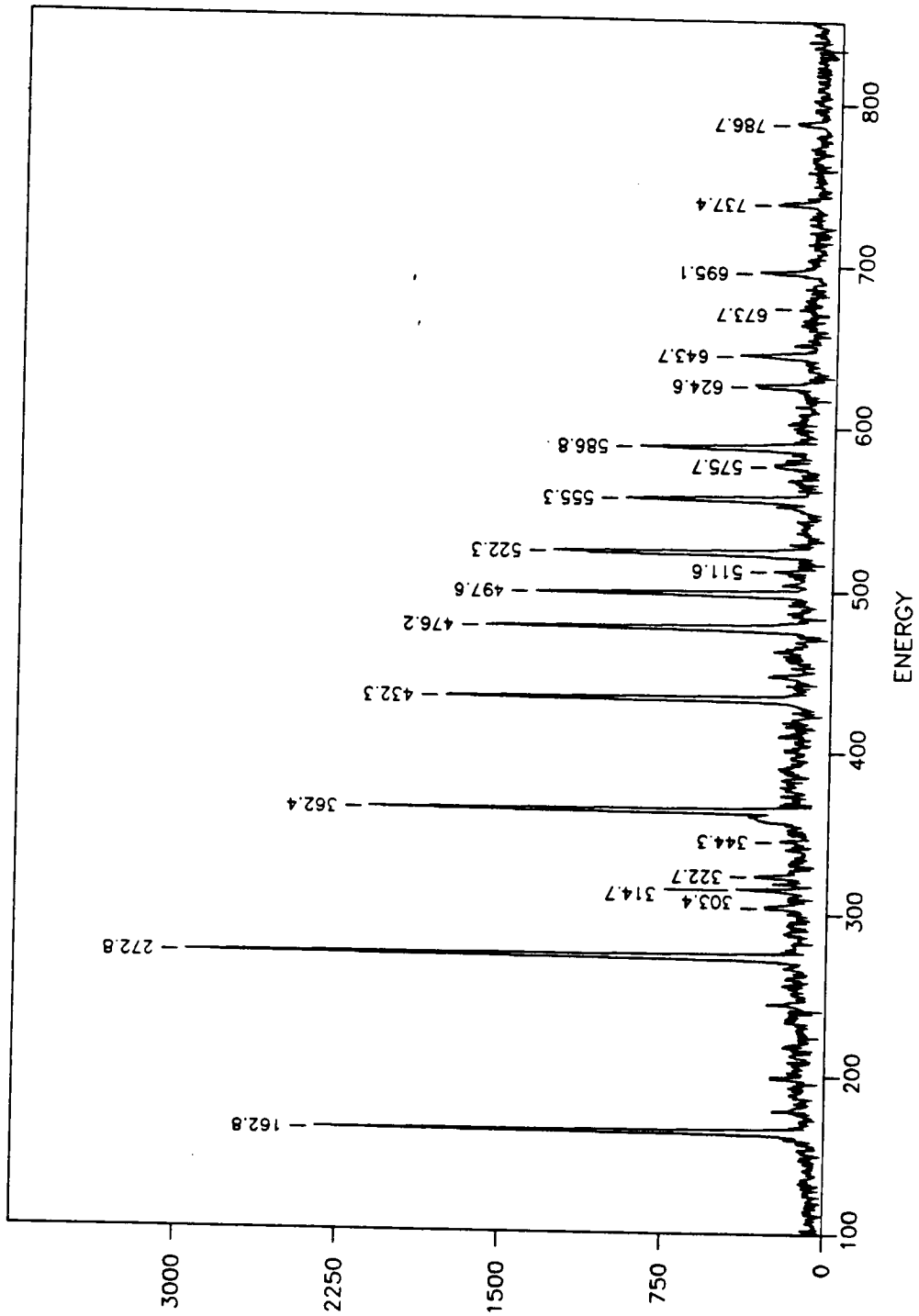

Figure 4.11: Sum of gates in band 7.

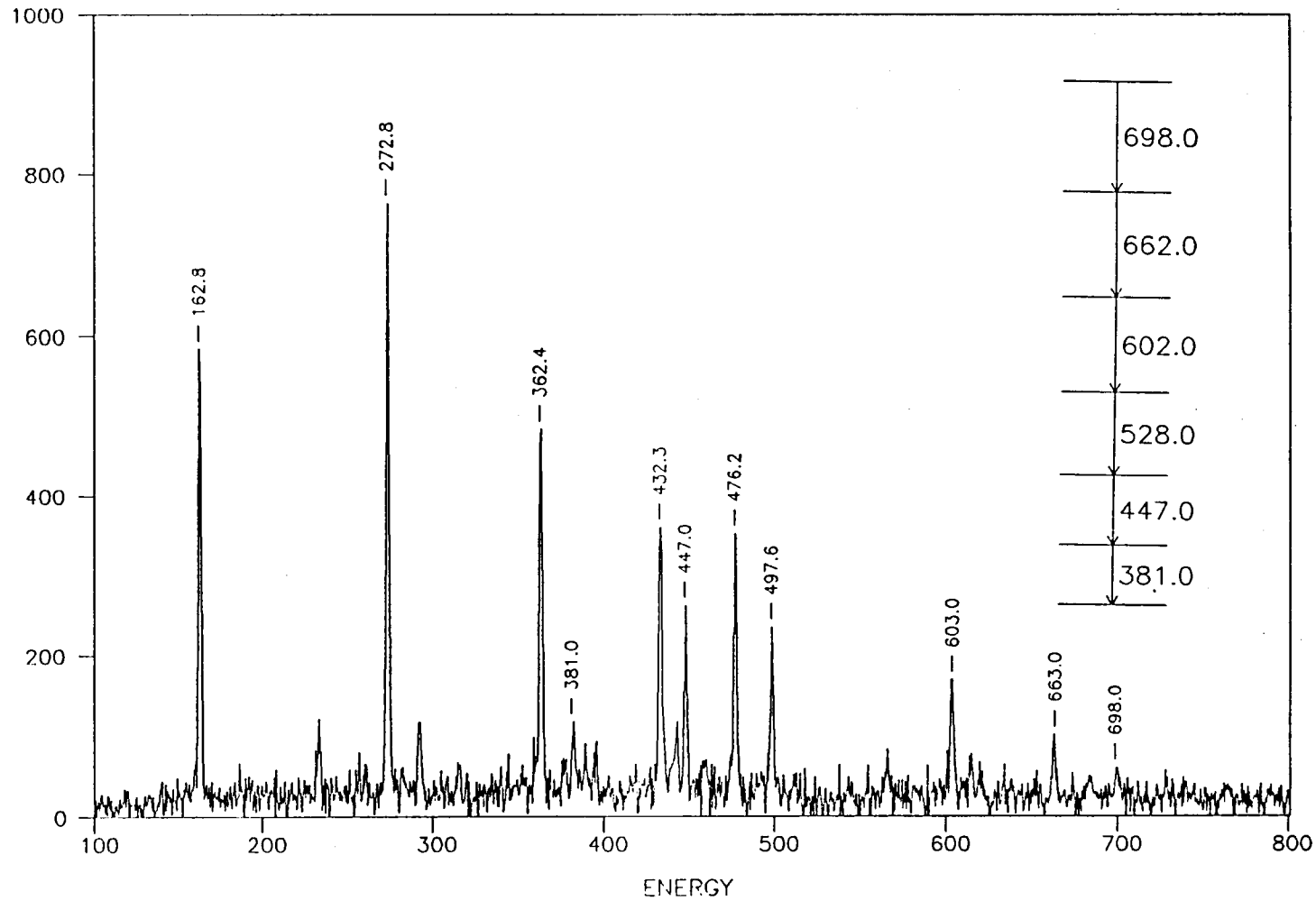

Figure 4.12: Gate taken on the 528 keV transition in band 8. The inset shows the proposed decay sequence of the band.

transitions higher than the 497.6 keV γ ray.

4.3 Decay Scheme for ^{183}Au

A recent study on the the decay of ^{183}Hg by Macias-Marques *et al.* (1984) has established the low-energy level structure of ^{183}Au. The current work represents the first in-beam study done on this nucleus, and the newly established level structure of ^{183}Au is shown in Fig. 4.13. Four rotational bands have been established, three of negative parity and one of positive parity. In this section, the angular distribution data and evidence supporting the decay scheme are presented. Chapter 6 will discuss the initial one-quasiparticle structure associated with each band and the alignment processes observed at the higher spins.

4.3.1 Angular Distribution Analysis

Angular distributions were measured for ^{183}Au using the data taken during the coincidence experiment. This was done by projecting out spectra for the individual Ge detectors, finding the areas of the peaks of interest, correcting for the detector efficiency, and fitting the angular intensities to Eq. 4.13. Even though eleven Ge detectors were used in this experiment, the cylindrical symmetry associated with the emitted radiation allows for only four angular distribution angles: 0°, 24°(156°), 63°(116°) and 87°.

Several experimental difficulties make it undesirable to measure angular distributions using the coincidence data from the Spin Spectrometer. As discussed in section 4.2.1, angular correlations arise when a coincidence requirement is placed on the recorded event. In this experiment, a coincidence between two Ge detectors defined an excepted event. For the angular distribution measurement on ^{184}Pt, the angular correlations arising from coincidences between a Ge detector and the NaI filter were assumed to be small. However, since different detectors

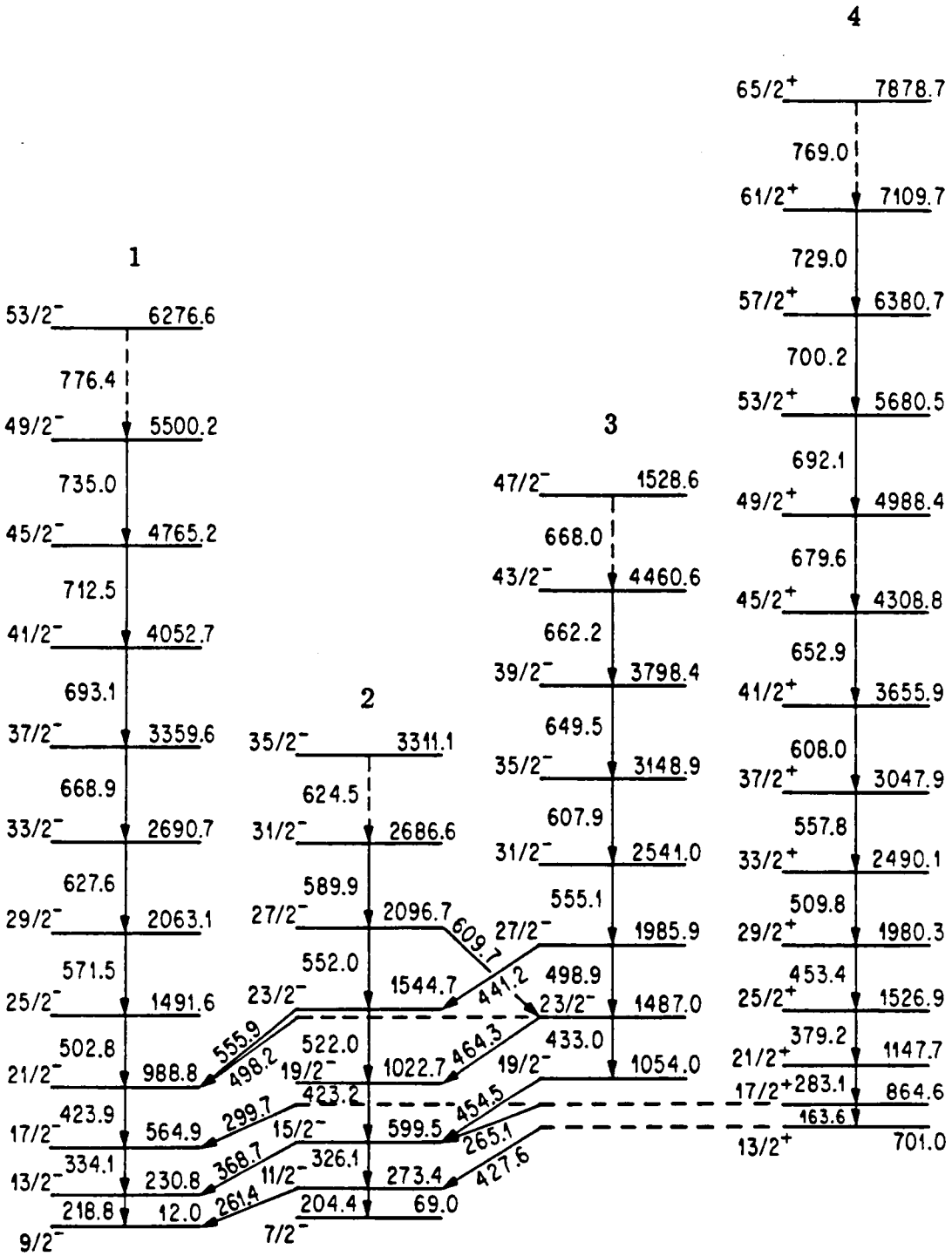

Figure 4.13: Level structure of ^{183}Au.

were used at different angles, the measured peak intensities had to be corrected for the detector coincidence efficiency. Unfortunately, only the singles efficiency is measured when using radioactive sources, but it was found that meaningful A_2 and A_4 coefficients could be extracted from the data by renormalizing each efficiency curve by a multiplicative constant. These constants were determined by calculating theoretical intensities and renormalizing the experimental intensities of several known $E2$ transitions so that they agree with the theoretical values. These correction factors were then used to normalize the efficiency curves.

This same procedure was used to correct the efficiency curves constructed for the ^{183}Au experiment. Table 4.6 lists the experimental A_2 and A_4 coefficients calculated using a least squares fit to the renormalized intensities. The A_2 values for the stretched $E2$ transitions should range between 0.35 and 0.2 and decrease smoothly as the spin increases. However, the data show the opposite trend; the quadrupole transitions exhibit relatively large increases in the A_2 coefficients as a function of I. The A_4 coefficients for these same $E2$ transitions should have values ranging roughly from -0.15 at low spins to -0.03 at the highest observed spin levels. Table 4.6 shows that while the experimental A_4 coefficient have negative values at the lowest spins, they take on positive values at moderate to high spins. The reasons for these deviations must be due to measurable angular correlations between the Ge detectors. The presence of these correlations does not prevent one from using these data to determine the multipolarity of a transition. By examining the A_2 coefficients for pure dipole and quadrupole transitions, one sees that the former gives negative A_2 coefficients while the latter positive. Utilizing this fact and the known systematics of the heavier Au isotopes, this work has assigned spins and parities to most of the levels in the decay scheme.

To aid in these assignments, a γ-γ matrix was created which recorded coincidences between the detectors at 24° and 156° with the detectors at 64°

Table 4.6: Summary of angular distribution data for ^{183}Au.

Energy (keV)	Relative Intensity	A_2	A_4	Ratio	$I_i \rightarrow I_f$	Multi-polarity
163.6	33.3(33)	0.210(267)	0.770(370)	1.12(14)	$17/2^+ \rightarrow 15/2^+$	$E2$
204.4	80.6(20)	0.351(65)	−0.27(14)	1.02(28)	$11/2^- \rightarrow 7/2^-$	$E2$
218.8	103.0(25)	0.390(66)	−0.15(9)	1.00(7)	$13/2^- \rightarrow 9/2^-$	$E2$
261.4	35.1(11)	−0.88(72)	−0.057(112)	0.74(22)	$11/2^- \rightarrow 9/2^-$	$M1(E2)$
265.1	47.8(48)	−0.326(171)	0.231(261)	0.58(9)	$17/2^+ \rightarrow 11/2^-$	$E1$
283.1	100.0(1)	0.318(171)	−0.038(90)	1.02(11)	$21/2^+ \rightarrow 17/2^+$	$E2$
326.1	58.6(10)	0.381(56)	0.12(9)	1.02(14)	$15/2^- \rightarrow 11/2^-$	$E2$
334.1	59.6(7)			1.07(13)	$17/2^- \rightarrow 13/2^-$	$E2$
368.7	10.9(7)			0.51(8)	$21/2^- \rightarrow 17/2^-$	$M1(E2)$
379.2	85.0(23)			0.99(15)	$25/2^+ \rightarrow 21/2^+$	$E2$
423.2	25.6(62)	0.509(63)	−0.10(8)	0.92(25)	$19/2^- \rightarrow 15/2^-$	$E2$
423.9	51.6(10)	0.509(63)	−0.10(8)		$21/2^- \rightarrow 17/2^-$	$E2$
427.6	36.0(36)	−0.743(74)	0.185(96)	0.75(41)	$13/2^+ \rightarrow 11/2^-$	$E1$
433.	7.3(7)	0.639(240)	0.16(35)		$23/2^- \rightarrow 19/2^-$	$E2$
453.4	74.5(51)	0.494(56)	0.027(90)	1.05(15)	$29/2^+ \rightarrow 25/2^+$	$E2$
454.5	7.0			1.3(6)	$19/2^- \rightarrow 15/2^-$	$E2$
464.3	13.3(20)	0.463(120)	-0.021(190)	1.00(30)	$23/2^- \rightarrow 19/2^-$	$E2$
498.2	13.7(30)	0.169(40)	0.28(8)	0.89(18)	$23/2^- \rightarrow 21/2^-$	$M1(E2)$
498.9	25.9(10)	0.169(40)	0.28(8)	0.89(18)	$27/2^- \rightarrow 23/2^-$	$E2$
502.8	37.9(40)	0.415(108)	0.015(19)		$25/2^- \rightarrow 21/2^-$	$E2$
509.8	72.7(56)	0.688(92)	0.047(134)	0.99(20)	$33/2^+ \rightarrow 29/2^+$	$E2$
522.	15.0(40)				$23/2^- \rightarrow 19/2^-$	$(E2)$
552.	5.0(2)			2.2(11)	$27/2^- \rightarrow 23/2^-$	$(E2)$
555.	1.8(3)				$25/2^- \rightarrow 21/2^-$	$E2$
555.1	14.3(18)	0.32(11)	−0.13(15)		$31/2^- \rightarrow 27/2^-$	$E2$
557.8	59.4(62)	0.556(93)	0.083(118)	1.23(40)	$37/2^+ \rightarrow 33/2^+$	$E2$
571.5	19.3(38)	0.53(10)	0.08(15)	1.00(40)	$29/2^- \rightarrow 25/2^-$	$E2$
588.9	6.0(3)				$31/2^- \rightarrow 27/2^-$	$(E2)$
607.9	6.2(5)	0.386(82)	−0.251(128)	0.90(17)	$35/2^- \rightarrow 31/2^-$	$E2$
608.0	27.4(37)	0.386(82)	0.251(128)	0.90(17)	$41/2^+ \rightarrow 37/2^+$	$E2$
627.6	16.0(40)	0.58(14)	−0.08(21)	0.91(14)	$33/2^- \rightarrow 29/2^-$	$E2$
649.5	5.5(20)	0.58(14)	0.28(23)	0.92(29)	$39/2^- \rightarrow 35/2^-$	$E2$
652.9	14.3(18)	1.009(156)	0.293(246)	0.74	$45/2^+ \rightarrow 41/2^+$	$E2$
662.2	3.4(10)				$43/2^- \rightarrow 39/2^-$	$(E2)$
668.9	13.(4)	1.02(23)	0.05(28)	1.19(30)	$37/2^- \rightarrow 33/2^-$	$E2$
679.6	12.0(10)	0.563(225)	0.159(311)		$49/2^+ \rightarrow 45/2^+$	$E2$
692.1	6.5(10)	0.719(201)	−0.379(361)		$53/2^+ \rightarrow 49/2^+$	$E2$
693.1	6.5(10)	0.719(201)	−0.379(361)	1.19(59)	$41/2^- \rightarrow 37/2^-$	$E2$
700.2	3.(2)				$57/2^+ \rightarrow 53/2^+$	$(E2)$
712.5	5.(2)				$45/2^- \rightarrow 41/2^-$	$(E2)$
729.	1.(1)				$61/2^+ \rightarrow 57/2^+$	$(E2)$
735.	2.(1)				$49/2^- \rightarrow 45/2^-$	$(E2)$

and 116°. Gates on known $E2$ transitions were projected from both axes. By taking intensity ratios between the same transition in both gates, one can see from Fig. 4.14 that the stretched quadrupole transitions have asymmetry ratios (R = Area(24°)/Area(63°)) which cluster around 1.1. The measured $\Delta I = 1$ transitions on the other hand have ratios which range between 0.5 and 0.75. It should also be noted that the peak intensities have not been corrected for detector efficiencies. However, this does not seem to be a problem since the transitions which are believed to be pure quadrupoles all give ratios which are relatively constant within the error bars over the full observed energy range.

4.3.2 Decay Scheme Assignments

Unfortunately, there are no common observed transitions between the data under discussion the radioactive decay work of Macias-Marques *et al.*. Thus, there are no known spin assignments which are associated with energy levels observed in this work. A $\frac{9}{2}^-$ level has been identified in the decay work at 12.3 keV. A similar level has been identified in ^{185}Au (Bourgeois *et al.*, 1982) at 8.9 keV, and rotational structures have been observed decaying into this level (Kahler *et al.*,1978; Larabee *et al.*, 1986). Fig. 4.15 shows a comparison of the low energy rotational structure for several odd-even Au nuclei. For ^{187}Au (Johansson, 1987) and ^{185}Au, the spins and parities of these bands have been well established. While this is not the case for ^{183}Au, the assignment of the lowest level observed in the in-beam data to the $\frac{9}{2}^-$ level at 12.3 keV identified in the decay work is justified by the systematics. With this level as a starting point, the remainder of the spin and parity assignments are made by using both systematic and angular distribution data.

A rotational structure has been found to be built on top of the $\frac{9}{2}^-$ level and is labeled as band 1 in Fig. 4.13. This structure has been tentatively estab-

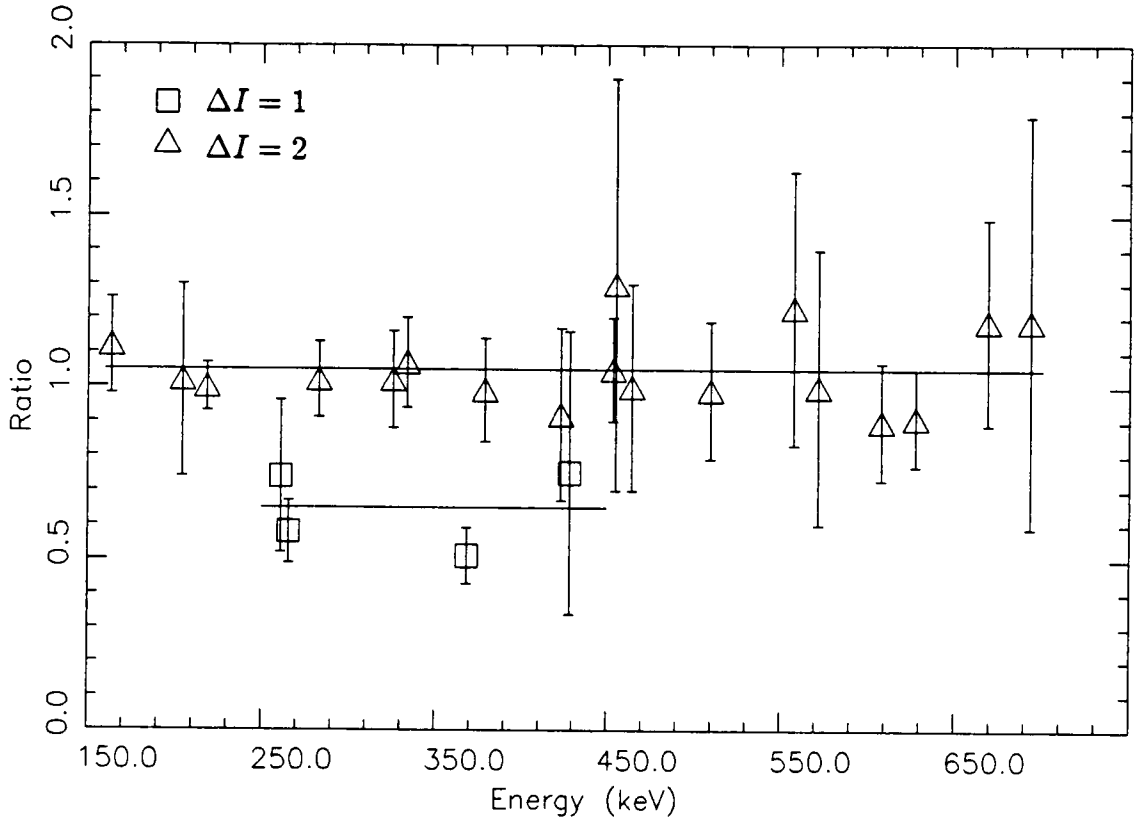

Figure 4.14: Ratio of peak intensities taken from sum the of 24° and 156° projections in coincidence with 63° and 117° detectors and the sum of 63° and 117° projections in coincidence with all 24° and 156° detectors. The projections were created by gating on selected $E2$ transitions.

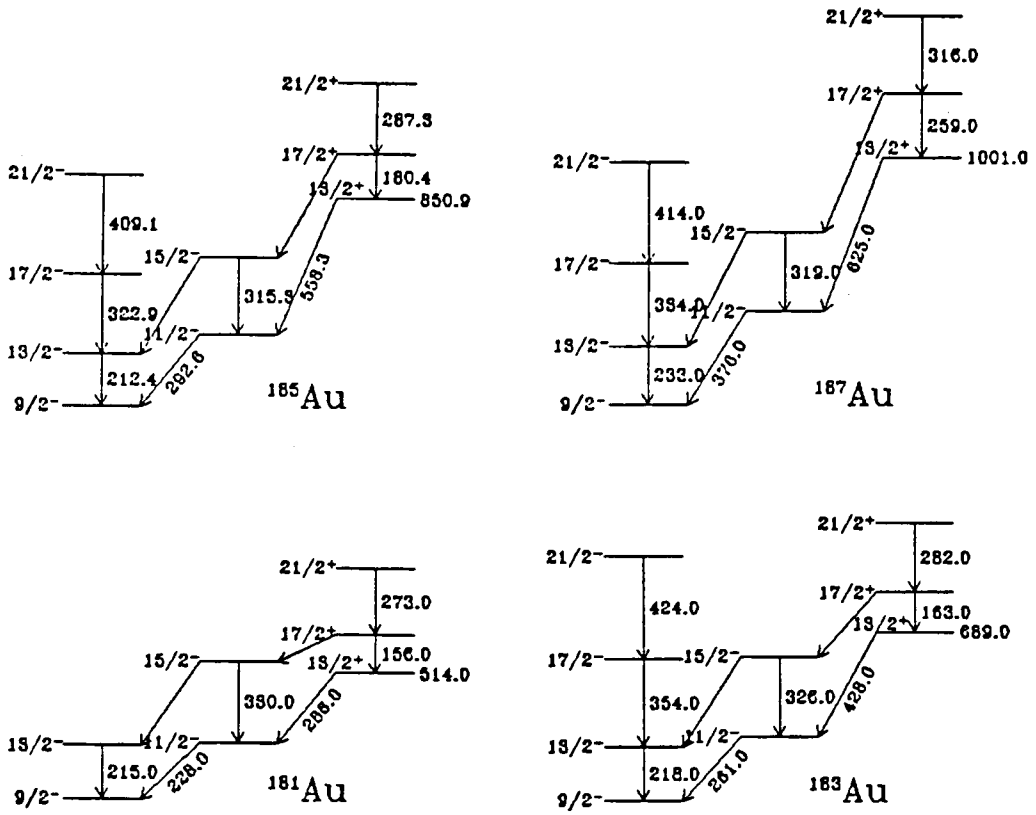

Figure 4.15: Partial level schemes for Au nuclei. The results are from Johansson (1987) for $A = 187$, Larabee *et al.* (1986) for $A = 185$, this work for $A = 183$, and Jin (1987) for $A = 181$.

lished up to the 5500.2 keV level ($I = \frac{49}{2}^-$). Fig. 4.16 shows a spectrum generated by summing the three gates taken on the 571.5, 627.6 and 668.9 keV transitions. These gates were chosen, because they give a spectrum which is dominated by the transitions in band 1. From the figure, transitions up to the 4765.2 keV are clearly identified. The last transition in this band, 735 keV, is tentative and suggested a sum of gates and not by gating on the transition itself.

Band 2 is observed to decay to band 1 predominantly by the 261.4 and 368.7 keV transitions. A large negative A_2 coefficient is found for the 261.4 keV transition (-0.88) while asymmetry ratios of 0.74 and 0.51 are found for the 261.4 and 368.7 keV transitions, respectively. All three of these values indicate that both these interband γ rays result from $\Delta I = 1$ transitions, leading to the establishment of $\alpha = -1/2$ for band 2. Negative parity is assigned to this band based on the systematics for the Au nuclei shown in Fig. 4.15.

Band 3 is not shown in the systematics of Fig. 4.15; however, a similar structure has been observed by Larabee *et al.* (1986) in ^{185}Au. The main decay out of this band is to bands 1 and 2 occurs at the 1487.0 keV level via the 498.6 and 464.3 keV transitions. Angular distribution data suggest that the 464.3 interband transition has a $\Delta I = 2$ character ($A_2 = 0.463$, R=1.00), which establishes both the parity and signature $(-, -1/2)$ of this band.

The 701.0 keV level in band 4 decays to the 273.4 keV level of band 2 by the 427.6 keV transition. Angular distribution data indicate that this is a $\Delta I = 1$ transition, and systematics establish the level as having positive parity. This band has tentatively been established up to the 7109.7 keV level. Fig. 4.17 shows a sum of gates on this band. The spectrum clearly shows all transitions up to $I = \frac{53}{2}^+$. The other two transitions are suggested by the sum of gates.

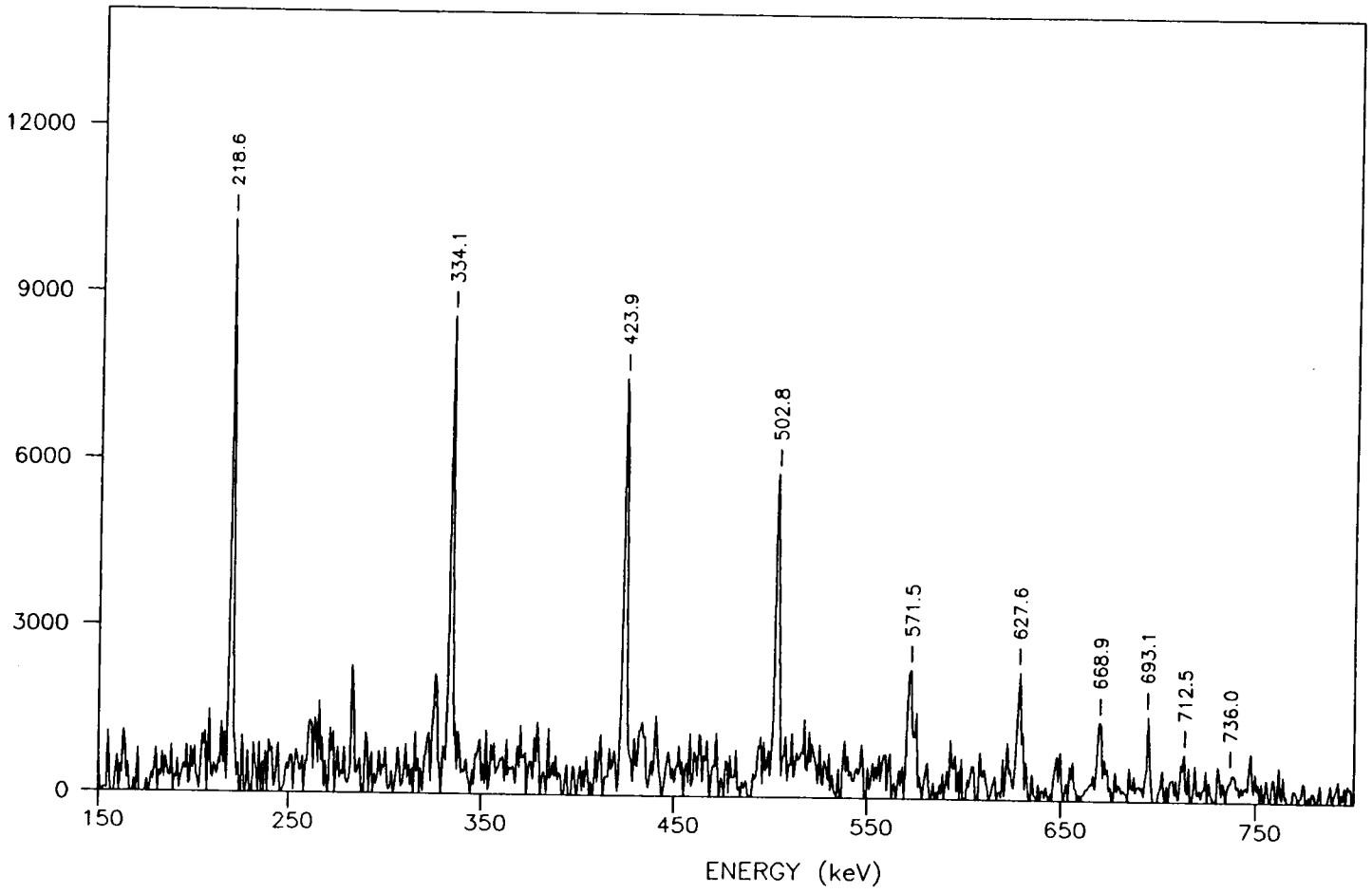

Figure 4.16: Summed spectrum of gates taken of the 571.5, 627.6 and 668.9 keV transitions in band 1.

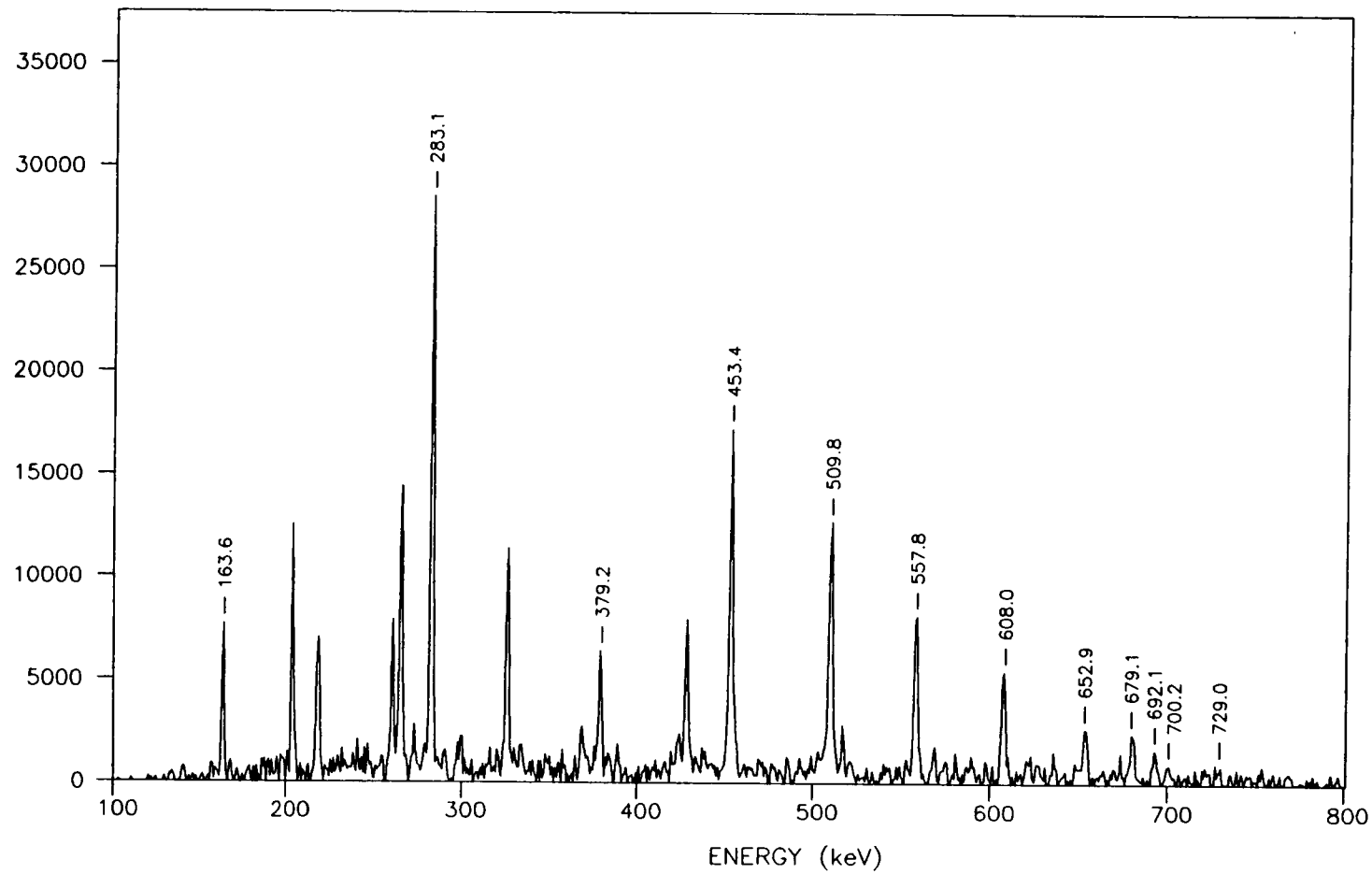

Figure 4.17: Summed spectrum of gates taken of the 379.2, 652.9 and 6791. keV transitions in band 4 of ^{183}Au. Only the members of the band are labeled in the figure.

CHAPTER 5

^{184}Pt EXPERIMENTAL ANALYSIS

5.1 Introduction

Shape coexistence has been well established in the Pt-Hg nuclei below $N = 110$ where observed rotational bands are built on both prolate and oblate ground states. This shape coexistence is an indication that the cores of these nuclei are soft with respect to deformation. One can thus expect major changes in the nuclear shape to be caused by aligned quasiparticles (Frauendorf and May, 1983). This chapter focus on the observed effects these high-j quasiparticles have on the rotational bands in ^{184}Pt. While the existence of structures built on prolate and oblate shapes has been previously discussed (see for example Bengtsson *et al.*, 1987), the work described herein examines an even greater sensitivity of the nuclear shape to the aligned quasiparticle.

The establishment of initial quasiparticle configurations of the bands in ^{184}Pt are determined by comparing the experimental Routhians and alignments with those of odd-A nuclei where the quasiparticle characteristics of each band is already known. The nature of the quasiparticle alignments are determined through the use of blocking arguments which also involve comparisons with odd-A nuclei. Conclusions about the dependence of the shape on the quasiparticle configuration comes from comparison of the spectroscopic data with the results of several total Routhian surface (TRS) calculations, which are performed using the shell correction method described in section 2.9. These calculations permit a determination of the shape parameters as a function of rotational frequency and quasiparticle configuration.

5.2 Low Frequency Band Analysis

5.2.1 Initial Quasiparticle Assignments

As discussed in 2.8, the yrast band of an even-even nucleus at low rotational frequencies defines the quasiparticle vacuum. Excited bands are either built on other zero-quasiparticle states (collective effect) or multi-quasiparticle configurations (single-particle effect). In ^{184}Pt, there are three observed bands which are associated with a vacuum structure: the prolate ground band (yrast), the oblate ground band and the γ-vibrational band. The remaining bands identified in the decay scheme pictured in Fig. 4.4 are thought to be built on different multi-quasiparticle configurations. One method for determining the initial quasiparticle nature of these bands is to examine the experimental quasiparticle Routhian, e', and quasiparticle alignment, i, of each band as a function of the rotational frequency using the phenomological expressions derived in 2.4:

$$e' = E - \omega I_x + \left(\frac{\omega^2}{2} \mathcal{J}_0 + \frac{\omega^4}{4} \mathcal{J}_1 - \frac{1}{8\mathcal{J}_1} \right), \tag{5.1}$$

and

$$i = I_x - \omega \left(\mathcal{J}_0 + \omega^2 \mathcal{J}_1 \right). \tag{5.2}$$

Fig. 5.1a shows a plot of the experimental quasiparticle Routhians for the established bands in ^{184}Pt, while Fig. 5.1b shows a plot of the quasiparticle alignments for the same bands. The reference parameters $\mathcal{J}_0$ and $\mathcal{J}_1$ were chosen as 30 $\hbar^2$ MeV^{-1} and 40 $\hbar^4$ MeV^{-3}, respectively. The choice of these parameters is discussed in greater detail in the next section.

In order to make definite conclusions about the configurations associated with the multi-quasiparticle bands in an even-even nucleus, one extracts effective one-quasiparticle energies and alignments by averaging together the one-quasiparticle configurations in the odd-A neighboring nuclei. The averaged quasi-

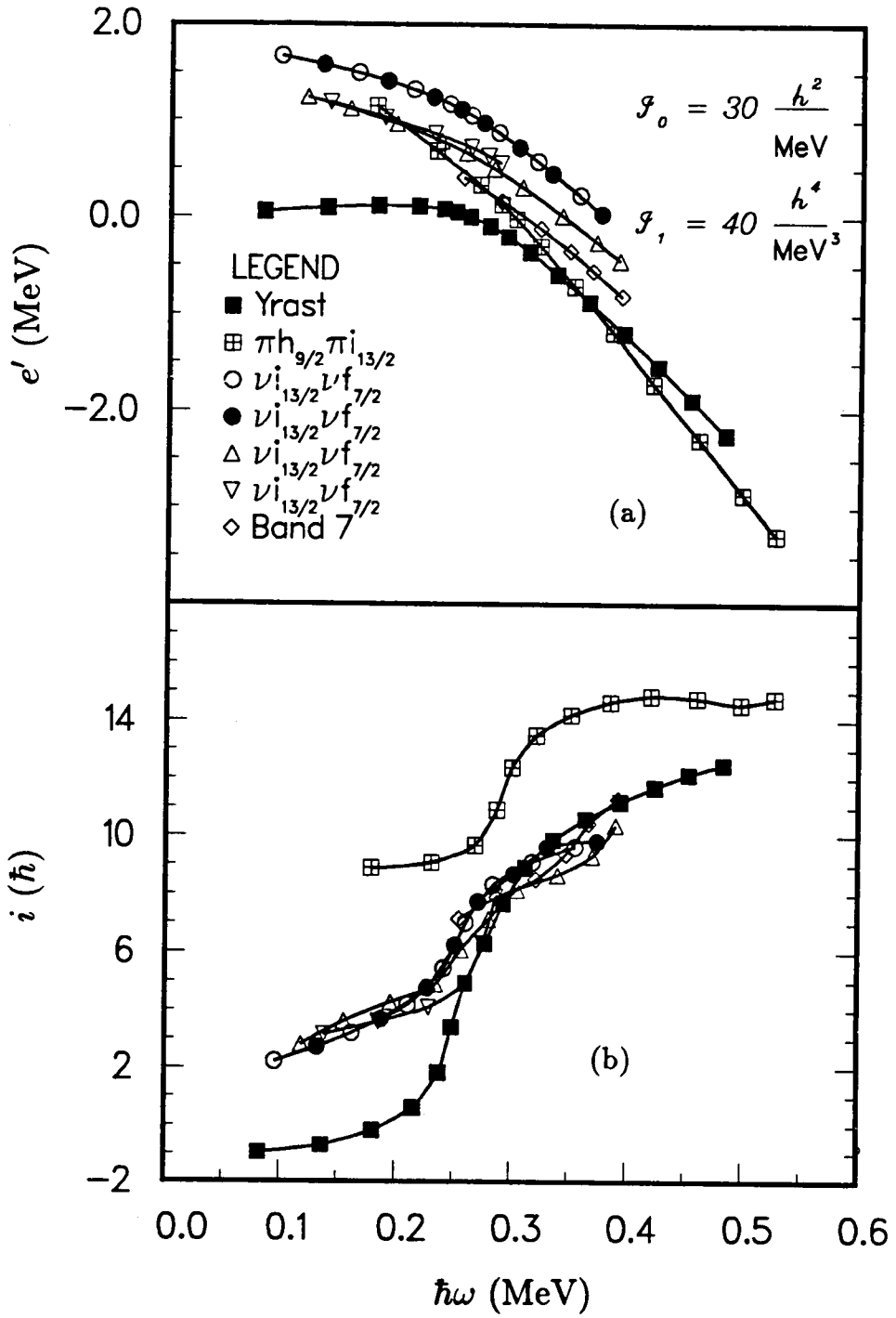

Figure 5.1: Experimental quasiparticle Routhians (a) and quasiparticle alignments (b) for the observed bands in ^{184}Pt.

particle energies and alignments are considered building blocks for the multi-quasiparticle bands in the even-even nuclei. By considering summed combinations of the these quasiparticle Routhians and alignments, one is able to determine the most likely multi-quasiparticle configuration associated with each band in the even-even nucleus. One is also able to make comparisons between the averaged and theoretical Routhians in the even system.

In order to determine the quasiparticle configurations of the observed side bands in ^{184}Pt, one must first know the one-quasiparticle composition for the known bands in the neighboring odd-A systems. For the odd-N Pt nuclei, ^{183}Pt (Nyberg *et al.*, 1987) and ^{185}Pt (Pilotte *et al.*, 1987) rotational bands have been observed built on the quasiparticle states associated with the asymptotic quantum numbers $\frac{9}{2}$[624] ($\nu i_{13/2}$), $\frac{7}{2}$[514] ($\nu f_{7/2}$), and $\frac{1}{2}$[521] ($\nu p_{3/2}$). The single-particle designations refer to the particle composition of the specified Nilsson orbital in the absence of deformation. The average experimental Routhians and alignments for the proton representations were determined using the odd-Z isotones ^{185}Au (Larabee *et al.*, 1986) and ^{183}Ir (Janzen *et al.*, 1987). In these nuclei, rotational bands are built on the quasiparticle states $\frac{1}{2}$[541] ($\pi h_{9/2}$), $\frac{1}{2}$[660] ($\pi i_{13/2}$), $\frac{1}{2}$[530] ($\pi f_{7/2}$), and $\frac{5}{2}$[402] ($\pi d_{5/2}$). Table 5.1 contains the averaged and predicted alignments for these states as pertaining to ^{184}Pt. The theoretical alignments were extracted from quasiparticle diagrams calculated using a Woods-Saxon potential and using deformations suggested by the TRS calculation at $\hbar\omega = 0.0$ MeV ($\beta_2 = 0.225$, $\beta_4 = -0.029$). Included in the table are the averaged Routhian energies at $\hbar\omega = 0.15$ MeV after adding the experimentally extracted pairing gaps to them ($\Delta_p = 0.945$ and $\Delta_n = 1.068$.

Bands 3 and 4 which decay to the yrast band via a 1.1 msec isomeric transition have been identified with the quasiparticle structure, $\nu i_{13/2} \otimes \nu f_{7/2}$, corresponding to the Nilsson configurations $\frac{9}{2}$[624] and $\frac{7}{2}$[514]. The establishment of

Table 5.1: Experimentally, averaged and calculated alignments of the one-quasiparticle configurations which are thought to make up the multi-quasiparticle bands in ^{184}Pt. Also included are the averaged quasiparticle energies extracted at $\hbar\omega = 0.15$. The small letters refer to quasiproton configurations, the large to quasineutron configurations.

	$\hbar\omega = 0$			
	Nilsson	i ($\hbar$)		e'
LABEL	Level	Avg.	CSM	(MeV)
a	1/2[660]	5.6	6.5	1.23
e	1/2[541]	3.2	3.2	0.43
A	9/2[624]	2.9	4.0	0.79
B	9/2[624]	2.9	4.0	0.83
E	7/2[514]	1.2	1.0	1.14
F	7/2[514]	1.2	1.0	1.14
G	1/2[521]	0.6	0.5	1.05

these bands as quasineutron bands is supported by the existence of similar structures in the lighter even-even isotones, *e.g.* ^{182}Os and ^{180}W (Burde *et al.*, 1966), ^{178}Hf (Gallagher and Nielsen, 1962) and ^{176}Yb (Vergnes *et al.*, 1965). It would be very unlikely that a quasiproton configuration would exist in all these nuclei as Z changes from 70 to 78. The fact that $K = 8$ these bands have negative parity and lie highest in energy in Fig. 5.1 suggest, upon comparison with Table 5.1, they must contain either a $\nu f_{7/2}$ or $\nu p_{3/2}$ quasiparticle in their configuration. However, the band head spin of 8^- in band 3 favors an $f_{7/2}$ quasineutron assignment ($\Omega = 7/2$), since the $\nu p_{3/2}$ orbital has only an $\Omega = 1/2$ associated with it. The most likely companion quasiparticle to be coupled with the $\frac{7}{2}$[514] is the positive parity orbital $\frac{9}{2}$[624]. If both these orbitals are aligned parallel with each other, a total K of 8 is obtained, thus producing the spin of the band head.

Bands 5 and 6 have also been identified with the quasiparticle structure $\nu i_{13/2} \otimes \nu f_{7/2}$, resulting from the low-K coupling of the $\frac{9}{2}$[624] and $\frac{7}{2}$[514] configurations. In the initial work by Burde *et al.* (1966), only the 5^- and 6^- states in

these bands were identified. As discussed in section 4.3, the 6^- state was originally identified as having positive parity, and thus the 5^- and 6^- states were associated with different quasiparticle structures. However, the observation of $\Delta I = 1$ transitions between the bands indicates that they are signature partners of one another. Burde *et al.* also attributed a $K = 6$ to band 6, and based on this assumption, a $K = 2$ was assigned to band 5. On the other hand, the current quasiparticle assignments favor a $K = 1$ for the two bands in the absence of strong mixing with other low-K states. Bands similar to 5 and 6 have also been observed in ^{182}Os (Lieder *et al.*, 1980; Fahlander and Dracoulis *et al.*, 1980). The similarity in transition energies at low spins between the Os and Pt bands strongly suggests that these bands have the same structure. The inclusion of $\nu i_{13/2}$ quasineutrons in the configuration of band 5 and 6 is also supported by the decay of band 5 to the oblate ground band. The $K = 9/2$ $\nu i_{13/2}$ quasiparticles should stabilize the core at negative γ deformations (see 2.9), resulting in an intermediate triaxial shape for bands 5 and 6 which lies between the oblate and prolate structures in the γ plane. The identification of the $\nu f_{7/2}$ quasiparticle as the companion to the $\frac{9}{2}$[624] is less clear. Another possibility would be the $\frac{1}{2}$[521] quasiparticle which lies slightly lower in energy to the $\frac{7}{2}$[514] orbital (see Table 5.1). For the remainder of this work, bands 5 and 6 are assumed to have a $\nu f_{7/2}$ component; however, future investigations might consider the consequences of assigning a $\nu p_{3/2}$ component to these bands.

Band 2 is the most dominant side band observed in ^{184}Pt. To deduce the quasiparticle composition of this band, it is important to examine the values of the aligned angular momentum for each quasiparticle listed in Table 5.1 more closely. From Fig. 5.1b, the initial alignment for band 2 is $9.1\hbar$. From the additivity of the experimental and theoretical one-quasiparticle alignments listed in Table 5.1, the only two-quasiparticle configuration which has this much alignment associated

with it for a (−,1) band is $\pi h_{9/2} \otimes \pi i_{13/2}$ ($\frac{1}{2}[541]\frac{1}{2}[660]$). Support for this assignment comes from other indications as well:

1. Fig. 5.1a shows that band 2 becomes yrast at $\hbar\omega \approx 0.36$ MeV. This same phenomenon is observed in Au nuclei where the $\pi i_{13/2}$ band initially lies highest in energy and eventually becomes yrast at $\hbar\omega \leq 0.3$ MeV.

2. The absence of any signature partner for this band. Since both proposed quasiparticles have $K = 1/2$, this leads to a doubly decoupled structure which should result in the unfavored signature lying significantly higher in energy than the favored signature.

3. The lack of observing any such band in the even-even Os nuclei. This is due to the fact that the $\pi i_{13/2}$ $\frac{1}{2}[660]$ orbital lies too far above the Fermi level to be observed experimentally at $Z = 76$.

4. The observation of a similar band in both ^{182}Pt (Popescu *et al.*, 1986) and ^{186}Pt (Pilotte *et al.*, 1986) with an initial alignment of 9 $\hbar$.

5. The identification of a highly aligned band in ^{185}Pt with an initial alignment of 12 $\hbar$. This band has been assigned the three-quasiparticle configuration $\nu i_{13/2} \otimes \pi h_{9/2} \otimes \pi i_{13/2}$. The observation of this band makes it unlikely that band 2 would be associated with a four quasiparticle structure, because the most probable four-quasiparticle configurations would involve the $\frac{9}{2}[624]$ quasineutron.

Quasiparticle assignments for band 7 are more difficult to make, because the parity and spin of the band are are not completely certain. The alignment gain for this band is roughly 7.5 $\hbar$; therefore, it is unlikely that it is a two-quasineutron band associated with a prolate shape. The experimental quasiparticle Routhian for this band shows that it lies lower in energy than the two-quasineutron bands

but higher in energy than band 2. The averaged one-quasiparticle Routhians indicate that this is just the case for the $\pi h_{9/2}$ band in relationship with the other quasiproton Routhians. Thus, it is reasonable to propose that band 7 may have an $h_{9/2}$ component associated with it also. One other possibility is that band 7 is associated with a multi-quasiparticle oblate structure. However, this may be a less likely possibility, since this band appears to mix strongly with the yrast band.

Table 5.2 summarizes both the experimental and summed one-quasiparticle Routhians. The summed contributions have the experimental pairing gap, Δ, added to each averaged one-quasiparticle Routhian. The Δ value is determined experimentally from the odd-even mass differences. However, these values have not been measured for the neutron deficient Pt nuclei centered around $N = 106$. Thus to estimate Δ_{eo} for both protons and neutrons in ^{184}Pt, the expression

$$\Delta_{eo} = \frac{1}{4}\left(E(N-1) - 3E(N) + 3E(N+1) - E(N+2)\right) \tag{5.3}$$

is used, which gives the approximate energy difference between the odd-N and even-N ground states at the particle number $N + \frac{1}{2}$. For ^{184}Pt, values of 1.068 MeV and 0.945 MeV are calculated for the neutron and proton odd-even mass differences using the energies for the mass excesses given by Wapstra (1985).

From Table 5.2, one can see that the energy and alignment for the experimentally observed two-quasiparticle bands are less than the summed one-quasiparticle components. This is expected and brought about by residual interactions between the quasiparticles. Frauendorf *et al.* (1984) have suggested that the energy of this residual interaction is just the difference in energy of the experimental and summed quasiparticle contributions

$$e'(\omega) - \sum_{\mu} e'_{\mu}(\omega) = \sum_{\mu<\nu} V_{\mu\nu}(\omega), \tag{5.4}$$

where e' is the single-particle Routhian of the multi-quasiparticle band, the summed energy includes all components in the multi-quasiparticle state, and $V_{\mu\nu}$ represents

Table 5.2: Experimental quasiparticle Routhian energy and alignment additivity for the excited two-quasiparticle bands in ^{184}Pt. The energies were extracted at $\hbar\omega = 0.20$ MeV and i was taken as the slope of the quasiparticle Routhians before the first band crossing. The signature assignments for these bands are discussed later in section 5.3.

Band		Proposed	$i(\hbar)$		e'(MeV)	
Number	(π,α)	Assignment	Exp.	Summed	Exp.	Summed
2	(−,1)	ae	9.1	8.8	0.97	1.21
3	(−,0)	AF	3.0	4.1	1.38	1.75
4	(−,1)	BF	3.0	4.1	1.38	1.69
5	(−,1)	AE	3.6	4.2	0.96	1.75
6	(−,0)	BE	3.3	4.2	0.99	1.69

the two quasiparticle interaction between states μ and ν. A portion of this residual interaction is associated with the pairing energy. For example, the single-particle Routhians have the full pairing energy added to them. However, it is well known that multi-quasiparticle bands have reduced pairing energies associated with them, due to the fact these unpaired particles effectively block their orbitals such that quasiparticle pairs cannot be scattered into them. Other differences may be accounted for by shape variations and changes in the Fermi level between the two- and one-quasiparticle states. Table 5.3 lists the experimental estimates of the quasiparticle interactions at three different rotational frequencies for the observed two-quasiparticle bands in ^{184}Pt.

One striking feature of the experimentally determined interaction matrix elements is the reduction of the low-K quasineutron states (Bands 5 and 6) by 350-400 keV relative to the high-K states (Band 3 and 4). This same difference is observed in the Os nuclei however the differences are larger, ranging from 500-750 keV (see Garrett 1984). Self-consistent calculations of the configuration-dependent shape, pairing and Fermi level are able to account for 50-100 keV of this deviation in ^{180}Os. Garrett (1984) has proposed that the remaining difference may be ac-

Table 5.3: Values of the quasiparticle interaction matrix elements as a function of the rotational frequency calculated using the formalism of Frauendorf *et al.* (1984). Values in parentheses result from extrapolated energies for some of the configurations.

Matrix element	Values of Matrix Elements (MeV) $\hbar\omega$ [MeV] = 0.125	0.150	0.200
V_{ea}	(−0.27)	(−0.25)	−0.24
V_{AF}	−0.43	−0.40	−0.31
V_{BF}	−0.46	−0.44	−0.37
V_{AE}	−0.82	−0.78	−0.73
V_{BE}	−0.85	−0.82	−0.76

counted for by the residual interactions between the much larger number of low-K configurations than high-K configurations in the continuum, resulting in larger values for the interaction matrices connected with the low-K states relative to the high-K states. While this work will not focus any further on these effects, it is interesting to note that the differences between the two configurations in ^{184}Pt is not as large as it is in the Os nuclei. Since similar quasineutron bands are observed in ^{182}Pt and ^{186}Pt, the systematics of these high-K and low-K matrix elements should be mapped out as a function of particle number and configuration in order to determine the exact nature of this effect.

5.2.2 Initial Deformations

In order to investigate the influence of shape effects on the rotational properties of nuclei in the Pt-Au transitional region, we have performed calculations of the total Routhian surface for ^{184}Pt and the neighboring nuclei. The total Routhian energy for a fixed deformation and frequency is given by Eq. 2.88. For our calculations, a non-axial Woods-Saxon potential (see Nazarewicz *et al.*, 1985) was used as the average field using the universal parameters of Dudek *et al.* (1981).

The pairing gap, Δ, was calculated self-consisently in the HFBC equations at $\hbar\omega = 0.0$ MeV and kept fixed at non-zero rotational frequencies, taking on the value as a function of ω,

$$\Delta(\omega) = \begin{cases} \Delta = \Delta_0[1 - \frac{1}{2}(\frac{\omega}{\omega_c})^2] & \omega \leq \omega_c \\ \Delta = \frac{1}{2}\Delta_0 \exp[2(1 - \frac{\omega}{\omega_c})] & \omega > \omega_c \end{cases}, \tag{5.5}$$

where Δ_0 is the self-consistent pairing gap at $\hbar\omega = 0.0$ MeV, and ω_c is a predefined critical frequency. For the deformations quoted in Table 5.4, ω_c was set to 0.7 MeV for both neutrons and protons. A typical grid used for these calculations is shown in Fig. 5.2, where each point represents a deformation in β_2-γ space for which a HFBC calculation is performed. In the Pt region, the β_4 deformation is usually allowed to cover a range from -0.08 to 0.04 by steps of 0.04. For the grid used for ^{184}Pt, a calculation was done for thirteen different rotational frequencies ranging from 0.0 MeV to 0.6 MeV by steps of 0.05 MeV at each deformation point. The Fermi level was also adjusted at each frequency to give the correct particle number for $< N >$.

The calculated deformations for the vacuum and two-quasiparticle configurations in ^{184}Pt are summarized in Table 5.4. These deformations were extracted from the calculations by minimizing the total Routhian energies of the grid in Fig. 5.2 with respect to the deformation parameters $(\beta_2, \gamma, \beta_4)$.

As discussed in chapter 2, competition between different shapes at low spins and excitation energies is thought to occur in both Pt and Hg nuclei centered around $N = 106$. Bengtsson *et al.* (1987) have performed TRS calculations for the ground states of these nuclei, and these calculations do indeed predict this shape coexistence. Fig. 5.3 taken from Bengtsson *et al.* shows the predicted shapes in ^{184}Pt and ^{184}Hg. In the case of ^{184}Hg, an oblate minimum is found to lie lowest in energy with $\beta_2 \approx 0.13$ and a excited secondary minimum is also observed at $\beta_2 \approx 0.22$. In ^{184}Pt, the ordering of the shapes is reversed which

Table 5.4: Calculated equilibrium deformations $(\beta_2, \gamma, \beta_4)$ for the observed bands in ^{184}Pt as a function of rotational frequency $\hbar\omega$. In the table the values of the total Routhian, $E'(\omega)$, and the projection of the angular momentum on the rotational axis, I_x are shown.

$\hbar\omega$ (MeV)	β_2	γ	β_4	E' (MeV)	I_x ($\hbar$)
Configuration: Prolate Ground (+,0)					
0.00	0.227	3.5	−0.028	−3.22	0.0
0.10	0.231	2.7	−0.027	−3.33	2.1
0.15	0.235	1.8	−0.027	−3.47	3.4
0.20	0.238	−1.7	−0.026	−3.71	5.0
Configuration: Oblate Ground (+,0)					
0.00	0.165	−61.8	−0.006	−2.83	0.0
0.15	0.173	−58.3	−0.003	−2.85	1.1
0.20	0.180	−57.0	−0.001	−2.90	2.5
Configuration: ae (−,1)					
0.15	0.240	11.2	−0.026	−1.51	10.7
0.20	0.251	9.2	−0.023	−2.23	14.3
0.25	0.249	9.3	−0.022	−3.13	16.2
Configuration: AE (−,1)					
0.10	0.243	1.8	−0.027	−1.71	5.4
0.15	0.241	0.7	−0.027	−2.07	7.5
0.20	0.236	−8.0	−0.029	−2.56	10.4
0.25	0.177	−28.8	−0.028	−3.83	13.1
Configuration: AF (−,0)					
0.10	0.244	1.4	−0.027	−1.72	5.5
0.15	0.242	0.1	−0.028	−2.07	7.6
0.20	0.239	−4.0	−0.029	−2.56	9.8
0.25	0.186	−20.1	−0.038	−3.75	12.6
Configuration: BE (−,0)					
0.10	0.243	1.7	−0.027	−1.72	5.5
0.15	0.241	0.6	−0.027	−2.07	7.5
0.20	0.240	−2.0	−0.027	−2.56	9.5
0.25	0.183	−20.6	−0.033	−3.53	11.9
Configuration: BF (−,1)					
0.10	0.244	1.4	−0.028	−1.72	5.5
0.15	0.242	0.9	−0.027	−2.08	7.6
0.20	0.240	−1.9	−0.027	−2.56	9.5
0.25	0.192	−17.3	−0.038	−3.52	11.3

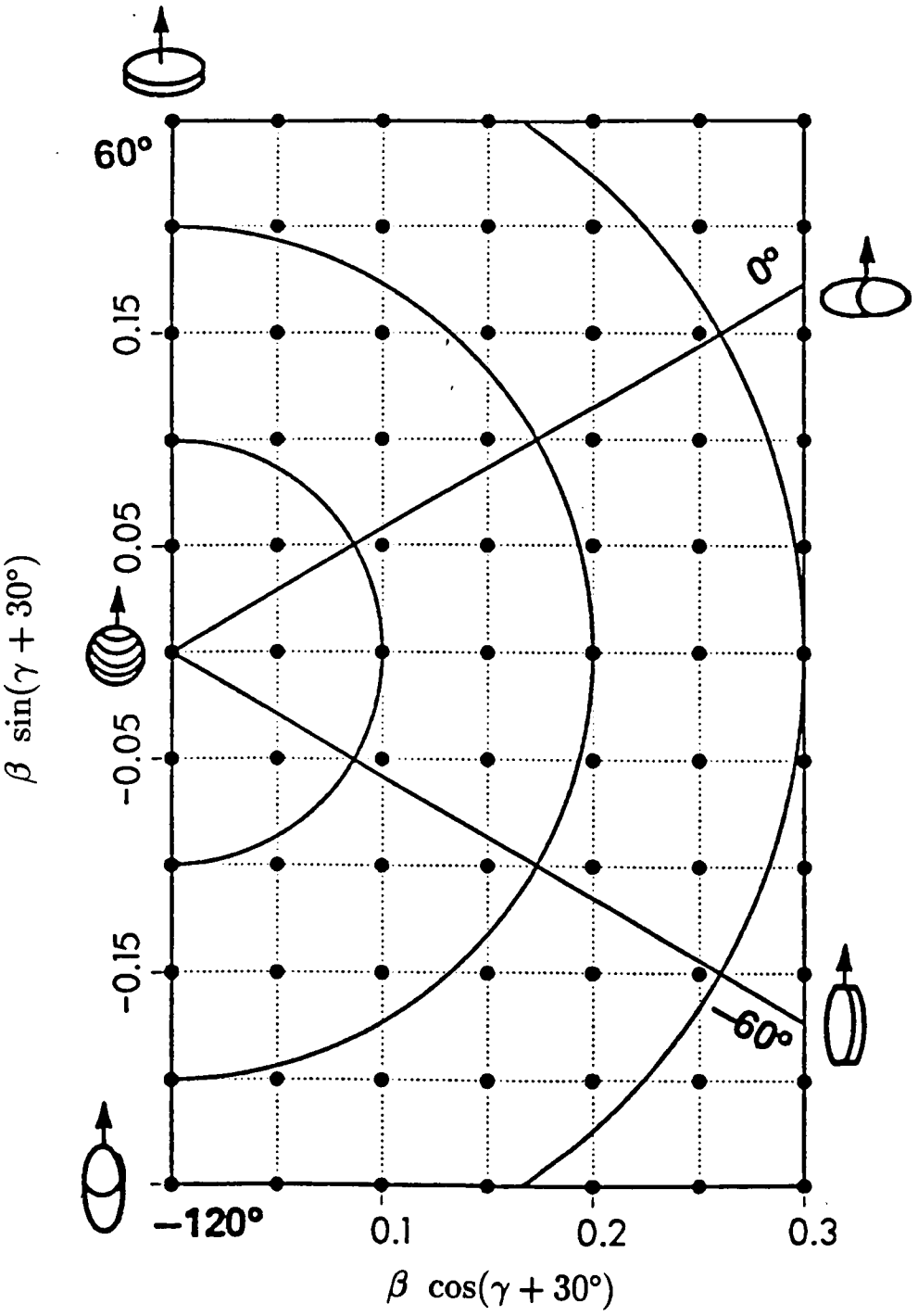

Figure 5.2: Typical deformation grid used for the Total Routhian calculation.

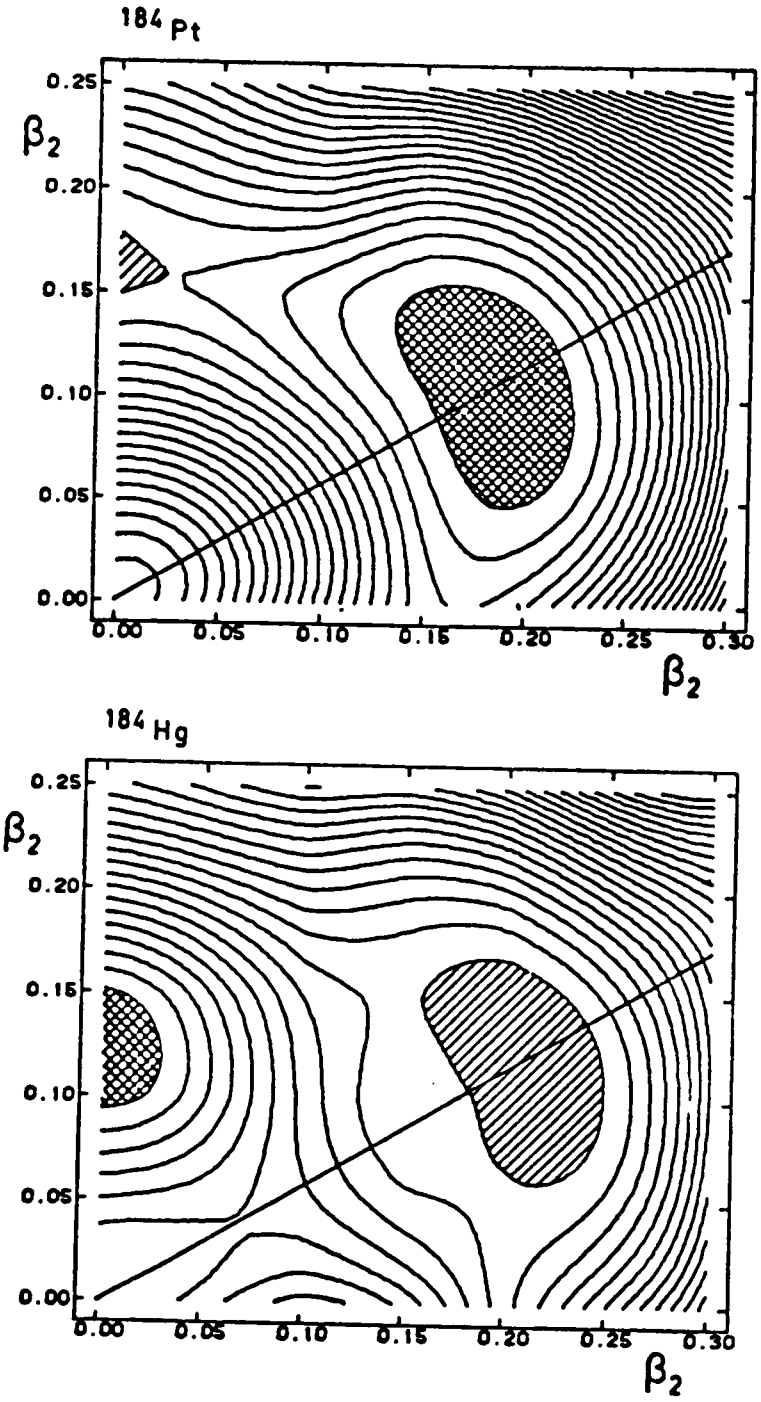

Figure 5.3: Potential energy surfaces in the (β_2, γ)-plane calculated with the Woods-Saxon potential for ^{184}Pt and ^{184}Hg at $\hbar\omega = 0.0$ MeV. The energy is minimized with respect to the hexadecapole deformation at each (β_2, γ) mesh point. The energy between contour lines is 0.1 MeV. Reproduced from Bengtsson *et al.* (1987).

agrees very nicely with what is observed experimentally. In general, Bengtsson *et al.* have found very good agreement between theory and experiment with regards to ground-state shape coexistence in the Pt-Hg transitional region. Table 5.4 lists the predicted equilibrium shapes for these two ground bands in ^{184}Pt from our frequency dependent TRS calculations. At $\hbar\omega = 0.0$ MeV an energy difference of 390 keV is predicted for these two shapes which agrees quite nicely with the 492 keV difference observed experimentally between the 0^+ states of these two bands.

Since the oblate ground band is observed experimentally only up to the 4^+ state in ^{184}Pt, a detailed analysis of its deformation as a function of frequency will not be performed here. On the other hand, the prolate ground band and two-quasiparticle bands are observed in all cases through the first backbend, and it should be instructive to compare the experimental bands with theoretical predictions of shape from the TRS calculations. From Table 5.4, the calculations predict that the yrast band for ^{184}Pt has a prolate shape with quadrupole deformation gradually increasing from $\beta_2 = 0.227$ to $\beta_2 = 0.238$. From the experimental coincidence data, direct determination of the nuclear deformation parameters is not possible. However, Garg *et al.* (1986) have measured the lifetime for the yrast states in ^{184}Pt, and have extracted reduced matrix elements, $B(E2)$, which are plotted as a function of spin in Fig. 5.4. The $B(E2)$ values are related to the nuclear shape parameters, β_2 and γ, through the expression

$$B(E2) = \frac{5}{16\pi} Q_t^2 < I2k0 \mid I - 2K >^2 \tag{5.6}$$

where Q_t is the transition quadrupole moment given by

$$Q_t = 2\left(\frac{3}{5\pi}\right)^{1/2} ZeR_0^2\beta_2 \cos(30^\circ + \gamma). \tag{5.7}$$

Utilizing the deformations extracted from the TRS calculations for the ground band, we have calculated $B(E2)$ values, and they also appear in Fig. 5.4. Qualitative agreement between the B(E2) values are reached up to $I = 6$. If one assumes

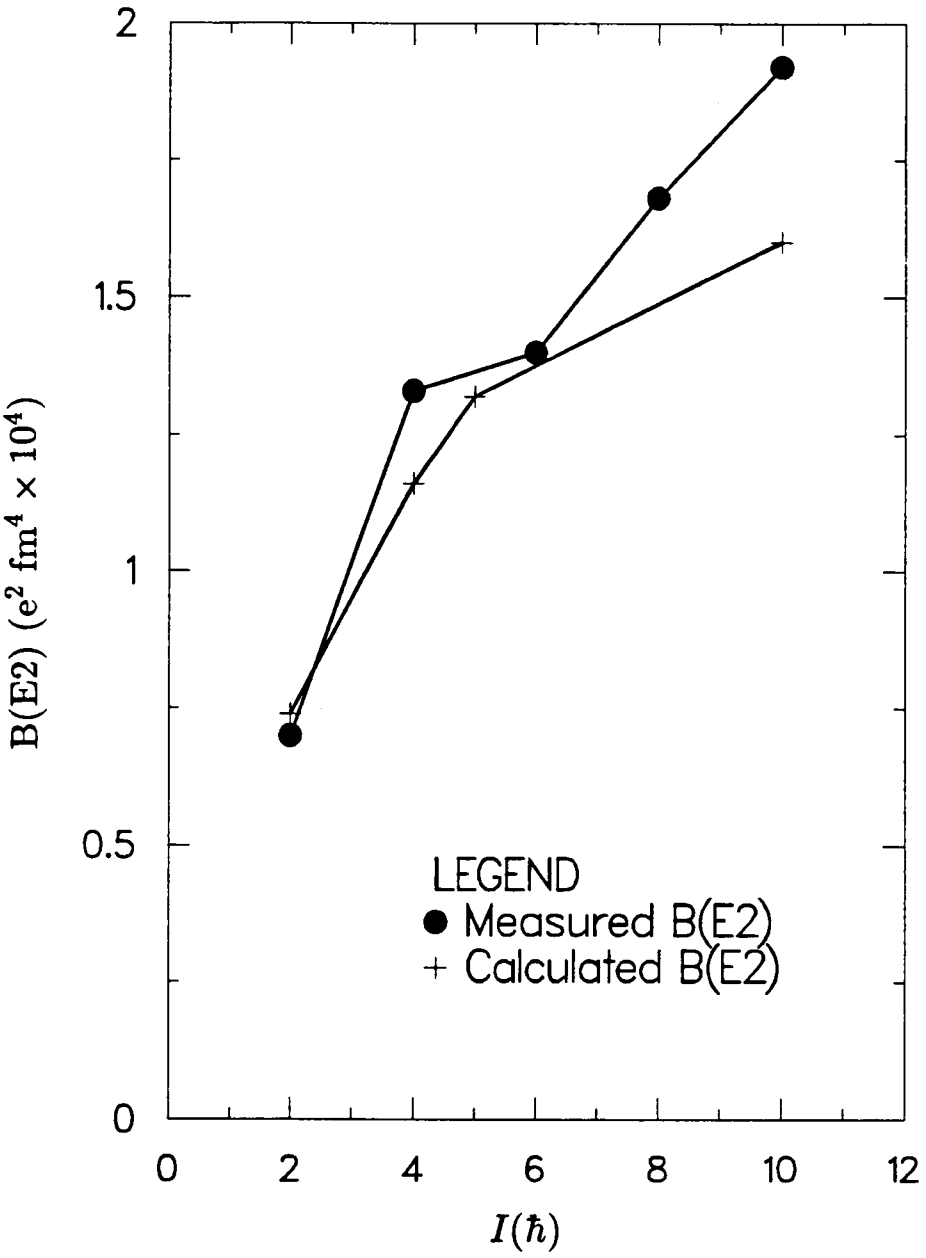

Figure 5.4: Measured $B(E2)$ values for the yrast band in ^{184}Pt (Garg *et al.*, 1986) (solid circles) versus the spin of the depopulating state. Also shown are calculated $B(E2)$ values using the equilibrium deformation parameters β_2 and γ extracted from the TRS calculations.

axial symmetry, the increasing experimental $B(E2)$ values suggest an increase in the parameter β_2 from ≈ 0.22 at $I = 2$ to ≈ 0.28 at $I = 10$.

Garg *et al.* have suggested one interpretation for this large increase in the $B(E2)$ values. They propose that the well-deformed prolate ground band interacts with the less-deformed oblate band at low spins, resulting in a smaller deformation for the yrast band. As the nucleus rotates, this mixing quickly disappears as the bands become further apart in energy and a rapid increase in the deformation is observed. Supporting this explanation is the observation of similar increases in the $B(E2)$ values of nuclei where shape coexistence is also thought to exist, *e.g.* ^{184}Hg and ^{186}Hg (Barfield *et al.*, 1984) and ^{176}Pt (Dracoulis *et al.*., 1986). The ^{176}Pt case is interesting because Bengtsson *et al.* (1986) have been able to explain the increase in the $B(E2)$ values within the context of a two band mixing phenomenon using TRS calculations similar to those reported above. The calculations suggest that the initial value of the deformation of the nucleus is greatly effected by the mixing of a triaxial band with the well-deformed prolate band at low spins. The calculations also show that by $I = 4$, the triaxial shape lies higher in energy than the prolate ground band and the mixing should no longer be present. This point agrees well with the measured $B(E2)$ values, which show a sharp rise going from the 2^+ to the 4^+ state. This case is slightly different from the heavier Pt and Hg nuclei, where shape coexistence results from a competition between small oblate and large prolate deformed bands.

In order to determine how well the TRS calculations match the observed rise in the $B(E2)$ values at spins 8 and 10 in ^{184}Pt, it is necessary to extract deformations for the ground band at higher rotational frequencies. At $I_x = 10$, equilibrium deformation parameters of $\beta_2 = 0.227$ and $\gamma = -12°$ are predicted for the ground band. While this deformation does not reproduce exactly the observed $B(E2)$ value at $I = 10$, the self-consistent HFBC calculations suggest that

part of the increase in the $B(E2)$ values is due to the core becoming triaxial. If a $\gamma = -12°$ is assumed, the quadrupole deformation at spin 10 would be on the order of 0.25 for the experimental data and not the 0.28 suggested by Garg *et al.* for an axial symmetric shape. In summary, the theoretical equilibrium deformations qualitatively reproduce the rise in the experimental $B(E2)$ values for ^{184}Pt. These calculations also suggest that other effects other than the two-band mixing proposal can account for increase in the quadrupole moments, *i.e.* centrifugal stretching and triaxiality.

Table 5.4 also lists the predicted deformations of the observed two-quasiparticle in ^{184}Pt. As discussed above, band 2 is thought to have the $\pi h_{9/2} \otimes \pi i_{13/2}$ configuration. In both shells the Fermi surface is near the $K = 1/2$ level and a polarizing effect towards larger β_2 values and positive γ values can be expected. This is confirmed by the calculation which gives $\beta_2 \approx 0.25$ and $\gamma \approx +10°$ for this configuration. On the other hand, bands 3–6 are all expected to have the configuration $\nu i_{13/2} \otimes \nu f_{7/2}$, however with different combinations of the signature. Since the Fermi surface lies in the upper part of the $\nu i_{13/2}$ shell, one would expect these bands to lie in the negative γ portion of the deformation plane with lower β_2 values. The calculations show that these bands initially have well-deformed axial symmetric shapes ($\beta_2 \approx 0.24$) at low spins. At some critical frequency, the driving forces of the $i_{13/2}$ quasineutrons cause a severe shape change to $\beta_2 \approx 0.185$ and $\gamma \approx -20°$. Since lifetime measurements are not available on the side bands in ^{184}Pt, it is not clear whether these bands actually possess the shapes indicated in Table 5.4. It is interesting to note however, that the observed bands in ^{184}Pt are predicted to have very different shapes ranging from $-60°$ to $+10°$ in the γ plane.

One suprising feature in the level scheme is the observation of interband $E2$ transitions between states 15^- and 13^- of bands 2 and 5. The 13^- states in these two bands lie only 13 keV apart which is suprising since K is likely to be

low for both structures, and the mixing should be strong. In order to estimate the configuration mixing of the two bands, a two-level mixing calculation has been performed. In such a calculation the perturbed $I^{\pi} = 13^{-}$ states are written in a form

$$\begin{aligned} \left|13^{-}, 3084\right\rangle &= a\,|2\rangle + b\,|5\rangle \\ \left|13^{-}, 3097\right\rangle &= b\,|2\rangle - a\,|5\rangle\,, \end{aligned} \tag{5.8}$$

where $|2\rangle$ and $|5\rangle$ are the unperturbed wave functions of bands 2 and 5. If one assumes that the 15^{-} states are unmixed (they lie 172 keV apart), Eq. 5.9 leads to the following $B(E2)$ branching ratios for the 15^{-} to 13^{-} transitions:

$$\begin{aligned} \frac{B(E2, 3443 \rightarrow 3097)}{B(E2, 3443 \rightarrow 3084)} &= \frac{b^2}{a^2} \\ \frac{B(E2, 3614 \rightarrow 3084)}{B(E2, 3614 \rightarrow 3097)} &= \frac{b^2}{a^2}. \end{aligned} \tag{5.9}$$

Experimental data from gated spectra yield values of 0.52 ± 0.17 and 0.53 ± 0.08 for these two respective $B(E2)$ ratio. The good agreement between the values verifies the assumption of just two-level mixing. Using the average value $b^2/a^2 = 0.52$ and the requirement that $a^2 + b^2 = 1$, values of $a = 0.81$ and $b = 0.59$ are obtained for the wave function amplitudes.

To calculate the interaction matrix element between the two 13^{-} states, one must solve the eigenvalue problem

$$\begin{pmatrix} e_1 & V \\ V^{*} & e_2 \end{pmatrix} \begin{pmatrix} a \\ b \end{pmatrix} = E \begin{pmatrix} a \\ b \end{pmatrix}, \tag{5.10}$$

where e_1 and e_2 are the unperturbed levels and V is the interaction matrix element. This then gives an expression for the energy of the mixed levels:

$$E_{\pm} = \frac{e_1 + e_2}{2} \pm \sqrt{\left(\frac{e_1 - e_2}{2}\right)^2 + |\,V\,|^2}. \tag{5.11}$$

From this expression and the condition that $a^2 + b^2 = 1$, a parameter p is defined such that

$$p = \left|\frac{e_2 - e_1}{2V}\right| = \sqrt{\frac{1}{4a^2(1-a^2)} - 1}. \tag{5.12}$$

The interaction matrix element is then determined by the relationship

$$|V| = \frac{E_+ - E_-}{2\sqrt{p^2+1}} \tag{5.13}$$

which is derived using Eq. 5.11 and Eq. 5.12. Since E_+ and E_- are just the energies of the two 13^- states and p is determined from a, the interaction matrix may now be calculated from observed quantities. For the data at hand, an interaction matrix element of only 6.3 keV is obtained. This small interaction is understandable for two reasons: (1) at $I = 13^-$, band 2 has a pure proton configuration while band 5 has a pure neutron configuration, and (2) these bands have very different deformations, with a difference in γ of about 30°. Both of these facts result in differing wave functions for the two bands, thus little mixing between the states.

5.3 Interpretation of Band Crossings in ^{184}Pt

Once the initial quasiparticle nature has been established for each band in ^{184}Pt at low frequency, the next step is to consider the origin of the observed band crossings at higher rotational frequencies. Before the current work by our group on ^{184}Pt, a question has persisted about whether the single upbend observed in the yrast band of ^{184}Pt results from $\nu i_{13/2}$ alignment or $\pi h_{9/2}$ alignment. In the $_{76}$Os nuclei and throughout the rare-earth region, the first observed band crossing has been attributed to the alignment of $i_{13/2}$ quasineutrons. However, in ^{180}Os and ^{181}Os (Lieder *et al.*) a second backbend is observed at $\hbar\omega \approx 0.37$ MeV, which could possibly be due to the alignment of $h_{9/2}$ quasiprotons. With an increase of two protons in going from Os to Pt, one might expect to observe this second crossing in the Pt isotopes at slightly lower rotational frequencies, because the

$h_{9/2}$ orbitals should lie closer to the Fermi surface. To determine the quasiparticle nature of the crossings in ^{184}Pt, it is instructive to compare the single-particle alignment, (i), defined in Eq. 5.2 as a function of the rotational frequency ($\hbar\omega$) for ^{184}Pt with the neighboring nuclei (see Fig. 5.5).

5.3.1 Choice of Reference Parameters

The choices for the references parameters, $\mathcal{J}_0$ and $\mathcal{J}_1$, are very important, because they influence significantly the shape of the alignment diagram. In well-deformed regions, $\mathcal{J}_0$ and $\mathcal{J}_1$ are chosen so as to make $i = 0$ for the ground band at all frequencies before the first band crossing. To determine the reference parameters for these cases, one uses the definition of the kinematical moment of inertia defined in 2.4:

$$\mathcal{J}^{(1)} = \frac{I_x}{\omega} = \frac{i}{\omega} + (\mathcal{J}_0 + \mathcal{J}_1\omega^2). \tag{5.14}$$

Thus, by plotting $\mathcal{J}^{(1)}$ as a function of ω^2 for the ground band, one should obtain a linear relationship where the slope is equivalent to $\mathcal{J}_1$ and the y-intercept defines $\mathcal{J}_0$.

In transitional regions, the fitting of the ground band is complicated by the fact that the nuclear cores are soft with respect to deformation. For example, both TRS calculations and experimental lifetime measurements indicate that the deformation increases rapidly in the ground band of ^{184}Pt as a function of spin. Thus by using the procedure described for fitting the reference parameters, one does not describe very well the alignment after the first crossing in the yrast band and in the multi-quasiparticle bands in ^{184}Pt. More specifically, the resulting value for $\mathcal{J}_1$ is too large to describe the multi-quasiparticle bands well, causing a drooping in the alignment curves of all bands at the highest frequencies.

To remedy this situation, reference parameters for ^{184}Pt were extracted

from the multi-quasiparticle bands, where the deformations should be more stable for constant quasiparticle configuration. However, Eq. 5.14 cannot be used to extract these parameters for the multiquasiparticle bands, because i is no longer zero for these bands. The confusing effect of the alignment term in $\mathcal{J}^{(1)}$ is eliminated by defining a moment of inertia based upon second differences

$$\mathcal{J}^{(2)} = \frac{dI_x}{d\omega} = \mathcal{J}_0 + 3\mathcal{J}_1\omega^2, \tag{5.15}$$

where $\mathcal{J}^{(2)}$ is the dynamical moment of inertia defined in 2.4.

In some ways this analysis is not completely satisfying either, since TRS calculations show that the multi-quasiparticle bands exhibit different equilibrium shapes, indicating different optimum values for $\mathcal{J}_0$ and $\mathcal{J}_1$. Because the choice of $\mathcal{J}_0$ and $\mathcal{J}_1$ determines the shape of the alignment curve, it is important that one use a single pair of reference parameters when comparing alignment plots for adjacent nuclei. Because of this, a systematic study of the dynamical moment of inertia has been done for the nuclei around ^{184}Pt, and a pair of optimum reference parameters have been chosen which seem to describe reasonably well the alignments of all bands in the region around ^{184}Pt.

These parameters, $\mathcal{J}_0 = 30\ \hbar^2\ \mathrm{MeV}^{-1}$ and $\mathcal{J}_1 = 40\ hbar^4\ \mathrm{MeV}^{-3}$, are not without their deficiencies. For example, Fig. 5.1 shows that the ground band has negative alignment before the first crossing. The initial alignment of a band is mainly dependent on $\mathcal{J}_0$, indicating this term is too large for the ground band. The $\mathcal{J}^{(2)}$ analysis supports this conclusion, indicating that $\mathcal{J}_0 \approx 26$ for the ground bands in $^{180-184}$Pt. This brings up the possibility that the initial alignments in the one- and two-quasiparticle bands may also be artificially low due to an overly large value for $\mathcal{J}_0$. This fact underscores the importance of keeping the reference parameters constant when comparing alignments between different bands. If the $\mathcal{J}_0$ results in an underestimation of the initial single-particle alignment, this is

done consistently for all bands, and thus additivity of alignments is conserved on a relative basis.

Another possible deficiency in the choice of references parameters is connected with the $\mathcal{J}_1$ term. Both the yrast band and band 2 in ^{184}Pt are seen to the highest spins of any nuclei in the region. This allows for a large range, in frequency,which seems devoid of any band crossings. However, the current choice of $\mathcal{J}_1$ gives constant alignment in band 2 while the yrast band continues to gradually gain alignment. If an $\mathcal{J}_1$ of 63 is chosen, the alignment of the yrast band remains constant at the highest frequencies, however band 2 loses alignment quickly at its highest observed spins, indicating that $\mathcal{J}_1$ is too large for band 2. Two possible explanations for this feature are possible: (1) the gradual alignment gain in the yrast band using a $\mathcal{J}_1 = 40$ is due to a large interaction band crossing or (2) the yrast band and band 2 have very different deformations indicated by the different values in $\mathcal{J}_1$ needed to give constant alignment at the highest frequencies. The implications of these two explanations and their effects on how the band crossing data is interpreted is discussed in the next several subsections.

5.3.2 Experimental Analysis of Band Crossings

The yrast band of ^{184}Pt was measured up to $I = 20\ \hbar$ by Beshai *et al.* (1976), and the singly observed upbend was interpreted to result from $\nu i_{13/2}$ quasiparticle alignment. Later Kahler *et al.* (1978) performed a blocking measurement using ^{185}Au and observed bands built on the $\frac{1}{2}[541]$ ($h_{9/2}$) and $\frac{1}{2}[660]$ ($i_{13/2}$) proton Nilsson states. The observation of an upbend in the latter and no crossing up to the observed angular momentum in the former led to the conclusion that the alignment of the $\pi h_{9/2}$ orbital was responsible for the crossing in ^{184}Pt. Recently, new data have been collected on both of these nuclei and nuclei in the surrounding region, and it has become quite clear that neither explanation adequately explains

all the observed band crossing phenomena. One must remember that this is a very complicated region due to the fact that large differences in the shape may occur between bands of different quasiparticle composition. This was shown in the previous section where the low-frequency deformations for the observed bands in ^{184}Pt are predicted to take on shapes ranging from $\gamma = -60°$ to $\gamma = +15°$.

From the most recent measurements on ^{185}Au (Larabee *et al.*, 1986) and ^{184}Pt (see this work), a proposal has been made that *both* $\nu i_{13/2}$ and $\pi h_{9/2}$ alignments are taking place below $\hbar\omega = 0.30$ MeV in these nuclei. The evidence supporting this proposal is best illustrated by comparing the alignment properties of the observed bands in ^{184}Pt with those of the neighboring odd-A nuclei. Fig. 5.5 shows such a plot for the bands of interest in the neighborhood of $N = 106$ and $Z = 78$. In the diagram for ^{184}Pt, all two-quasiparticle bands experience an upbend and gain roughly 5-6 units of alignment. On the other hand, the initial upbend in the yrast band gains approximately 10 units of alignment. Band 2, whose quasiparticle configuration is $\pi h_{9/2} \otimes \pi i_{13/2}$, shows an upbend at $\hbar\omega \approx 0.28$ MeV. Since the $\pi h_{9/2}$ alignment is blocked in this band, the single observed band crossing must be due to $i_{13/2}$ (AB) quasineutrons. Because the alignment gain is roughly half that observed in the yrast band, a reasonable conclusion is that the alignment gain in the yrast band cannot be attributed to the alignment of a single pair of $i_{13/2}$ quasineutrons. Due to this blocking experiment with the $\pi h_{9/2}$ orbital, it is logical to propose that the $\pi h_{9/2}$ alignment is responsible for the added alignment gain in the yrast band.

If the near degenerate crossings of an $(\nu i_{13/2})^2$ band and a $(\pi h_{9/2})^2$ band is the correct interpretation for the observed alignment gain in the yrast band of ^{184}Pt, then a similar type blocking experiment utilizing odd-Z nuclei with the $h_{9/2}$ orbital should confirm this argument. In ^{183}Ir (Janzen *et al.*, 1987), rotational bands built on the $\pi h_{9/2}$ and $\pi d_{5/2}$ ($\frac{5}{2}$[402]) orbitals are observed. It is clear from

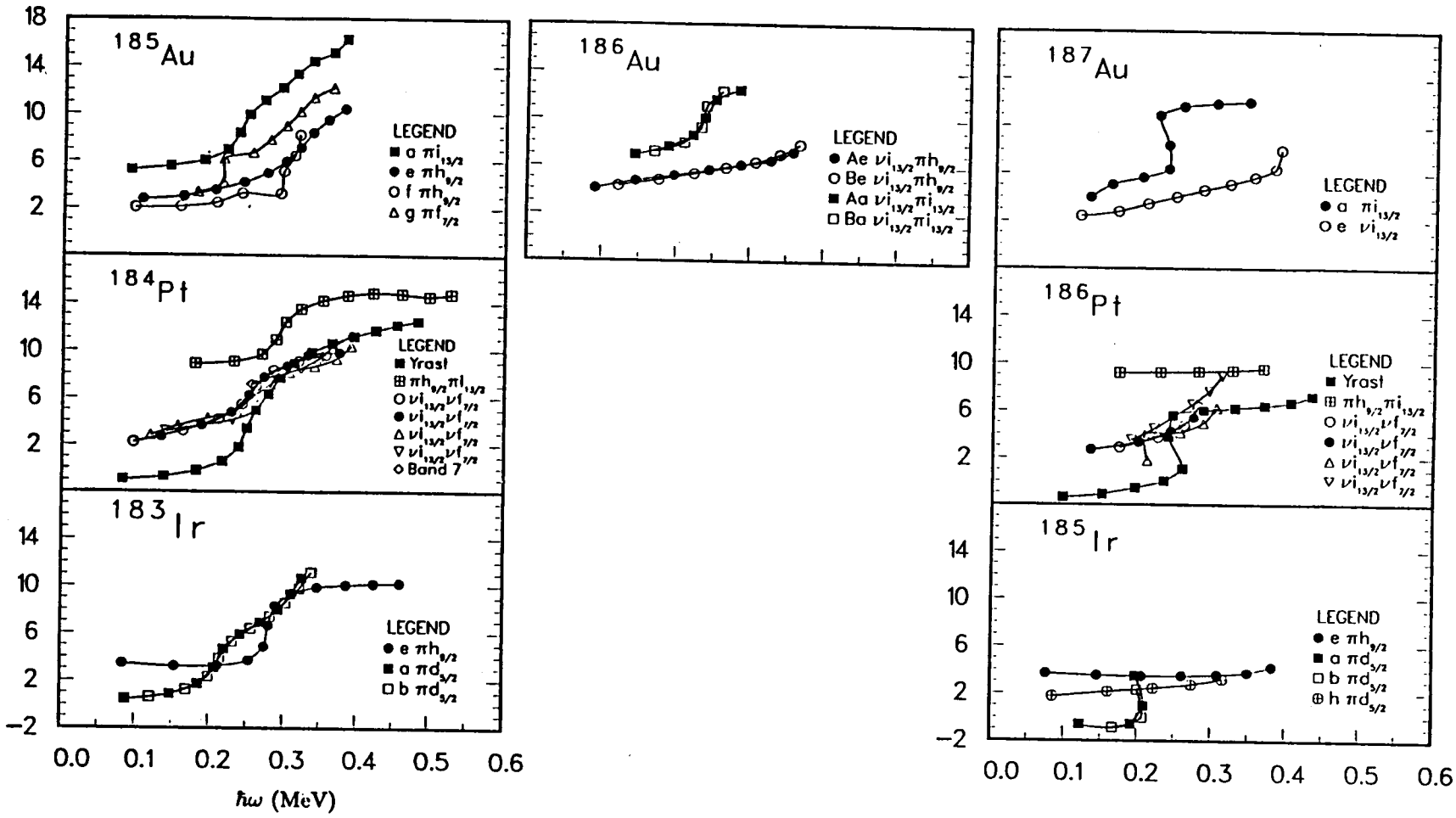

Figure 5.5: Alignment diagrams for the bands of interest in the region of ^{184}Pt.

the diagram for ^{183}Ir in Fig. 5.5 that the alignments for these two bands are quite different. In the $h_{9/2}$ band, an alignment gain of 6.8 $\hbar$ is seen at $\hbar\omega \approx 0.29$ MeV. While the total alignment gain cannot be accurately determined in the $d_{5/2}$ band, it appears to be at least 10 $\hbar$. Furthermore, the interaction in the $d_{5/2}$ band occurs over a frequency range comparable to that for the yrast band in ^{184}Pt, and it appears that this interaction region is composed of two distinct crossings. The conclusions are the same as in ^{184}Pt, the $h_{9/2}$ band undergoes the expected $\nu i_{13/2}$ crossing, while the $d_{5/2}$ band experiences both the neutron and proton crossings.

In the other neighboring odd-Z isotone of ^{184}Pt, ^{185}Au, the presence of two crossings is not as clear. Instead of a rotational band built on the $d_{5/2}$ orbital, a band is observed which is associated with the $\frac{1}{2}$[660] Nilsson orbital ($i_{13/2}$). Similar blocking arguments can be employed, because a one-quasiparticle band with an $h_{9/2}$ composition is also observed in this nucleus as well. The $i_{13/2}$ band parallels quite closely the yrast band in ^{184}Pt, with both upbends covering the same frequency range and gaining roughly the same amount of alignment. On the other hand, the alignment gain in the $h_{9/2}$ band is only 7.2 $\hbar$, and the crossing frequency is delayed to $\hbar\omega \approx 0.32$ MeV. Certainly, the alignment differences as they stand do not argue for a second crossing in the $\pi i_{13/2}$ band, because the observed differences are less than that expected for a $\nu i_{13/2}$ alignment. However, both bands are not observed through the crossing, and thus, the additivity argument is inconclusive.

Further support for both proton and neutron alignment comes in Fig. 5.6 from second moment-of-inertia plots, which are sensitive to changes in the alignment. All three bands, which may experience two degenerate alignments, exhibit two peaks in Fig. 5.6, one at $\hbar\omega \approx 0.24$ MeV and another at roughly $\hbar\omega \approx 0.30$ MeV. On the other hand, the $\mathcal{J}^{(2)}$ curve for the three bands discussed above with an $\pi h_{9/2}$ component, show only a single intense peak. Since the $\mathcal{J}^{(2)}$ measures the continuity of a rotational band, a peak in such a plot is indicative of a disconti-

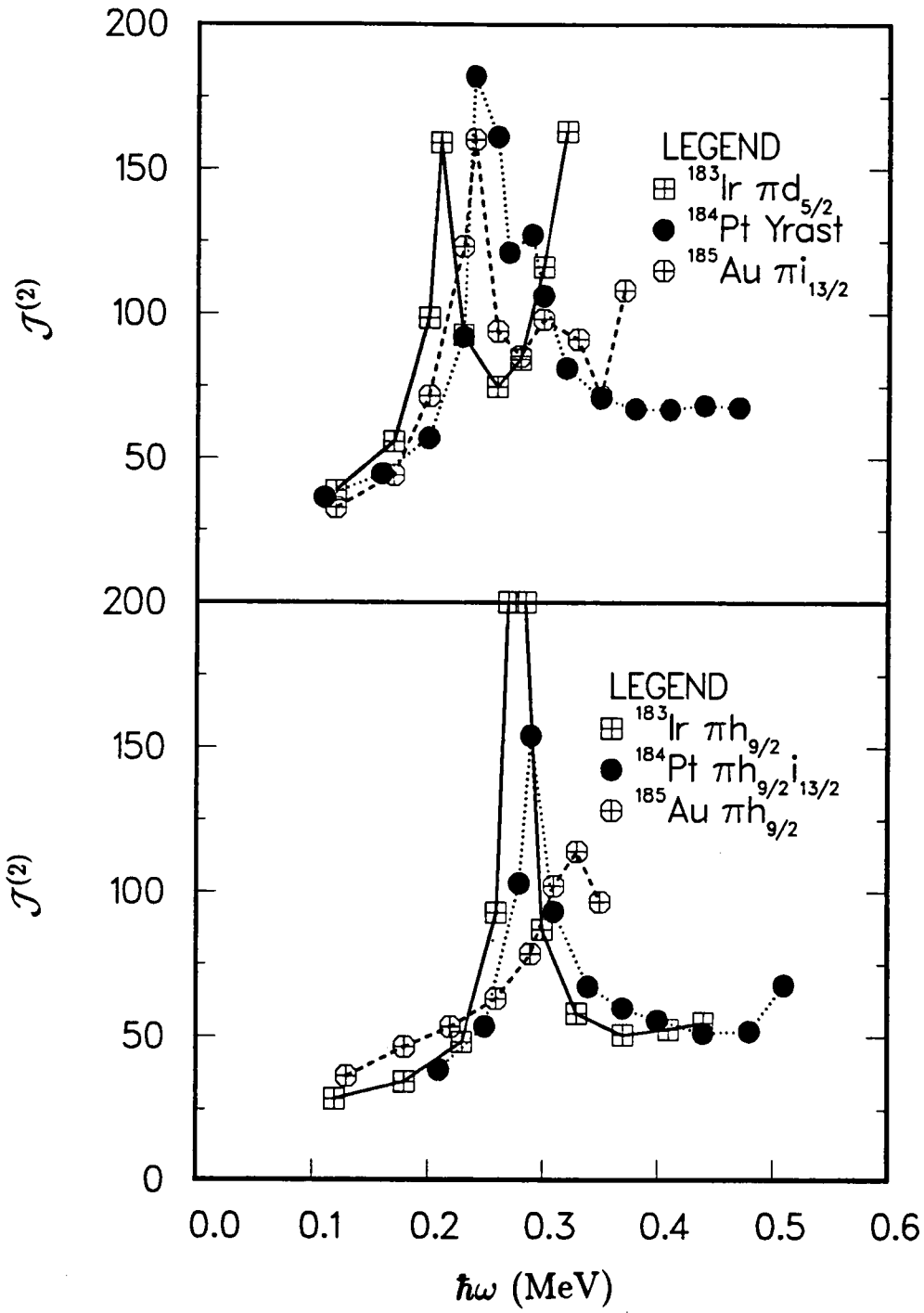

Figure 5.6: Plot of the dynamical moments of inertia, $\mathcal{J}^{(2)}$, for bands in the $N = 106$ isotones.

nuity in the band, and such discontinuities may indicate a band crossing. Thus, one interpretation for the presence of two humps in the $J^{(2)}$ plot in Fig. 5.6 is that these bands experience two band crossings, and the most likely candidates for these crossing are the $\nu i_{13/2}$ (AB) and $\pi h_{9/2}$ (ef) quasiparticles.

The proposal that both $\nu i_{13/2}$ and $\pi h_{9/2}$ are aligning at low rotational frequencies is also supported by other blocking arguments involving the $\pi h_{9/2}$ orbital for the bands plotted in Fig. 5.5. This evidence is summarized as follows:

1. In the odd-odd nucleus, ^{186}Au (Janzen *et al.*, 1986), a single crossing at $\hbar\omega \approx 0.26$ MeV is observed in bands with the configuration $\nu i_{13/2} \otimes \pi i_{13/2}$ while no crossing is observed in bands with the configuration $\nu i_{13/2} \otimes \pi h_{9/2}$. Since the $\nu i_{13/2}$ crossing is blocked in both cases and the $\pi h_{9/2}$ crossing is blocked only for the Ae and Be bands, the single band crossing observed in the Aa and Ba bands is most likely due to $h_{9/2}$ quasiprotons.

2. In ^{187}Au (Johansson *et al.*, 1987), the $\pi i_{13/2}$ band experiences a band crossing at $\hbar\omega \approx 0.26$ which gains 6 $\hbar$ units of alignment, while the $\pi h_{9/2}$ band indicates no crossings up to $\hbar\omega = 0.40$. This fact is important, because it indicates that the observed crossing in the $\pi i_{13/2}$ band is due to $h_{9/2}$ protons and that the $\nu i_{13/2}$ crossing is delayed up to at least $\hbar\omega = 0.40$ MeV.

3. The yrast band in ^{186}Pt experiences a sharp crossing at $\hbar\omega = 0.25$ and gains 7 $\hbar$ units of alignment. The $\pi h_{9/2} \otimes \pi i_{13/2}$ two-quasiparticle band indicates no crossing up to $\hbar\omega = 0.40$ MeV. This, coupled with what is observed in ^{187}Au supports the contention that $h_{9/2}$ quasiprotons are responsible for the observed alignments in Fig. 5.5 at $N = 108$, and that the $\nu i_{13/2}$ (AB) crossing occurs at higher frequencies.

4. The absence of any crossings in the $\pi h_{9/2}$ band in ^{185}Ir supports the conclusions reached above concerning the status of the neutron AB-crossing and

the proton ef-crossing at $N = 108$.

While the above discussion indicates that the $h_{9/2}$ $\frac{1}{2}$[541] quasiprotons align themselves at low rotational frequencies, it is important to review the above arguments and point out some systematic information which argues for a single crossing proposal for the yrast band in ^{184}Pt. One major objection for proposing a low-frequency $\pi h_{9/2}$ crossing lies in the fact that all theoretical calculations, using current parameters for the pairing constant, G, for this region and the universal parameters of the Woods-Saxon potential, predict that the $h_{9/2}$ quasiprotons will not align until $\hbar\omega > 0.35$ MeV for ^{184}Pt. These theoretical predictions are discussed in detail in section 5.3.3.

Focusing on the experimental data, much of the blocking and additivity arguments at $N = 106$ involve the discrepancy in alignment between the yrast band in ^{184}Pt, the $d_{5/2}$ band in ^{183}Ir, and the $\pi i_{13/2}$ band is ^{185}Au as compared with the alignment gained in bands with a $\pi h_{9/2}$ component for these nuclei. It should be noted that such discrepancies also exist in Re and Ta nuclei where one-quasiparticle $h_{9/2}$ bands are also observed. As an example, Fig. 5.7 shows ^{179}Re (Lieder), where the alignment, the interaction strength, and the crossing frequencies are significantly different when comparing bands associated with $\pi d_{5/2}$ and $\pi h_{11/2}$ quasiparticles to those associated with a $h_{9/2}$ configuration. For these bands it is thought that all observed alignments are due to the crossing of $\nu i_{13/2}$ quasiparticles only. Much of these discrepancies have been attributed to shape differences between the bands. One other effect which is known to effect the properties of band crossings is the pairing. It is not obvious that this is important in these cases, because the odd-proton should not effect directly the pairing field associated with the aligning quasineutrons. However, the pairing field may be effected indirectly through the deformation.

It is quite reasonable to expect the same situation to occur in Ir and

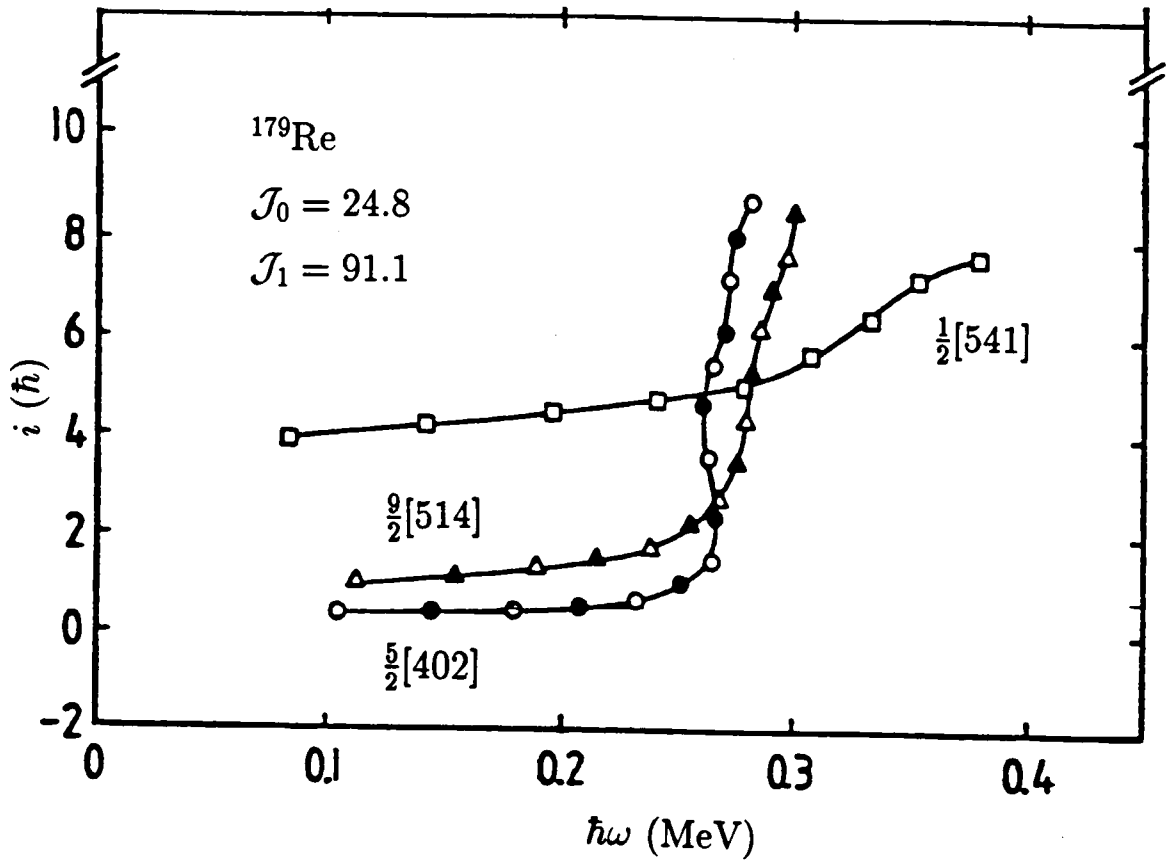

Figure 5.7: Alignment diagram for ^{179}Re (Lieder). Notice that the alignment in the $h_{9/2}$ quasiproton band differs from that in the $\pi d_{5/2}$ ($\frac{5}{2}$[402]) and $\pi h_{11/2}$ ($\frac{9}{2}$[514]) bands, even though the crossings in all bands are attributed to $i_{13/2}$ quasineutrons.

possibly Au nuclei, where there is a loss of alignment in bands with an $h_{9/2}$ component. Therefore, it may be possible that both the yrast band and band 2 in ^{184}Pt experience only one crossing and any alignment differences are due to shape effects. This explanation has some validity if one compares the alignments of both bands after the crossing. As mentioned above, the $\mathcal{J}_1$ reference was chosen so that the alignment in band 2 would be nearly constant after the crossing. The yrast band on the other hand gradually gains alignment after the initial upbend. As mentioned in section 5.3.1, this may be due to a band crossing involving a large interaction or it may be due to a reference problem. The latter explanation implies that the bands have different shapes. If only a single $\nu i_{13/2}$ crossing is occuring in both bands, this argument has some validity. The TRS calculations show that the (AB) neutron crossing polarizes the nucleus at a $\gamma \approx -20°$ while the $\pi h_{9/2} \otimes \pi i_{13/2} \otimes (\nu i_{13/2})^2$ configuration minimizes in γ at roughly $+10°$.

Further support for only a single crossing in these bands comes from comparing I_x plots for the even-even Pt isotopes with those of Os (see Fig. 5.8). These plots are preferable over alignment plots in some instances, because they are independent of the reference parameters. For ^{182}Os (Lieder *et al.*, 1982) and ^{184}Os (Neskakis *et al.*, 1976), the single backbend in the yrast line has been interpreted as resulting from the alignment of a single pair of $i_{13/2}$ quasineutrons. The behavior of the I_x plots for the lighter two isotones do not reflect this same sharp backbending behavior in the region of the first crossing. In ^{180}Os (Lieder *et al.*, 1987), the first crossing occurs over a wide frequency range. Deviations from the gradual gain in alignment indicative of large interaction crossings may indicate that more than one alignment is occurring in this crossing region for ^{180}Os. If two low-frequency band crossings are present, one might propose that the second pair of aligning quasiparticles may be $\pi h_{9/2}$. It is more reasonable however to attribute the $\pi h_{9/2}$ quasiparticle alignment to the sharp backbend observed in this nucleus

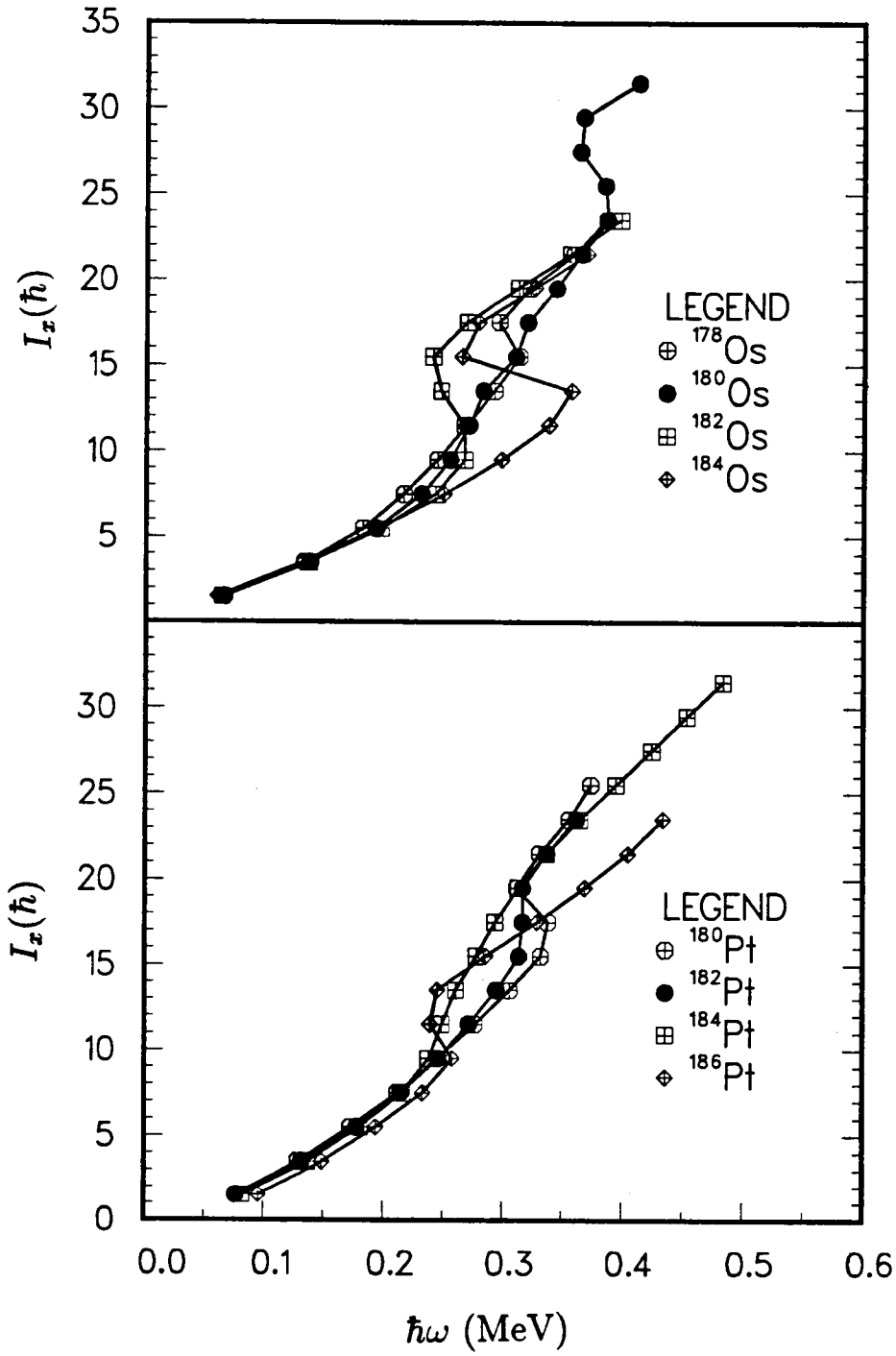

Figure 5.8: Diagram of the angular momentum projected onto the rotational axis, I_x, versus the rotational frequency, $\hbar\omega$, for (a) Os isotopes and (b) Pt isotopes.

at $\hbar\omega = 0.37$ MeV. On the other hand, ^{178}Os (Dracoulis *et al.*, 1980) begins to smoothly gain alignment in the same fashion as ^{180}Os, however at a critical frequency, $\hbar\omega = 0.30$, it experiences a sharp upbend indicating that two low-frequency crossings occur in this nucleus as well.

While the I_x plots for the Os nuclei indicate structural differences among the isotopes in the crossing region, the nearly identical values for I_x after the first crossings have occurred suggests the opposite, *i.e.* that the same alignment processes are taking place in all four nuclei. In view of the sharp backbends for ^{182}Os and ^{184}Os, the most likely explanation for the equivalent alignments is that all bands experience a single $(\nu i_{13/2})^2$ band crossing. In fact, the $\pi h_{9/2}$ alignment is ruled out due to it occuring at a higher frequency in ^{180}Os. If this interpretation is correct, the anomalies observed in ^{178}Os and ^{180}Os, where the crossing region suggests two alignments, become interesting. These anomalies indicate that the interaction between the crossing bands does not remain constant throughout the crossing region but may experience very sharp changes at critical rotational frequencies.

In Fig. 5.8b, the I_x plots for the even-even Pt isotopes which are isotones to the plotted Os nuclei are shown. This diagram shows that even though structural changes occur in the I_x plot for ^{180}Pt (Riezebos, 1987), ^{182}Pt (Popescu, 1986), and ^{184}Pt in the region of the crossing, the total I_x after the crossings is nearly identical for all three nuclei and similar to values reached in the Os nuclei. This fact would suggest that the alignment processes involved in the Os nuclei also are responsible for the observed crossing in the ^{184}Pt isotones. This picture would be very consistent if it were not for the obvious difference of ^{186}Pt. This nucleus has a reduced value of I_x when compared with its isotonic partners. Since the blocking arguments discussed above indicate that $\pi h_{9/2}$ protons are responsible for the observed crossing in ^{186}Pt, one interpretation is that the difference in I_x between

this nucleus and the other Pt isotopes is due to the absence of a $\nu i_{13/2}$ alignment in ^{186}Pt. However, it should be noted that ^{186}Pt is truly a transitional nucleus. All heavier Pt nuclei are thought to exhibit predominantly oblate shapes while all lighter Pt isotopes are believed to exhibit predominantly prolate structures. Thus one should be very careful in attributing the differences in the I_x plots for ^{186}Pt to simple alignment effects. It is quite possible that the decrease in alignment is due to more fundamental structural differences.

In summary, by examining the alignment diagrams pictured in Fig. 5.5, it seems logical that a low-frequency $h_{9/2}$ proton crossing is present in Ir-Au nuclei at $N = 106$ and $N = 108$. However, examinations of the systematics in the lighter isotones (Os and Re) suggest that the alignment differences observed between bands with and without an $h_{9/2}$ component may be due to shape changes effecting the alignment of the $\nu i_{13/2}$ crossing and not due to a low $(h_{9/2})^2$ alignment. The latter explanation hinges on the presence of changing interaction strengths in large interaction crossings. While this possibility has not been examined in great detail, it is a reasonable hypothesis in view of the fact that large shape fluctuations are thought to occur in this region due to aligning quasiparticles. If one subscribes to the single $\nu i_{13/2}$ crossing proposal at $N = 106$, the $N = 108$ nuclei truly become anomalous, because it is clear that only one crossing is present in these nuclei and blocking arguments strongly suggest that this crossing is due to $(h_{9/2})^2$ quasiprotons and not AB quasineutrons.

Since blocking arguments are not totally conclusive for identifying the quasiparticle structure of the crossings in the yrast band in ^{184}Pt, it is very difficult to determine what crossings are responsible for the 5 unit gains in alignment in the two-quasineutron bands, 3-6. These bands are expected to have the configuration $\nu i_{13/2} \otimes \nu f_{7/2}$; however, the signature combinations for each band are not certain. Since all four bands are believed to have a $\frac{9}{2}[624]$ component, the first

neutron crossing, AB, is blocked in all of these bands. However, secondary neutron crossings BC and AD are not prohibited from occuring. Also, the $(\pi h_{9/2})^2$ alignment is not blocked and must be considered in view of the above arguments.

In order to establish the initial signature combinations for bands 5 and 6 in ^{184}Pt, it is instructive to examine bands which should have the identical configuration in ^{180,182}Os. For both these nuclei, the two signatures experience band crossings at different rotational frequencies. In ^{181}Os, this same shift in the crossing frequencies is observed in the A and B signatures of the $\frac{9}{2}$[624] quasiparticle bands and is attributed to the difference in the crossing frequencies of the BC and AD alignments. The shift in crossing frequencies in the even-even Os isotopes is most likely due to the same effect, indicating that the signature combination for these $\nu i_{13/2} \otimes \nu f_{7/2}$ bands are AE and BE.

This assignment in the Os nuclei is also supported by the observed signature splitting between these two-quasineutron bands before the first band crossing. For example, Carpenter *et al.* (1986) have done an analysis on the γ driving forces of the A and B $i_{13/2}$ and E and F $f_{7/2}$ one-quasineutron bands in ^{183,185}Pt. This analysis has shown that the signature splitting observed between the two signatures of the $i_{13/2}$ quasineutron structure results from the negative γ deformations preferred by these bands due to the driving forces imposed by the $\frac{9}{2}$[624] orbital. On the other hand, the signature partners of the $\nu f_{7/2}$ structure show no signature splitting due to their preference for axial symmetric shapes. Thus, if the two-quasineutron structures under consideration were to differ in their $f_{7/2}$ component, *e.g.* an assigned AE and AF configuration, no signature splitting would be expected in view of the analysis done for the odd-Pt nuclei.

Since one would expect the two-quasineutron bands in ^{184}Pt to have the same signature combination as the analog band in ^{182}Os, bands 5 and 6 most likely have the configuration AE and BE respectively. This assignment is confirmed

by the observed signature splitting between these two bands before the crossing which is on the order of what is observed in the odd-N neighbors. Bands 3 and 4, therefore, most likely have the configurations AF and BF respectively. One suprising feature of these bands is the lack of signature splitting throughout the observed frequency range. This same lack of signature splitting is also observed in the high-K bands in the Os nuclei as well. Since signature splitting in high-K bands results from a mixing of a $K = 1/2$ component into the band, a lack of signature splitting would indicate that this mixture is not present. Since the analysis of the interaction matrix elements performed in section 5.2 suggest that these high-K bands do not mix with low-K bands, the lack of signature splitting in these bands agrees very well with this explanation. It should also be noted that the HFBC calculations under discussion should not reflect this observation, since they do not couple these quasiparticles together during the calculation of the total Routhian.

While the observed band crossings in the Os nuclei allowed for the determination of the most probable quasiparticle configuration for bands 3-6 in ^{184}Pt, the exact nature of the observed band crossing is more difficult to deduce due to the fact that low frequency neutron and proton band crossings are predicted to occur in Pt nuclei. In order to determine which alignments are most probable in these bands, a more theoretical examination of the predicted crossings must be carried out.

5.3.3 Theoretical Analysis of Band Crossings

The standard model for predicting the rotational frequencies at which band crossings occur is the cranked-shell model of Bengtsson and Frauendorf (see section 2.8). However, one of its deficiencies is that it supplies no direct information about the nuclear shape. While it is possible to infer nuclear deformations from

the experimental crossing frequencies, this is most believable in well-deformed nuclei where large fluctuations in the shape are not thought to occur. In the Pt-Au region, the cores are soft and the situation is complicated by the fact that the experimental data are not totally conclusive over which band crossings are responsible for the observed alignments. Therefore, it is preferable to extract theoretical crossings in a more self-consistent manner as was shown in section 2.9, using Strutinsky-HFBC calculations which are performed as a function of the deformation. A detailed analysis of these calculations follow for the yrast band in ^{184}Pt, partly to examine the validity of the double crossing proposal and partly to show how these calculations are used to described observed phenomena.

Fig. 5.9 shows a succession of total Routhian surfaces as a function of rotational frequency for the yrast band in ^{184}Pt. The pairing was varied as a function of ω using equation Eq. 5.5 with $\omega_c = 0.70$ MeV for both neutrons and protons. Since the ground band is predicted to be deformation soft, it should be sensitive to the driving forces of aligning quasiparticles, and this effect should be observed in the TRS calculations. Also represented in each TRS map shown in Fig. 5.9 is a "path of least resistance". This path is defined as the line connecting the γ points which lie lowest in energy when minimized with respect to β_2 and β_4. The projection of the energy and spin along this path for the proton, neutron and total Routhian contributions is also shown in Fig. 5.9 for each frequency.

As was discussed in section 5.2, the ground band corresponds to an axial symmetric prolate shape. The γ deformation varies little up through $\hbar\omega = 0.20$ MeV as was shown in Table 5.2. Other zero-quasiparticle shapes are predicted to exist at low rotational frequencies as well, *i.e.* collective and non-collective oblate shapes and a non-collective prolate structure. Currently, structures corresponding to the non-collective shapes have not been observed in ^{184}Pt, however, structures believed to be associated with a $\gamma = -120°$ prolate shape have recently been

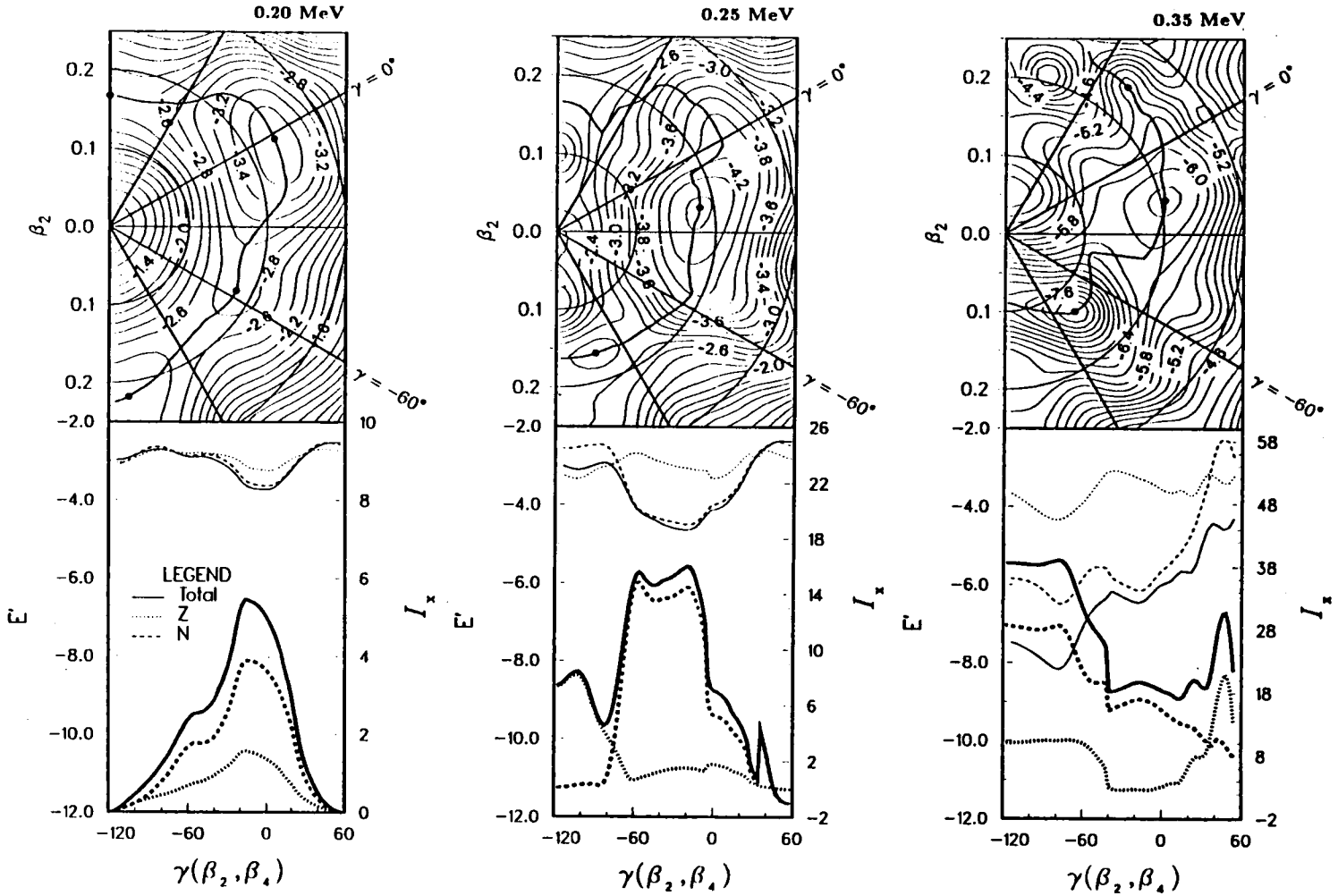

Figure 5.9: TRS maps (upper diagrams) and energy and spin projections (lower diagrams for the quasiparticle vacuum configuration in ^{184}Pt at selected rotational frequencies. The spin projections are the given by the thicker lines, and the contour levels are separated by 0.2 MeV.

identified in ^{182}Os (Lieder *et al.*, 1987).

At $\hbar\omega = 0.25$ MeV, a transition to smaller β_2 values (0.182) and negative γ values ($-20°$) is observed in Fig. 5.9 for the prolate structure. From the discussions in section 2.9, such shape changes are brought about by aligning quasiparticles when the Fermi level lies in the middle of a shell. Since $i_{13/2}$ quasineutrons with $K = 9/2$ meet this criterion, one attributes this shape transition to the crossing of the ground band with the $(\nu i_{13/2})^2$ quasiparticle band. This is confirmed by examining the neutron energy projection whose shape is almost identical to the total Routhian projection in the region of this minimum. This close correspondence also indicates that the proton core does not in any way resist the driving forces of the aligning quasineutrons. Another signature that quasineutrons are aligning comes about by examining the spin projections which show that there is a large increase in the total angular momentum when going from $\hbar\omega = 0.20$ MeV to 0.25 MeV in the region of the minimum.

Since the rotational frequency at which quasiparticles align is dependent on the deformation, it is reasonable to expect that not all of the β_2-γ plane around $\gamma = 0°$ is associated with this two-quasineutron configuration, $(\nu i_{13/2})^2$, at $\hbar\omega = 0.25$ MeV. In fact, boundaries between different quasiparticle configurations can be roughly mapped out in some cases where rapid changes in the β_2 deformation of the γ projections occur. Such a change is observed at $\gamma \approx -5°$ for the 0.25 MeV TRS map, and this marks a boundary which divides the quasineutron AB configuration with the ground band configuration. This boundary is also reflected in the energy projections, where a change in structure is indicated by a discontinuity in both the neutron and proton projections, and the spin projections, where a rapid rise in the angular momentum for the neutron spin projection occurs at this pseudo boundary.

Other changes in structure at $\hbar\omega = 0.25$ are associated with the minimum

at $\gamma \approx -100°$. From the spin and energy projections, it is clear that this structure is associated with aligning quasiprotons. Since these quasiprotons are adding roughly 8 units of alignment to the system, this minimum is most likely due to alignment of $(\pi h_{9/2})^2$ quasiparticles. It should also be noted that the collective oblate ground band experiences a $(\nu i_{13/2})^2$ alignment by 0.25 MeV, driving the nucleus towards $\gamma = -30°$. Its equilibrium deformation is obscured by the AB alignment associated with the prolate structure. Because of this fact, the minimum associated with the yrast band at $\gamma = -20°$ is most likely perturbed by the aligned oblate structure. Thus the β_2 deformation for the yrast band is probably larger than indicated by the the TRS map due to this mixing of structures.

At $\hbar\omega = 0.35$ the maps of the total Routhian surface indicates that other changes in structure have occurred. A minimum associated with $(\nu i_{13/2})^2$ structure is still present, however its quadrupole deformation has increased to $\beta_2 = 0.205$ which may be due to a decrease in mixing with the two-quasineutron oblate structure. A secondary prolate-like minimum appears at this frequency at $\beta_2 = 0.242$ and $\gamma = +20°$. The proton Fermi surface is close to the $K = 1/2$ level of the $h_{9/2}$ shell, and therefore this alignment is associated with an $(\pi h_{9/2})^2$ band crossing. The entire configuration of this band $(\pi h_{9/2})^2 \otimes (\nu i_{13/2})^2$ is deduced from CSM diagrams which indicate that the AB quasineutrons have aligned in this region of deformation before $\hbar\omega = 0.35$ MeV. From the projections, the boundary between the proton ground and ef configuration at this frequency occurs at $\gamma \approx 10°$.

Even though the two structures, $(\nu i_{13/2})^2$ and $(\pi h_{9/2})^2 \otimes (\nu i_{13/2})^2$, are present in the TRS map for the yrast configuration at $\hbar\omega = 0.35$, the two-quasiparticle structure (AB) lies significantly lower in energy ($\approx$ 750 keV) than the four-quasiparticle structure ($ABef$). Thus the HFBC-Strutinsky calculations favor the explanation that the upbend in ^{184}Pt is due to only $(\nu i_{13/2})^2$ quasineu-

trons, and that an excited four-quasiparticle band, $ABef$, should be observed at higher excitation energies. One of the experimental evidences for a low frequency $\pi h_{9/2}$ crossing comes from alignment arguments. However, from the spin projections, both the two- and four-quasiparticle structures are predicted to have almost identical alignments. This is due to the difference in I_x for the AB quasineutrons at the predicted equilibrium deformations. This change in the alignment experienced by the $i_{13/2}$ quasineutron pair is important, because it indicates that the alignment gain brought about by aligning $i_{13/2}$ quasineutrons is dependent on deformation. For example, the difference in the AB alignment between $\gamma = -15°$ and $\gamma = 10°$ at 0.35 MeV is approximately 4 $\hbar$, which is roughly the alignment difference observed in the single band crossings for the yrast and $\pi h_{9/2} \otimes \pi i_{13/2}$ band in ^{184}Pt. If both of these bands experience only the $(\nu i_{13/2})^2$ band crossing, these bands should take on the above γ deformations. Thus, the difference in alignment is accounted for theoretically in view of a single band crossing proposal.

It should be noted that the pairing plays an important role in determining the energy of the $(\pi h_{9/2})^2$ configuration relative to the ground band. It should also be mentioned that the phenomological neutron pairing after the crossing of the $\nu i_{13/2}$ quasineutron pair at $\hbar\omega = 0.25$ MeV is too large for this calculation. Self-consistent pairing calculations show that the static BCS neutron pairing completely breaks down after the $(\nu i_{13/2})^2$ band crossing occurs. Similar Strutinsky-HFBC calculations have been done which assume that the neutron pairing is only 0.3-0.4 MeV after the neutrons have aligned and that the proton pairing is roughly 0.8 MeV at $\hbar\omega = 0.30$ MeV or 70% of its initial value. Such TRS calculations predict that the AB configuration is only 350 keV lower in energy than the $ABef$ configuration and that this energy difference reduces to only 50 keV at $\hbar\omega = 0.35$ MeV. These assumptions for the pairing do not solve the dilemma concerning the quasiparticle nature of the yrast band in ^{184}Pt, rather they

indicate that the AB and $ABef$ minima are very close in energy at $\hbar\omega = 0.35$. Thus from energy considerations these calculations show it is possible for the $i_{13/2}$ quasineutron pair to align first, driving the nucleus to $\gamma \approx -15°$, followed by the alignment of $h_{9/2}$ quasiprotons which drive the nucleus back to an axial symmetric prolate shape.

Reasons for decreasing the proton pairing to 70% of its initial self-consistent value at $\hbar\omega = 0.30$ MeV are two-fold: (1) examination of experimental and theoretical Routhians suggest that the calculated $\pi h_{9/2}$ and $\pi i_{13/2}$ single-particle orbitals may lie too high in energy, and (2) experimental estimations of the proton pairing gap indicate that Δ_p is on the order of 0.95 MeV and not the self-consistent HFB value of 1.15 MeV calculated at $\hbar\omega = 0.0$ MeV. Reduction in the proton pairing for the HFBC calculations should bring the proton quasiparticle orbits closer to the Fermi surface; thus the $h_{9/2}$ quasiprotons should align at lower rotational frequencies. Clearly, a more detailed analysis of the proton pairing and single-particle structure is necessary in order to determine if adjustments in the average field and pairing parameters are indeed necessary in the region around $N = 106$ for the Pt-Au nuclei.

While the above analysis has not settled the question whether low frequency $\pi h_{9/2}$ band crossings are occurring in ^{184}Pt, it has clarified the problem and pointed out the conditions which would favor a two-band crossing scenario in the yrast band of ^{184}Pt. A similar analysis of the Strutinsky-HFBC calculations has been done for the observed multi-quasiparticle bands in ^{184}Pt. Fig. 5.10 summarizes the regions of deformation (β_2, γ) associated with these bands. From this figure, the Strutinsky-HFBC calculations indicate that configurations with either a $\pi h_{9/2}$ or $\pi i_{13/2}$ component take on positive γ deformations. On the other hand, pure quasineutron configurations containing a $\nu i_{13/2}$ component drive the equilibrium shape to negative γ deformations.

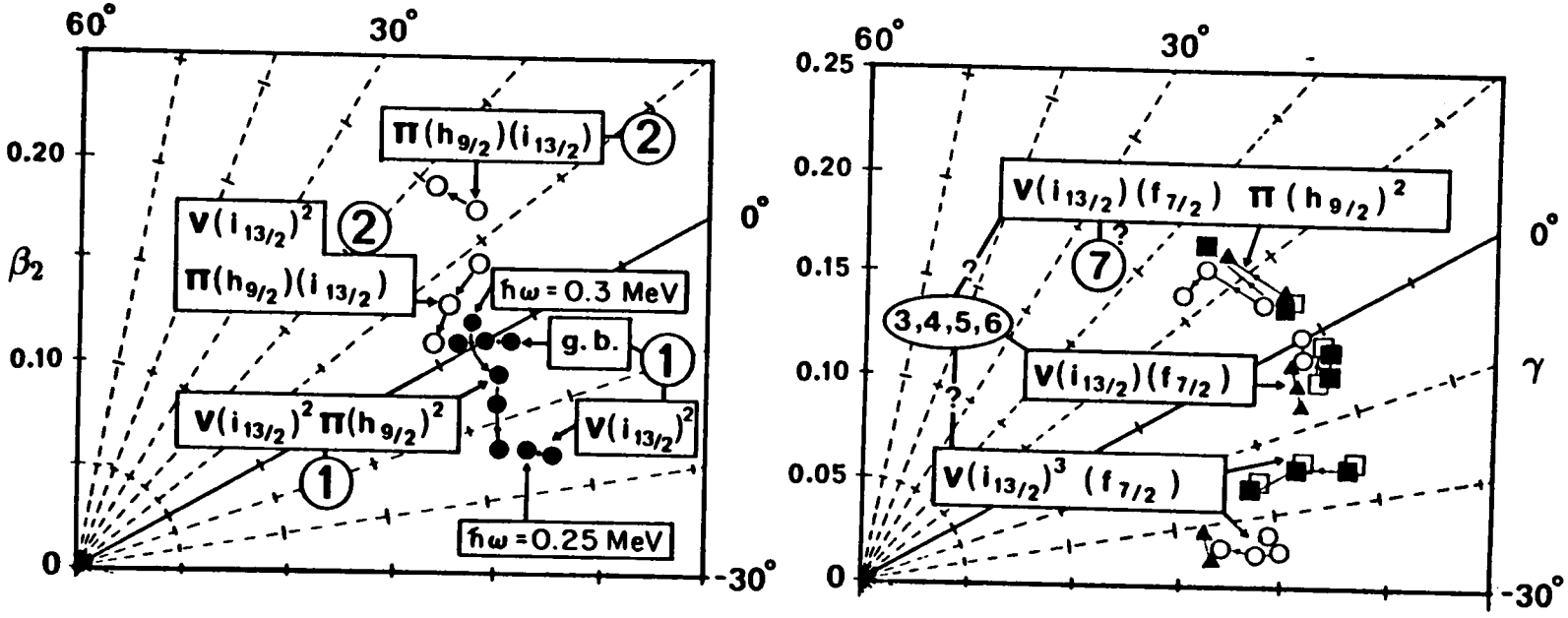

Figure 5.10: Calculated regions of deformation (β_2, γ) associated with the multi-quasiparticle prolate bands in ^{184}Pt. Configurations are marked by symbols: ● - $(\pi = +, \alpha = 0)$; ○ and □ - $(\pi = -, \alpha = 1)$; ▲ and ■ - $(\pi = -, \alpha = 0)$. The encirled numbers associate calculated deformations with the experimental data. These calculations are taken from Carpenter *et al.* (1987).

As discussed earlier, band 2 is associated with the configuration $\pi h_{9/2} \otimes \pi i_{13/2}$. The observed alignment is due to $(i_{13/2})^2$ quasineutrons, however these quasiparticles have little effect on the overall equilibrium shape defined by the quasiprotons. By using the deformations extracted from the TRS maps, CSM calculations predict that the AB band crossing occurs at $\hbar\omega \approx 0.28$ MeV with an alignment gain of 6.6 $\hbar$. These predictions agrees well the with experimentally observed band crossing and alignment. If $h_{9/2}$ quasiprotons are aligning at rotational frequencies below $\hbar\omega = 0.30$ MeV, one would expect a secondary fg proton crossing to have occurred by 0.40 MeV in band 2. Its absence detracts from the arguments of a low frequency $(\pi h_{9/2})^2$ band crossing. However, it should be noted that a lack of an fg crossing could also be explained by a quenching of the proton pairing brought about the initial $\pi h_{9/2} \otimes \pi i_{13/2}$ configuration.

As mentioned above, bands 3-6 are expected to have the configuration $\nu i_{13/2} \otimes \nu f_{7/2}$. Bands 3 and 4 most probably have the signature combination AF and BF. Fig. 5.1 shows that these two bands experience no signature spitting due to the high-K of the band. On the other hand, the Strutinsky-HFBC calculations do predict signature splitting between these two bands, and the discrepancy between predicted and observed phenomena probably results from the fact that the calculations do not couple the quasiparticles together in the proper way. Bands 5 and 6 have been assigned the configuration combination AE and BE and low-K. These two bands do experience signature splitting and thus may be described better by the theoretical calculations.

Fig. 5.11 shows an alignment diagram for the $\nu i_{13/2}$ bands in ^{183}Pt and ^{185}Pt, and bands 5 and 6 in ^{184}Pt. These bands all experience a single crossing at roughly the same rotational frequency ($\hbar\omega \approx 0.27$ MeV), and the alignments all have the curious feature that the unfavored signature crosses the favored signature in the region of the crossing. From the figure, a systematic change in the

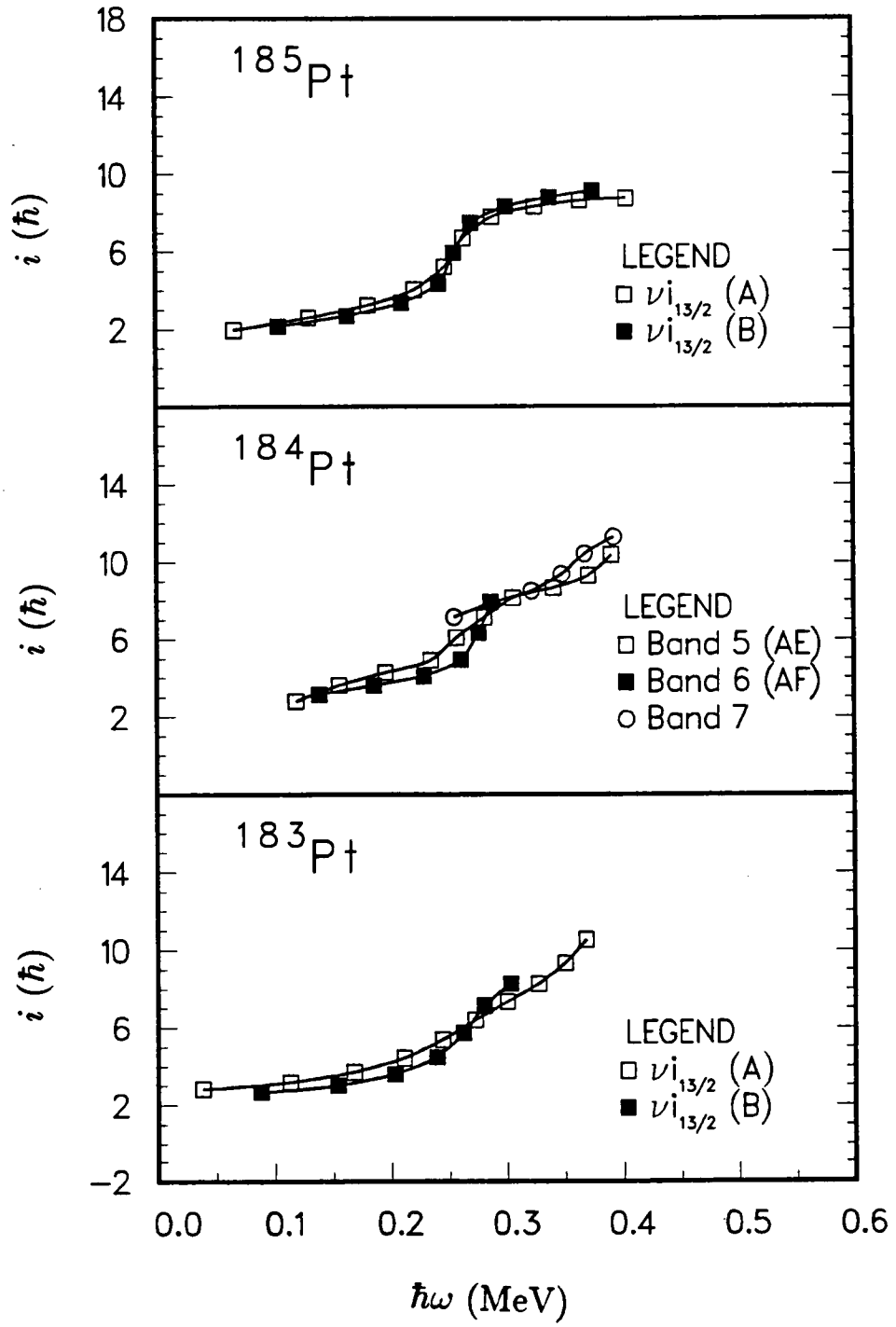

Figure 5.11: Alignment diagram showing the A and B bands in ^{183}Pt (Nyberg *et al.*, 1987) and ^{185}Pt (Pilotte *et al.*, 1986), and the AE and AF bands in ^{184}Pt.

interaction strengths of each signature is also observed as neutron number decreases. The Strutinsky-HFBC calculations show that the $\nu i_{13/2}$ A quasiparticle drives the nucleus to more negative γ deformations than the B quasiparticle, thus this difference in the interaction strengths may well be a shape effect.

The TRS calculations show a complicated situation for the predicted crossings in these bands. At $\hbar\omega = 0.30$, the calculations show that the AD and BC crossings have occurred and drive the nucleus to small quadrupole shapes ($\beta_2 \approx 0.170$) and negative γ deformation ($\approx -25°$). The calculations also show a minimum for theses configurations at positive γ deformations, and the frequency at which this minimum crosses the proton ground configuration is dependent on the pairing for the reasons discussed above. If low frequency $\pi h_{9/2}$ band crossings are occuring in ^{184}Pt, the TRS calculations show that either the secondary $i_{13/2}$ quasineutron alignment or the primary $h_{9/2}$ quasiproton alignment is responsible for the observed configuration crossing in these bands. These calculations also show that whatever crossing occurs, the other will be delayed to higher frequencies due to the large shape differences between the ABC (or ABD) and Aef configurations. On the other hand, if the yrast band only experiences a $(\nu i_{13/2})^2$ alignment, the TRS calculations show that the neutrons should be responsible for the observed alignments in bands 3-6.

If one is to determine whether $h_{9/2}$ quasiprotons are aligning below $\hbar\omega =$ 0.30 MeV, more direct evidence must be gathered which would indicate the quasiparticle composition of the observed band crossings. One such measurement has been done for the $\nu i_{13/2}$ band in ^{185}Pt where $B(M1)/B(E2)$ ratios for ^{185}Pt (Janzen *et al.*, 1987) have been calculated from experimental data taken by Pilotte *et al.* (1987). This ratio of reduced transition probabilities is determined from

values of the branching ratio, λ, and the mixing ratio, δ, by the usual equation:

$$\frac{B(M1;I\rightarrow I-1)}{B(E2;I\rightarrow I-2)} = 0.693\frac{E_\gamma^5(I\rightarrow I-2)}{E_\gamma^3(I\rightarrow I-1)}\frac{1}{\lambda(1+\delta^2)}\left(\frac{\mu_N}{eb}\right)^2. \qquad (5.16)$$

The experimental values of $B(M1)/B(E2)$ for ^{185}Pt are shown in Fig. 5.12 as a function of angular momentum. At low spins, this ratio is low (0.2), however, after the band crossing, this ratio rises by a factor of three to six.

To interpret the large increase in the $B(M1)/B(E2)$ values in ^{185}Pt, the formalism of Dönau and Frauendorf (1983) is used. This theoretical model expresses the ratio of reduced transition probabilities as

$$\begin{aligned}\frac{B(M1;\ I\rightarrow I-1)}{B(E2;\ I\rightarrow I-2)} &= \frac{12}{5Q_0^2\cos^2(30^\circ+\gamma)}\left[1-\frac{K^2}{(I-\frac{1}{2})^2}\right]^{-2}\frac{K^2}{I^2} \\ &\times \left\{(g_1-g_R)[(I^2-K^2)^{1/2}-i_1]-(g_2-g_R)i_2\right\} \qquad (5.17)\end{aligned}$$

where Q_0 is the intrinsic quadrupole moment, g_R is the gyromagnetic ratio for a rotating core (and is approximated by Z/A), g_1 is this ratio for the single quasiparticle excitation in an odd-A nucleus, and g_2 for the aligning quasiparticle in a band crossing. The $B(E2)$ value is approximated by the expression $5Q_0^2\cos^2(30^\circ+\gamma)$, while the remaining part of the equation represents the $B(M1)$ value.

Since $(g_K - g_R)$ is positive for a proton and negative for a neutron, it is clear from Eq. 5.17 that the $M1$ transition rate will increase if a proton backbend occurs in a neutron band and decrease if a neutron backbend occurs. This gives the fingerprint needed to determine if the $\nu i_{13/2}$ band in ^{185}Pt experiences a band crossing caused by the alignment of $i_{13/2}$ neutrons or $h_{9/2}$ protons. Concerning the parameters for the $E2$ rate, the self-consistent TRS calculations were used to give equilibrium (β_2,γ) values for the different quasiparticle configurations. The calculation is seen to describe well the value of approximately 0.2 before the observed band crossing, and predicts an increase of a factor of two if the crossing results from the alignment of $\pi h_{9/2}$ quasiparticles, and a decrease of 30% if it is the BC

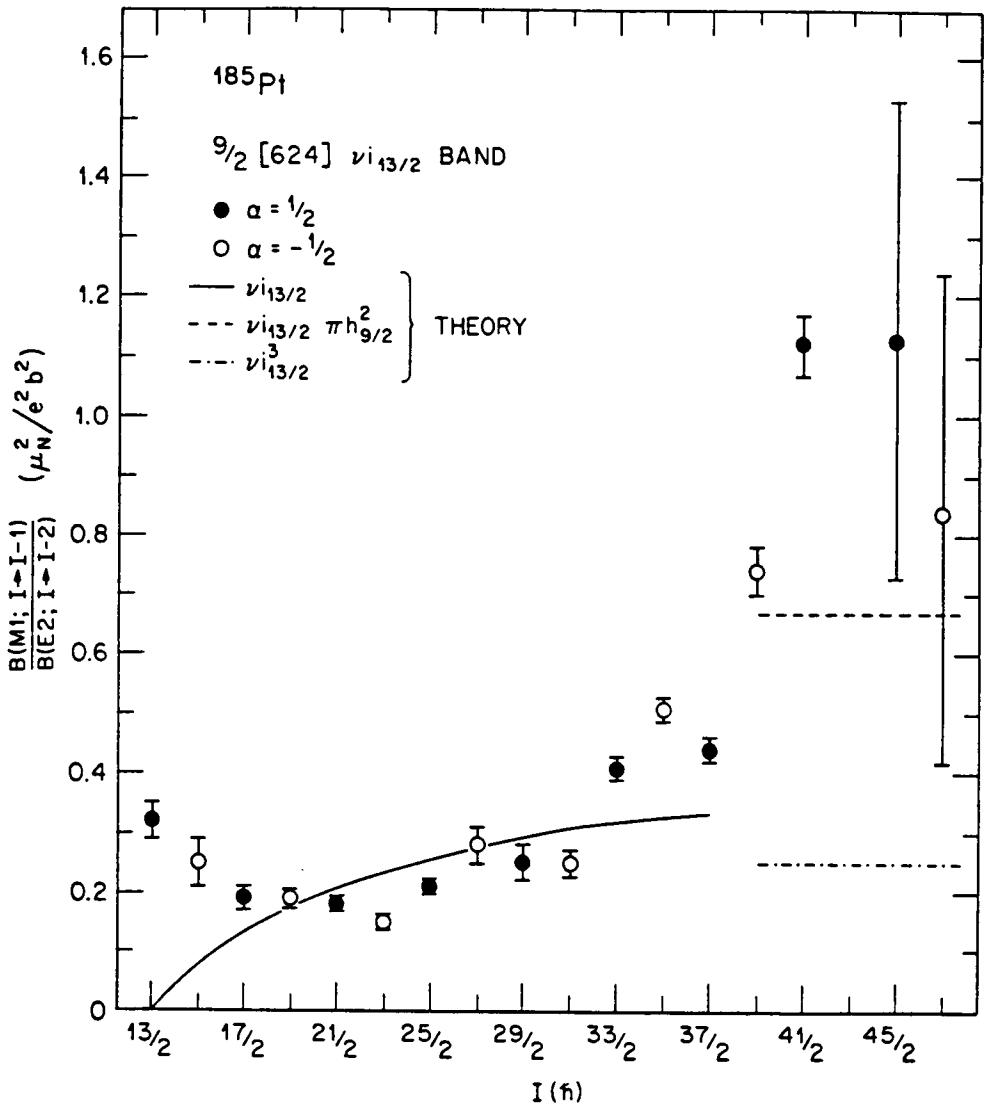

Figure 5.12: Measured and calculated $B(M1)/B(E2)$ values for the $\frac{9}{2}[624]$ band for ^{185}Pt. Reproduced from Riedinger *et al.* (1987).

crossing. These changes in the ratio include the changes expected in both the $M1$ and the $E2$ rates. In the case of the proton crossing, the increase in the $M1$ rate gives about half of the rise in the ratio seen in Fig. 5.12, the other half coming from the predicted decrease in the $E2$ rate since γ changes from $-18°$ to $+10°$ through that crossing. In the case of the neutron crossing, the decrease in the $M1$ rate actually gives a decrease in the ratio that is about twice as large as that shown in Fig. 5.12. Half of this decrease is removed, however, by the $E2$ change.

The theoretical approach of Dönau and Frauendorf does appear to present a clear conclusion on the observed rise in the experimental $B(M1)/B(E2)$ values in the $\frac{9}{2}[624]$ band in ^{185}Pt. If the crossing observed in this band were due to the alignment of the secondary $i_{13/2}$ neutron pair, BC, the ratio should clearly decrease. The observed rise in the measured values can only be explained by the alignment of a pair of proton quasiparticles, and $h_{9/2}$ is the obvious choice assuming that both the $B(M1)$ and $B(E2)$ values are described well by the models. The validity of this conclusion would be greatly enhanced if a direct measurement of the $B(E2)$ values showed that they behaved as predicted.

The interpretation that $h_{9/2}$ quasiprotons are responsible for the observed alignment in the A and B bands of ^{185}Pt agrees with what blocking arguments suggest for the Ir-Au systematics in the $N = 108$ isotones discussed in the previous subsection. It also indicates that it is a reasonable proposal that $(\pi h_{9/2})^2$ alignments play some role in ^{184}Pt. However, it certainly does not indicate which alignment is observed in bands 3-6 in ^{184}Pt, only that both interpretations must be considered. It should be noted that band crossings observed in the $\frac{9}{2}[624]$ bands in ^{183}Pt (Nyberg *et al.*, 1987) and ^{181}Pt (Riezebos 1987) have been interpreted as secondary $\nu i_{13/2}$ alignments.

Based on the present experimental data on bands 3-6, it cannot be decided whether the observed alignments are due to proton or neutron crossings.

Both crossings should not coexist in the same band below $\hbar\omega = 0.35$ MeV, based on the equilibrium shapes predicted by the TRS calculations. However, TRS calculations which favor a low frequency proton crossing predict that both crossings should be observed in bands 3-6 by $\hbar\omega = 0.40$ MeV. This prediction seems to be supported by the data, since the alignment curve for band 5 (see Fig. 5.11) appears to be experiencing the beginning of a band crossing at $\hbar\omega \approx 0.375$ MeV. It is also interesting to note that band 7 is beginning to show evidence of a band crossing in the same frequency range. Since the first crossing observed in band 5 is blocked in band 7, the initial quasiparticle structure of band 7 should help establish the order of the crossings in band 5.

Band 7 must have either an A or B $i_{13/2}$ quasineutron associated with its configuration due to the fact that the AB alignment is not observed. As discussed in the previous section, a Routhian plot suggests that this band has a $\pi h_{9/2}$ component associated with it. If so, one possible initial configuration would be $\nu i_{13/2} \otimes \nu f_{7/2} \otimes \pi h_{9/2} \otimes \pi f_{7/2}$. The presence of an $f_{7/2}$ quasiproton is feasible since such a band has been identified in ^{185}Au. If band 7 does have a $\pi h_{9/2}$ quasiparticle associated with it, the first crossing in band 5 must be due to the $(\pi h_{9/2})^2$ alignment. However, other assignments for band 7 are possible, and more systematic information is needed if the quasiparticle structure of band 7 is to be confidently determined.

In summary, from the experimental data using both blocking arguments and $B(M1)/B(E2)$ ratios, it appears that $\pi h_{9/2}$ band crossings are occuring at low rotational frequencies in Pt and Au nuclei. However, this is not supported by self-consistent theoretical calculations using standard values for the pairing constant, which suggest that this quasiproton crossing is delayed to higher rotational frequencies. Since the experimental evidence favors a single $h_{9/2}$ quasiproton crossing in the Pt-Au nuclei at $N = 108$, it appears that the parameters used for these

models should be re-evaluated for this region. Thus, the fact that the TRS calculations predict only a $\nu i_{13/2}$ alignment for the yrast band in ^{184}Pt should not be taken as clear evidence that $h_{9/2}$ quasiprotons do not align in the same frequency range. As indicated, if the proton pairing is reduced by 70% of its initial self-consistent value, the $\pi h_{9/2}$ crossing competes with the the $\nu i_{13/2}$ alignment in the frequency range 0.30-0.35 MeV. Even though experimental evidence has been given which seems to contradict a the double alignment interpretation in the yrast band of ^{184}Pt, the idea that degenerate crossings are present at $N = 106$ is a reasonable interpretation of the data in view of what is known at $N = 107$ and $N = 108$.

CHAPTER 6

^{183}Au EXPERIMENTAL ANALYSIS

6.1 Introduction

Shape coexistence has been well established in the Pt-Hg nuclei below $N = 110$, where observed rotational bands are built on both prolate and oblate ground states. As reported above, the ground states of light Pt nuclei, $A \leq 108$, are thought to have well-deformed prolate shapes. However, Hg nuclei exhibit a staggering in their deformation between even and odd isotopes beginning at ^{185}Hg (N=105). This staggering has been observed in the measurement of the root-mean squared (rms) charge radius (*e.g.* Bonn *et al.*, 1972; Ulm *et al.*, 1986), and it has been interpreted as being due to a shape change from slightly deformed oblate to well deformed prolate shapes. The most recent measurement of these rms charge radii is summarized in Fig. 6.1.

Isotope shift measurements on Au nuclei by Wallmeroth *et al.* (1987a) indicate that a sudden change in the rms charge radius occurs at ^{186}Au (see Fig. 6.1), two neutron numbers higher than in the Hg nuclei. In contrast to the Hg case, however, there is no evidence for odd-even staggering. It has been suggested that this may indicate that the neutron pairing energy is not sufficient in the even-neutron Au nuclei to stabilize the near-spherical shape. Radioactive decay and in-beam spectroscopy studies have shown that strong deformation driving orbitals, $\pi h_{9/2}$ and $\pi i_{13/2}$, which come from above the closed shell at $Z = 82$, continually lower in energy relative to the less deformed states as the neutron number decreases. Recent measurements on the magnetic moments in ^{185,186}Au by van Walle *et al.* show that the $\pi h_{9/2}$ proton orbital $\frac{9}{2}[541]$ is responsible for the ground state proton configuration in both of these nuclei is responsible for their well-deformed shapes

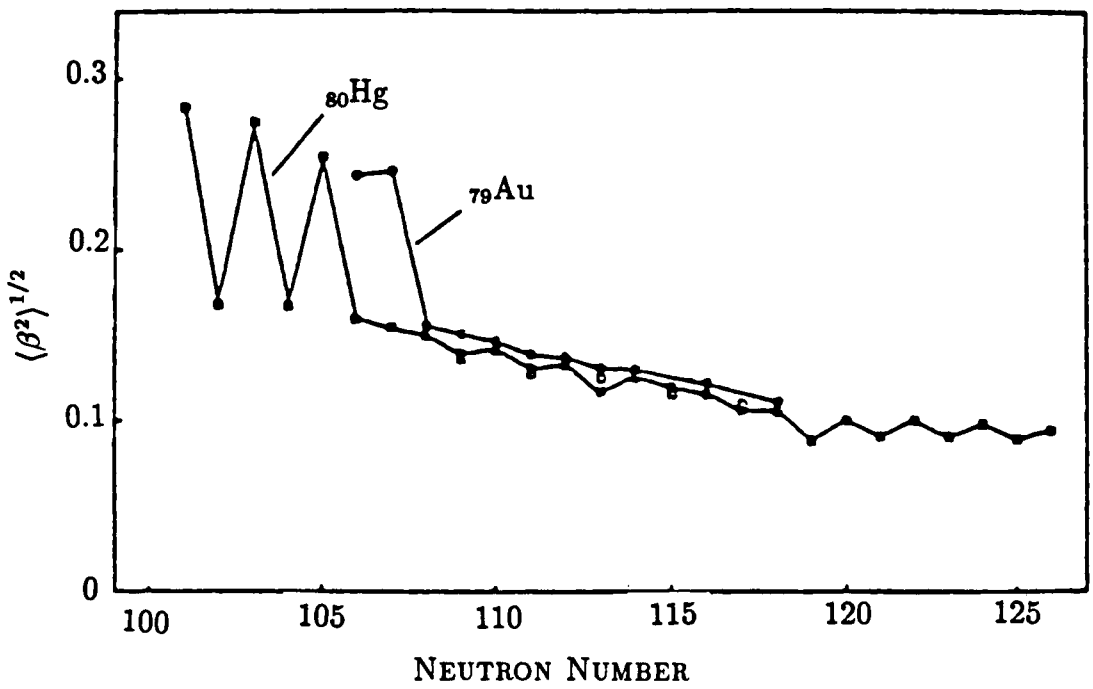

Figure 6.1: Quadrupole deformation $< \beta^2 >^{1/2}$ calculated from the measured rms charge radius for Au (Wallmeroth *et al.*, 1987a) and Hg (Ulm *et al.*, 1986) isotopes. Reproduced from Wallmeroth *et al.* (1987b).

($\beta_2 \approx 0.25$). In the heavier Au nuclei, the ground state is the $\pi d_{3/2}$ configuration which couples to the even-even Hg cores, resulting in slightly deformed oblate shapes.

In the region where these sharp shape changes occur, rotational structures have been identified which are built on both oblate and prolate configurations. In view of these observations, an experiment on ^{183}Au serves two purposes: (1) the identification of rotational bands allows for further systematic data on where the oblate- and prolate-like structures lie in energy relative to each other at mid-shell, and (2) the observations of these rotational bands to high spins allows one to use blocking arguments to help establish which alignment processes are responsible for the observed band crossings at $N = 104$.

6.2 Initial Quasiparticle Identification

From the work of Macias-Marques *et al.*, the ground-state spin and parity in ^{183}Au has been identified as $\frac{5}{2}^-$. This same level has been observed as the ground state in ^{185}Au (Ekström *et al.*, 1976), and recent measurements of its magnetic moment show that the configuration associated with this level is 90% $\frac{1}{2}$[541] ($\pi h_{9/2}$). Based on these measurements and the systematics of the Au isotopes, the $\frac{5}{2}^-$ ground state of ^{183}Au has also been associated with this orbital. As reported above, the decay work has also identified a level at 12.3 keV which we have assigned to the lowest energy level observed in our in-beam measurement. Based on systematics, the rotational structure observed on top of this level (band 1) has been associated with the favored signature of the $\pi h_{9/2}$ configuration. The band labeled 2 in Fig. 4.13 is thought to be the unfavored signature of the $\pi h_{9/2}$ configuration. The single particle Routhian diagram (Fig. 6.2) shows that these two bands have a large signature splitting which indicates large Coriolis mixing. This is expected if the bands have the suggested configuration since K would equal 1/2

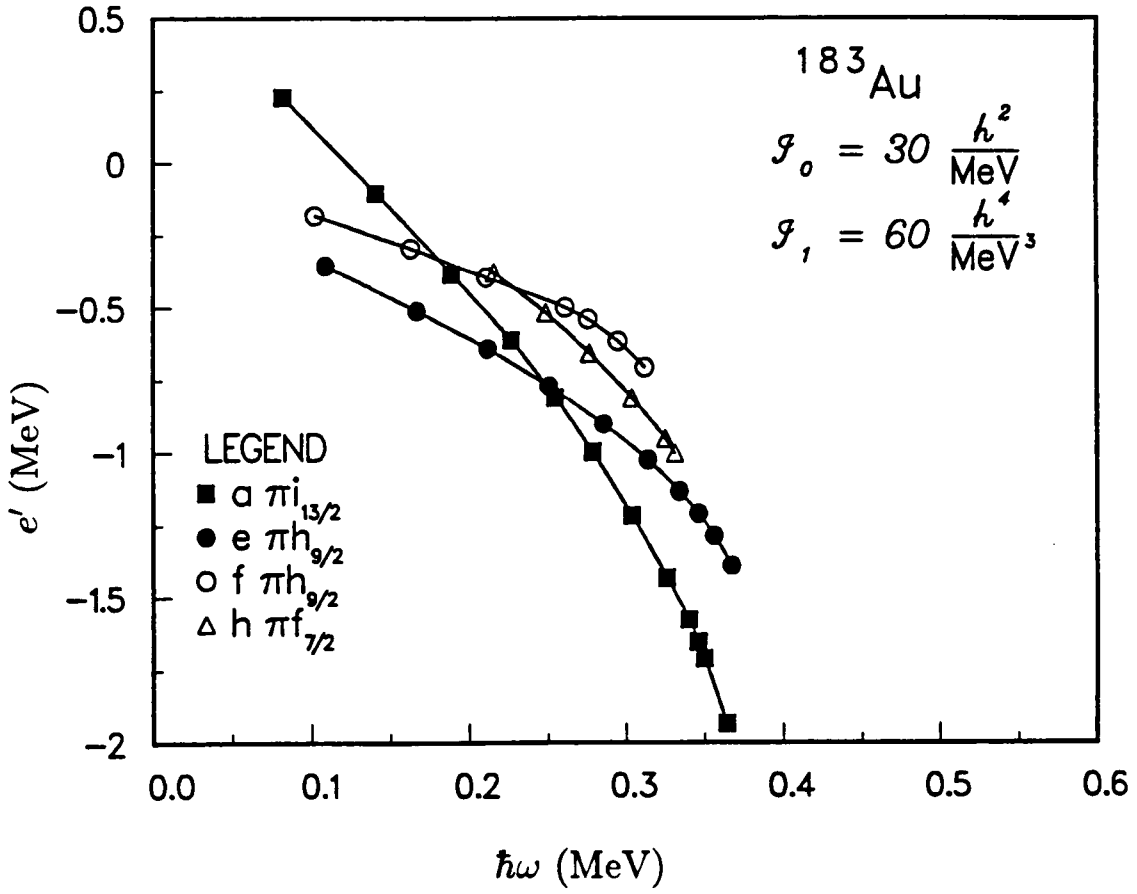

Figure 6.2: Experimental quasiparticle Routhians for the observed bands in ^{183}Au.

for these orbitals.

The band labeled 4 in Fig. 4.13 has been associated with the $\frac{1}{2}$[660] $\pi i_{13/2}$ configuration. Its identification is quite clear from the Au systematics. For example, the lowest observed level in this band is $\frac{13}{2}^+$. This same spin and parity is assigned to the lowest member of the established $\pi i_{13/2}$ band in ^{185}Au and ^{187}Au. The experimental Routhian plot of this band also lends a clue to its configuration. Fig. 6.2 shows that band 4 becomes yrast at $\hbar\omega \approx 0.25$ MeV where it crosses the favored $\pi h_{9/2}$ band. A similar occurrence is observed in the heavier odd-Au isotopes for the $\pi i_{13/2}$ band.

As discussed above, bands having both prolate and oblate shapes are thought to coexist in the same nucleus for the even-even isotopes in Pt and Hg centered around $N = 104$. A coexistence of structures has also been identified in $^{185-187}$Au. ^{187}Au is probably the best example of strongly competing shapes at high spins in Au nuclei, since examples of both oblate and prolate structures have been observed as high as $I = \frac{49}{2}\ \hbar$ by Johansson (1987). While it has already been mentioned that the $\pi h_{9/2}$ and $\pi i_{13/2}$ particle states coupled to a Pt core are the configurations associated with prolate rotational bands in the Au nuclei, it is the $\pi h_{11/2}$ hole state coupled to a Hg core which is responsible for the observed oblate rotational bands in the lighter Au isotopes. It was our hope that similar rotational structures would be identified in our data. In fact, the decay work of Macias-Marques has identified a $\frac{11}{2}^-$ state decaying to the $\frac{9}{2}^-$ level at 12.3 keV via a 218.2 keV transition with a lifetime greater than 5 nano-seconds. Similar isomeric decays between these two levels have been identified in ^{185}Au and ^{187}Au with lifetimes of 26ns and 50 ns (Berg *et al.*, 1983), respectively. These delayed transitions are believed to result from the different shapes of the the $\frac{11}{2}^-$ (oblate) and $\frac{9}{2}^-$ (prolate) structures. Due to these systematic observations, the $\frac{11}{2}^-$ state at 230.5 keV in ^{183}Au has been associated with the $\pi h_{11/2}$ $\frac{11}{2}$[505] oblate

configuration. Unfortunately, there were no γ rays in our in-beam work which have been identified as decaying to this level.

Band 3 has been identified as having a large $\pi f_{7/2}$ $\frac{1}{2}$[530] component. A band with this configuration was first identified at $Z = 79$ by our group in ^{185}Au (see Larabee *et al.*, 1986). In order to confirm this assignment, we performed calculations of the band-head energies using the Strutinsky-HFB formalism described in section 2.9. The axially symmetric Woods-Saxon potential of Dudek *et al.* (1979) was used as the average field utilizing the "universal" Woods-Saxon parameters (Dudek *et al.*, 1981). The results of these calculations are summarized in Fig. 6.3 where the deformation-energy curves for various band heads are plotted as a function of β_2. At every β_2, the minimization was carried out for the hexadecapole deformation, β_4. From this figure, it is apparent that the high-j orbitals $h_{9/2}$, $i_{13/2}$ and $h_{11/2}$, which have been associated with structures in the Au isotopes, are seen to have low-lying minima for both prolate and oblate shapes. By examining the experimental Routhian diagram in Fig. 6.2, one observes that band 3 lies between the $\pi h_{9/2}$ and $\pi i_{13/2}$ bands in energy if one extrapolates back towards the predicted band head of band 3. Fig. 6.3 shows that the $K = 1/2$ $f_{7/2}$ configuration is predicted to lie between the other two observed prolate bands at low rotational frequency. Other possible configuration assignments for this band in ^{185}Au have been ruled out due to their assignment to other observed structures.

It is interesting to note that the preferred pathway through the unfavored $h_{9/2}$ quasiproton band in ^{183}Au occurs via the decay of either the $\pi i_{13/2}$ or $\pi f_{7/2}$ structures to this band and not from the higher spin levels of the band itself (see Fig. 4.13). This same type of decay pattern is seen in ^{185}Au, supporting the assignment of band 3 to a different quasiparticle structure from band 2. From the experimental quasiparticle Routhian plots in Fig. 6.2, it appears that these two bands cross one another at $\hbar\omega \approx 0.22$ MeV. Since, they have the same parity

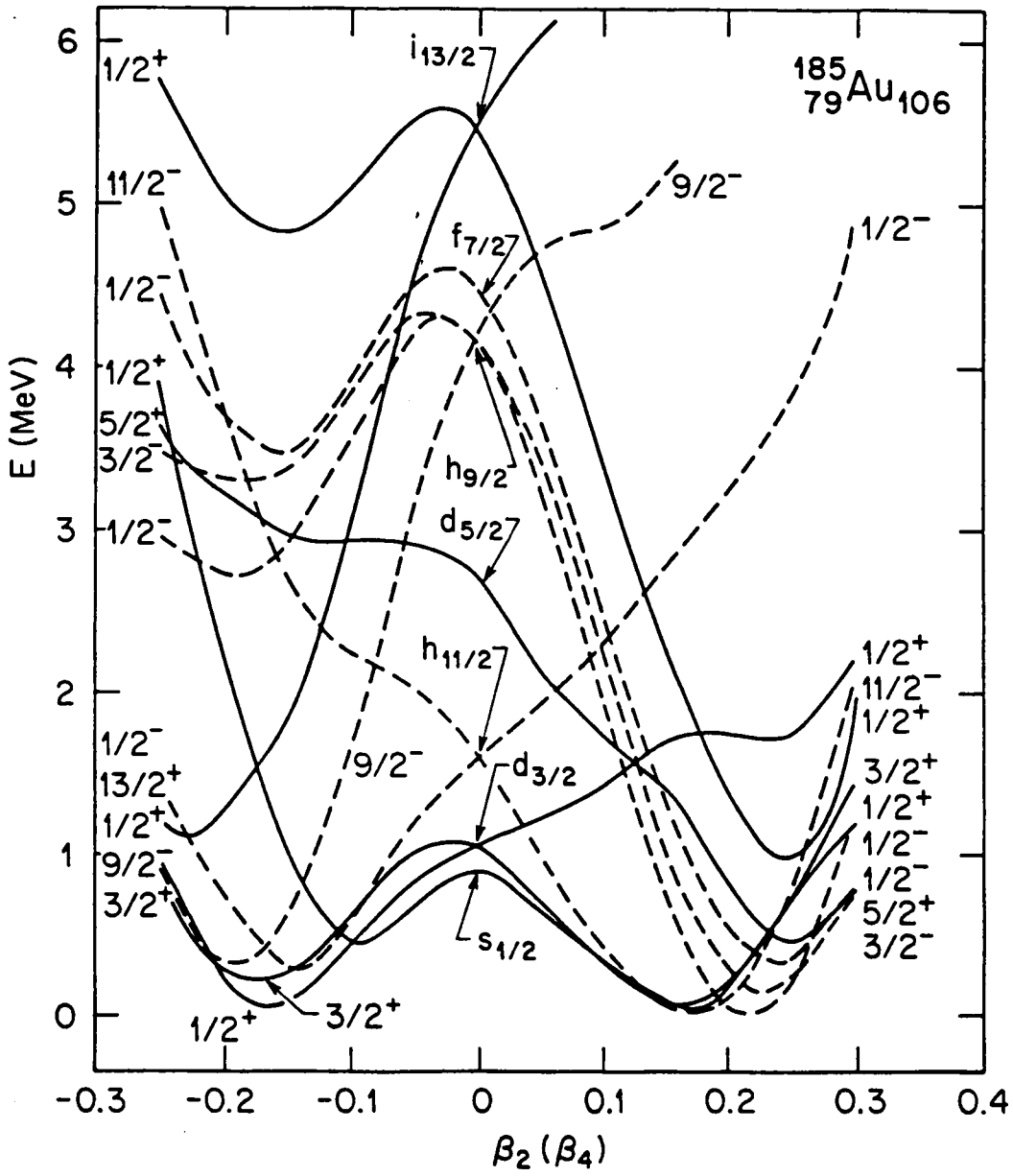

Figure 6.3: Deformation-energy curves for the band heads of the low lying states in ^{185}Au as a function of β_2. At every β_2 point a minimization was carried out for the β_4 deformation. The pairing was calculated self-consistently at each deformation point, using approximate particle number projection before variation.

and signature $(-,-\frac{1}{2})_{\pi,\alpha}$ such a crossing should be evident in the cranked shell model calculations. Larabee *et al.* have shown that a weak interaction crossing between these two quasiparticle orbitals occurs at $\hbar\omega \approx 0.35$ MeV in ^{185}Au, while the experimental crossing is observed at $\hbar\omega \approx 0.25$ MeV. A similar discrepancy in these crossing frequencies are obtained for ^{183}Au. The fact that the two bands cross at lower rotational frequencies than is theoretically predicted suggests that the calculated $\pi f_{7/2}$ $(-,-\frac{1}{2})$ orbital initially lies too high in energy relative to the $\pi h_{9/2}$ $(-,-\frac{1}{2})$ quasiparticle orbital. Recently, Zhang *et al.* (1987) have used the identification of a $f_{7/2}$ quasiparticle band in ^{185}Au to re-adjust the κ and μ parameters of the Nilsson model in order to reproduce the observed quasiproton levels in this region.

As discussed in section 2.3 of this work, one interpretation for the observed shape coexistence is that it is due to the residual force between valence protons and neutrons. It has been proposed that this attractive force lowers in energy the deformation driving orbitals which lie above the $Z = 82$ gap at spherical shapes, allowing them to compete in energy with near spherical orbitals in the Ir-Au-Tl nuclei. The shape coexistence is brought about by the excitation of nucleons into orbitals with different deformations. Since the strength of the proton-neutron interaction is dependent on the number of protons and neutrons in the valence shell, the deformed states should lie lowest at mid-shell ($N = 104$) (see for example Wood 1982).

In view of this proposal, one would expect the $\pi h_{9/2}$ and $\pi i_{13/2}$ orbitals to continually lower in energy to a minimum value at $N = 104$ (^{183}Au) and then begin to rise again as the system becomes more neutron deficient. Such an effect is observed in the Tl isotopes. To determine whether this is also true for Au nuclei, level identification in the lightest Au systems is needed. Fig. 6.4 shows a diagram of the experimental band head energies for the Au system including

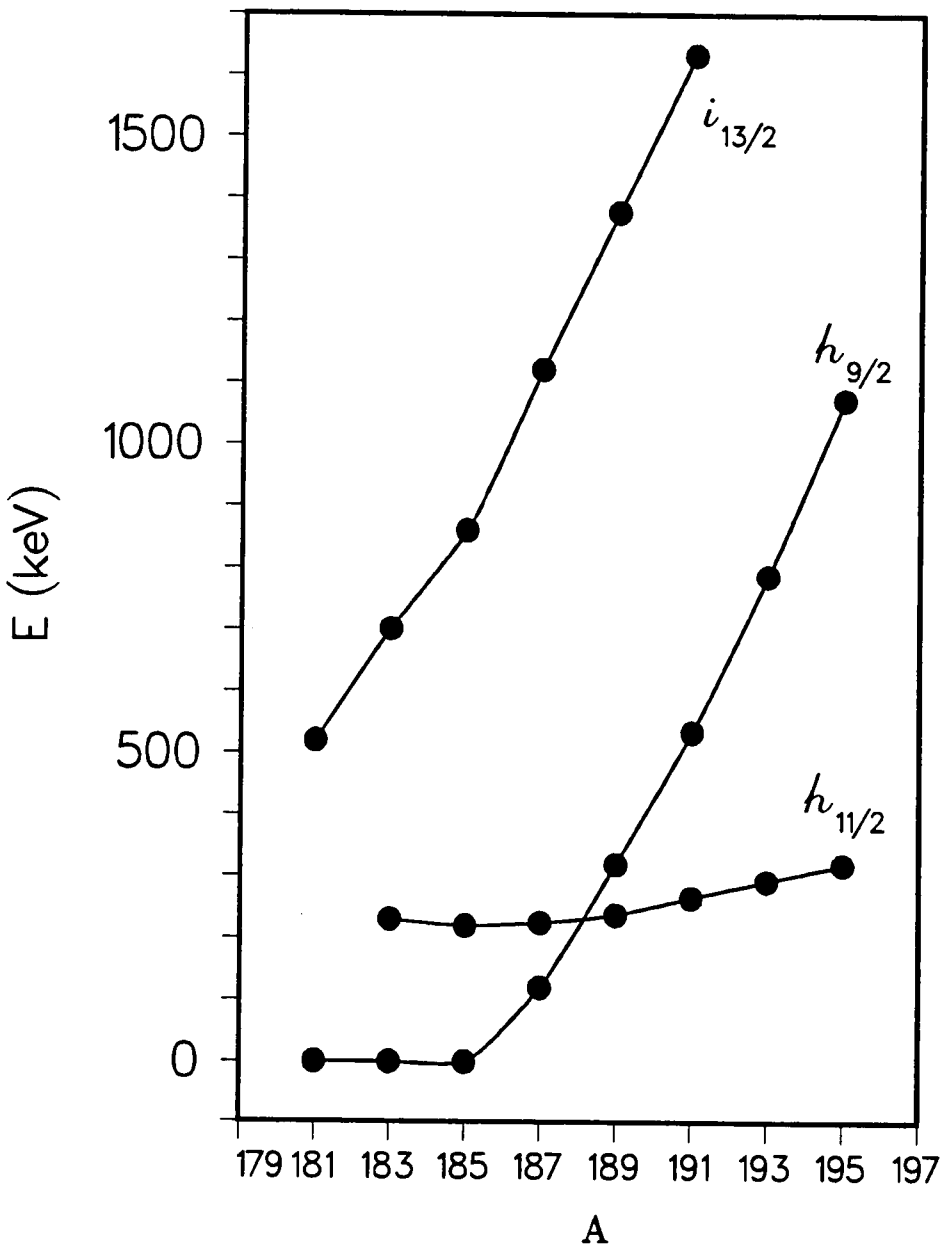

Figure 6.4: Experimental band-head energies in Au nuclei.

^{183}Au (Macias-Marques *et al.*; this work) and ^{181}Au (Jin). From the figure, it is apparent that the deformation driving orbitals fall quickly in excitation energy as one approaches $N = 104$. This decrease appears to continue at $N = 102$ where the energy difference between the $h_{9/2}$ and $i_{13/2}$ levels is a minimum.

The independent particle model does not consider interactions between neutrons and protons, however it was shown that Strutinsky-HFBC calculations are able to reasonably reproduce the predicted shape coexistence in both the Pt and Hg nuclei. This fact is not incompatible with the idea of residual proton-neutron forces. Since the residual force is thought to give rise to nuclear deformation, it has been proposed the proton-neutron interaction is included in the IPM by the coupling together of the proton and neutron states by the collective deformation.

Strutinsky-HFBC calculations have been performed for the Au isotopes, and one would like to use them in a similar way as was done for ^{184}Pt. Fig. 6.5 shows three TRS maps of ^{183,185,187}Au at $\hbar\omega = 0.10$ for the $(-, \frac{1}{2})$ e configuration. One can clearly see two minima in these maps: the prolate minimum corresponds to the $\pi h_{9/2}$ configuration, and the minimum appearing at $\gamma \approx -45°$ is associated with the $\pi h_{11/2}$ configuration. Two features of these maps are interesting and should be pointed out. The first is that the deformation of the $h_{11/2}$ band is not oblate but rather triaxial. The second feature concerns the relative energy differences between the prolate and oblate minima. In ^{187}Au, $V_p - V_o = -200$ keV, while in ^{185}Au and ^{183}Au this difference is +8 and +36 keV, respectively. This calculated V_{p-o} does not agree with the difference obtained between the $\frac{9}{2}^-$ and $\frac{11}{2}^-$ levels observed experimentally and associated with the $\pi h_{9/2}$ and $\pi h_{11/2}$ structures (^{183}Au: 218.3 keV, ^{185}Au: 211.1 keV, and ^{186}Au: 103.9 keV). This is to be expected, since the theoretical energies are calculated in the intrinsic frame. Other factors such as the pairing force could also influence these relative energies. However, qualitative

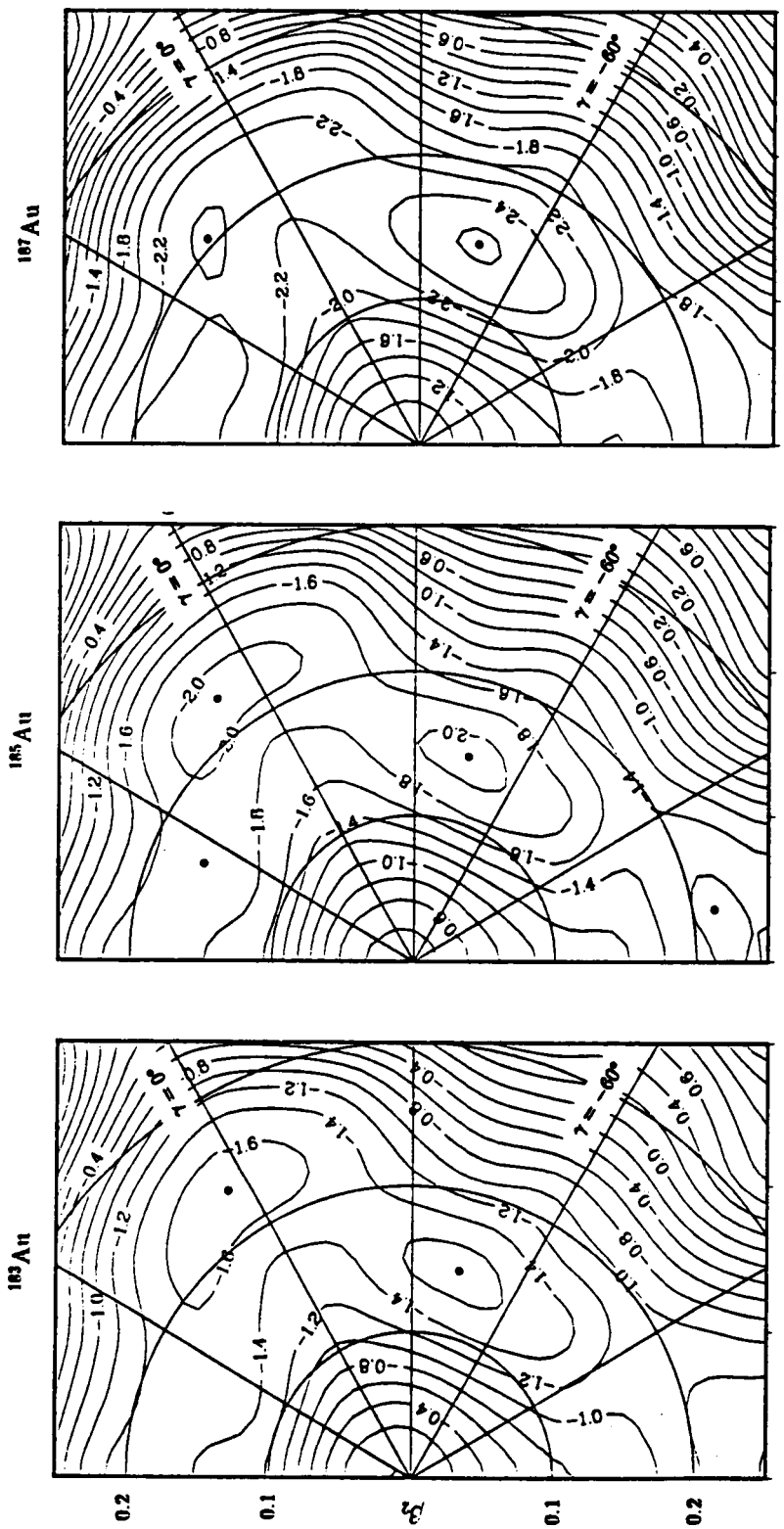

Figure 6.5: Total Routhian surfaces of ^{183,185,187}Au at $\hbar\omega = 0.10$ MeV for the $(-,+\frac{1}{2})$ e configuration.

Table 6.1: Predicted deformations for selected configurations in the odd-Au isotopes which are known to have prolate structures. The deformations for the prolate bands were taken at $\hbar\omega = 0.20$ MeV while the deformations for the $h_{11/2}$ configuration were extracted at $\hbar\omega = 0.15$ MeV.

	$h_{11/2}(e)$			$h_{9/2}(e)$			$i_{13/2}(a)$		
	β_2	β_4	γ	β_2	β_4	γ	β_2	β_4	γ
^{187}Au	0.149	−0.022	−50.7°	0.227	−0.038	1.7°	0.252	−0.029	10.9°
^{185}Au	0.150	−0.017	-49.5°	0.235	−0.026	−1.0°	0.258	−0.017	8.8°
^{183}Au	0.151	−0.015	−45.8°	0.247	−0.014	2.2°	0.268	−0.004	5.4°
^{181}Au	0.152	−0.016	−35.8°	0.257	−0.033	1.7°	0.283	0.007	2.9°

agreement is reached between the observed and calculated oblate-prolate energy differences, *i.e.* the V_{po} for ^{183}Au and ^{185}Au are nearly equivalent while the V_{po} for ^{187}Au decreases significantly relative to the other two.

One would also expect that the Strutinsky-HFBC calculations should reproduce the predicted increase in deformation of the prolate configurations as the Au system approaches mid-shell. Table 6.1 lists the extracted deformations of the observed structures in the Au nuclei at a rotational frequency slightly below the first band crossing. This table shows two systematic trends for the prolate configurations: (1) the quadrupole deformations of both the $h_{9/2}$ and $i_{13/2}$ quasiproton configurations increase with decreasing neutron number, and (2) the triaxiality of the $\pi i_{13/2}$ structure decreases with decreasing neutron number. For the $h_{11/2}$ structure Table 6.1 shows that quadrupole deformation is constant for all four isotopes. On the other hand, the γ deformation shows a migration towards $-30°$ for the lighter Au nuclei. Unfortunately, no rotational structures have been identified with the $h_{11/2}$ configuration in ^{183}Au or ^{181}Au. It would be interesting to see how these structures interact with other configurations if they increase their triaxiality as predicted.

In summary, the prolate configurations in odd-Au nuclei show a decrease

in their band head energies as the neutron number decreases. This decrease continues to $N = 102$ which is the last Au nucleus for which level information is known. This decrease is believed to be due to increasing deformations in these bands. Strutinsky-HFBC calculations predict that the quadrupole deformation of both the $\pi h_{9/2}$ and $\pi i_{13/2}$ quasiparticle configurations increase with decreasing neutron number as suggested by the experimental data.

6.3 Analysis of Band Crossings

In chapter 5, it was shown that the nature of the observed upbend in ^{184}Pt is uncertain and open to two possibilities: $(\nu i_{13/2})^2$ or $(\nu i_{13/2})^2 \otimes (h_{9/2})^2$. In order to gather more systematic information concerning observed low-frequency crossing in the Pt-Au nuclei, the $N = 104$ isotones must be analyzed. Fig. 6.6 shows an alignment plot of the observed bands in ^{181}Ir (Janzen *et al.*, 1987b), ^{182}Pt (Popescu *et al.*, 1986), and ^{183}Au (this work) using reference parameters $\mathcal{J}_0 = 30\ \hbar\ \text{MeV}^{-1}$ and $\mathcal{J}_1 = 60\ \hbar^2\ \text{MeV}^{-3}$.

Beginning with ^{182}Pt, the yrast band shows a gradual increase in alignment over a frequency range of approximately 0.15-0.32 MeV, followed by a sharp upbend at $\hbar\omega \approx 0.32$ MeV. The $\pi i_{13/2}$ band in ^{183}Au shows a similar structure, indicating that the two different features observed in ^{182}Pt could well result from two alignments, the first of which is due to a large interaction band crossing. The total alignment gained in the yrast band of ^{182}Pt is roughly ten units while that in $\pi i_{13/2}$ band in ^{183}Au is approximately 11.0 $\hbar$. Since the last two transitions observed in the $i_{13/2}$ quasiproton are tentative, the total observed gain in alignment is not absolutely certain.

In the $\pi h_{9/2}$ bands in ^{181}Ir and ^{183}Au alignments are observed to occur at $\hbar\omega \approx 0.30$ MeV and $\hbar\omega = 0.35$ MeV respectively, and the total gain in alignment in both of these bands is roughly 7.5 $\hbar$. Based on the single upbend observed

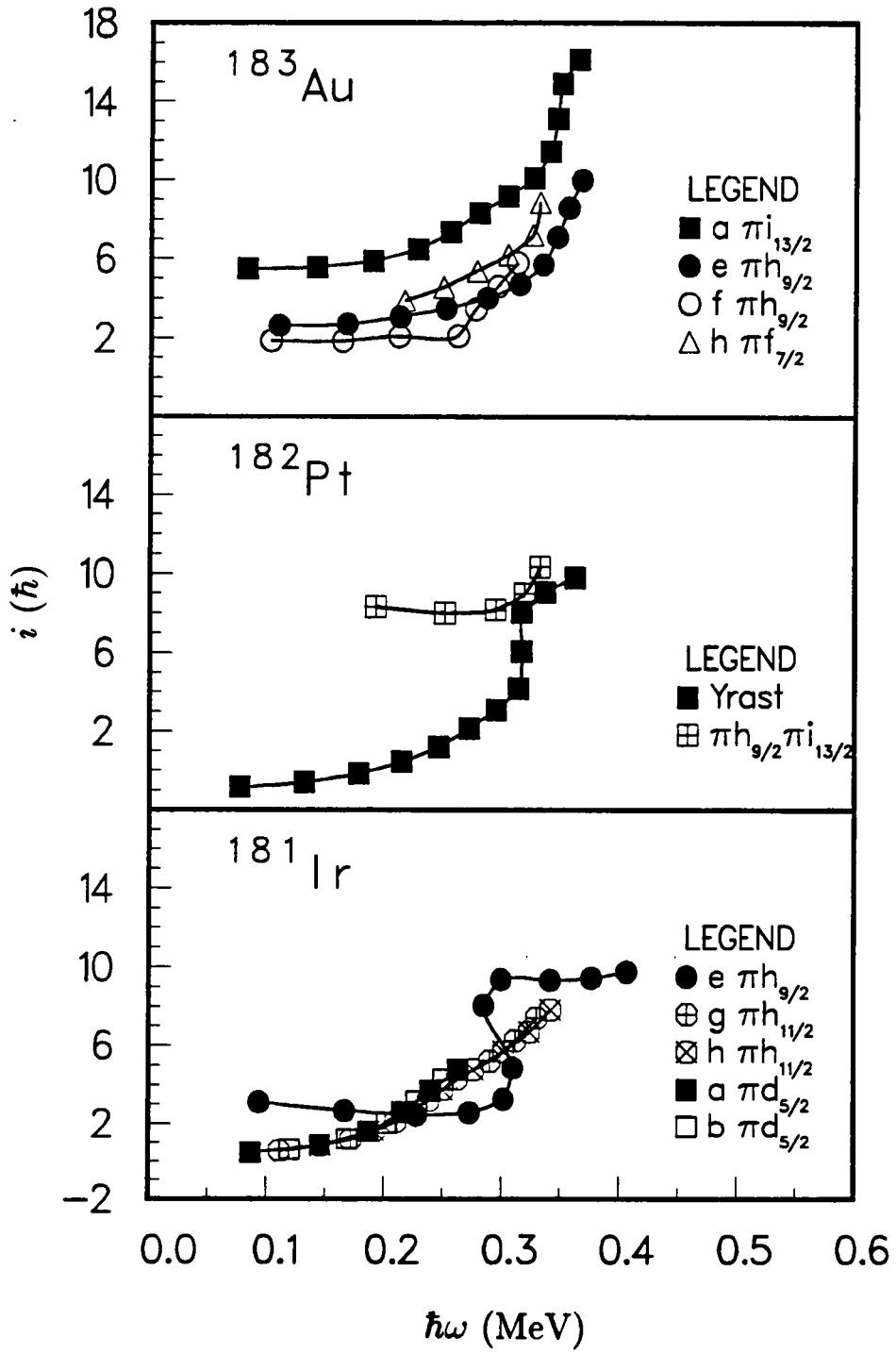

Figure 6.6: Alignment diagram for the $N = 104$ nuclei (^{181}Ir: Janzen *et al.* (1987b), ^{182}Pt: Popescu *et al.* (1986), and ^{183}Au (this work).)

in these two bands, the sharp band crossings in the yrast band of ^{182}Pt and the $\pi i_{13/2}$ band of ^{183}Au are most probably due to the alignment of a pair of $i_{13/2}$ quasineutrons. Therefore, if one is to interpret the gentle upbends which precede the $\nu i_{13/2}$ alignment as band crossings, the most obvious candidate based on the analysis of the previous chapter is the $h_{9/2}$ quasiproton alignment. However, caution should be taken when interpreting these smooth upbends as conventional alignment processes. As was shown in chapter 5, examples where the nucleus appears to smoothly gain alignment, followed by a sharp upbend is also observed in some Os nuclei. It was also shown that the yrast bands of the Os nuclei all converge to the same value of I_x after the first backbend even though the I_x plots suggest that ^{178}Os and ^{180}Os may experience more than one alignment at low rotational frequency. The fact that the $h_{9/2}$ quasiproton alignment is observed at higher rotational frequencies in ^{180}Os indicates that a single $\nu i_{13/2}$ band crossing is responsible for low frequency alignment even though the alignment diagrams suggest otherwise.

The Au TRS maps are difficult to interpret in the regions of band crossings due to a number of different configurations which lie close together in energy. In order to simplify matters, we have made CSM calculations using the deformation parameters listed in Table 6.1. Fig. 6.7 shows two sets of these calculations for ^{183}Au and ^{187}Au using deformation parameters associated with the $\pi i_{13/2}$ configuration. The pairing for the quasiproton diagrams has been decreased by 20% of the self-consistent value in order to compensate for pair blocking due to the odd proton.

In section 5.3, Fig. 5.5 shows that in ^{187}Au the $\pi i_{13/2}$ configuration experiences a crossing at $\hbar\omega \approx 0.23$ MeV while the $\pi h_{9/2}$ band shows no alignment until 0.40 MeV, leading to the conclusion that the low frequency alignment is due to $h_{9/2}$ quasiprotons. However, the CSM calculations predict that this crossing

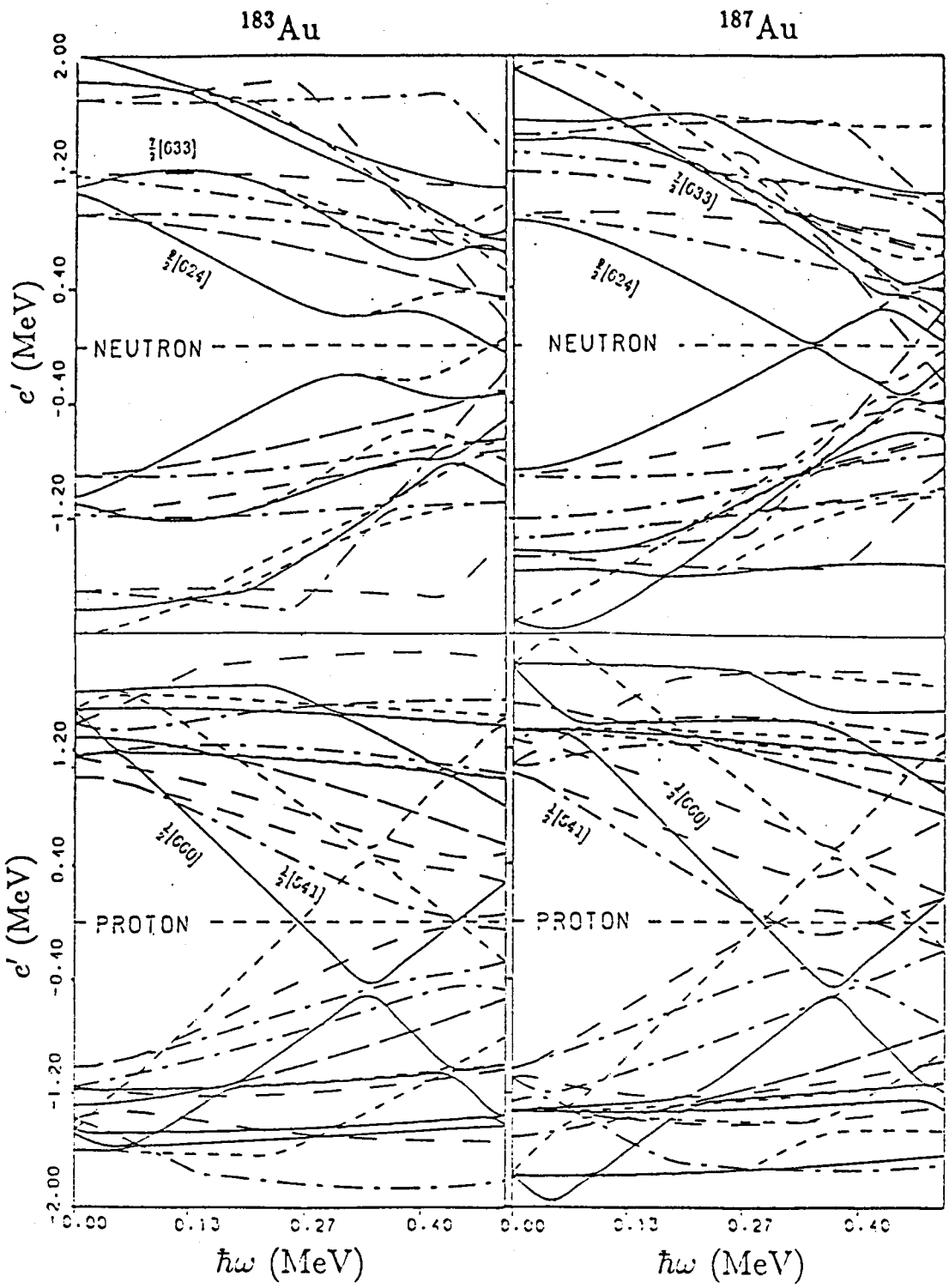

Figure 6.7: Wood-Saxon quasiparticle diagrams using deformations extracted from the TRS-calculations for the $\pi i_{13/2}$ configuration in ^{183}Au and ^{187}Au.

also does not occur until $\hbar\omega \approx 0.35$ MeV. On the other hand, the calculations predict that the $i_{13/2}$ quasineutrons will not align until $\hbar\omega = 0.35$ MeV. Thus, it is not anomalous that the protons are aligning at low rotational frequency in ^{187}Au rather it is anomalous that any crossing is observed.

The fact that no neutron crossing is observed in ^{187}Au is easily explained. On each quasineutron diagram in Fig. 6.7, the $i_{13/2}$ orbitals are labeled. At ^{183}Au, the $\frac{9}{2}[624]$ and $\frac{7}{2}[633]$ orbitals lie very close to each other. This results in a mixing of low K states which is needed if a quasiparticle pair is to be aligned. At ^{187}Au, the $\frac{7}{2}[633]$ orbital lies significantly higher in energy relative to the $\frac{9}{2}[624]$ orbital. This results in less $K = \frac{1}{2}$ mixing with the AB orbitals, thus delaying the neutron crossing. The fact the neutron crossing lies so much higher than predicted may indicate that the low-K members of the $i_{13/2}$ family of states lie further away from the Fermi surface at $N = 108$ than indicated by the calculations.

The explanation for lowering the $h_{9/2}$ proton crossing is not as easily explained. If our interpretation at $N = 108$ is correct, the calculations clearly do not indicate this. In order to bring the theoretical proton crossing in line with experimental indications, both the single-particle levels and pairing constants must be re-examined and the current Woods-Saxon parameters readjusted to fit more closely the experimental data in this region. If the theoretical $\pi h_{9/2}$ crossing is lowered to agree with experimental data at $N = 108$, this should also lower the frequency of this crossing in the other Au isotopes. The difference between the $h_{9/2}$ crossing in ^{183}Au and ^{187}Au shown in Fig. 6.7 is approximately 0.05 MeV. If this crossing in ^{183}Au scales like that in ^{187}Au the predicted $h_{9/2}$ alignment in ^{183}Au would occur at $\hbar\omega \approx 0.28$ MeV. This is precisely where the smooth upbend in the $\pi i_{13/2}$ band occurs. The $h_{9/2}$ interaction strength is also quite large for ^{183}Au as shown in Fig. 6.7 which also agrees with what is observed experimentally.

CHAPTER 7

SUMMARY AND CONCLUSIONS

This thesis has presented data from measurements on ^{184}Pt and ^{183}Au , where high-spin states have been observed up to $I = 37\ \hbar$ in the former and to $I = 65/2\ \hbar$ in the latter. The Pt-Hg region centered around $N = 106$ is rich in nuclear shapes and structures. The shell-structure of the region is such that both prolate and oblate configurations compete in energy, resulting in shape-coexistence within the same nucleus. The results presented in this work have concentrated on establishing the quasiparticle content of the observed alignments in this region. Also, estimations of the nuclear shape have been made by comparing spectroscopic data with the results of Strutinsky-HFBC calculations, which allow for a self-consistent determination of the nuclear shape parameters as a function of rotational frequency and quasiparticle configuration.

In summary, ^{184}Pt lies in the transitional mass region of soft nuclei, where different quasiparticles polarize the nuclear shape in different ways, leading to large shape variations. This point is well illustrated in Fig. 5.11 where it is shown that the calculated equilibrium deformations for different bands cover a considerable part of the deformation (β_2, γ) plane. While not discussed in great detail, it should also be noted that large variations in β_4 as a function of configuration were also observed. Of the seven newly observed side bands, one (band 2) is assigned an initial two-quasiproton configuration and four (bands 3-6) to two-quasineutron structures. Calculations suggest that these latter bands have equilibrium γ-values which are rather negative, while the former should have positive γ deformations. Transitions observed between bands 2 and 5 allow an extraction of the mixing matrix element, which is small and consistent with the different shape parameters suggested by the calculations. A quasiparticle configuration for band 7 has been

suggested, but this assignment is not certain due to the lack of similar bands being observed in neighboring nuclei.

Comparison of ^{184}Pt with ^{183}Ir and ^{185}Au suggests that the yrast band in ^{184}Pt exhibits a degenerate double crossing ($\nu i_{13/2}$) and ($\pi h_{9/2}$). This interpretation is supported by the $N = 108$ systematics which indicate that the single alignment observed in these nuclei is due to $h_{9/2}$ quasiprotons. However, by comparing the yrast bands for $^{178-184}$Os with those of the Pt isotones, it appears that the yrast upbend could result from a single $(\nu i_{13/2})^2$ crossing. With current theoretical parameters, Strutinsky-HFBC calculations favor a $\nu i_{13/2}$ single-band crossing. However, in view of the apparent low $\pi h_{9/2}$ band crossing in the $N = 108$ isotones, ^{186}Pt and ^{187}Au, it seems that the fitted pairing and one-body potential parameters associated with this region should be readjusted to agree better with experimental data. For example, $B(M1)/B(E2)$ measurements in ^{185}Pt indicate that $h_{9/2}$ quasiprotons are aligning at $\hbar\omega \approx 0.3$ MeV, while current parameter calculations indicate this crossing should be delayed until $\hbar\omega > 0.35$ MeV. Such adjustments would result in a lower crossing frequency for the $h_{9/2}$ quasiprotons. Side bands 3-6 all exhibit a crossing at a similar frequency, but the exact origin cannot be concluded due to a question concerning the shape and pairing associated with these bands. Clearly, if $h_{9/2}$ quasiprotons are not aligning in the yrast band, the crossings in bands 3-6 are due to secondary $\nu i_{13/2}$ alignments, BC and AD. However, if a low-frequency $\pi h_{9/2}$ band crossing is present in ^{184}Pt, theoretical calculations indicate that either secondary quasineutron or $h_{9/2}$ quasiproton crossings are occurring below $\hbar\omega = 0.35$ MeV, depending on the shape of nucleus.

The measurement on ^{183}Au has extended the systematics of the Au region into the middle of the neutron shell, where nuclear deformations are predicted to be the largest. Our identification of rotational bands built on $\pi h_{9/2}$, $\pi i_{13/2}$, and $\pi f_{7/2}$ quasiparticle states shows that these orbitals, which lie above the lead closed

shell for spherical shapes, continue to come lower in energy with respect to the oblate configurations as the neutron number is decreased. This effect is thought to result from an increase in the quadrupole deformation as one approaches mid-shell, and TRS calculations predict this increase in deformation.

Alignment plots of the observed rotational bands in ^{183}Au indicate that the $i_{13/2}$ neutron crossing is occuring at $\hbar\omega \approx 0.35$ MeV. Both the $\pi i_{13/2}$ and $\pi f_{7/2}$ structures show a gradual increase in the alignment preceding this crossing, and this same effect observed in the yrast band of ^{182}Pt. However, it is noticeably absent from the $\pi h_{9/2}$ configuration. This blocking measurement with $h_{9/2}$ quasiprotons suggest that these quasiparticles are aligning at rotational frequencies below $\hbar\omega = 0.30$. However, the same systematic observations which argued against a low frequency $h_{9/2}$ crossing at $N = 106$ are also applicable at $N = 104$.

A close analysis of the Au nuclei reveal that the standard model is unable to explain the low frequency band crossing in ^{187}Au. Both neutrons and protons are predicted to align at $\hbar\omega \geq 0.35$ MeV. Experimental blocking measurements clearly favor a $\pi h_{9/2}$ quasiproton alignment to explain the observed band crossing at $N = 108$. The measured $B(M1)/B(E2)$ ratios for ^{185}Pt indicate that this quasiproton crossing is also present at $N = 107$. Blocking arguments using the $\pi h_{9/2}$ bands observed in Au and Ir nuclei at $N = 106$ and $N = 104$ indicate that the $h_{9/2}$ quasiproton alignment occurs low in frequency in ^{184}Pt and ^{182}Pt as well. However, due to the fact that the $h_{9/2}$ band crossing competes in frequency with the $\nu i_{13/2}$ band crossing in these Pt nuclei, it is more difficult to distinguish these crossings in the data. Even though experimental evidence has been given which seems to contradict the presence of a low-frequency $\pi h_{9/2}$ alignment at $N = 106$ and $N = 104$, the apparent observation of proton band crossings in these nuclei is reasonable in view of the establishment of this crossing in the Pt and Au nuclei at $N = 107$ and $N = 108$.

Experimentally, more direct measurements on the nuclei in this region will determine the exact quasiparticle nature of the observed crossings. Lifetime and g-factor measurements are good methods for extracting information about the nuclear wave function which would lead to a determination of the quasiparticle compostion. In conclusion, much progress has been made in the past several years on interpreting the high-spin data in this difficult transitional region. From all available data, it seems rather clear that the $\frac{1}{2}[541]$ quasiprotons are aligning at rotational frequencies below $\hbar\omega = 0.35$ in prolate bands in the neutron deficient Pt-Au isotopes. However, it is unclear whether this alignment persists for the more neutron deficient nuclei. Certainly, more high-spin measurements on nuclei farther from stablility in this region should help address these questions.

BIBLIOGRAPHY

BIBLIOGRAPHY

Andersson, C. G., S. E. Larsson, G. Leander, P. Möller, S. G. Nilsson, I. Ragnarsson, S. Åberg, R. Bengtsson, J. Dudek, B. Nerlo-Pomorska, K. Pomorski and Z. Szymański, 1976, Nucl. Phys. **A268**, 205.

Baktash, C., Y. Schutz, I. Y. Lee, F. K. McGowan, N. R. Johnson, M. L. Halbert, D. C. Hensley, M. P. Fewell, L. Courtney, A. J. Larabee, L. L. Riedinger, A. W. Sunyar, E. der Mateosian, O. C. Kistner, and D. G. Sarantites, 1985, Phys. Rev. Lett. **54**, 978.

Bardeen, J., L. N. Cooper and J. R. Schrieffer, 1957, Phys. Rev. **108**, 1175.

Barfield, A. F. and B. R. Barret, 1984, Phys. Lett. **149B**, 277.

Bass, R., 1980, *Nuclear Reactions with Heavy Ions* (Springer-Verlag, Berlin).

Bengtsson, R., S. E. Larsson, G. Leander, P. Möller, S. G. Nilsson, S. Åberg and Z. Szymański, 1975, Phys. Lett. **57B**, 301.

Bengtsson, R. and S. Frauendorf, 1979a, Nucl. Phys. **A314**, 27.

Bengtsson, R. and S. Frauendorf, 1979b, Nucl. Phys. **A327**, 139.

Bengtsson, R. and J. D. Garrett, 1983, *International Review of Nuclear Physics*, Vol. 2, ed. T. Engeland, J. Rekstad and J. S. Vaagen (World Scientific, Singapore)

Bengtsson, R., J.-y. Zhang, J. H. Hamilton and L. K. Peker, 1986, J. Phys. G. **12**, L223.

Bengtsson, R., T. Bengtsson , J. Dudek, G. Leander, W. Nazarewicz and J.-y. Zhang, 1987, Phys. Lett. **183B**, 1.

Berg, V., Z. Hu, J. Oms and C. Ekström, 1983, Nucl. Phys. **A410**, 445.

Beshai, S., K. Fransson, S. Hjorth, A. Johnson, Th. Lindblad and J. Sztarkier,

1976, Z. Phys. **A277**, 351.

Blatt M. and V. F. Weisskopf, 1952, *Theoretical Nuclear Physics* (Springer, Berlin).

Bohr, A. and B. R. Mottelson, 1969 and 1975, *Nuclear Structure*, Vols. 1 and 2 (Benjamin, New York).

Bohr, A. and B. R. Mottelson, 1981, Phys. Scr. **24**, 71 (*Nuclei at Very High Spin—Sven Gösta Nilsson in Memoriam*, Proceedings, Nobel Symposium, Örenäs, 1980, ed. G. Leander and H. Ryde).

Bohr, N. and F. Kalckar, 1937, Mat.-Fys. Medd. Dan. Vidensk. Selsk. **14**, no. 10; reprinted in *Niels Bohr's Collected Works*, 1986, ed. E. Rudinger (North Holland, Amsterdam) Vol. 9, p. 225.

Bonn, J., G. Huber, H.-J. Kluge, L. Kugler and E.-W. Otten, 1972, Phys. Lett. **38B**, 308.

Bourgeois, P. Kilcher, B. Roussiere, J. Sauvage-Letessier and M. G. Porquet, 1982, Nucl. Phys. **A386**, 308.

Burde, J., R. M. Diamond and F. S. Stephens, 1966, Nucl. Phys. **A85**, 451.

Burde, J., R. M. Diamond and F. S. Stephens, 1967, Nucl. Phys. **A92**, 306.

Butler, P. A. and P. J. Nolan, 1981, Nucl. Inst. Meth. **190**, 283.

Cailliau, M., R. Foucher, J. P. Husson and J. Letessier, 1974, Journal de Phys. **35**, 469.

Carpenter, M. P., C. R. Bingham, L. H. Courtney, S. Juutinen, A. J. Larabee, Z.-m. Liu, L. L. Riedinger, C. Baktash, M. L. Halbert, N. R. Johnson, I. Y. Lee, Y. Schutz, A. Johnson, J. Nyberg, K. Honkanen, D. G. Sarantites and D. R. Haenni, 1985, Bull. Am. Phys. Soc. **30**, 762.

Carpenter, M. P., C. R. Bingham, L. H. Courtney, S. Juutinen, A. J. Larabee, Z.-m. Liu, L. L. Riedinger, Z.-y. Zhang, J. Nyberg, A. Johnson, C. Baktash, M. L. Halbert, N. R. Johnson, I. Y. Lee, Y. Schutz, K. Honkanen, D. G. Sarantites and D. Haenni, 1986, in *Proceedings of the XXIV International Meeting on Nuclear Physics, Bormio, Italy.*

Carpenter, M. P., C. R. Bingham, L. H. Courtney, V. P. Janzen, A. J. Larabee, Z.-m. Liu, L. L. Riedinger, W. Schmitz, R. Bengtsson, T. Bengtsson, W.

Nazarewicz, J.-y. Zhang, J. K. Johansson, D. Popescu, J. C. Waddington, C. Baktash, M. L. Halbert, N. R. Johnson, I. Y. Lee, Y. Schutz, J. Nyberg, A. Johnson, J. DeBuc, S. Monaro, S. Pilotte, K. Honkanen, D. G. Sarantites and D. Haenni, 1987, University of Tennessee preprint and to be published.

Carpenter, M. P., C. R. Bingham, L. H. Courtney, V. P. Janzen, L. L. Riedinger, W. Schmitz, J. K. Johansson, D. G. Popescu, D. D. Rajnauth, J. C. Waddington, J. DeBuc, G. Kajrys, S. Monaro, S. Pilotte, 1987b, Bull. Am. Phys. Soc. **34**, 1110.

Chen, Y. S. and G. A. Leander, 1986, University of Tennessee Progress Report, p. 90.

Cohen, S., F. Plasil, and W. J. Swiatecki, 1974, Ann. Phys. **82**, 557.

Damgaard, J., H. C. Pauli, V. V. Pashkevich and V. M. Strutinsky, 1969, Nucl. Phys. **A135**, 432.

Dönau, F. and S. Frauendorf, 1982, in *High Angular Momentum Properties of Nuclei*, ed. by N. R. Johnson (Harwood Academic, New York) p. 143.

Dracoulis, G. D., C. Fahlander and M. P. Fewell, 1980, Phys. Rev. Lett. **45**, 1831.

Dracoulis, G. D., A. E. Stuchbery, A. P. Byrne, A. R. Poletti, J. Ger and R. A. Bark, 1986, J. Phys. G **12**, L97.

Dudek, J. and T. Werner, 1978, J. Phys. G **4**, 1543.

Dudek, J., A. Majhofer, J. Skalski, T. Werner, S. Cwiok and W. Nazarewicz, 1979, J. Phys. G **5**, 1359.

Dudek, J., Z. Szymanski, and T. Werner, Phys. Rev. **C23** (1981) 920.

Dudek, J., 1983, *Selected Aspects of the Nuclear High-Spin Structure (Part I)*, CRN preprint, Strasbourg.

Dudek, J., 1987, *Superdeformed Nuclear Shapes: New Features, Systematics and Predictions*, CRN preprint, Strasbourg.

Ekstrom, C., I. Lindgren, S. Ingelman, M. Olsmats and G. Wannberg, 1976, Phys. Lett. **60B**, 146.

Fahlander, C. and G. D. Dracoulis, 1982, Nuc. Phys. **A375**, 263.

Ferentz, M. and N. Rosenzweig, 1955, Argonne National Laboratory, ANL-5324 (unpublished).

Finger, M., R. Foucher, J. P. Husson, J. Jastrzebski, A. Johnson, G. Astner, B. R. Erdal, A. Kjelberg, P. Patzelt, A. Hoglund, S. G. Malmskog and R. Henck, 1972, Nucl. Phys. **A188**, 369.

Frahn, W. E. and K. E. Rehm, 1978, Annals of Physics **24**, 243.

Frauendorf, S. and F. R. May, 1983, Phys. Lett. **125B**, 245.

Frauendorf, S., L. L Riedinger, J. D. Garrett, J. J. Gaardhoje, G. B. Hagemann and B. Herskind, 1984, Nuc. Phys. **A431**, 511.

Gallagher, C. J. and H. L. Nielson, 1962, Phys. Rev. **126**, 1520.

Garg, U., A. Chaudhury, M. Drigert, E. Funk, J. Mihelich, D. Radford, H. Helppi, R. Holzmann, R. Janssens, T. L. Khoo, A. M. Van Den Berg and J. L. Wood, 1986, Phys. Lett. **180B**, 319.

Garrett, J. D., 1984, presented at Nuclear Structure Workshop at Risö, Niels Bohr Institute.

Garrett, J. D., 1986, presented at the International School of Heavy Ion Physics, Erice, Italy, Niels Bohr Institute preprint.

Glagola, B. G., B. B Back and R. R. Betts, 1984, Phys. Rev. **C29**, 486.

Goodman, A. L., 1974, Nucl. Phys. **A230**, 466.

Grover, J. R., 1967, Phys. Rev. **157**, 832.

Harris, S. M., 1965, Phys. Rev. **138**, 509B.

Herskind, B., 1984, talk given at the Workshop on Electromagnetic Properties of High Spin Nuclear Levels, Israel, Niels Bohr Institute preprint.

Hillis, D. L., J. D. Garrett, O. Christensen, B. Fernandez, G. B. Hagemann, B. Herskind, B. B. Back and F. Folkmann, 1979, Nucl. Phys. **A325**, 216.

Inglis, D. R., 1954, Phys. Rev. **96**, 1059.

Inglis, D. R., 1955, Phys. Rev. **97**, 701.

Jääskeläinen, M., D. G. Sarantites, R. Woodward, F. A. Dilmanian, R. Jääskeläinen, M. L. Halbert, D. C. Hensley and J. H. Barker, 1983, Nucl. Instr. and Meth. **204**, 385.

Jacobi, C. G. J., 1834, Poggendorf Annalen der Physik und Chemie 33, 229; reprinted in *Gesammelte Werke 2* (Reimer, 1882, Berlin) p. 17.

Janzen, V. P., Z. M. Liu, M. P. Carpenter, L. H. Courtney, A. J. Larabee, L. L. Riedinger, J. K. Johansson, D. G. Popescu and J. C. Waddington, 1986, University of Tennessee Progress Report, p. 36.

Janzen, V. P., D. D. Rajnauth, J. K. Johansson, G. Kajrys, D. Popescu, J. C. Waddington, C. R. Bingham, M. P. Carpenter, L. H. Courtney, L. Cuellar, L. L. Riedinger, W. Schmitz, J. DeBuc, S. Monaro and S. Pilotte, 1987, University of Tennessee preprint.

Janzen, V. P., C. R. Bingham, M. P. Carpenter, K. Hart, H. Q. Jin, L. L Riedinger, L. Zhou, C. Baktash, M. L. Halbert, N. R. Johnson, I. Y. Lee, F. K McGowan, M. A. Riley, 1987, ORNL Physics Division Progress Report for the Period Ending September 30, 1987, in press.

Jin, H., private communication.

Johansson, J. K., 1987, *High-Spin States and Deformation Changes in* ^{187}Au, (McMaster University), M.Sc. dissertation.

Johnson, A., H. Ryde and S. Hjorth, 1972, Nucl. Phys. **A179**, 753.

Johnson, N., I. Y. Lee, C. Baktash, F. K. McGowan, J. W. Johnson, R. P. Cumby, D. C. Hensley, M. L. Halbert, L. L. Riedinger, D. G. Sarantites, J. W. McConnell and M. E. Whitley, 1985, ORNL Physics Division Progress Report for the Period Ending September 30, 1985, p. 158.

Kahler, A. C., L. L. Riedinger, N. R. Johnson, R. L. Robinson, E. F Zganjar, A. Visavanathan, D. R. Zolnowski, M. B. Hughes and T. T. Sugihara, 1978, Phys. Lett. **72B**, 443.

Krane, K. S., 1972, Nucl. Inst. Meth. **98**, 205.

Krane, K. S., R. M Steffen and R. M. Wheeler, 1973, Nuclear Data Tables **A11**, 351.

Larabee A. J., M. P. Carpenter, L. L. Riedinger, L. H. Courtney, J. C. Waddington,

V. P. Janzen, Y. Liang, and G. Leander, 1984, Phys. Lett. **29**, 1049.

Larabee A. J., M. P. Carpenter, L. L. Riedinger, L. H. Courtney, J. C. Waddington, V. P. Janzen, W. Nazarewicz, J.-y. Zhang, R. Bengtsson and G. Leander, 1986, Phys. Lett. **169B**, 21.

Leander, G. A., S. Frauendorf and F. R. May, 1982, in *High Angular Momentum Properties of Nuclei*, ed. by N. R. Johnson (Harwood Academic, New York) p. 281.

Lieder, R. M. Lieder, G. Sletten, J. Borggreen and J. Pedersen, 1982, Nuc. Phys. **A375**, 291.

Lieder, R. M., private communication.

Lieder, R. M., A. Neskakis, J. Skalski, G. Sletten, J. D. Garrett and J. Dudek, 1987, Jülich preprint (to be published).

Macias-Marques, M. I., C. Bourgeois, P. Kilcher, B. Roussiére, J. Sauvage and M. C. Abreu, 1984, Nucl. Phys. **A427**, 205.

Mariscotti, M. A. J., G. Scharff-Goldhaber and B. Buck, 1969, Phys. Rev. **178**, 1864.

Mottelson, B. R. and J. G. Valatin, 1960, Phys. Rev. Lett. **5**, 511.

Nazarewicz, W., J. Dudek, R. Bengtsson, T. Bengtsson and I. Ragnarsson, 1985, Nuc. Phys. **A435**, 397.

Nazarewicz, W., 1986, in *International Conference on Nuclear Structure, Reactions and Symmetries, Dubrovnik, Yugoslavia* (preprint).

Neskakis, A., R. M. Lieder, M. Muller-Veggian, H. Beuscher, W. F. Davidson and C. Mayer-Böricke, 1976, Nuc. Phys. **A261**, 189.

Newton, J. O., B. Herskind, R. M. Diamond, E. L. Dines, J. E. Draper, K. H. Lindenberger, C. Schuck, S. Shih and F. S. Stephens, 1981, Phys. Rev. Lett. **46**, 1383.

Nilsson, S. G., 1955, K. Dan. Vidensk. Selsk. Mat. Fys. Medd. **29**, No. 16, 1.

Nilsson, S. G., C. F. Tsang, A. Sobiczewski, Z. Szymański, S. Wyceck, G. Gustafson, I. L. Lamm, P. Möller, and B. Nilsson, 1969, Nucl. Phys. **A131**, 1.

Nyako, B. M., J. Simpson, P. J. Twin, D. Howe, P. D. Forsyth and J. F. Sharpey-Schafer, 1986, Phys. Rev. Lett. **56**, 2680.

Nyberg, J., A. Johnson, M. P. Carpenter, C. R. Bingham, L. H. Courtney, V. P. Janzen, S. Juutinen, A. J. Larabee, Z.-m. Liu, L. L. Riedinger, C. Baktash, M. L. Halbert, N. R. Johnson, I. Y. Lee, Y. Schutz, K. Honkanen, D. G. Sarantites and D. R. Haenni, 1987, to be submitted to Nucl. Phys. A.

Palameta, G. and J. C. Waddington, 1985, Nucl. Instr. Meth. **A234**, 476.

Pilotte, S., J. DeBuc, S. Monaro, V. P. Janzen, M. P. Carpenter, L. L. Riedinger, J. K. Johansson, D. Popescu and J. C. Waddington, 1986, McMaster Accelerator Laboratory Ann. Rep., 26, and to be published.

Pilotte, S., 1987, *Étude de la Déformation des Noyaux de* $^{185,186}Pt$, (Université de Montréal, Doctoral dissertation.

Popescu, D., J. K. Johansson, J. C. Waddington, V. P. Janzen, M. P. Carpenter, L. L. Riedinger, S. Pilotte, J. DeBuc and S. Monaro, 1986, McMaster Accelerator Laboratory Ann. Rep., 26, and to be published.

Preston, M. A. and R. K. Bhaduri, 1975, *Structure of the Nucleus*, (Addison-Wesley, Reading, Massachusetts).

Ragnarsson, I., T. Bengtsson, W. Nazarewicz, J. Dudek, and G. A. Leander, 1985, Phys. Rev. Lett. **54**, 982.

Riedinger, L. L., A. J. Larabee and J.-y. Zhang, 1986a, in *Nuclei Off the Line of Stability*, ed. by R. A. Meyers and D. S. Brenner, p.323.

Riedinger, L. L., M. P. Carpenter, L. H. Courtney, V. P. Janzen and W. Schmitz, 1986b, in *Proceedings of Beijing International Symposium on Physics at Tandem*, ed. by J. Chenglie, L. Shounan, S. Zuxun and Z. Huanqiao (World Scientific, Singapore) p. 469.

Riedinger, L. L., V. P. Janzen and M. P. Carpenter, 1987a, in *Proceedings of the XXII Winter School on Physics*, Zakopane, Poland, in press.

Riedinger, L. L., M. P. Carpenter, L. H. Courtney and V. P. Janzen, 1987b, Nucl. Instr. and Meth. **B24/25** 468.

Riezebos, H. J., 1987, *Shape Coexistence and Shape Change Phenomena in Dy and Pt Isotopes from Low to Very High Angular Momentum*, (Drukkerij Van

Denderen, B.V., Groningen), Doctoral dissertation.

Riley, M. and W. Nazarewicz, 1987, to be published.

Riley, M. A., 1984, *Discrete Line Gamma-Ray Spectroscopy up to Spin 45ħ in the N = 90 Isotones* ^{156}Dy *and* ^{158}Er, (University of Liverpool), Doctoral dissertation.

Ring, P. and P. Schuck, 1980, *The Nuclear Many-Body Problem*, (Springer-Verlag, New York).

Rose, H. J. and D. M. Brink, 1967, Rev. Mod. Phys. **39**, 306.

Sarantites, D. G., M. Jääskeläinen, J. T. Hood, R. Woodward, J. H. Barker, D. C. Hensely, M. L. Halbert and Y. D. Chan, 1980, J. Phys. (Paris) Colloq. **41**, 269 (International Conference on Nuclear Behavior at High Angular Momentum, Strasbourg).

Satchler, G. R., 1980, *Introduction to Nuclear Reactions* (John Wiley and Sons, New York).

Simon, R. S., 1980, J. Phys. (Paris) Colloq. **41**, 281.

Stephens, F. S. and R. S. Simon, 1972, Nucl. Phys. **A183**, 257.

Strutinsky, V. M., 1968, Nucl. Phys. **A122**, 1.

Szymański, Z., 1983, *Fast Nuclear Rotation*, (Clarendon Press, Oxford).

Twin, P. J., B. M. Nyako, A. H. Nelson, J. Simpson, M. A. Bentley, H. W. Cranmer-Gordon, P. D. Forsyth, D. Howe, A. R. Mokhtar, J. D. Morrison, J. F. Sharpey-Schafer and G. Sletten, 1986, Phys. Rev. Lett. **57**, 811.

Twin, P. J., 1987, presented at the International School of Physics "Enrico Fermi" on Trends in Nuclear Physics, Daresbury Laboratory preprint.

Ulm, G., S. K. Bhattacherjee, P. Dabkiewicz, G. Huber, H.-J. Kluge, T. Kühl, H. Lochmann, E.-W. Otten, K. Wendt, S. A. Ahmad, W. Klempt, R. Neugart and the ISOLDE Collaboration, 1986, Z. Phys. **A325**, 247.

Vergnes, M., G. Rotbard, G. Ronsin and J. Kalifa, 1965, Phys. Lett. **18**, 325.

Voigt, M. J. A. de, J. Dudek and Z. Szymański, 1983, Rev. Mod. Phys. **55**, 949.

Wallmeroth, K., G. Bollen, A. Dohn, P. Egelhof, J. Grüner, F. Lindenlauf, U. Krönert, J. Campos, A. Rodriquez Yunta, M. J. G. Borge, A. Venugopalan, J. L. Wodd, R. B. Moore and H.-J. Kluge, 1987a, Phys. Rev. Lett. **58**, 1516.

Wallmeroth, K., G. Bollen, M. J. G. Borge, J. Campos, A. Dohn, P. Egelhof, H.-J. Kluge, U. Krönert, R. B. Moore, A. Rodriguez, A. Venugoplan, J. Wood and the ISOLDE Collaboration, 1987b, in *Proceedings of the 5th International Conference on Nuclei far from Stability*, Rosseau Lake, Canada, in press.

Wapstra, A. H., and G. Audi, 1985, Nucl. Phys. **A432**, 1.

Ward, D., H. R. Andrews and J. S. Geiger, 1984, Chalk River Nuclear Laboratory Report, TASCC-1-19-07 (unpublished).

Woods, R. D. and D. S. Saxon, 1954, Phys. Rev. **95**, 577.

Wood. J, 1982, in *Lasers in Nuclear Physics*, (Harwood Academic, New York), ed. C. E. Bemis and H. K. Carter, p. 481.

Yamazaki, T., 1967, Nuclear Data Table **3**, 1.

Zganjar, E. F., C. D. Papanicolopoulos, J. L. Wood, R. A. Braga, R. W. Fink, A. J. Larabee, M. Carpenter, D. Love, C. R. Bingham, L. L. Riedinger and J. C. Waddington, 1986, in *Nuclei off the Line of Stability*, ed. by R. Meyer and D. Brenner (American Chemical Society, Washington) p. 245.

Zhang, J.-y., L. L. Riedinger and J. D. Garrett, 1983, Phys. Rev. **C28**, 446.

Zhang, J.-y., A. J. Larabee and L. L. Riedinger, 1987, J. Phys. G **13**, L75.

VITA

Michael Patten Carpenter was born in Pittsburgh, Pennsylvania on August 19, 1960. His entire primary and secondary education was spent in the Churchill Area school system until his graduation from Churchill Area High School in June 1978. In the fall of 1978, he entered Dickinson College, a small liberal arts college located in Carlisle, Pennsylvaina, and in May 1982 he received his Bachelor of Science degree in both Physics and English. The following September he accepted a teaching assistanthsip at The University of Tennessee, Knoxville in the Department of Physics and Astronomy. At the same time he began his studies towards a Doctoral degree in Physics. In the spring of 1983, he began working as a research assistant with the nuclear phyiscs group at the university. On March 16, 1985, he married Janice Marie Grissom.

The author currently is a member of Beta Theta Pi, Sigma Pi Sigma and the American Physical Society. He is presently employed through a joint collaberation by the University of Tennessee and the Niels Bohr Institute.